AN ABSTRACT OF THE DISSERTATION OF

Jun Li for the degree of Doctor of Philosophy in Chemistry presented on March 18, 2005.

Title: Synthesis, Structure and Properties of Some Transition Metal Oxides

Abstract approved: Redacted for privacy

Arthur W. Sleight

Transition metal oxides possess optical, electric, dielectric, magnetic, thermal, catalytic and many other properties with fascinating structure-property relations.

For the transparent p-type conducting oxides $CuScO_{2+y}$, $CuSc_{1-x}Mg_xO_2$ and $CuSc_{1-x}Mg_xO_{2+y}$ the limits of $x$ and $y$ were determined. Structural studies using neutron diffraction data established the position of the intercalated oxygen. Compositions with low $y$ were found to first gain oxygen and then lose oxygen when heated in air.

Zinc oxide powders prepared by peroxide and nitrate decomposition show the evidence of holes in the O 2*p* band by iodometric titrations and the presence of nitrogen in nitrate-derived samples by chemical analysis. Complex impedance spectra were used to determine the electrical conductivity of these powders.

The high dielectric constant in "$SrCu_3Ti_4O_{12}$" and the giant dielectric constant in $CaCu_3Ti_4O_{12}$ are rationalized on a barrier layer mechanism. Our study on ceramic samples showed that the conductivity in the conducting regions is related to Ti on Cu sites, and the insulating barriers are between the crystallites in "$SrCu_3Ti_4O_{12}$" but

within the crystallites in $CaCu_3Ti_4O_{12}$. Comfirmation was obtained by complex impedance measurements on a $CaCu_3Ti_4O_{12}$ crystal.

Spintronics is an emerging technology that combines electronics with magnetics through the manipulation of electron spins. We find that on application of a magnetic field to $La_2NiMnO_6$ there are significant changes in its electrical resistance and dielectric constant below 280 K. Our neutron diffraction studies on $La_2NiMnO_6$ confirm that it is ferromagnetic below 280 K.

Negative thermal expansion of the O–Cu–O linkage was found in $CuMO_2$ (M = La, In, Sc, Al) delafossite compounds by Rieveld analysis of neutron diffraction data. The behavior was especially strong for $CuLaO_2$ ($\alpha = -6.3 \times 10^{-6}$/K) and $CuScO_2$ ($\alpha = -4.5 \times 10^{-6}$/K) up to 600 K. This is an unusual example of strong negative thermal expansion in a metal oxide based on an O–M–O linkage instead of an M–O–M linkage.

Orthorhombic β-$AgAlO_2$ was prepared by an ion-exchange reaction. The structure was characterized by neutron powder diffraction and all the positional parameters were reported for the first time. Structural systematics of tetrahedral $MM'X_2$ compounds were carefully examined.

# Synthesis, Structure and Properties of Some Transition Metal Oxides

by
Jun Li

A DISSERTATION

submitted to

Oregon State University

in partial fulfillment of
the requirements for the
degree of

Doctor of Philosophy

Presented March 18, 2005

Commencement June 2005

Doctor of Philosophy dissertation of Jun Li presented on March 18, 2005.

APPROVED:

Redacted for privacy

Major Professor, representing Chemistry

Redacted for privacy

Chair of the Department of Chemistry

Redacted for privacy

Dean of the Graduate School

I understand that my dissertation will become part of the permanent collection of Oregon State University libraries. My signature below authorizes release of my dissertation to any reader upon request.

Redacted for privacy

Jun Li, Author

# ACKNOWLEDGEMENTS

This dissertation could never have been written without help from numerous individuals. To each and all of those involved directly or indirectly, my sincere thanks.

First and foremost, I would like to express my heartfelt and everlasting gratitude to my advisor, Dr. Arthur W. Sleight, for his outstanding guidance, endless patience and constant support over the past few years. My research work was made so much easier by his profound knowledge, preeminent wisdom and invaluable input, to which I shall be forever indebted. It is my great honor to be the last student of him, a world-class scientist and a great teacher.

I am also deeply grateful to Dr. Douglas Keszler, Dr. Janet Tate, Dr. Glenn Evans, Dr. Philip Watson, and Dr. William Warren for serving in my graduate committee. Beyond that, Dr. Keszler and Dr. Watson taught me classes, Dr. Tate and Dr. Warren collaborated in my projects, Dr. Evans had interesting discussion with me and impressed me with his great sense of humor and sharp questions. I wish to thank all of them for their earnest teachings as well as the wonderful time they shared with me.

A special acknowledgement is made to Dr. Alexandre F. T. Yokochi, who taught me the basics of crystallography and introduced me to various software on Rietveld method. His expertise and inspiration have facilitated this work in countless ways.

There are a number of people in Sleight's group to whom I owe a debt of gratitude for different kinds of help at various stages: Tammy, Uma, Niangao, Tao, Raj, Rebecca, Vanaja, Sasha and Masa. I also received enthusiastic support from friends

and colleagues in Chemistry: Cheol-Hee, Ning, Sangmoon, Jeremy, Joa-Young, Heather, Peter, Bahar, Wei, Nipaka, Watcharee, Guoqiang and Bin, to name but a few.

The author wants to express sincere appreciation to all who have contributed substantially in one way or another to this dissertation. My greatest thanks go to Dr. M.A. Subramanian for assisting with synthesis and characterization of $SrCu_3Ti_4O_{12}$ and $La_2NiMnO_6$, whose extraordinary expertise and professional diligence enormously enriched this work. I am much indebted to Drs. B.H. Toby, C.Y. Jones and J.K. Stalick for collecting neutron diffraction data for many of my samples at NIST and for the helpful discussions. Drs. N.S. Rogado and H.D. Rosenfeld assisted in getting magnetization and synchrotron data. Dr. Tate, Robert, Ben, Andrew and Jayaraj were involved in $CuScO_2$ and/or ZnO projects, their contributions have been of inestimable value. Dr. Rochefort, Dr. Lerner, Dr. Pastorek and Dr. Chang kindly allowed me to use their equipments, and Dr. Lerner offered guidance on initial impedance measurements. I am especially obliged to Dr. Lioubov Kabalnova for her time and great help with BET and SEM measurements. Thanks are also tendered to Dr. Q.Z Huang, Dr. J. Cui and Dr. P. Woodward for their assistance with solving the magnetic structure, and to Dr. Wakimoto and Dr. Ramirez for supplying the CCTO crystal.

I acknowledge Chemistry Department for giving me the chance to study and live in this beautiful small town whose fresh berries I am so in love with. The department staff provided me with the strongest support ever that is truly appreciated.

Last, with love and gratitude I thank my father, mother, sister and niece for always standing behind me throughout the years of my graduate study. It is their love, encouragement and trust that enabled me to pursue and complete this very degree.

# TABLE OF CONTENTS

Page

TABLE OF CONTENTS (Continued)

TABLE OF CONTENTS (Continued)

# LIST OF FIGURES

LIST OF FIGURES (Continued)

## LIST OF FIGURES (Continued)

LIST OF FIGURES (Continued)

LIST OF FIGURES (Continued)

## LIST OF FIGURES (Continued)

# LIST OF TABLES

# Synthesis, Structure and Properties of Some Transition Metal Oxides

## Chapter 1

## Introduction

### 1.1 Transition Metal Oxides

No other class of materials has as much versatility as the oxides. Oxides have many interesting properties: magnetic, ferroelectric, insulating, conducting, optical, catalytic, and many more. There is no reason to believe we have exhausted the possibility of exciting new properties with oxides [1].

Transition metal oxides have a long and distinguished history. They are known for their enormous range of electronic properties as insulators, semiconductors, metals and high-temperature superconductors [2]. Some new interest in their thermal behavior has been aroused due to the discovery of negative thermal expansion of $ZrW_2O_8$ over a wide temperature range [3].

In ternary and more complex transition metal oxides, the additional metallic elements may be from the pre-transition, inner-transition, or post-transition groups. The compounds studied in this work are: $CuScO_2$, $CuLaO_2$, $CuAlO_2$, $CuInO_2$, $AgInO_2$, $AgAlO_2$, $SrCu_3Ti_4O_{12}$, $CaCu_3Ti_4O_{12}$, $La_2NiMnO_6$ and ZnO. The different properties exhibited strongly correlate to their structure and chemical environment.

## 1.2 p-type Semiconductivity

Materials that are good electrical conductors are not in general optically transparent, yet a combination of high conductivity and transparency is desirable for a wide variety of emerging optoelectronic applications.

Transparent conductors (TCs) are used as transparent electrodes for solar cells and flat-panel displays. Their ability to reflect thermal infrared heat is exploited to make energy-conserving (low-emissivity) windows. Airplane windows and automobile windshields use them for electrical defrosting. Touch-sensitive control panels such as ATM screens are etched from TC layers. Electromagnetic signals can be blocked by EMI/RFI shielding formed by TCs to prevent eavesdropping on computers and communications. Conductive AR coatings consisting of TCs can increase substrate transmission and reduce surface reflection over a specific wavelength range [4].

TCs can be made from ultra thin metal films, metal oxide/metal/metal oxide or semiconducting metal oxide films. Most of the TCs, however, are made from transparent conducting oxides (TCOs) due to their stability and durability, combined with a good balance between conductivity and transmissivity.

The first TCO thin film was made in 1907 [5]. Since then, TCOs have become vital components of products ranging in size from a semiconductor chip to architectural coatings. They may not be the critical performance-limiting factor at the present time for many of the applications, but they soon will be for the next generation devices.

### *1.2.1 Definition and Criteria*

What is a transparent conductor? By definition, a conductor with high transparency to visible light and high electrical conductivity. More precisely, TCs should have visible transmission more than 70%, electrical conductivity more than $10^3$ $S \cdot cm^{-1}$, and carrier density more than $10^{17}$ $cm^{-3}$ while maintaining a decent mobility.

High transparency is favored by a wide band gap. Metal oxides frequently have wide band gaps due to the ionic nature of the chemical bonds formed between the metallic cations and the oxide ions. But the ionic bonds, on the other hand, tend to enhance localization of the charge carriers.

Mathematically, conductivity is a function of mobility and free carrier concentration:

$$\sigma = N \cdot \mathrm{e} \cdot \mu$$

where $\sigma$ is conductivity, $S \cdot cm^{-1}$; $N$ is carrier concentration, $cm^{-3}$; e is electron charge, $1.602 \times 10^{-19}$ coul; and $\mu$ is mobility, $cm^2/V \cdot s$. There is generally a tradeoff between these properties. Making a layer thinner increases the transparency but also increases the electrical resistance. High carrier concentration will lower light transmission, and loss of mobility is associated with grain boundary scattering, ionized impurity (dopant) concentration, continuity of the film, lattice defect density and effective electron mass. In addition, the thin film deposition processes selected for the manufacturing of TCs play a major role in the micro-structure, mobility, carrier concentration, optical properties and durability of the films.

### *1.2.2 p-type TCOs*

The widely used TCOs all have n-type semiconductivity. They are normally oxides or doped oxides of In, Sn, Zn, Cd and Ga [6]. Tin-doped $In_2O_3$ (ITO) is a TCO of choice for most optoelectronic devices because of its high performance [7,8].

TCOs with p-type conductivity could be used to form a transparent p-n junction, which is an essential component in semiconductor devices such as diodes, transistors and LEDs. Therefore, development of p-type TCOs with a high figure of merit would open the way to new applications for next generation devices [9].

Research on p-type TCOs was initially spearheaded by work in Japan [10,11]. The first reported p-type TCO film was NiO [10]. In 1997 there was a report of another p-type TCO film with considerable improvement over NiO [11]. Various new p-type materials have been developed since then, including the $AMO_2$ (A = Cu or Ag, M = Al, Sc, In, Ga, Cr) type of ternary oxides with the delafossite structure [12-17], the nitrogen-doped or co-doped ZnO [18], and $SrCu_2O_2$ [19]. Current TCOs do not yet match the performance of their n-type counterparts. They are difficult to acceptor-dope without self-compensation (defect associates), and they tend to form large carriers with large effective masses, i.e., small polarons.

Transparent p-NiO/n-ZnO and p-$SrCu_2O_2$/n-ZnO hetero-junctions were fabricated in thin film form [10,20]. Transparent p-n homo-junction of $CuInO_2$ was also made by pulsed laser deposition technique [21]. All these indicate the potential of all-oxide transparent electronics.

### *1.2.3 p-type Delafossites*

The term delafossite comes from the mineral cuprous metaferrite, i.e. $CuFeO_2$ [22]. The p-type semiconductivity in several $CuMO_2$ (M = Al, Y, Ga, Cr) compounds with the delafossite structure (Fig. 1.1) was first observed by Benko and Koffyberg [23-26]. However, delafossite type oxides as new potential p-type TCOs did not attract too much attention until Kawazoe and co-workers prepared the thin films of $CuAlO_2$ in 1997 [11]. They believed that cations with $d^{10}$ closed shell electrons could form bonds of considerable covalency with oxygens, and the introduction of covalency to the usually ionic bonds would enhance delocalization of electrons at the valence band edge (Fig. 1.2). Ionized Cu vacancies and interstitial oxygen ions were considered to be the origin of positive holes since no acceptor was intentionally doped.

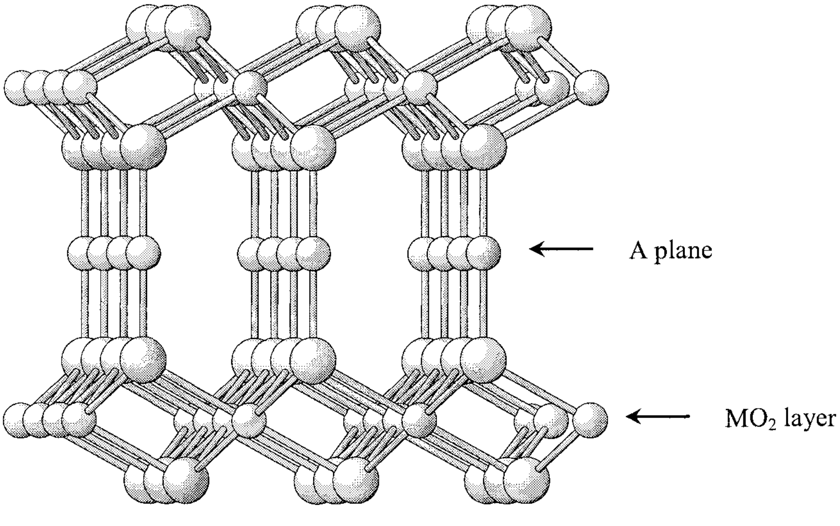

Figure 1.1 Delafossite structure of $AMO_2$ compounds, in which A is a monovalent cation ($Cu^{1+}$ or $Ag^{1+}$) and M is a trivalent cation ($Al^{3+}$, $Y^{3+}$, $Ga^{3+}$ etc.). The A planes and $MO_2$ octahedral layers are stacked alternatively along the *c* axis.

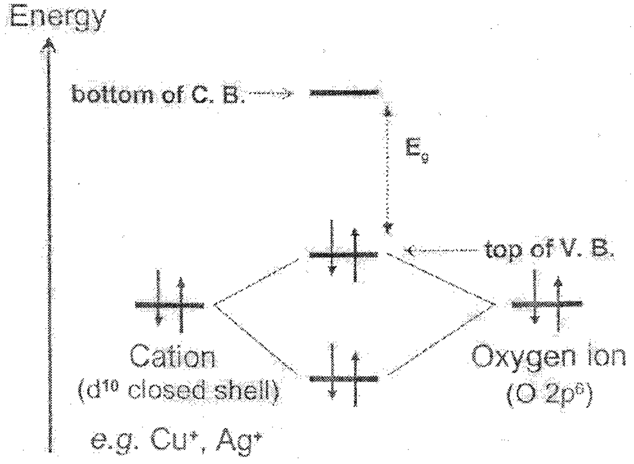

Figure 1.2 Schematic illustration of chemical bonding between an oxide ion and a cation with closed shell electronic configuration [11].

Thin film is the form required for most applications and to evaluate transparency. Thin films of $CuScO_2$ [13,27], $CuAlO_2$ [28], $CuCrO_2$ [16], $CuInO_2$ [14] and $CuGaO_2$ [29] have been reported to be p-type TCOs up to now. $CuInO_2$ was found to exhibit both p-type and n-type conduction by Ca or Sn doping [14], while n-type conductivity was observed in $AgInO_2$ [30].

The p-type conductivity of semiconducting delafossites derives from the introduction of holes into a predominantly Cu 3*d* valence band. Holes can be created by doping and/or oxygen intercalation. Doping is usually by the substitution of divalent cations onto the octahedral sites of trivalent M cations. Oxygen intercalation is the introduction of excess oxygen onto the Cu planes formed by triangle arrangement of Cu atoms in the layered delafossite structure (Fig. 1.1).

Oxygen intercalation into $CuMO_2$ (M = Sc, Y, La) has been reported [31,32] and it is apparently prohibited when the trivalent cation M is smaller than Sc. Mg substitution for Al or Ga in $CuAlO_2$ and $CuGaO_2$ thin films have failed to give any indication of success. We chose $CuScO_2$ in the present work for systematic study of the relative effectiveness of the different types of hole dopants (divalent cations vs oxygen) because divalent cations like Mg can readily substitute for Sc and $CuScO_2$ has the smallest Cu—Cu distance for which oxygen intercalation would occur. Moreover, $CuScO_2$ is known to exist in both 2H and 3R polymorphs, therefore it would be interesting to see whether these two polytypes behave differently (or not) with respect to their structure and transport properties.

## 1.3 Mixed Electronic-Ionic Conductivity

There has been a growing interest in fabrication of a p-type ZnO semiconductor for its possible applications in UV light emitters, transparent high-power electronics, surface acoustic wave device, piezoelectric transducers, and chemical and gas sensors [33-35]. Many of the p-type ZnO thin films were made by doping with N [36-38] or codoping with N and In or Ga [39-41], but the results are not very satisfactory and some are not even convincing. Zinc oxide is naturally an n-type semiconductor due to its intrinsic defects such as oxygen vacancies and interstitial Zn; p-type doping of ZnO has been proved to be very difficult.

Highly conductive n-type ZnO powders were successfully synthesized before [42,43]. In this work, attempts were made to prepare p-type ZnO powders by thermal decomposition of zinc peroxide and zinc nitrate. Impedance spectroscopy measurements showed a mixed electronic-ionic conductivity for peroxide-decomposed samples in which the grain boundaries in ZnO nanoparticles are responsible for the proton conductivity. Mixed electronic-ionic conduction properties are not unusual in transition metal oxides [44], and proton conduction in doped perovskite oxides has been the subject of extensive investigation due to the utility of such materials in hydrogen sensors, fuel cells and other solid state ionic devices [45].

## 1.4 Dielectric Properties

Dielectric materials have wide application throughout the electronics, microwave, communication and aerospace industries including: printed circuit boards, substrates, electronic and microwave components, sensor windows, microwave absorbers, wireless communication equipments, cellular base stations, radio links, wideband networks and antenna radomes and lenses.

### *1.4.1 Dielectric Constant and Loss*

Dielectrics are poor conductors of electricity and hence are widely used in capacitors and as electrical insulation. If a dielectric of relative permittivity $\varepsilon_r$ were inserted into a parallel plate capacitor whose plate area $A$ was very large, the capacity, for a plate spacing $d$ would be,

$$C = \varepsilon_0 \, \varepsilon_r \frac{A}{d}$$

Therefore,

$$\varepsilon_r = \frac{C}{C_0} = \frac{\varepsilon}{\varepsilon_0}$$

where $\varepsilon_0$ is the permittivity of free space = $8.854 \times 10^{-12}$ F/m, $\varepsilon$ the permittivity of the dielectric material, and $C_0$ the capacitance of vacuum. The relative permittivity $\varepsilon_r$ is also known as the dielectric constant $\kappa$; it is a measure of the ability of the dielectric material to store charge relative to vacuum. Strictly speaking, $\varepsilon_r$ is far from being constant, it can vary with temperature and frequency, the bonding, crystal structure, phase constitution and structural defects of the dielectric [46].

The magnitude of $\varepsilon_r$ depends on the degree of polarization or charge displacement that can occur in the material. Substances with a low dielectric constant include a perfect vacuum, dry air, and most pure, dry gases such as helium and nitrogen. Materials with moderate dielectric constants include ceramics, distilled water, paper, mica, polyethylene, and glass. Metal oxides, in general, have higher dielectric constants. At room temperature, for air, $\varepsilon_r \approx 1$ (1 kHz); for most ionic solids, $\varepsilon_r = 5$ to 10 (1 MHz); for ferroelectric materials such as $BaTiO_3$, $\varepsilon_r = 10^3$ (100 Hz) [47,48].

If the polarization lags the applied field strength, it leads to an electrical energy loss that appears as heat,

$$\text{Power loss} = \pi f V_0^2 \, \varepsilon_r \tan\delta$$

where $f$ is the frequency, $V_0$ the maximum value of the voltage, $\tan\delta$ the loss tangent or dissipation factor, and the product $\varepsilon_r \cdot \tan\delta$ the loss factor. The loss factor consequently characterizes the usefulness of a material as a dielectric or as an insulator; in both cases a low loss tangent is desirable [46].

All dielectrics lose their insulating properties when placed in an electric field with field strength exceeding certain critical value. This is called the dielectric breakdown, and dielectric strength is defined as the maximum voltage gradient which a dielectric can withstand before failure occurs. Dielectric breakdown arises from electron migration into the conduction band at very high applied field [46].

For practical use as a capacitor, a good dielectric should therefore possess high dielectric constant, low dielectric loss and high dielectric strength. It must also have reasonable physical stability, and none of its characteristics should vary much over a fairly wide temperature range.

### *1.4.2 High κ Materials*

For more than three decades, the on-chip insulator for gate dielectrics and storage capacitors has been silicon dioxide with a dielectric constant of 3.9. As integrated circuit design rules shrink, elements of the circuit must be miniaturized. The thickness of the $SiO_2$ gate oxide has been scaled down to less than 2 nm (i.e. a few $SiO_2$ units), and further device size reduction is restricted because of the leakage currents due to direct tunneling. For this reason, alternative materials featuring higher κ values have been considered for such critical dielectric films in both the gate electrodes and in DRAM (dynamic random access memory) storage capacitors. High κ material can increase capacitance, reduce the current leakage and allow transistors to operate at a lower voltage. The result is less power consumed and less power dissipated as heat.

Materials with a dielectric constant greater than that of silicon nitride ($Si_3N_4$, $\kappa = 7.5$) are classified as high κ materials. According to the ITRS (International Technology Roadmap for Semiconductor) data, the best candidate for gate material should possess κ in the 10 ~ 25 range. Material for memory capacitors should have much higher κ value. Investigators have focused on early transition metal oxides and their silicates, for example, titanium, zirconium and hafnium oxides ($TiO_2$, $\kappa = 80$; $ZrO_2$, $\kappa = 25$; $HfO_2$, $\kappa = 25$) or tantalum oxide ($Ta_2O_5$, $\kappa = 26$) [49], as well as perovskite type ferroelectrics, such as $(Ba,Sr)TiO_3$, $SrTiO_3$, and $KTa_{1-x}Nb_xO_3$ [50-52], especially for DRAM applications.

In oxides with the perovskite structure, a very high κ is often observed. Dielectric constants above 1000 are found to be related to ferroelectric ordering or relaxor behavior, and the dielectric constant is strongly temperature-dependent, which is highly undesirable for practical device application.

A few years ago, Subramanian, Sleight and coworkers found a perovskite-related material $CaCu_3Ti_4O_{12}$ (CCTO) shows a dielectric constant at 1 kHz of about 12,000 that is nearly constant from 150 to 600 K [53]. Its giant dielectric constant over a wide frequency range and temperature-independence around room temperature (Fig. 1.3) make CCTO a promising material for microelectronic applications. Considerable interest has been generated in this material and related materials [54-66]. The origin of the unusual dielectric behavior of CCTO, however, is still under debate [55-57, 60-65].

We synthesized $SrCu_3Ti_4O_{12}$ (SCTO) in this work because it might be the closest analogue to CCTO. The composition and structure of SCTO were determined by both neutron and synchrotron X-ray diffraction data. The defects identified in SCTO provide a basis for understanding the giant dielectric constant in CCTO. A study on a CCTO crystal through complex impedance spectroscopy further proved the existence of internal barriers within the crystal grains.

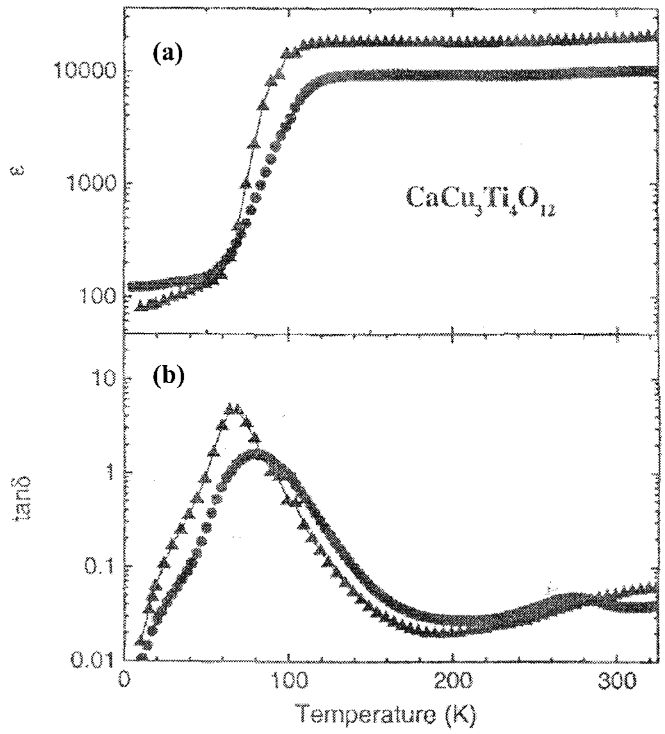

Figure 1.3 The temperature dependence of (a) dielectric constant ε and (b) loss tangent tanδ data for two different CCTO ceramic samples [54].

## 1.5 Magnetic Properties

### *1.5.1 Ferromagnetism and Magnetic Structure*

Transition metals and lanthanides with unpaired *d* and *f* electrons exhibit magnetic behavior such as paramagnetic, ferromagnetic, antiferromagnetic and ferrimagnetic, depending on the alignment of their unpaired electrons. Introduction of interatomic coupling permits the possibility of a spontaneous ordering of the atomic moments below some critical temperature. A substance is called ferromagnetic if its unpaired electrons are oriented parallel giving a spontaneous magnetic moment at low temperatures (Fig. 1.4).

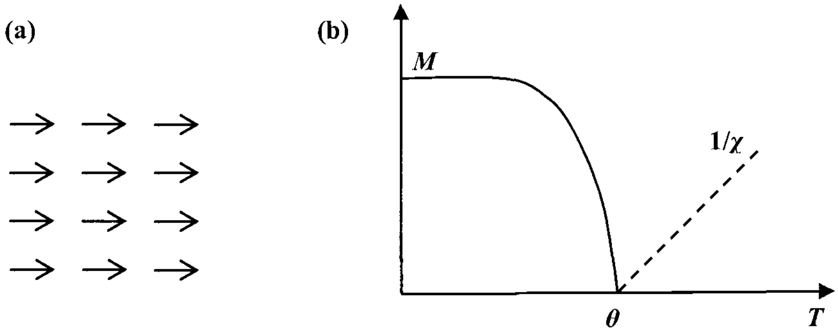

Figure 1.4 Ferromagnetism shown as (a) spin alignment; (b) temperature dependence of magnetization $M$ and reciprocal susceptibility $1/\chi$, positive value of Weiss constant $\theta$ coinciding with the ferromagnetic Curie temperature Tc, below which the material is ferromagnetic.

A ferromagnetic material is composed of many small domains with different magnetization orientations; within each domain the magnetic moments are all aligned in the same direction. As an external field $H$ is cycled from one direction to the other, a hysteresis loop is followed in which the total magnetic flux density $B$ lags behind the applied field $H$ due to the domain action.

Based on the early work of Kramers [67] and Anderson [68], Goodenough [69] and Kanamori [70] proposed so-called GK rules to predict whether a ferromagnetic or antiferromagnetic interaction exists between two magnetic cations on opposite sides of a nonmagnetic anion through a 180° superexchange interaction (Fig. 1.5). These rules assume that the predominant contribution to the superexchange comes from the covalency of the $\sigma$ bonds, i.e., the interactions of cation $e_g$ orbitals dominate over those between cation $t_{2g}$ orbitals due to greater cation-anion orbital overlap [71].

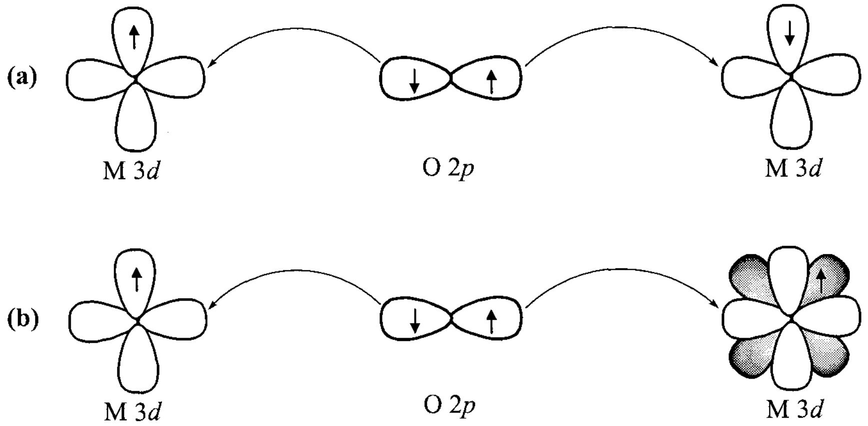

Figure 1.5 Schematic illustration of GK rules showing (a) an antiferromagnetic interaction between the neighboring metal cations with half-filled *d* orbitals and (b) a ferromagnetic interaction between one metal cation with a half-filled *d* orbital and the adjacent metal cation with an empty *d* orbital through an intervening oxygen ion in a 180° superexchange interaction. Here the electron transfer, or partial covalence, is shown between the oxygen $p\sigma$ orbital and the metal $e_g$ orbital of principal overlap. The shaded *d* orbital of the second metal cation in (b) is a $t_{2g}$ orbital, and the intra-atomic interaction between electrons in different orbitals of this second metal cation would lead to a lower energy if the occupied $t_{2g}$ orbital also has a spin-up electron.

Although magnetic susceptibility measurements give an indication of the type of magnetic ordering, they do not show the detailed arrangement of spins. Neutrons possess a magnetic moment, which can interact with the magnetic moment associated with unpaired electrons and give rise to magnetic scattering. Neutron diffraction, therefore, can display magnetic peaks in addition to nuclear peaks when magnetic sublattices are present. For a ferromagnetic material the magnetic unit cell will be identical with the ordinary chemical cell, but it increases in at least one cell direction for an antiferromagnetic material (Fig. 1.6). Complications may arise when it comes to some ferrimagnetic materials [72].

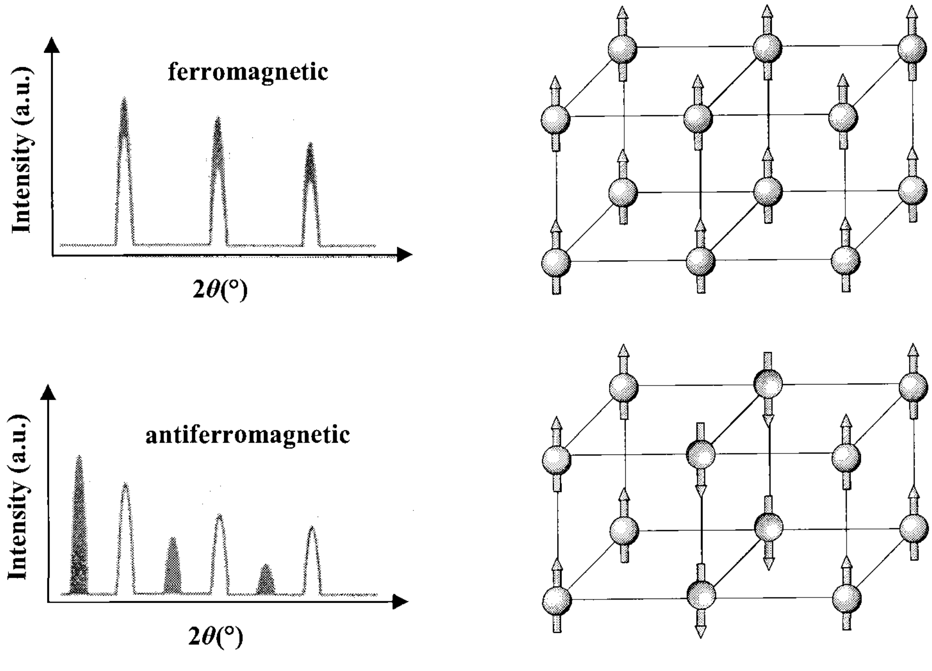

Figure 1.6 Schematic neutron diffraction patterns for ferromagnetic (overlapping of nuclear and magnetic peaks) and antiferromagnetic (separate nuclear and magnetic peaks) materials. Magnetic unit cells are shown on the right.

### *1.5.2 Spintronics*

Magnetism utilized for information storage has been known for a long time; even the earliest computer hard drives used magnetoresistance to read data stored in magnetic domains. Many recent attempts have been made to exploit the "spin" of the electron, in addition to its charge, to manufacture "spintronic" devices that will be much more powerful than traditional electronic devices. Making use of this additional degree of freedom of the electron, spintronics, or spin electronics, may double data storage and processing speed by combining two states of electric charge (+ and -) and two states of electron spin (spin-up and spin-down). The potential market is worth hundreds of billions of dollars a year.

Spintronics burst on the scene in 1988 when Baibich *et al.* in France [73] and Binasch *et al.* in Germany [74] discovered independently the so-called GMR, giant magnetoresistance effect, which is a very large change in electrical resistance in a multilayer film composed of alternate ferromagnetic and nonmagnetic layers when the relative orientations of the magnetic moments in ferromagnetic layers change as a function of applied magnetic field. The effect of GMR can be 200 times (Fig 1.7) stronger than ordinary magnetoresistance [75].

In specially designed multilayers, known as spin valves, the magnetic configuration can be switched between parallel and antiparallel by a field of a few Oersted, so that a large change of resistance can be induced by a very small field. IBM was the first to market hard disks incorporating GMR read heads that increase the storage capacity by almost two orders of magnitude, and all modern computers today use spin valves for the read heads of the hard discs. Another important application is magnetic random access memory (MRAM), a non-volatile memory that would not be lost even when the power was switched off [76].

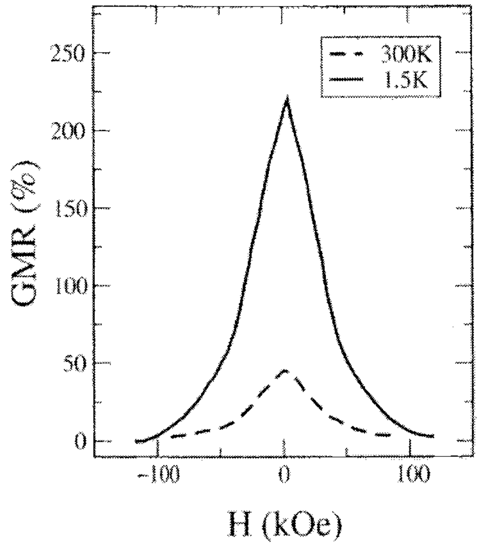

Figure. 1.7 Magnetoresistance curve of an Fe/Cr multilayer [75].

Ongoing research is driven by the need for integration of spin-electronic devices into conventional semiconductor technology. Challenges exist in determining efficient ways of injection, transportation, and detection of spin-polarized currents into semiconductors at or above room temperature without using strong magnetic fields.

The idea of enabling spin-polarized current flow through semiconductors was first proposed during the early 70's in tunneling studies using ferromagnetic electrodes [77]. Currently two methods of spin-injection are investigated, namely injection from a metallic ferromagnetic electrode or through a ferromagnetic semiconductor.

Devising economic ways to combine ferromagnetic metals and semiconductors in integrated circuits is, however, a very demanding task given different crystal structures and chemical bonding, and different conductivity and spin relaxation time in metals and semiconductors. Semiconductor based spintronics, on the other hand, can inject spin-polarized current into semiconductors more effectively and are much easier to integrate with traditional semiconductor devices. In addition, due to their optical properties they can amplify both optical and electrical signals, and they have the ability to incorporate both p-type and n-type dopants. To achieve semiconductors that are ferromagnetic and exhibit magnetoelectric and magnetodielectric effects at room temperature will therefore lead to new multifunctional electronics that combine storage, detection, logic and communications on a single chip.

Research on ferromagnetic semiconductors and their magnetotransport properties dates back to 1950 [78]. In general, ferromagnetic semiconductors only show magnetic ordering and magneto-effect far below room temperature. Claims of room-temperature ferromagnetism in so-called diluted magnetic semiconductors in the past few years are not very well accepted [79-81].

Goodenough and coworkers found an ordered double-perovskite, $La_2Ni^{2+}Mn^{4+}O_6$, to be an apparent ferromagnetic semiconductor with a Curie temperature very close to room temperature ($T_c = 275$ K) [82-85]. Previous studies on $La_2NiMnO_6$ were focused on verification of GK rules [69,70]. The crystal structure including charge ordering was neither completely identified nor satisfactorily solved [86,87]. The magnetic structure was never reported.

In present work the ferromagnetic semiconductor, $La_2NiMnO_6$, was synthesized, the magnetic, electric and dielectric properties were investigated, and the Curie temperature was found to be above 274 K. Both atomic and magnetic structures were refined, and the ferromagnetism of $La_2NiMnO_6$ was confirmed by neutron powder diffraction studies.

## 1.6 Negative Thermal Expansion

### *1.6.1 Thermal Expansions*

It is very common that matter expands when heated and contracts when cooled, or should we say, it used to be common. Research has revealed that some materials exhibit very low or no thermal expansion and some even shrink upon heating, which gives rise to three different types of thermal expansion: positive (or usual) thermal expansion, zero (or near zero) thermal expansion and negative thermal expansion (NTE). The degree of thermal expansion is quantitatively described by thermal expansion coefficient $\alpha$, which is defined as $\alpha_l = \frac{1}{l}\left(\frac{\partial l}{\partial T}\right)_p$ for linear thermal expansion and $\alpha_V = \frac{1}{V}\left(\frac{\partial V}{\partial T}\right)_p$ for volumetric thermal expansion, where $l$, $V$, and $T$ represent length, volume and temperature, respectively, and subscript p stands for constant pressure. The type of the thermal expansion depends on the sign of $\alpha$. A negative sign denotes a negative thermal expansion.

The usual thermal expansion can be explained by the anharmonic potential well of two bonded atoms (Fig. 1.8). When increasing temperature, the average interatomic distance increases (from $r_1$ to $r_3$) due to the asymmetry of the potential well. A harmonic well, on the other hand, would produce no thermal expansion or contraction as the temperature rises. As chemical bonds become stronger, the potential well becomes more symmetric and thus the vibrations become more harmonic. Therefore, strong bonds lead to low thermal expansion; weak bonds high thermal expansion.

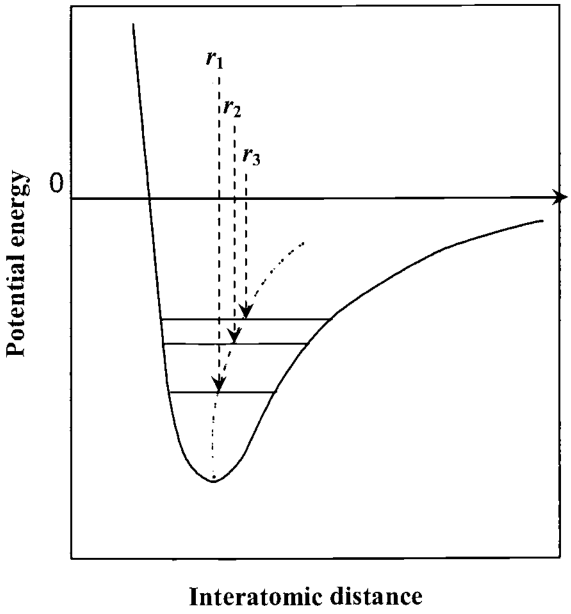

Figure 1.8 Anharmonic potential well for a diatomic molecule. The dotted curve shows the average interatomic distance.

Negative thermal expansion had been considered rare prior to 1995. Some perovskite ferroelectrics such as $PbTiO_3$ [88], Si, $Cu_2O$ [89] and amorphous $SiO_2$ [90] contract at low temperatures, while $ZrV_2O_7$ [91,92] and certain crystalline forms of

$SiO_2$ (quartz, cristobalite and tridymite) [90] contract at high temperatures. NTE of β-eucryptite ($LiAlSiO_4$) [93] up to room temperature is strongly anisotropic with negative thermal expansion in 1D only. More attention has been drawn to the study of NTE behavior when Sleight and coworkers found cubic $ZrW_2O_8$ has the strongest negative thermal expansion ($-8.7 \times 10^{-6}$/K) known for any isotropic material from absolute zero to nearly 1000 K [94]. Many oxides have been reported recently to show NTE behavior [95].

By combining NTE materials with polymer, metal, or ceramic, one can control the thermal expansion of the designed composite. Applications include electronics, optics, fuel cells, oxygen sensors, thermostats, dental restorations and so on. Isotropic NTE like in $ZrW_2O_8$ is favored in ceramic applications due to microcracking related to anisotropic expansion.

### *1.6.2 Mechanisms of NTE*

While the positive thermal expansion is readily rationalized on the anharmonicity of the potential well shown in Figure 1.8, negative thermal expansion cannot be explained the same way unless above potential well is reversed so that shorter bond distances become energetically more favored over longer distances with thermal excitation. Such a situation, however, has never been proved experimentally or theoretically.

Sleight proposed four mechanisms for NTE behavior exhibited by a large family of oxides with open frameworks: 1) Polyhedra becoming more regular (symmetry-related NTE); 2) Networks with normal bond expansion; 3) Interstitial cations changing sites; and 4) Transverse thermal motion [95,96].

The ferroelectric perovskite $PbTiO_3$ is cubic with regular polyhedra above 490 °C, below this temperature it becomes tetragonal. The $PbO_{12}$ and $TiO_6$ polyhedra of tetragonal $PbTiO_3$ are increasingly distorted along the *c* axis with decreasing temperature, which gives rise to an increasing anion-anion repulsion and thus larger polyhedra. Therefore, negative thermal expansion is observed below 490 °C for cell edge *c* [88].

Corderite $Mg_2Al_4Si_5O_{18}$ [97], β-eucryptite $LiAlSiO_4$ [93] and NZP $NaZr_2P_3O_{12}$ [98] have edge- or face-sharing polyhedra; the underlying mechanism of NTE is basically the same in all of the three compounds [99]. Due to the connectivity in these network structures, normal bond expansion in some directions causes contractions in the other directions.

Structural analysis by neutron diffraction over the temperature range 10 to 809 K revealed that the volume thermal expansion of β-eucryptite is much more negative below room temperature [96]. DLS (Distance Least Squares) modeling studies suggest that the normal Li–O bond expansion plus movement of interstitial $Li^+$ ions from tetrahedral to octahedral sites with increasing temperature can explain the thermal expansion behavior above room temperature, which is consistent with the increasing $Li^+$ ionic conductivity with increasing temperature [96]. This approach can also apply to some of the NZP compounds known as good $Na^+$ ion conductors. The more pronounced low-temperature NTE of β-eucryptite, however, cannot be explained. It can be, instead, ascribed to the mechanism mentioned in the following paragraphs.

The largest NTE family discovered to date are oxide networks based on corner-sharing octahedra $AO_3$ and/or corner-sharing tetrahedra $MO_2$ with the framework oxygen in two-fold coordination to two metal atoms (Table 1.1). The general formulae come from different combinations of $AO_3$ and $MO_2$ polyhedra, and the structural network contains both octahedra and tetrahedra sharing corners only with possible linkages of A–O–M, M–O–M and A–O–A.

Table 1.1 Negative and "zero" thermal expansion family with two-fold coordination bridging oxygen and corner-sharing polyhedra only in a open framework.

| **$MO_2$** | **$AM_2O_7$** | **$A_2M_3O_{12}$** | **$AMO_5$** | **$AO_3$** |
|---|---|---|---|---|
| $SiO_2$ [100] | $Zr(Hf)V_2O_7$ [92,102] | $Sc_2W_3O_{12}$ [107,108] | $NbOPO_4$ [111,112] | $TaO_2F$ [114] |
| $AlPO_4$-17 [101] | $Zr(Hf)P_2O_7$ [103] | $Y_2W_3O_{12}$ [109] | $TaOPO_4$ [113] | |
| | $ZrW_2O_8$ [94,104-106] | $Lu_2W_3O_{12}$ [110] | $TaOVO_4$ [113] | |

Note: M = tetrahedral cation; A = octahedral cation.

The negative thermal expansion is caused by the transverse thermal motion of the bridging oxygen that pulls the two metal atoms closer, provided that there is insignificant M–O bond expansion (Fig. 1.9). Considering each polyhedron as a rigid or semirigid unit, rocking of these linked polyhedra back and forth (Fig. 1.10) creates transverse thermal motion of the M–O–M linkages in a correlated manner [95].

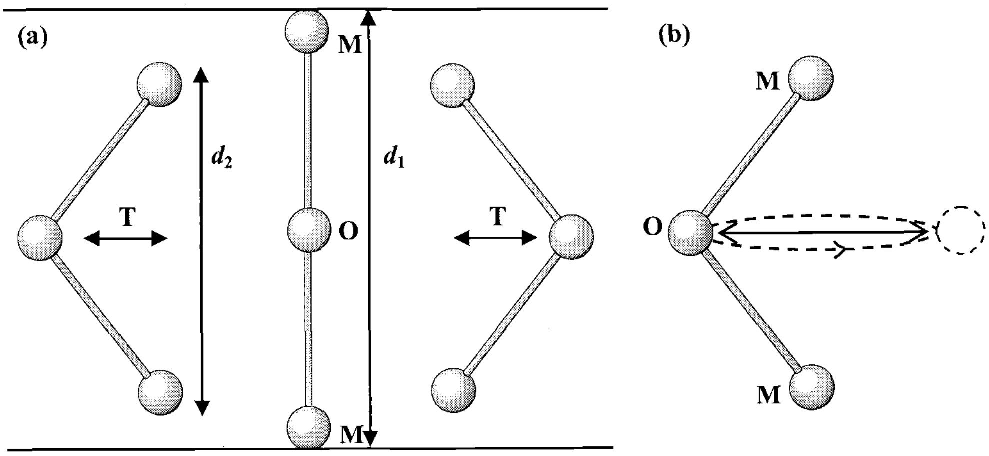

Figure 1.9 (a) Decreased interatomic distance ($d_2 < d_1$) between two unbonded metal atoms due to thermal vibration of a 2-coordinated oxygen atom; (b) Two possible thermal vibrations of the oxygen atom: ellipsoid model (solid line) and torus model (dotted oval).

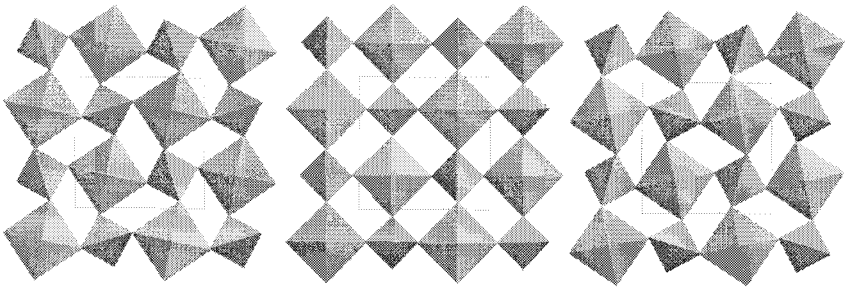

Figure 1.10 Tetragonal $NbOPO_4$ shown as $NbO_6$ and $PO_4$ polyhedra on *ab* plane. Central structure is in space group P4/nmm, rocking back and forth to P4/n on either side with thermal excitation [111].

Dove and coworkers proposed a geometrical modeling based on Rigid Unit Modes (RUM: no polyhedral shape change with rocking) and quasi-Rigid Unit Modes (qRUM: small changes with rocking) to look for the correlation between the existence of RUMs or qRUMs in a structure and the sign of its thermal expansion [115]. The theoretical calculations of our group suggest that there is no simple and direct correlation between RUMs and NTE [116].

Cubic $ZrW_2O_8$ is special in the $AM_2O_7$ family because the $WO_4$ tetrahedral groups are not linked to each other. This makes $ZrW_2O_8$ structure much more flexible and the polyhedra can rock back and forth without any change in shape. While in other compounds of the cubic $AM_2O_7$ family the rocking motions of the linked polyhedra cannot occur without concurrent changes in polyhedral shapes [95].

Thermal contraction in metal (M) oxides is usually the result of the thermal motion of oxygen transverse to M–O–M linkages. However, thermal motion of M transverse to O–M–O linkages can also give rise to thermal contraction. There are few examples of this because two-fold coordination of metal cations is unusual. $Cu_2O$ and $Ag_2O$ contain linear O–M–O linkages and both exhibit NTE behavior [117]. Linear O–M–O linkages where M can be Cu(I) or Ag(I) also exist in compounds with the delafossite structure (Fig. 1.1). In present work, delafossite type of compounds $CuAlO_2$, $CuInO_2$, $CuLaO_2$, $CuScO_2$, and $AgInO_2$ were studied by temperature-dependent neutron powder diffraction in search for possible negative thermal expansion property. Structural trends were discussed with respect to both composition and temperature.

## 1.7 Tetrahedral MM'$X_2$ Compounds

The compounds with tetrahedral structure form only a small group of the inorganic compounds, yet they have very interesting characteristic features for which a set of possible structures can be postulated. A structure is called a normal tetrahedral structure if every atom in the structure has four nearest neighbors located at the vertices of a surrounding tetrahedron. Depending on the shape of the tetrahedra, one can differentiate between regular and distorted tetrahedral structures. There is also a defect tetrahedral structure where some atoms have fewer than four neighbors, and a filled tetrahedral structure where the tetrahedron is stuffed with extra atoms. They could be elements, binary, ternary and quaternary compounds, and they are all characterized by tetrahedral bonding [118].

The orthorhombic compound $\beta$-$AgAlO_2$ with tetrahedral structure was made by accident. The initial intention was to obtain $\alpha$-$AgAlO_2$ with the delafossite structure to look for possible negative thermal expansion behavior. We found it interesting to study not only because the positional parameters in this structure have never been reported before, but also because of the fascinating structural systematics shown by a series of $MM'X_2$ tetrahedral compounds, where X = O, S, Se, N, and M could be either univalent or divalent cations and M' could be either trivalent or tetravalent cations.

In present work, the orthorhombic $\beta$-$AgAlO_2$ with tetrahedral structure was synthesized and the crystal structure (Fig. 1.11) was refined from neutron diffraction data, together with an examination of the structural systematics of $MM'X_2$ compounds with tetrahedral $MX_4$ and $M'X_4$ units. The main interest of our work does not concern the crystal structure itself but rather the systematic trends revealed by the careful analysis of the observed deformation of tetrahedral structure with respect to M/M' ionic radii ratio and the electronegativity.

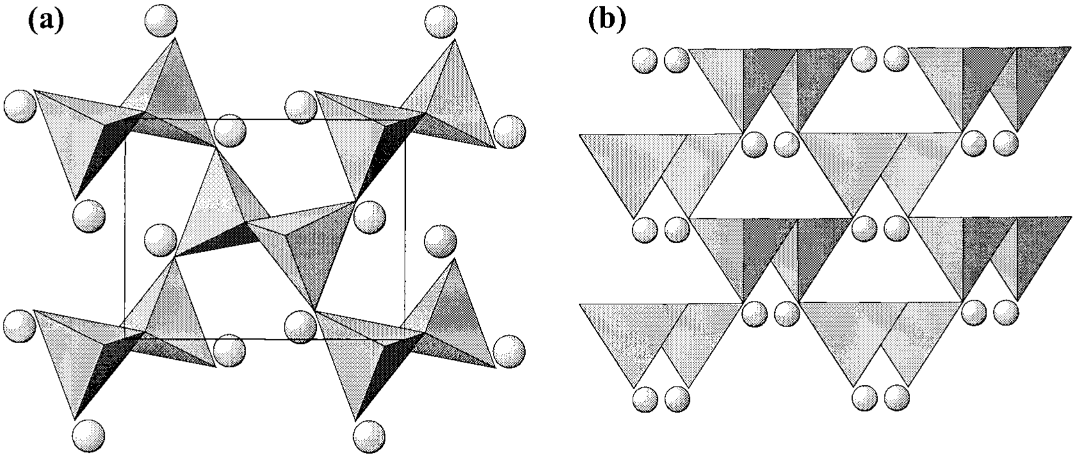

Figure 1.11 Structure of β-$AgAlO_2$ shown as (a) $AlO_4$ tetrahedral framework on the *ab* plane with Ag atoms unbonded; and (b) $O1Ag_2Al_2$ tetrahedral framework on the *bc* plane with O2 atoms unbonded.

## 1.8 Materials and Methods

The chemical materials used for this study were synthesized by typical solid state reactions in different atmospheres and pressures and by ion-exchange, hydrothermal, and solution reactions. A single crystal of 2H $CuScO_2$ was grown in an inert atmosphere using PbO as a flux. A single crystal of $CaCu_3Ti_4O_{12}$ was grown by Dr. Wakimoto in MIT and supplied by Dr. Ramirez of Bell Labs.

The structure characterization was carried out using high-resolution neutron powder diffraction, X-ray powder diffraction and in some cases synchrotron X-ray diffraction. Equipment involved includes the NIST BT-1 neutron diffractometer (Fig. 1.12(a)), the OSU Siemens D5000 X-ray diffractometer (Fig. 1.12(b)) and the APS synchrotron source of Argonne National Laboratory.

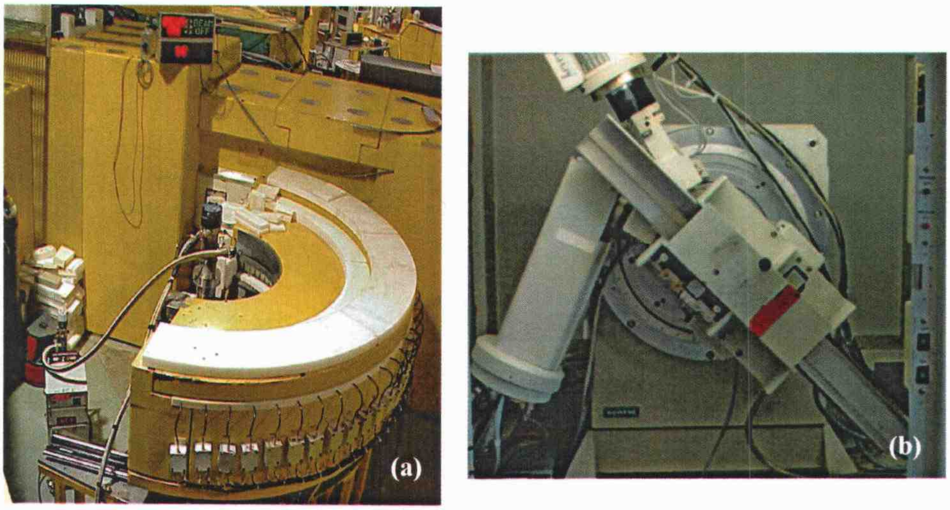

Figure 1.12 NIST BT-1 high-resolution neutron diffractometer (a) and OSU Siemens D5000 X-ray diffractometer (b).

Thermal properties of the materials were analyzed by thermogravimetric analysis (TGA) and differential scanning calorimetry (DSC) using a TGA/DSC 2950 analyzer.

BET surface area was measured using a Micromeritics ASAP 2000 and Scanning Electron Microscope (SEM) images were taken on an AmRay of OSUEMF (OSU electron microscope facility).

The electrical properties of sintered pellet and bar samples were measured using four-probes and thermoelectric power (Seebeck coefficient). Optical properties of powder samples were characterized by diffuse reflectance in the UV-visible region.

Both electrical and optical measurements were done by Robert Kykyneshi of Tate's Lab in OSU Physics Department [119].

The dielectric, magnetic and transport properties of some samples were characterized using a Quantum Design Physical Property Measurement System (PPMS) in the DuPont company by Dr. M.A. Subramanian and Dr. N.S. Rogado. Transport properties were measured using the four-wire resistivity option of the PPMS. Capacitance and loss tangent measurements were taken on HP 4275A and HP 4284 LCR meters.

The measurement of conductivities as a function of frequency by complex impedance spectroscopy (IS) allows a separation of contributions to impedance from grains, grain boundaries and electrode polarization [120]. This technique therefore permits the separation of the electrical properties of grain boundaries from those of grains, and it is sensitive to both ionic and electronic conductivity. An equivalent circuit is normally assumed in order to interpret the complex impedance data. The conductivities of some of our ceramic samples, in pellet, bar and powder forms, were measured by the complex impedance method. Instruments used are a Solartron SI 1287 electrochemical interface and a Schlumberger SI 1260 impedance/grain-phase analyzer. For high temperature measurements, a specially designed impedance cell (Fig. 1.13) was used, and a special setup with a delrin® die was used for measurements performed in powder form (Fig. 1.14).

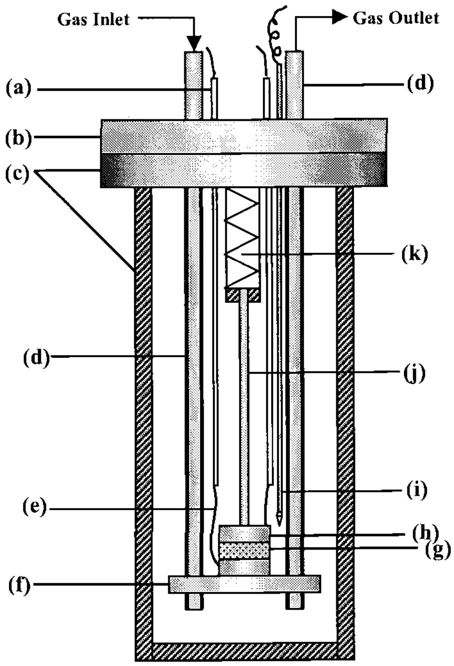

Figure 1.13 Impedance cell used in high temperature measurements. (a) BNC connectors (connecting to impedance analyzer); (b) top flange; (c) steel outer shell; (d) hollow stainless steel tubes; (e) platinum wires; (f) bottom pedestal; (g) sample; (h) sample holder wrapped with platinum foil; (i) thermocouple; (j) push-down rod; (k) spring.

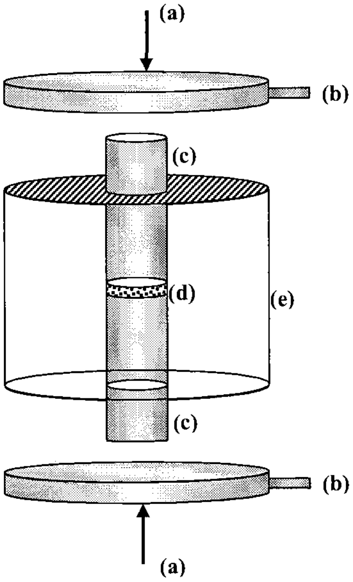

Figure 1.14 Schematic of the setup for measuring conductivities of powder samples. (a) pressure applied on top and bottom disks; (b) stainless steel disks connected to electrical leads; (c) tool steel rods; (d) powder sample; (e) delrin® die.

## 1.9 References

1. A.W. Sleight. *Supercurrents*, 5, 2 (1988)
2. J.B. Goodenough. *Prog. Solid State Chem.*, 5, 145 (1971)
3. T.A. Mary, J.S.O. Evans, A.W. Sleight, T. Vogt. *Science*, 272, 90 (1996)
4. R.G. Gordon. *MRS Bull.*, 25, 52 (2000)
5. K. Badeker. *Ann. Phys.* (Leipzig), 22, 749 (1907)
6. K.L. Chopra, S. Major, T.K. Pandya. *Thin Solid Film*, 102, 1 (1983)
7. I. Hamberg, C.G. Granqvist. *J. Appl. Phys.*, 60, R123 (1986)
8. H. Ohta, M. Orita, M. Hirano, H. Tanji, H. Kawazoe, H. Hosono. *Appl. Phys. Lett.*, 77, 475 (2000)
9. G. Thomas. *Nature*, 389, 907 (1997)
10. H. Sato, T. Minami, S. Takata, T. Yamada. *Thim Solid Films*, 236, 27 (1993)
11. H. Kawazoe, M. Yasukawa, H. Hyodo, M. Kurita, H. Yanagi, H. Hosono. *Nature*, 389, 939 (1997)
12. H. Yanagi, H. Kawazoe, A. Kudo, M. Yasukawa, H. Hosono. *J. Electroceram.*, 4, 427 (2000)
13. N. Duan, A.W. Sleight, M.K. Jayaraj, J. Tate. *Appl. Phys. Lett.*, 77, 1325 (2000)
14. H. Yanagi, T. Hase, S. Ibuki, K. Ueda, H. Hosono. *Appl. Phys. Lett.*, 78, 1583 (2001)
15. H. Kawazoe, H. Yanagi, K. Ueda, H. Hosono. *MRS Bull.*, 25, 28 (2000)
16. R. Nagarajan, A.D. Draeseke, A.W. Sleight, J. Tate. *J. Appl. Phys.*, 89, 8022 (2001)
17. R. Nagarajan, N. Duan, M.K. Jayaraj, J. Li, K.A. Vanaja, A. Yokochi, A. Draeseke, J. Tate, A.W. Sleight. *Int. J. Inorg. Mater.*, 3, 265 (2001)

18. T. Yamamoto, H. Katayama-Yoshida. *Jpn. J. Appl. Phys.*, 38, L166 (1999)

19. A. Kudo, H. Yanagi, H. Hosono, H. Kawazoe. *Appl. Phys. Lett.*, 73, 220 (1998)

20. A. Kudo, H. Yanagi, K. Ueda, H. Hosono, H. Kawazoe, Y. Yano. *Appl. Phys. Lett.*, 75, 2851 (1999)

21. H. Yanagi, K. Ueda, H. Ohta, M. Orita, M. Hirano, H. Hosono. *Solid State Commun.*, 121, 15 (2002)

22. A. Pabst. *Am. Mineral.*, 31, 539 (1946)

23. F.A. Benko, F.P. Koffyberg. *J. Phys. Chem. Solids*, 45, 57 (1984)

24. F.A. Benko, F.P. Koffyberg. *Can. J. Phys.*, 63, 1306 (1985)

25. F.A. Benko, F.P. Koffyberg. *Phys. Status Solidi A*, 94, 596 (1986)

26. F.A. Benko, F.P. Koffyberg. *Mater. Res. Bull.*, 21, 753 (1986)

27. Y. Kakehi, S. Nakao, K. Satoh, T. Yotsuya. *Thin Solid Films.*, 445, 294 (2003)

28. H. Yanagi, S. Inoue, K. Ueda, H. Kawazoe, H. Hosono. *J. Appl. Phys.*, 88, 4159 (2000)

29. K, Ueda, T. Hase, H. Yanagi, H. Kawazoe, H. Hosono, H. Ohta, M. Orita, M. Hirano. *J. Appl. Phys.*, 89, 1790 (2001)

30. T. Otabe, K. Ueda, A. Kudoh, H. Hosono, H. Kawazoe. *Appl. Phys. Lett.*, 72, 1036 (1998)

31. M. Elazhari, A. Ammar, M. Elaatmani. *Eur. J. Solid State Inorg. Chem.*, 34, 503 (1997)

32. R.J. Cava, H.W. Zandbergen, A.P. Ramirez, H. Takagi, C.T. Chen, J.J. Krajewski, W.F. Peck Jr., J.V. Waszczak, G. Meigs, R.S. Roth, L.F. Schneemeyer. *J. Solid State Chem.*, 104, 437 (1993)

33. H. Ohta *et al. Appl. Phys. Lett.*, 77(4), 475 (2000)

34. D.C. Look. *Mater. Sci. Eng. B*, 80, 383 (2001)

35. D.C. Look *et al. Phys. Status Solidi A*, 195(1), 171 (2003)

36. D.C. Look, D.C. Reynolds, C.W. Litton, R.L. Jones, D.B. Eason, G. Cantwell. *Appl. Phys. Lett.*, 81(10), 1830 (2002)

37. J.G. Lu, Z.Z. Ye, L. Wang, J.Y. Huang, B.H. Zhao. *Mater. Sci. Semicond. Proc.*, 5, 491-496 (2003)

38. J.M. Bian, X.M. Li, C.Y. Zhang, W.D. Yu, X.D. Gao. *Appl. Phys. Lett.*, 85(18), 4070 (2004)

39. M. Joseph, H. Tabata, T. Kawai. *J. Appl. Phys.*, Part 2 (11A), L1205 (1999)

40. A.V. Singh, R.M. Mehra, A. Wakahara, A. Yoshida. *J. Appl. Phys.*, 93(1), 396 (2003)

41. J.M. Bian, X.M. Li, X.D. Gao, W.D. Yu, L.D. Chen. *Appl. Phys. Lett.*, 84(4), 541 (2004)

42. R.P. Wang, A.W. Sleight, R.Platzer, J.A. Gardner. *J. Solid State Chem.*, 122, 166-175 (1996)

43. R.P. Wang, A.W. Sleight, D. Cleary. *Chem. Mater.*, 8, 433-439 (1996)

44. Q. Xu, D.P. Huang, W. Chen, J.H. Lee, B.H. Kim, H. Wang, R.Z. Yuan. *Ceram. Int.*, 30(3), 429-433 (2004)

45. H. Iwahara, T. Esaka, H. Uchida, N. Maeda. *Solid State Ionics*, 3/4, 359 (1981)

46. R.M. Rose, L.A. Shepard, J. Wulff. *Electronic Properties*; John Wiley and Sons: New York, 1966

47. A.R. West. *Basic Solid State Chemistry*, 2nd ed.; John Wiley & Sons: New York, 1999

48. In *Ceramic Materials for Electronics, Processing, Properties, and Applications*; R.C. Buchanan Ed.; Marcel Dekker, Inc.: New York, 1986

49. D.S. Yoon, J.S. Roh. *Crit. Rev. Solid State Mater. Sci.*, 27, 143 (2002)

50. D.E. Kotecki, J.D. Baniecki, H. Shen, R.B. Labibowitz, K.L. Saenger, J.J. Lian, T.M. Shaw, S.D. Athavale, C. Cabral, Jr.,P.R. Duncombe, M. Gutsche, G. Kunkel, Y.J. Park, Y.Y. Wang, R. Wise. *IBM J. Res. Dev.*, 43, 367 (1999)

51. H.C. Li, W. Si, A.D. West, X.X. Xi. *Appl. Phys. Lett.*, 73, 464 (1998)

52. G.A. Sumara, L.A. Boatner. *Phys. Rev. B*, 61, 3889 (2000)

53. M.A. Subramanian, D. Li, N. Duan, B.A. Reisner, A.W. Sleight. *J. Solid State Chem.*, 151, 323 (2000)

54. A.P. Ramirez, M.A. Subramanian, M. Gardel, G. Blumberg, D. Li, T. Vogt, S.M. Shapiro. *Solid State Commun.*, 115, 217 (2000)

55. C.C. Homes, T. Vogt, S.M. Shapiro, S. Wakimoto, A.P. Ramirez. *Science*, 293, 673 (2001)

56. M.A. Subramanian, A.W. Sleight. *Solid State Sci.*, 4, 347 (2002)

57. D.C. Sinclair, T.B. Adams, F.D. Morrison, A.R. West. *Appl. Phys. Lett.*, 80, 2153 (2002)

58. Y. Lin, Y.B. Chen, T. Garret, S.W. Liu, C.L. Chen, L. Chen, R.P. Bontchev, A. Jacobson, J.C. Jiang, E.I. Meletis, J. Horwitz, H.D. Wu. *Appl. Phys. Lett.*, 81, 631 (2002)

59. W. Si, E.M. Cruz, P.D. Johnson, P.W. Barnes, P. Woodward, A.P. Ramirez. *Appl. Phys. Lett.*, 81, 2056 (2002)

60. C.C. Homes, T. Vogt, S.M. Shapiro, S. Wakimoto, M.A. Subramanian, A.P. Ramirez. *Phys. Rev. B*, 67, 092106 (2003)

61. I.P. Raevski, S.A. Prosandeev, A.S. Bogatin, M.A. Malitskaya, L. Jastrabik. *J. Appl. Phys.*, 93, 4130 (2003)

62. L. He, J.B. Neaton, D. Vanderbilt, M.H. Cohen. *Phys. Rev. B*, 67, 012103 (2003)

63. A. Tselev, C.M. Brooks, S.M. Anlage, H. Zheng, L. Salamanca-Riba, R. Ramesh, M.A. Subramanian. *Phys. Rev. B*, 70, 144101 (2004)

64. P. Lunkenheimer, R. Fichtl, S.G. Ebbinghaus, A. Loidl. *Phys. Rev. B*, 70, 172102 (2004)

65. G. Chiodelli, V. Massarottie, D. Capsoni, M. Bini, C.B. Azzoni, M.C. Mozzati, P. Lupotto. *Solid State Commun.*, 132, 241 (2004)

66. E. Giulotto, M.C. Mozzati, C.B. Azzoni, V. Massarotti, D. Capsoni, M. Bini. *Ferroelectrics*, 298, 61 (2004)

67. H.A. Kramers. *Physica*, 1, 182 (1934)

68. P.W. Anderson. *Phys. Rev.*, 79, 350 (1950)

69. J.B. Goodenough, A.L. Loeb. *Phys. Rev.*, 98, 391 (1955); J.B. Goodenough. ibid. 100, 564 (1955)

70. J. Kanamori. *J. Phys. Chem. Solids*, 10, 87 (1959)

71. J.B. Goodenough. *Magnetism and the Chemical Bond*; John Wiley & Sons: New York, 1963

72. G.E. Bacon. *Neutron Scattering in Chemistry*; Butterworths Inc.: Boston, 1977

73. M.N. Baibich, J.M. Broto, A. Fert, F. Nguyen Van Dau, F. Petroff, P. Eitenne, G. Creuzet, A. Friederich, J. Chazelas. *Phys. Rev. Lett.*, 61, 2472 (1988)

74. G. Binasch, P. Grunberg, F. Saurenbach, W. Zinn. *Phys. Rev. B*, 39, 4828 (1989)

75. R. Schad, C.D. Potter, P. Belien, G. Verbanck, V.V. Moschchalkov, Y. Bruynseraede. *Appl. Phys. Lett.*, 64, 3500 (1994)

76. G.A. Prinz. *Science*, 282, 1660 (1998)

77. D.R. Scifres, B.A. Huberman, R.M. White, R.S. Bauer. *Solid State Commun.*, 13, 1615 (1973)

78. J.H. van Santen, G.H. Jonker. *Physica* (*The Hague*), 16, 599 (1950); G.H. Jonker, J.H. van Santen. ibid. 16, 337-349 (1950); J. Volger. ibid. 20, 49-66 (1954)

79. In *Diluted Magnetic Semiconductors*; J.K. Furydna, J. Kossut. Eds.; Semiconductors and Semimetals; Academic Press: New York, 1988; Vol. 25

80. Y. Ohno, D.K. Young, B. Beschoten, F. Matsukura, H. Ohno, D.D. Awschalom. *Nature*, 402, 790 (1999)

81. H. Ohno. *Science*, 281, 951 (1998); *J. Magn. Magn. Mater.*, 200, 110 (1999)

82. A. Wold, R.J. Arnott, J. B. Goodenough. *J. Appl. Phys.*, 29, 387 (1958)

83. J.B. Goodenough, A. Wold, R.J. Arnott, N. Menyuk. *Phys. Rev.*, 124, 373 (1961)

84. N.Y. Vasanthacharya, P. Ganguly, J.B. Goodenough, C.N.R. Rao. *J. Phys. C: Solid State Phys.*, 17, 2745 (1984)

85. R.I. Dass, J.Q. Yan, J.B. Goodenough. *Phys. Rev. B*, 68, 064415/1-064415/12 (2003)

86. J. Blasco, M.C. Sanchez, J. Perez-Cacho, J. Garcia, G. Subias, J. Campo. *J. Phys. Chem. Solids*, 63, 781 (2002)

87. C.L. Bull, D. Gleeson, K.S. Knight. *J. Phys.: Condens. Matter*, 15, 4927 (2003)

88. G Shirane, S. Hoshino. *J. Phys. Soc. Jpn.*, 6, 265 (1951)

89. M. Blackman. *Philos. Mag.*, 9, 831 (1958)

90. D. Taylor. *Br. Ceram. Trans. J.*, 83, 129 (1984)

91. D. Taylor. *Br. Ceram. Trans. J.*, 87, 39 (1988)

92. V. Korthius, N. Khosrovani, A.W. Sleight, N. Roberts, R. Dupree, W.W. Wareen Jr.. *Chem. Mater.*, 7, 412 (1995)

93. F.H. Gillery, E.A. Bush. *J. Am. Ceram. Soc.*, 42, 175-177 (1959)

94. T.A. Mary, J.S.O. Evans, A.W. Sleight, T. Vogt. *Science*, 272, 90 (1996)

95. A.W. Sleight. *Inorg. Chem.*, 37(12), 2854-2860 (1998)

96. N. Khosrovani, A.W. Sleight. *J. Inorg. Mater.*, 1, 3-10 (1999)

97. M.F. Hochella, G.E. Brown, F.K. Ross, G.V. Gibbs. *Am. Mineral.*, 64, 337 (1979)

98. J.P. Boilot, J.P. Salanie, G. Desplanches, D Le Potier. *Mater. Res. Bull.*, 14, 1469 (1979)

99. A.W. Sleight. *Endeavor*, 19(2), 64 (1995)

100. M.P. Attfield, A. W. Sleight. *Chem. Commun.*, 601-602 (1998)

101. M.P. Attfield, A. W. Sleight. *Chem. Mater.*, 10, 2013-2019 (1998)

102. N. Khosrovani, A.W. Sleight, T. Vogt. *J. Solid State Chem.*, 132, 355 (1997)

103. N. Khosrovani, V. Korthuis, A.W. Sleight, T. Vogt. *Inorg. Chem.*, 35, 485 (1996)

104. J.S.O. Evans, T.A. Mary, T. Vogt, M.A. Subramanian, A.W. Sleight. *Chem. Mater.*, 8, 2809 (1996)

105. G. Ernst, C. Broholm, G.R. Kowach, A.P. Ramirez. *Nature*, 396(12) 147 (1998)

106. N. Duan, U. Kameswari, A.W. Sleight. *J. Am. Chem. Soc.*, 121, 10432 (1999)

107. J.S.O. Evans, T.A. Mary, A.W. Sleight. *J. Solid State Chem.*, 137, 148 (1998)

108. M.T. Weller, P.F. Henry, C.C. Wilson. *J. Phys. Chem. B*, 104, 12224 (2000)

109. P.M Forster, A.W. Sleight. *Int. J. Inorg. Mater.*, 1, 123-127 (1999)

110. P.M. Forster, A. Yokochi, A.W. Sleight. *J. Solid State Chem.*, 140, 157 (1998)

111. T.G. Amos, A. Yokochi, A.W. Sleight. *J. Solid State Chem.*, 14, 303 (1998)

112. T.G. Amos, A.W. Sleight. *J. Solid State Chem.*, 160, 230 (2001)

113. T.G. Amos. Negative Thermal Expansion in $AOMO_4$ Compounds. Ph.D. Thesis, Oregon State University, Corvallis, OR, 2001

114. J.Z. Tao, A.W. Sleight. *J. Solid State Chem.*, 173, 45-48 (2003)

115. M.T. Dove, V. Heine, K.D. Hammonds. *Mineral. Magn.*, 59, 629 (1995)

116. J.Z. Tao, A.W. Sleight. *J. Solid State Chem.*, 173, 442-448 (2003)

117. W. Tiano, M. Dapiaggi, G. Artioli. *J. Appl. Crystallogr.*, 36, 1461 (2003)

118. E. Parthe. *Crystal Chemistry of Tetrahedral Structures*. Gordon and Breach Science Publishers: New York, 1964

119. R. Kykyneshi. M.S. Thesis, Oregon State University, Corvallis, OR, 2004

120. In *Impedance Spectroscopy : Emphasizing Solid Materials and Systems*. J.R. Macdonald Ed.; John Wiley & Sons: New York, 1987

# Chapter 2

# Structure and Properties of Two Polymorphs of $CuScO_2$

## 2.1 Introduction

Oxides with the delafossite ($CuFeO_2$) structure have been of interest for their thermopower, catalytic, and luminescent properties [1-9]. Delafossite $CuAlO_2$ was first shown to be a p-type transparent conductor by Benko and Koffyberg [10] in 1984, and 13 years later thin films of $CuAlO_2$ were prepared by Kawazoe et al [11]. Our main interest in delafossites has been to obtain p-type materials with higher conductivity [12-17]. Another of our interests has been the strong negative thermal expansion of the O—Cu—O linkage, which can lead to strong negative thermal expansion of the *c* cell edge [18]. Oxidized delafossites are of interest as frustrated magnetic systems and potential superconductors [1,19,20].

Many $A^{1+}M^{3+}O_2$ compounds are known with the delafossite structure [13], which can be described as the alternate stacking of edge-shared $MO_6$ octahedral layers and $A^{1+}$ ion layers perpendicular to the *c* axis, where each $A^{1+}$ ion is linearly coordinated by two $O^{2-}$ ions (Fig. 2.1). Because of the two-fold linear coordination of the $A^{1+}$ cation, the most common $A^{1+}$ cations in this structure are $Cu^{1+}$ and $Ag^{1+}$. Such compounds are usually semiconductors. However, a few compounds are known where the $A^{1+}$ cation is Pd or Pt. These compounds exhibit metallic properties, and the unusual oxidation state for these cations is stabilized by Pd-Pd or Pt-Pt bonding [21]. For the $Cu^{1+}M^{3+}O_2$ delafossites, the $M^{3+}$ cation can range in size from Al to La.

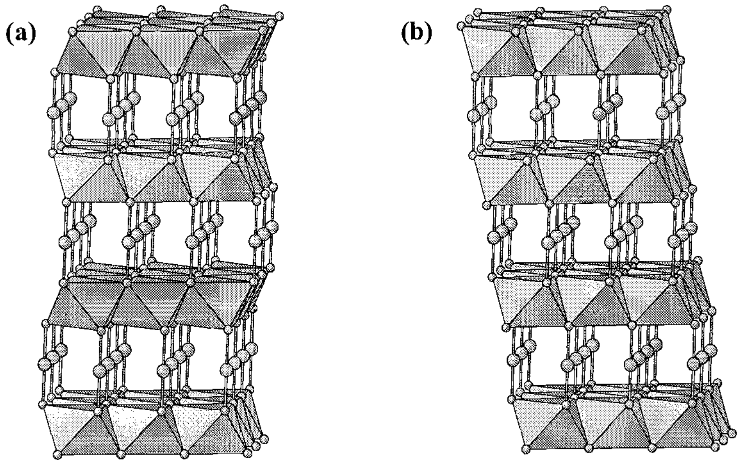

Figure 2.1 Structures of the 2H (a) and 3R (b) forms of $AMO_2$ delafossites with the hexagonal *c* axis vertical. Large spheres are $A^{1+}$ (Cu, Ag, Pd, Pt) cations, and small spheres are $O^{2-}$ ions. The 2H structure is based on ABAB stacking, and the 3R structure is based on ABCABC stacking. The orientation of the $MO_6$ octahedra is the same for all layers in the 3R form but switches back and forth in the 2H form.

It has been suggested that high covalency of the Cu—O bond gives a valence band favorable for good p-type conductivity in $Cu^{1+}M^{3+}O_2$ delafossites [11]. However, this explanation is implausible because there are no Cu—O—Cu connections in the delafossite structure to take advantage of such covalency. Instead it is likely that direct Cu—Cu interactions are responsible for the hole conductivity in $Cu^{1+}M^{3+}O_2$ delafossites. Several calculations have shown that Cu—Cu interactions between $Cu^{1+}$ cations are significant at the distances that occur in $Cu_2O$ and the delafossite structure [22–26]. This interaction is bonding in nature but produces only a very weak bond. No such bonding is expected for the formal $d^{10}s^0$ electronic configuration for $Cu^{1+}$.

However, the *d-s* hybridization that occurs due to the two-fold linear coordination of Cu to O transfers some electron density from the 3*d* shell to the 4*s* shell, thus allowing a very weak bond between Cu atoms. This interaction provides a reasonable pathway for the holes and is consistent with the observed strongly anisotropic conductivity [21]. A different situation arises when M is a transition metal with *d* levels close to the Fermi level. Now Cu—O—M—O—Cu linkages can provide a pathway for holes. In fact, the highest conductivity yet observed for a p-doped semiconductor with the delafossite structure is for $CuCr_{1-x}Mg_xO_2$ [15].

The p-type conductivity can be introduced by doping, i.e. substitution of a divalent cation into the octahedral site of the trivalent M cation, and/or by oxygen intercalation. Doping into both $CuAlO_2$ and $CuGaO_2$ systems has been proved to be very difficult. Significant quantities of oxygen can be intercalated into the $Cu^{1+}M^{3+}O_2$ delafossites only when the M cation exceeds a certain size. This is presumably because this oxygen must pass between Cu atoms in the Cu plane (Fig. 2.1). As the M cations become smaller the Cu—Cu distances become too short for such oxygen passage. Oxygen intercalation of $Cu^{1+}M^{3+}O_2$ delafossites is not possible if the M cation is smaller than Sc, and oxygen intercalation is rapid if M is larger than Sc. For $CuScO_2$ oxygen intercalation is very slow, and overall compositions more oxidized than $CuScO_{2.37}$ had not been reported on heating $CuScO_2$ in air or 1 atm of oxygen [13,27,28]. Some $CuMO_2$ delafossites can be oxidized at room temperature, but only if the M cation is larger than Sc [27,29]. However, the Cu—Cu distance increases with increasing size of the M cation, which tends to decrease the conductivity.

We chose to study $CuScO_{2+x}$ phases in detail because these are the $Cu^{1+}M^{3+}O_{2+x}$ delafossites with the smallest Cu—Cu distances for which oxygen intercalation is possible. We might then expect the highest conductivities for such oxygen intercalated phases, except for the situation where the conductivity is enhanced by a transition metal M cation. Moreover, divalent cations like Mg can readily substitute for Sc in the octahedral site. $CuScO_2$ is, therefore, a good intermediate case in which to test the efficacy of each type of dopant.

There has been no systematic study of the effect of different types of hole dopants on the transport properties of bulk $CuSc_{1-x}Mg_xO_{2+y}$ samples. In previous experiments on $CuSc_{1-x}Mg_xO_{2+y}$ films, $x$ for Mg was fixed and only $y$ for intercalated oxygen was varied [30]. In present study, both $x$ and $y$ for Mg and O were systematically changed in $CuScO_2$ powders and in films. Initial attempts to determine the structure of oxygen intercalated delafossites did not lead to reasonable structures [31]. Recently, two convincing structural studies have appeared. For $CuYO_{2.5}$ an ordered arrangement for the interstitial oxygen was reported [32]. For $CuLaO_{2.66}$ a complete rearrangement of the Cu—O layer was observed [33].

$CuScO_2$ is known to exist in both 2H and 3R polymorphs (Fig. 2.1) [13,34,35]. The difference is in the nature of the stacking along the hexagonal $c$ axis. Most preparations yield a mixture of the two forms. This mixing commonly extends to the atomic level leading to extensive stacking faults. The high concentration of stacking faults leads to diffraction patterns having peaks of different widths and shapes (Fig. 2.2). We refer to such materials as mixed-layer phases. Adding further to the complexity of the situation is that intercalated mixtures of the 2H and 3R $CuScO_{2+x}$ typically give diffraction patterns with four phases being present: low $x$ 2H, high $x$ 2H, low $x$ 3R, and high $x$ 3R. It is extremely challenging to obtain single phase $CuScO_{2+x}$ relatively free of stacking faults.

## 2.2 Experimental

### *2.2.1 Synthesis of 2H and 3R Polymorphs*

Polycrystalline samples of both 2H and 3R $CuScO_2$ were prepared by solid-state reactions, and 3R $CuScO_2$ was also prepared by an ion exchange reaction following a procedure described first by Doumerc *et al.* with some modifications [28,35]. A mixed-layer form of $CuScO_2$ (intergrown 3R and 2H) generally results when heating mixtures of equimolar amounts of $Cu_2O$ and $Sc_2O_3$ under various conditions. For example, heating at 1040 °C in air and then quenching in air to room temperature, heating at 900 °C in evacuated silica ampoules, and heating at 900 °C under an Ar flow all produced this mixed-layer form, which gives a very complex X-ray diffraction pattern (Fig. 2.2). Reduction of $Cu_2Sc_2O_5$ under argon at 900 °C or in air at 1040 °C also gave the mixed-layer delafossite phase. These mixed-layer products were dominated by a 3R type structure with stacking faults of the 2H type. We have calculated the diffraction patterns of such mixed-layer samples using DIFFaX [36]. Samples prepared in air were gray, presumably due to slight oxidation of $Cu^{1+}$ to $Cu^{2+}$

on cooling in air. Samples prepared under Ar were much lighter in color, and samples prepared in evacuated and sealed silica tubes were nearly colorless with a pink cast.

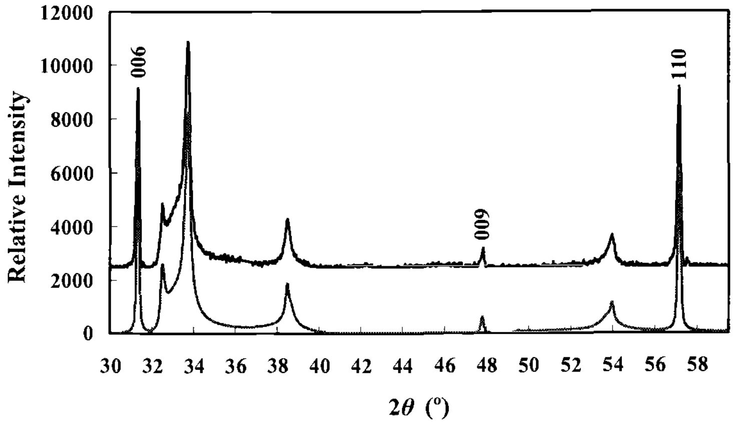

Figure 2.2 A typical powder X-ray diffraction pattern of a mixed-layer $CuScO_2$ sample in which the 3R form dominates. The upper spectrum is experimental data. The lower plot simulates the impact of stacking faults perpendicular to the *c* axis. Peaks that are not broadened by the stacking faults arise from 00*l* and *hk*0 reflections, respectively.

Doping with divalent cations, such as $Cu^{2+}$, $Mg^{2+}$, $Zn^{2+}$ and $Ca^{2+}$ was found effective to stabilize the 2H $CuScO_2$ phase. For example, 2H $CuSc_{0.95}Mg_{0.05}O_2$ free of 3R was prepared by placing a pellet of a mixture of $Cu_2O$ (Cerac, 99%), $Sc_2O_3$ (Stanford Materials, 99.95%), and MgO (Aldrich, 99%) with a molar ratio 1.00:0.95:0.10 into a furnace preheated to 1100 °C. After heating for 24 hr in air, the sample was quenched in air to room temperature. The color of this powder was dark blue due to the Mg doping. The furnace must be preheated to 1100 °C prior to placing samples in the furnace to prevent the formation of the 3R phase. A variation of this synthesis procedure gave 3R $CuScO_2$ with only very small amount of 2H impurity. A pellet of a $Cu_2O/Sc_2O_3$ mixture with a 1% Sc excess was heated in air at 600 °C/hr to

1100 °C. After 24 hr at 1100 °C, the sample was quenched in air to room temperature. The color of this powder was light gray, presumably due to the slight oxidation that occurs during cooling. The synthesis of $CuScO_2$ in air must be above 1040 °C because $Cu^{1+}$ in this system oxidizes to $Cu^{2+}$ at lower temperatures. However, the temperature must be further increased to 1100 ~ 1150 °C to avoid forming a predominately mixed-layer phase. Complete decomposition of the delafossite structure occurred when heating in air at temperatures exceeding 1200 °C.

To obtain high-purity 3R $CuScO_2$ completely free of the 2H polymorph, an ion exchange reaction was used. $LiScO_2$ was prepared by heating equimolar amounts of $Li_2CO_3$ (Sigma, 99.6%) and $Sc_2O_3$ in air at 1050 °C for 24 hr. We found that all commercial sources provided CuCl that was badly contaminated with $Cu^{2+}$ hydroxychloride. Using such a reagent always resulted in impurities in the 3R product regardless of the container used for the ion exchange reaction. The container may, however, be important. In previous studies the container has been silica or alumina [28,35]. We used Cu metal crucibles; thus, there is no opportunity for contamination and a very low oxygen partial pressure is insured. CuCl (Cerac, 99%) was purified following the method of Sakida et al [37]. A mixture of $LiScO_2$ and CuCl with a molar ratio 1:1.3 was placed in a Cu crucible inside a stainless steel vessel with Ar flowing through. The vessel was then heated to 650 °C for 5 hr. After cooling to room temperature the powder was washed with 2M aqueous $NH_3$ to remove LiCl and excess CuCl. After drying in air for 24 hr, the product obtained was slightly off white, lighter in color than the 3R sample prepared in air by direct synthesis.

### *2.2.2 Oxygen Intercalation of Powders and Crystals*

A 28 g sample of 3R $CuScO_{2.5}$ was prepared for a neutron diffraction study by heating 3R $CuScO_2$ powder prepared by the ion-exchange reaction at 420 °C for 6 days under 120 atm of oxygen pressure. An even longer oxidation time was required to oxidize the air-prepared 3R sample to $CuScO_{2.5}$. Oxidizing the same amount of the Mg-doped 2H sample over 12 days with intermediate grindings of the sample still was not adequate to produce single phase $CuScO_{2.5}$. Oxidative intercalation can be accelerated by increasing the temperature to 440 °C, but this causes some decomposition of the delafossite structure. Good quality fully oxidized $CuScO_{2.5}$ can only be prepared using long oxidation times at low temperatures. Samples with smaller particle size oxidize more rapidly than those with larger particles, explaining the differences in oxidation rates mentioned above for 2H and 3R samples.

Some 2H CuScO2 crystals of about 0.1 mm × 0.1 mm × 0.1 mm were also oxidized under the same condition for 12 days. The color of the crystals changed from colorless to black.

### *2.2.3 Doping and Oxidation of Pressed Pellets*

Samples of $CuSc_{1-x}Mg_xO_2$ varing $x$ from 0.01 to 0.15 were prepared from stoichiometric mixtures of $Cu_2O$ (Cerac, 99%), $Sc_2O_3$ (Stanford Materials, 99.95%), and MgO (Aldrich, 99%) following the procedures in 2.2.1. The resulting pellets were pulverized for XRD analysis. After phase characterization 0.5 g of each sample was pressed into a pellet of 12 mm in diameter under a pressure of 4.5 tons. These pellets were replaced in the preheated furnace and sintered in air at 1100 °C for 20 hr and then quenched to room temperature, producing materials with 76% ~ 85 % of theoretical density. Pure (no Mg doping) $CuScO_2$ pellets were also prepared, in both 2H and 3R forms. The phase pure 2H form was obtained by the same process as the Mg-doped samples, except that a small Cu excess was used instead of MgO. To obtain phase pure 3R $CuScO_2$, a small (about 1%) Sc excess was used.

Since oxygen intercalation is prohibitively slow in sintered material, another 0.5 g of each above sample was cold-pressed into a bar shape of about 8 mm × 5 mm × 1.5 mm before treating under 120 atm of oxygen pressure at 420 °C for 6 days in a quartz tube inside a high-pressure stainless steel tube furnace. The density of oxygenated bars is around 71% ~ 79 % of the theoretical value.

In what follows, measurements are reported for samples with the same Mg content but different oxygen contents. Two sintered pellets were produced under identical conditions from the same starting powder, ensuring identical Mg content, and one of the pellets was reground, cold-pressed and oxidized.

Corresponding thin films of $CuSc_{1-x}Mg_xO_2$ were prepared through rf sputtering followed by rapid thermal anneal (RTA) and Ar reduction, and further oxidized to $CuSc_{1-x}Mg_xO_{2+y}$. All the experiments concerning thin films were carried out by Tate's lab in Physics Department of OSU and experimental details can be found in Ref. [38].

### *2.2.4 Characterizations and Calculations*

X-ray powder diffraction data were obtained using a Siemens D5000 diffractometer with Cu Kα radiation. For accurate determination of cell dimensions, data were collected over 25 ~ 150° $2\theta$ with KCl as an internal standard. Single crystal X-ray diffraction data were taken at room temperature on a Rigaku AFC6R diffractometer with monochromatic Mo Kα radiation ($\lambda = 0.71069$ Å). Large samples of unoxidized and oxidized 2H and 3R $CuScO_2$ were also characterized by neutron powder diffraction using the BT-1 32-counter high resolution diffractometer at the NIST Center for Neutron Research at the National Institute of Standards and Technology. A Cu (311) monochromator, yielding a wavelength of 1.5402 Å, was employed. Collimation of 15' or 7' of arc was used before the monochromator, 20' before the sample, and 7' before the detectors. The samples were loaded into vanadium containers 15.6 mm in diameter and 50 mm in length. Data were collected at room temperature over a $2\theta$ range of 3 ~ 168°. Crystal structures were refined by Rietveld method using Fullprof software [39].

EUTAX software [40] was used to calculate the Madelung energies and potentials. For the Madelung energy comparison of the 2H and 3R forms of $CuScO_2$ the $a$ cell edges were fixed to be exactly the same and the $c$ value of the 2H form was fixed at precisely 2/3 of the value for the 3R form. Furthermore, values of the $z$ parameter of oxygen were fixed to give the same Cu–O and Sc–O bond distances in both forms. This was done so that one is comparing only the difference between the stacking sequences in the two polymorphs. Bond valence calculations utilized the software of Hormillosa *et al.* [41].

The oxygen content of the oxidized delafossite phase was determined through the weight loss on heating samples under Ar in a TGA apparatus. Some partially oxidized samples were also analyzed by Electron Microprobe. BET surface area measurement and SEM images were used for a qualitative size analysis.

The following transport and optical property measurements were conducted by Tate's Lab in Physics Department of OSU. Temperature-dependent conductivities of pellets were measured in a liquid nitrogen cryostat in the range of 120 ~ 290 K. Silver contacts were used to minimize contact resistance and a 4-probe co-linear geometry was used for the unoxidized circular pellets. Silver contacts and a 4-probe technique appropriate to bar geometry were used for the oxidized samples. The carrier type was determined by measurements of the Seebeck coefficient at room temperature. A temperature gradient of about 3 K was established across the sample, and the resulting thermoelectric voltage was measured.

Diffuse reflectance spectra of powdered samples between 250 and 900 nm were obtained using a Xe lamp and a grating double monochromator as the source. The light diffusely reflected by the powders was collected with an integrating sphere and detected with a Si diode detector. These data were normalized to the signal obtained from MgO powder under the same conditions.

## 2.3 Results

### *2.3.1 Cell Dimensions from XRD Data*

Most synthesis approaches for $CuScO_2$ gave a mixed-layer product. Figure 2.2 shows a typical example of a diffraction pattern of such a product. The pattern resembles that expected for the 3R structure. Both *hk0* and *00l* peaks are sharp, but other peaks are broadened, shifted, and asymmetric due to stacking faults perpendicular to the *c* axis. The pattern simulated with DIFFaX assumes a 3R structure, which is heavily faulted with stacking of the type that occurs in the 2H form (Fig. 2.1). On heating these mixed-layer phases to higher temperatures the diffraction pattern shows only sharp peaks of two phases, a dominant pattern of 3R $CuScO_2$ with some 2H $CuScO_2$ present.

The Mg doping obviously helped stabilizing the 2H form. XRD patterns showed single phase of 2H $CuSc_{1-x}Mg_xO_2$ ($x$ = 0.01 to 0.15) up to 5% Mg doping. Small amount of $Cu_2O$ and MgO were present when the doping concentrations were too high. The ionic radius of $Mg^{2+}$ (0.72 Å) is smaller than that of $Sc^{3+}$ (0.745 Å) in octahedral coordination [42], therefore a lattice contraction upon substitution is expected. The result of lattice refinement on XRD data is shown in Figure 2.3. The decreasing cell edge *a* up to 3% Mg doping indicates that Mg is incorporated in the $CuScO_2$ lattice up to a doping level of at least 3% although neutron diffraction refinement suggests a slightly higher solubility (around 5%). The pure 2H sample without Mg doping was prepared with a slight Cu excess, which is functioning as

$Mg^{2+}$ in the form of $Cu^{2+}$. The $Cu^{2+}$ ion (0.73 Å) is an even closer match to the size of $Sc^{3+}$, so this substitution is highly likely. Moreover, substitution of $Cu^{2+}$ on an octahedral site has been known to occur in the delafossite structure like $Cu_2(CuTi)O_4$ in both 2H and 3R forms [43,44].

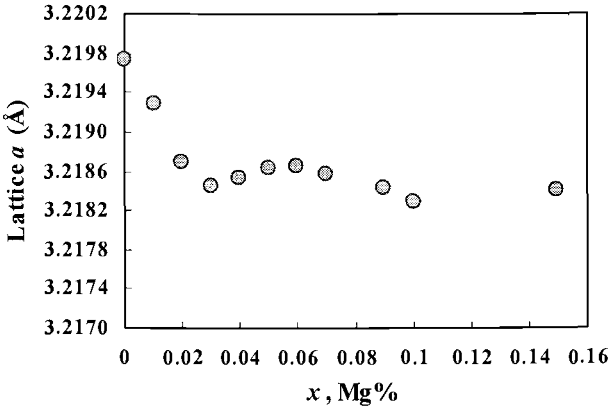

Figure 2.3 Lattice parameter *a* as a function of Mg doping in $CuSc_{1-x}Mg_xO_2$.

The oxygen intercalation reaction is very slow for both the 2H and 3R polymorphs of $CuScO_2$. Oxidized samples are black and usually contain two phases of $CuScO_{2+x}$, one with high *x* and one with low *x*. This was shown by both XRD and electron microprobe analysis.

The oxidation behavior is shown for 2H $CuScO_{2+x}$ phases in Figure 2.4(a). As oxidation commences, new peaks occur at lower angles. These are from a phase with a composition close to $CuScO_{2.5}$. With further oxidation these peaks grow in size while the original peaks decrease in size. The position of the 004 peak hardly changes on oxidation because there is only a very small change in the *c* axis on oxygen intercalation. A composition of $CuScO_{2+x}$ with *x* higher than 0.37 was only obtained by heating powder samples under high oxygen pressures. In Figure 2.4(b) X-ray diffraction patterns for pure phases with *x* values close to 0.0 and 0.5 are superimposed for both the 2H and 3R forms of $CuScO_{2+x}$. The 110 reflection shifted the most to the low angle region because the intercalated oxygen stuffed between Cu atoms. The *a* cell edge increase on oxidation is 1.46% and 1.61% for 2H and 3R forms, respectively. The slight shift of 004 reflection to low angle in 2H and 006 peak to high angle in 3R is caused by a 0.23% expansion in 2H and a 0.30% contraction in 3R along the *c* axis.

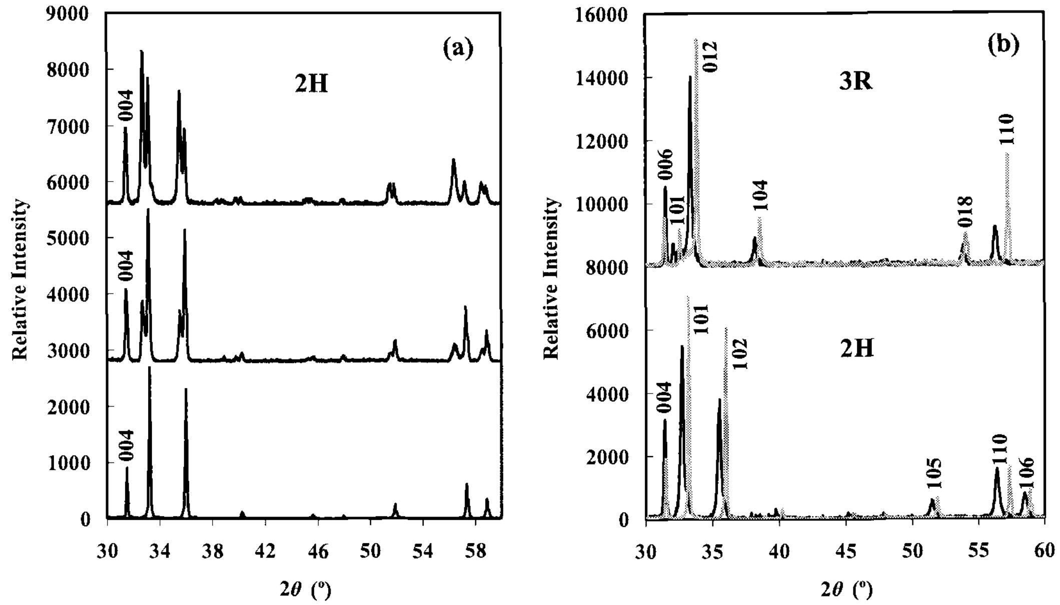

Figure 2.4 X-ray diffraction patterns for several $CuScO_{2+x}$ samples. (a) From bottom to top, peaks of oxidized 2H $CuScO_{2.5}$ phase appear and increase with increasing oxidation time; (b) Overlapping patterns of single phase $CuScO_2$ (light line) and $CuScO_{2.5}$ (dark line) samples.

The large changes in the *a* cell edge on oxygen intercalation can be correlated with the amount of intercalation. Using our TGA analysis for the overall oxygen content for these samples and assuming a linear relationship between *x* and the *a* cell edge, we can estimate the phase fields for the high *x* and low *x* phases (Fig. 2.5). Data for 2H $CuScO_{2+x}$ phases were sufficient for good definition of the stability limits. We have much less information for 3R $CuScO_{2+x}$ phases, but qualitatively they show the same pattern. The values of *x* in Figure 2.5(a) were determined by TGA, an overall intercalated oxygen content of the two-phase mixture. Paired (up and down) open circle and cross are for the low and high *x* phases from X-ray diffraction of each 2H sample, paired solid and open triangles are for the low and high *x* phases from neutron diffraction of a 2H sample, and the diamond and solid circle are for unoxidized 2H samples from X-ray and neutron diffraction, respectively. Figure 2.5(b) is derived from the data in plot (a) by assuming a linear relationship between cell edge *a* and the intercalated amount of oxygen *x* in individual phases. The open and filled squares are from neutron diffraction of a 3R sample. The *x* values for neutron diffraction are determined directly from Rietveld refinement.

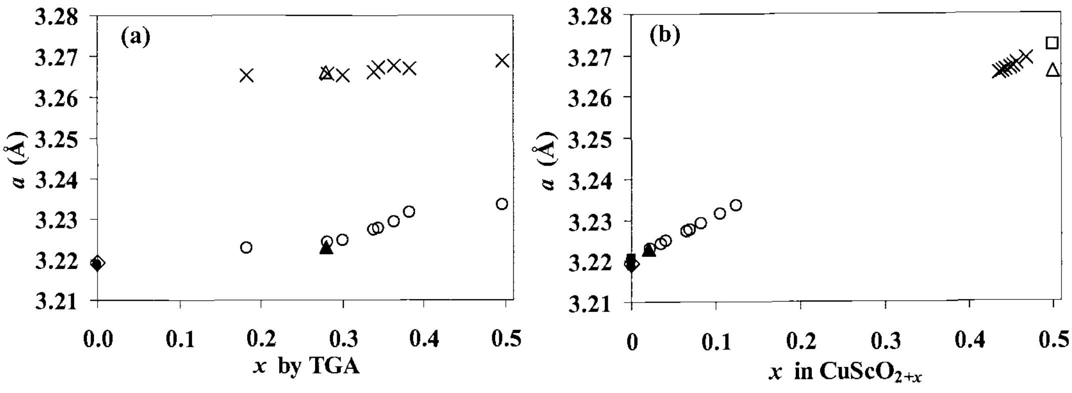

Figure 2.5 The *a* cell edge vs. *x* for $CuScO_{2+x}$ compositions.

Attempts to intercalate single crystals of 2H $CuScO_2$ about 0.1 mm on an edge over 10 days were unsuccessful. Although the crystals darkened to black, this was due to a very thin surface layer. Cell edge *a* was essentially not changed based on XRD data. Likewise, attempts to oxygen intercalate sintered pellets were unsuccessful, indicating that oxygen diffusion along grain boundaries is not high. Thin films are, however, readily oxidized to $CuScO_{2.5}$ [12,38].

### *2.3.2 Size Analysis by BET and SEM*

BET surface area was measured to be 2.1 $m^2/g$ for 3R $CuScO_2$ prepared by ion exchange reaction and 0.7 $m^2/g$ for Mg-doped 2H $CuScO_2$. Although this is a somewhat qualitative analysis, it does show that the particle size of the 2H is much larger than that of the 3R.

SEM images of $CuScO_2$ were taken for Mg-doped 2H and 3R made by direct synthesis in air and by ion exchange (I.E.) reaction, before and after oxygen intercalation. The results are shown in Figure 2.6. We can see a size distribution in all of the three samples, and the average particle size of 2H sample is definitely the largest, air-made 3R the medium, and I.E.-made 3R the smallest. Some break up of the particles is observed for all of the three samples upon oxidation, which leads to a smaller particle size for the oxidized samples. This has been further proved by the Rietveld refinements of the neutron diffraction data.

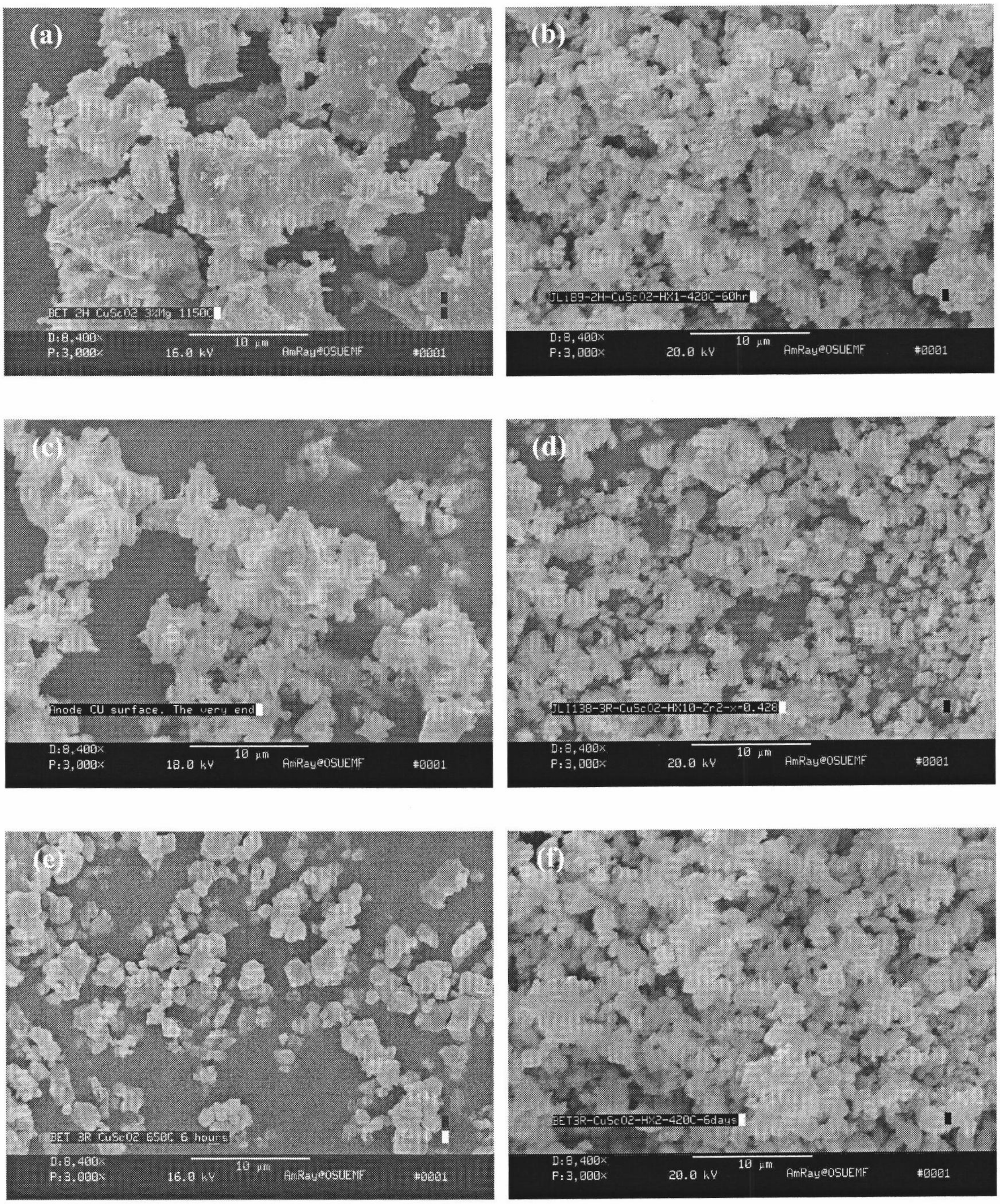

Figure 2.6 SEM images of 2H and 3R $CuScO_2$ before and after oxygen intercalation. The marker in each image is 10 µm. (a) 2H before oxidation; (b) 2H after oxidation; (c) air-made 3R before oxidation; (d) air-made 3R after oxidation; (e) I.E.-made 3R before oxidation; (f) I.E.-made 3R after oxidation.

### 2.3.3 *Thermogravimetric Analysis (TGA)*

Highly unusual behavior was observed when 2H and 3R $CuScO_2$ powders were heated under air or oxygen in TGA experiments (Fig. 2.7(a)). Heating under oxygen produces only weight gain in the case of 3R $CuScO_2$, but in the case of 2H $CuScO_2$ the weight initially gained is lost at about 440 °C. Heating 2H $CuScO_2$ under air results in the weight loss at a slightly lower temperature; the slower the heating rate, the higher the oxygen uptake before the loss commences (Fig. 2.7(b)). Heating 3R $CuScO_2$ under air results in behavior similar to that observed for 2H $CuScO_2$ under oxygen except that weight loss commences at about 580 °C (Fig. 2.7(c)). Starting with oxidized $CuScO_2$ produces very similar results (Fig. 2.7(d)). It is thus evident that the intercalated oxygen is only weakly held in $CuScO_2$, but it is more tightly held in the 3R form than the 2H form.

The second weight increase region observed by TGA around 600 °C corresponds to the destruction of the delafossite structure. Initially, $Cu_2Sc_2O_5$ is not observed as a decomposition product. Instead, the products are $Cu_2O$, CuO, and $Sc_2O_3$. As temperature is further increased to 1000 °C in air or pure oxygen at 1 atm, the only phase present is $Cu_2Sc_2O_5$. The observed mixture containing $Cu_2O$ and $Sc_2O_3$ suggests that $CuScO_2$ becomes thermodynamically unstable as temperature is decreased from 1000 °C, regardless of the oxygen partial pressure. Precisely such behavior has been reported in the Cu/Al/O system where below 1030 °C a mixture of $Cu_2O$ and $Al_2O_3$ is stable and will not react to form $CuAlO_2$ [45]. Thus, $CuAlO_2$ and possibly $CuScO_2$ are entropy stabilized compounds. Of course, oxygen intercalated delafossites are presumably thermodynamically metastable under all temperature and pressure conditions.

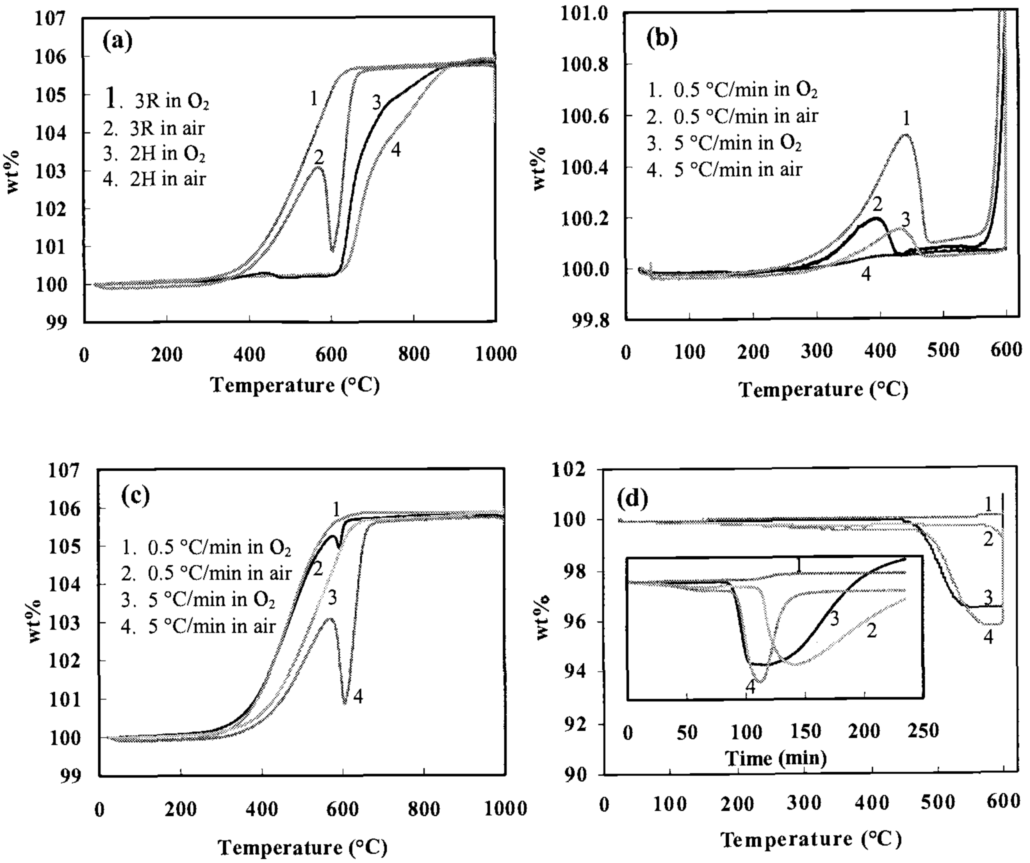

Figure 2.7 Thermal gravimetric results for heating $CuScO_{2+x}$ samples under flowing air or $O_2$ at 100 mL/min. (a) heating $CuScO_2$ samples at 5 °C/min; (b) oxidation of 2H $CuScO_2$ samples at different heating rates; (c) oxidation of 3R $CuScO_2$ samples at different heating rates; (d) heating 3R $CuScO_{2.43}$ in $O_2$ (1), heating 3R $CuScO_{2.43}$ in air (2), heating 2H $CuScO_{2.38}$ in air (3), heating 2H $CuScO_{2.38}$ in $O_2$ (4).

Cold-pressed bar samples of $CuSc_{1-x}Mg_xO_2$, with or without Mg doping, all turned black after high pressure oxygen intercalation. XRD patterns are very similar to what is shown in Figure 2.4(a), a two-phase mixture of different intercalated oxygen content with $y$ varying from 0 to 0.5 per formula unit of $CuSc_{1-x}Mg_xO_{2+y}$. Thermogravimetric analysis showed a systematic change of average oxygen uptake with doping levels (Fig. 2.8(a)). The calculated excess oxygen content $y$ based on the percentage weight loss is shown in Figure 2.8(b) as a function of Mg doping.

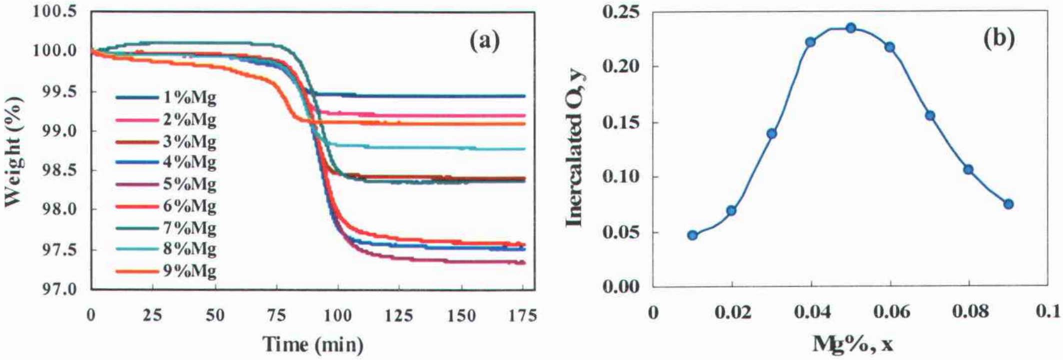

Figure 2.8 Determination of average oxygen uptake in $CuSc_{1-x}Mg_xO_{2+y}$ bar samples as a function of doping level by TGA.

### 2.3.4 *Structure Refinement of Neutron Diffraction Data*

Results of the Rietveld refinements of the neutron diffraction data for 2H and 3R $CuScO_2$ and $CuScO_{2.5}$ are summarized in Tables 2.1 and 2.2.

The 2H structure was refined in space group $P6_3/mmc$ with atom positions of Cu (1/3, 2/3, 1/4), Sc (0, 0, 0), O (1/3, 2/3, $z$) and interstitial oxygen (Oi) in sites 0, 0, 1/4 and 2/3, 1/3, 1/4. The 3R structure was refined in space group $R\bar{3}m$ with hexagonal atom positions of Cu (0, 0, 0), Sc (0, 0, 1/2), O (0, 0, $z$) and interstitial oxygen (Oi) in 1/3, 2/3, $z$.

Table. 2.1 Results of Rietveld Refinement using Fullprof

| | **Unoxidized 2H** | **Oxidized 2H** | **Unoxidized 3R** | **Oxidized 3R** |
|---|---|---|---|---|
| $R_\mathrm{p}$ | 4.16 | 3.90 | 4.95 | 5.03 |
| $R_\mathrm{wp}$ | 5.23 | 4.98 | 5.98 | 6.17 |
| $\chi^2$ | 1.30 | 2.72 | 1.29 | 1.30 |
| $a$, Å | 3.2187(1) | 3.2660(1) | 3.2204(1) | 3.2722(1) |
| $c$, Å | 11.4037(1) | 11.4297(1) | 17.0999(1) | 17.0484(3) |
| $V$, Å$^3$ | 102.313(1) | 105.583(1) | 153.582(1) | 158.083(4) |
| O ($z$) | 0.08954(6) | 0.0872(1) | 0.1071(1) | 0.1083(2) |
| Oi[a] ($z$) | | 0.0 | | 0.0174(5) |
| Oi occ. | | 0.56(2)[b] | | 0.54(2) |
| Cu $U_{11}$[c] | 0.0156(4) | 0.0058(9) | 0.0167(6) | 0.011(2) |
| Cu $U_{33}$ | 0.0005(4) | 0.0041(9) | 0.0035(6) | 0.008(2) |
| Sc $U_{11}$ | 0.0048(3) | 0.0060(7) | 0.0074(4) | 0.009(1) |
| Sc $U_{33}$ | 0.0066(3) | 0.0212(9) | 0.0114(5) | 0.051(2) |
| O $U_{11}$ | 0.0052(4) | 0.0061(9) | 0.0059(5) | 0.014(2) |
| O $U_{33}$ | 0.0024(4) | 0.0017(8) | 0.0025(5) | 0.009(2) |
| Oi $U_{11}$ | | 0.015(4) | | |
| Oi $U_{33}$ | | 0.026(4) | | |
| Oi $U_\mathrm{iso}$ | | | | 0.007(3) |
| Size 00$l$[d], Å | $f$ | $f$ | 327.25 | 280.72 |
| Size $hk$0[d], Å | $f$ | $f$ | 781.50 | 241.07 |
| Strain 00$l$[e] | 0.0000(1) | 0.0006(1) | 0.0000(1) | 0.0022(1) |
| Strain $hk$0[e] | 0.0003(1) | 0.0024(1) | 0.0016(1) | 0.0033(1) |

[a] Oi represents interstitial oxygen.

[b] This is the total interstitial oxygen, 55% of which is at 0,0,1/4 and 45% of which is at 2/3,1/3,1/4.

[c] Anisotropic temperature factors are expressed as: $\exp[-2\pi^2(U_{11}h^2a^{*2}+ U_{22}k^2b^{*2}+ U_{33}l^2c^{*2}+2U_{12}hka^*b^*+2U_{13}hla^*c^*+2U_{23}klb^*c^*)]$.

[d,e] Anisotropic size and strain parameters parallel or perpendicular to the $c$ axis.

[f] The calculated crystallite size of 2H samples is too large to be significant.

Table 2.2 Bond distances (Å), angles (°) and valences

| | **Unoxidized 2H** | **Oxidized 2H** | **Unoxidized 3R** | **Oxidized 3R** |
|---|---|---|---|---|
| Cu–Cu[a] | 3.2187(1) | 3.2660(1) | 3.2204(1) | 3.2722(1) |
| Cu–O | 1.8299(7) | 1.861(2) | 1.832(1) | 1.846(3) |
| Cu–Oi | | 1.8856(0) | | 1.912(1) |
| Sc–O | 2.1203(3) | 2.1326(7) | 2.1199(5) | 2.135(1) |
| Sc–Oi | | 2.8574(0) | | 2.545(9) |
| O–O | 2.7611(7) | 2.743(2) | 2.758(1) | 2.745(3) |
| O–Oi | | 2.649(1) | | 2.443(6) |
| O–Oi’ | | | | 2.857(7) |
| Oi–Oi | | 1.8856(0) | | 1.980(4) |
| Sc–O–Sc | 98.75(1) | 99.94(3) | 98.85(2) | 100.02(5) |
| Cu–O–Sc | 118.79(2) | 117.85(5) | 118.71(4) | 117.8(1) |
| $h_{Sc\text{-}O}$[b] | 2.0422 | 1.9933 | 2.0368 | 1.9901 |
| BV(Cu)[c] | 1.074 | 2.080 | 1.068 | 2.066 |
| BV(Sc) | 2.880 | 2.823 | 2.886 | 2.848 |
| BV(O) | 1.977 | 2.006 | 1.977 | 2.019 |
| BV(Oi1) | | 1.716 | | |
| BV(Oi2) | | 1.749 | | |
| BV(Oi) | | | | 1.637 |

[a] Distances of Sc–Sc and the other O–O are the same as Cu–Cu distance.

[b] The $h_{Sc\text{-}O}$ represents the thickness of $[ScO_2]^{1-}$ sheets in Å.

[c] BV stands for bond valence.

Agreement between calculated and observed neutron diffraction patterns for oxidized and unoxidized 2H $CuScO_2$ is shown in Figure 2.9. Surface area measurements and SEM images qualitatively confirm the peak shape analysis (Table 2.1) indicating that our 3R sample has a much smaller average particle size than does our 2H sample. The crystallite size of our 2H sample was too large to produce peak broadening significantly greater than instrumental broadening. For our 3R sample it is apparent that crystallite size decreases on intercalation. For both the 2H and 3R samples, strain increases on intercalation. Some break up of crystallites is expected during intercalation and it can be seen clearly from SEM images. The increased strain is likely due to some nonuniformity of the distribution of intercalated oxygen. Because the *a* cell edge is more sensitive to the intercalation than is the *c* cell edge, strain is expected to be anisotropic as observed. Significant decomposition of the delafossite structure was observed during intercalation of the 3R form prepared by ion exchange reaction but not for the 2H form or the 3R form prepared by direct synthesis in air.

Oxygen intercalation occurred much more slowly in the 2H form relative to the 3R form, which is attributed to the larger particle size of the 2H form. Thus, the large sample prepared for neutron diffraction studies contained 2H phases with low and high oxygen content. For the slightly oxidized 2H phase the *a* cell edge had increased from 3.219 to 3.223 Å. Refinement of the oxygen occupancy indicated a composition of $CuScO_{2.02}$ with essentially all of the oxygen residing in the site with Sc atoms above and below. Strain in the *ab* plane increased from 0.0003 to 0.0012 suggesting some nonuniformity in the distribution of the intercalated oxygen.

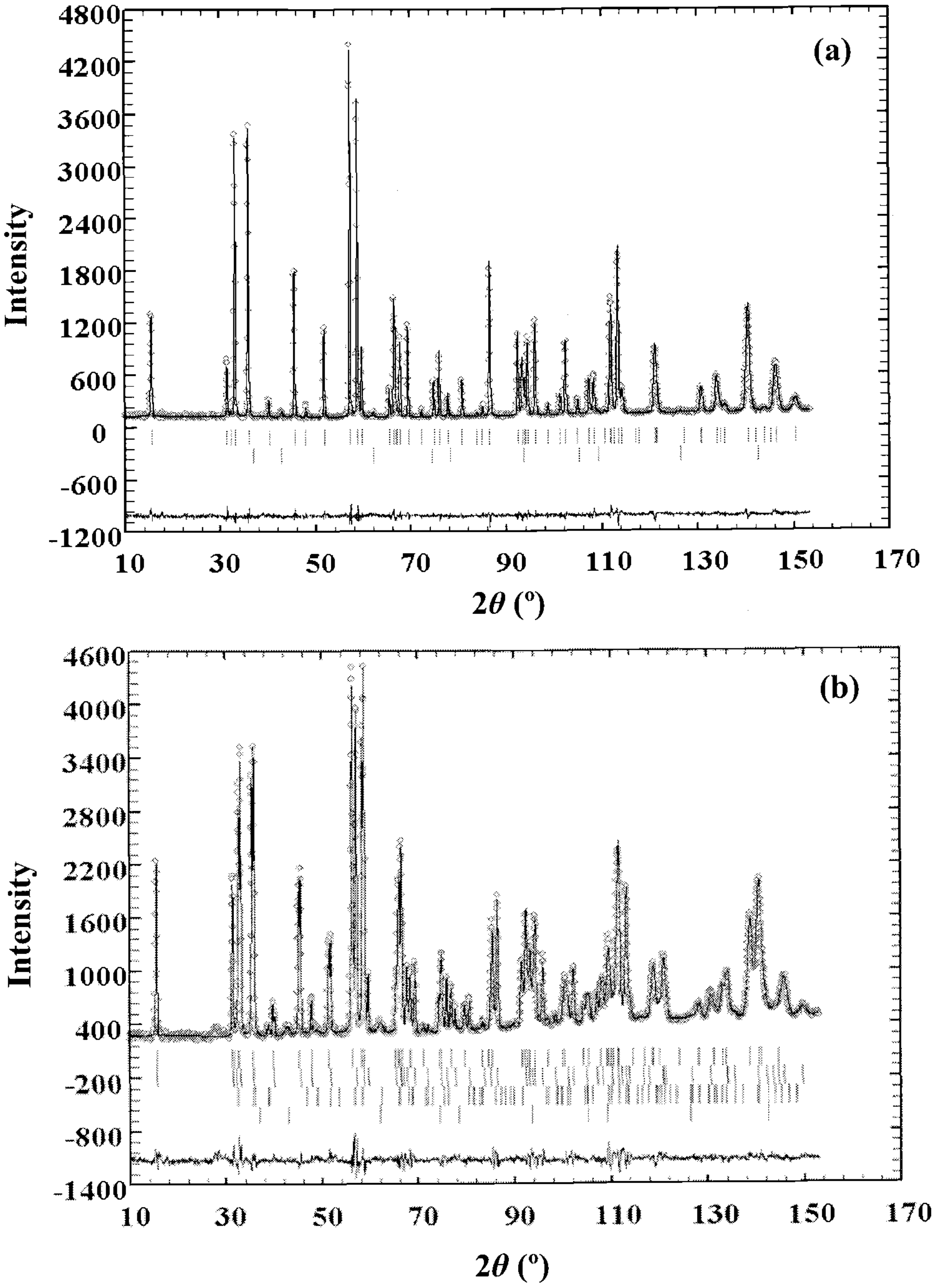

Figure 2.9 Observed (open circles) and calculated (solid line) neutron diffraction patterns for 2H $CuScO_2$ before (a) and after (b) oxidation. The bottom curve is the difference ($I_{obs} - I_{calc}$) pattern on the same scale. The vertical bars indicate allowed peak positions for each phase: (a) top vertical bars are for $CuScO_2$ (98.2%) and lower vertical bars are for MgO (1.8%); (b) vertical bars, from top to bottom, are for $CuScO_{2.5}$ (50.8%), $CuScO_{2.02}$ (43.9%), CuO (3.2%) and MgO (2.1%), respectively.

Within the accuracy of our ability to determine unit cell parameters, the *a* cell edges for 3R and 2H $CuScO_2$ are the same, and the *c* cell edge of 2H $CuScO_2$ is two thirds of the *c* cell edge for 3R $CuScO_2$. The apparent discrepancy with this conclusion indicated in Table 2.1 is due to the Mg substitution for Sc in the 2H form. There were no indications that space groups of 2H and 3R $CuScO_2$ changed during intercalation. Likewise there were no indications that the intercalated oxygen was ordered in the way reported for $CuYO_{2.5}$ [32]. Refinements assuming the orthorhombic $CuYO_{2.5}$ structure did not account for the observed peak broadening any better than assuming that this broadening was due to crystallite size and strain effects. More importantly, the superstructure peaks that should occur with this ordering were not present in diffraction patterns of 2H $CuScO_{2.5}$. It remains possible that electron diffraction studies might reveal indications of ordering of the interstitial oxygen.

The possibility that $CuScO_2$ could intercalate water was also considered. Samples were placed under water at room temperature for 8 days and under water at 100 °C for 24 hr. X-ray diffraction and TGA analysis indicated that no water uptake or decomposition had occurred.

### *2.3.5 Transport and Optical Properties*

The room temperature conductivity as a function of Mg doping for cold-pressed $CuSc_{1-x}Mg_xO_{2+y}$ bar samples before and after oxidation in high pressure $O_2$ is shown in Figure 2.10 (a) and (b), along with the Seebeck coefficient for the same samples. The conductivity introduced by doping alone increases almost linearly with increasing Mg content up to $x = 0.06$ and peaks at $1.5 \times 10^{-2}$ S/cm (Fig. 2.10(a)). Further increase of the dopants has an inverse effect on the conductivity. The conductivity of the "undoped" 2H $CuScO_2$ (with 1% Cu excess) is comparable to that of the 1% Mg-doped sample, which suggests that the excess Cu added initially to stabilize the 2H polytype does substitute $Sc^{3+}$ on the octahedral site as $Cu^{2+}$ and contributes a hole just as $Mg^{2+}$ does. On the other hand, the conductivity of the real undoped 3R $CuScO_2$ is an order of magnitude lower. The Seebeck coefficients are all positive, indicating p-type conductivity.

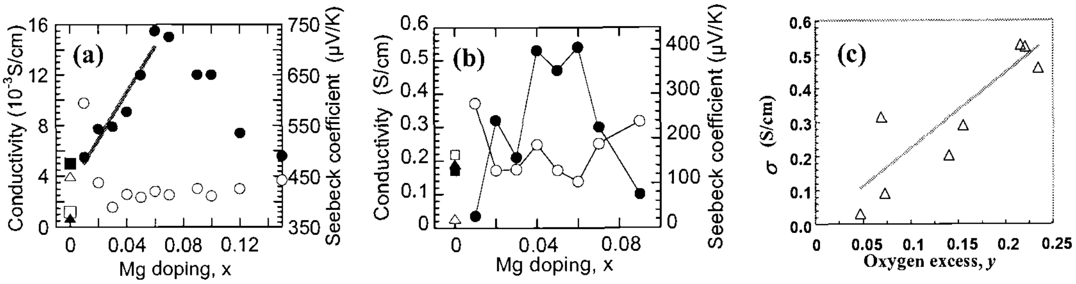

Figure 2.10 (a), (b) Room temperature conductivity (closed circles, left scale) and Seebeck coefficients (open circles, right scale) of $CuSc_{1-x}Mg_xO_{2+y}$ bar samples as a function of Mg doping before (a) and after (b) oxidation. Squares and triangles are for undoped 2H and 3R $CuScO_{2+y}$, respectively. (c) Room temperature conductivity of $CuSc_{1-x}Mg_xO_{2+y}$ induced by excess oxygen alone as a function of average intercalated oxygen content determined by TGA (courtesy of Dr. J. Tate and R. Kykyneshi).

Oxygen intercalation increased the conductivity by about 1.5 orders of magnitude with a maximum value of approximately 0.5 S/cm at $x = 0.05$ and 0.07 doping levels (Fig. 2.10(b)). The Seebeck coefficients are still positive but in general dropped by a factor of 3 ~ 4, indicating higher p-type conductivities. Notice that this is a conductivity that combined contributions from both cation doping and oxygen intercalation, in Figure 2.10(c) the effect of Mg doping is subtracted and the conductivity induced by excess oxygen alone is shown as a function of average intercalated oxygen per formula unit of $CuSc_{1-x}Mg_xO_{2+y}$ determined by TGA. The conductivity increases with increasing amount of intercalated oxygen as expected.

The conductivity of non-doped, or 1% Cu-doped, 2H $CuScO_{2+y}$ is slightly higher than its Mg-doped counterpart after oxidation, while that of the 3R $CuScO_{2+y}$ increases dramatically from 7 × $10^{-4}$ S/cm to 0.2 S/cm upon oxidation. This can be ascribed to the smaller grain size of 3R powder which greatly facilitated the oxygen intercalation.

Diffuse reflectance spectra of the unoxidized $CuSc_{1-x}Mg_xO_2$ ($x$ = 0, 0.02, 0.04) powders are shown in Figure 2.11. The measured diffuse reflectance as a function of wavelength was normalized with respect to MgO. The absorption of the sample in

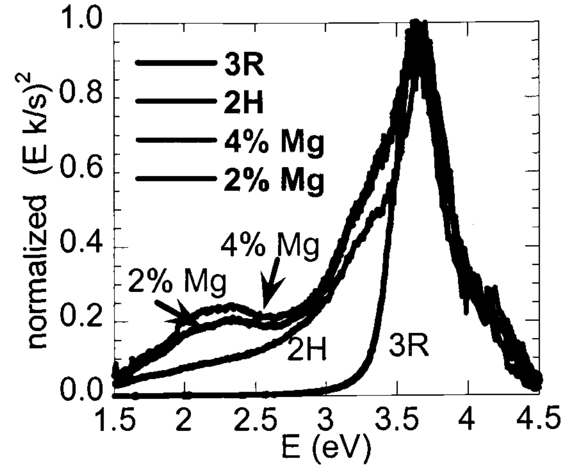

Figure 2.11 Diffuse reflectance spectra of $CuSc_{1-x}Mg_xO_2$ powders (courtesy of Dr. J. Tate and R. Kykyneshi).

visible region increases as the color of the sample darkens. From 3R to "undoped" 2H to Mg-doped 2H $CuSc_{1-x}Mg_xO_2$, the color of the powders darkens from slightly off-white to gray to dark blueish gray. Compared with 3R, the extra features of 2H samples in the spectra are induced by different levels of doping (Cu or Mg).

## 2.4 Discussion

### *2.4.1 On Chemical Structures*

The difference between the 2H and 3R delafossite structures is analogous to the difference between hexagonal and cubic close packing, i.e., ABAB vs. ABCABC stacking. Our Madelung energy calculations show that the 3R structure (ABCABC stacking) is more stable than the 2H structure (ABAB stacking) from an electrostatic point of view, but only by 0.83 kJ/mol or 0.008%. This increase is due to an increase in cation-cation repulsion for the third nearest neighbors in the 2H polymorph. It is interesting to contrast this with the situation for hexagonal vs. cubic close packing in the wurzite (ZnO) vs. sphalerite (ZnS) structures. In this case, the hexagonally close packed structure is electrostatically more stable due to a more favorable second near neighbor attractive interaction, and it is observed that the more ionic compounds prefer the hexagonal structure [46]. The cubic NaCl structure is electrostatically favored over the hexagonal NiAs structure mainly due to the cation-cation repulsion across the shared octahedra faces in the NiAs structure. Again the observation is that the NaCl structure is preferred for more ionic compounds. We find that the 3R form of $CuScO_2$ always dominates the diffraction patterns of our samples prepared in many different ways, except in the case where intentionally doped samples were placed in preheated furnace. This disorder produced by doping may disrupt the long range forces along the *c* axis necessary to obtain the 3R form. An examination of the entire delafossite family shows that all the compounds exist either only in 3R form or in both 2H and 3R forms, but none exists only in 2H form. Although a 6H form has been suggested, no structure for such a form has been proposed. Furthermore, the diffraction pattern for a mixture of the 2H and 3R forms can be completely indexed assuming a single 6H phase. Thus, there is no reported experimental evidence for the existence of a 6H delafossite structure.

Oxygen intercalated into $CuScO_2$ is sited in the triangles formed by Cu in the Cu sheet (Fig. 2.12). In the 2H form there are two different sites for this interstitial oxygen: one with Sc atoms both above and below the site and another site with Sc atoms neither above nor below. For the 3R form all the sites for interstitial oxygen are the same. They have a Sc atom either above or below. In the 2H form the interstitial oxygen is in the same plane as the Cu atoms whereas in the 3R form this oxygen is displaced out of plane by 0.3 Å toward a Sc atom. Thus, the coordination of interstitial oxygen in the 3R form may be considered to be four, but all of these bonds are weak and this oxygen is underbonded according to our bond valence calculations (Table 2.2). Nonetheless, it appears that this fourth bond causes the interstitial oxygen to be more tightly held in the 3R form relative to the 2H form. The very fact that the oxygen has displaced out of the Cu triangle toward Sc indicates that it becomes more strongly bound by so doing. The 2H form loses oxygen when heated under an atmosphere of oxygen, but the interstitial oxygen in the 3R form is not released under these conditions. However, if the oxygen partial pressure is decreased to 0.2 atmospheres (air), oxygen is released from the 3R form on heating.

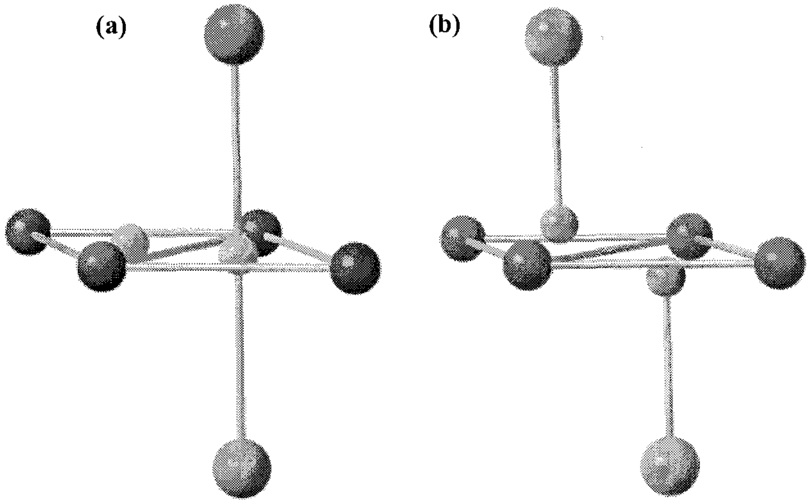

Figure 2.12 Environment of interstitial oxygen (Oi) in the 2H (a) and 3R (b) polymorphs. View along the *c* axis: dark spheres forming triangles are Cu atoms, large gray spheres are Sc atoms, and small and light spheres are Oi atoms.

Electrostatic energy calculations (Fig. 2.13) show the effect of Sc in 3R and indicate a displacement toward Sc considerably less than the observed value. Within the electrostatic model this difference between the minimum in Figure 2.13 and the observed $z$ value for interstitial oxygen Oi could be attributed to the greater effective charge on Sc relative to Cu thus increasing its pulling power relative to a point charge model assuming formal charges for Sc and Cu.

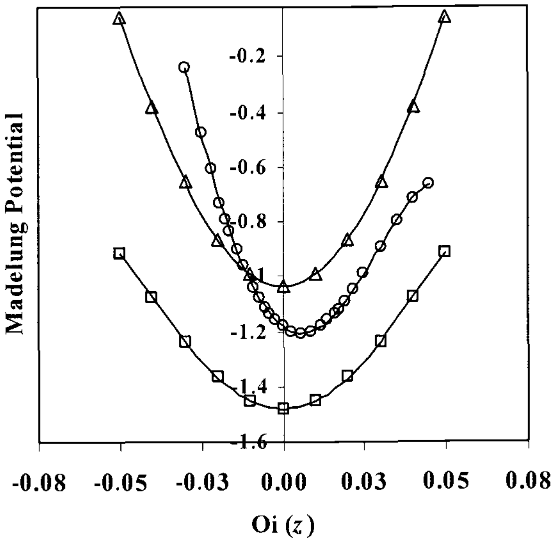

Figure 2.13 Electrostatic potential curves calculated by EUTAX. The sign of the potential was changed in order to show these as potential energy wells for anions. The *z* parameters of Oi were shifted by 0.25 for 2H $CuScO_2$ so that $z = 0.0$ corresponds to the Cu plane in both 2H and 3R forms. Triangles are for Oi at 2/3,1/3,*z* in the 2H form, squares are for Oi at 0,0,*z* in the 2H form, and open circles are for Oi at 1/3,2/3,*z* in the 3R form. The interstitial oxygen with two Sc above and below is in the lowest curve, with one Sc either above or below in the middle curve, without any Sc neighbors in the upper curve.

Given the fact that interstitial oxygen in 3R $CuScO_{2.5}$ displaces toward a Sc atom, one might expect a tendency in 2H $CuScO_{2.5}$ for interstitial oxygen to occupy the site with Sc above and below. Our calculations of the electrostatic energy well indicate the site with Sc above and below is 50% deeper than the site without Sc neighbors (Fig. 2.13). But only a weak tendency of Oi to prefer the electrostatically favored site is observed: 55% of the interstitial oxygen in the site with Sc above and below. However, the strong preference for $Cu^{2+}$ to adopt a square planar coordination to oxygen if its coordination number is four will result in much of the interstitial oxygen being in the site without Sc above and below it. The average coordination of Cu is 3.5, which could mean that one half of this Cu has a coordination number of four and the other half a coordination of three, as reported for the structure of $YCuO_{2.5}$ [32]. Placing one interstitial oxygen in the site with Sc above and below means that the interstitial oxygen on the other side of Cu would be in the site without Sc above and below to produce square planar coordination. If the driving force for four coordination is very strong relative to three coordination, the result could be that 3/4 of the Cu is four coordinated and 1/4 is two coordinated. This would then explain the nearly equal amounts of interstitial oxygen on the two sites. Essentially all the interstitial oxygen in the 2H $CuScO_{2.02}$ phase resides in the site with Sc above and below, indicating that the stabilization effect of Sc dominates at low concentrations of Oi.

On heating CuO in air, reduction to $Cu_2O$ occurs at 1025 °C. This reduction of $Cu^{2+}$ to $Cu^{1+}$ is known to occur at lower temperatures in some ternary systems. For example, delafossite $CuCrO_2$ forms at 890 °C in air [47]. For the reduction of $Cu^{2+}$ to $Cu^{1+}$ to occur at oxygen partial pressures of 0.2 to 1.0 atm at a temperature as low as 440 °C is highly unusual and apparently unprecedented. However, bond valence calculations (Table 2.2) do show that this intercalated oxygen is more weakly bound than the oxygen forming bonds to 1 Cu and 3 Sc atoms.

On oxidation of $CuScO_2$ to $CuScO_{2.5}$ there is an expansion of the Cu–O distance along the *c* axis of both the 2H and 3R forms from 1.831 to 1.861 or 1.846 Å, respectively. This expansion might be considered unexpected because interatomic distances normally decrease as a cation is oxidized. The expansion is presumably caused by the fact that the coordination number of Cu is increasing from 2 to an average of 3.5 as $CuScO_2$ is oxidized to $CuScO_{2.5}$, and interatomic distances increase as coordination number increases. Bond valence calculations (Table 2.2) support this explanation. The shorter and stronger Cu–O bonds in 3R $CuScO_{2.5}$ relative to 2H $CuScO_{2.5}$ can be attributed to the longer, weaker Cu–Oi bonds in this form (Table 2.2). Although the *a* cell edge expansion on oxidation of both 2H and 3R $CuScO_2$ to $CuScO_{2.5}$ might be attributed to stuffing O between Cu atoms in the *ab* plane, this seems not to be a correct explanation because the Cu bonds to this oxygen should actually be shorter according to bond valence calculations. A possible explanation for this expansion is increased Cu–Cu repulsion as the formal charge on Cu increases from one to two. The slightly greater expansion of the *a* cell edge in the 3R form is presumably a result of the interstitial oxygen pushing toward the faces of the $ScO_6$ octahedra from both above and below. The $ScO_6$ octahedra are highly distorted as indicated by the O–Sc–O angles. The O–O distances in these octahedra are 2.74 Å for edges shared between two Sc atoms and 3.27 Å in the face that the interstitial oxygen pushes into in the case of the 3R form. An expansion of the *c* cell edge might also be expected on oxidation because the Cu–O distance along this direction increases. Such an increase is found for 2H $CuScO_{2.5}$, while for 3R $CuScO_{2.5}$ there is a small decrease in the *c* cell edge. The expansion of the *a* cell edge on oxidation causes increased Sc–Sc distances and a decrease in the thickness of the $(ScO_2)^{1-}$ layer, this decrease being about the same for the 2H and 3R forms. The greater expansion of the Cu–O bond length on oxidation of the 2H form overcomes the contraction of the $(ScO_2)^{1-}$ layer to give an overall expansion of the *c* cell edge. On the other hand, the smaller expansion of the Cu–O bond length on oxidation of the 3R form is insufficient to compensate for the contraction of the $(ScO_2)^{1-}$ layer, leading to an overall contraction of the *c* cell edge. Indirectly, it is the weak bond between Oi and Sc that causes the *c* cell edge contraction in the 3R form.

Our finding that $CuScO_{2+x}$ phases could only be prepared with $x$ close to 0.0 and 0.5 is very similar to observations for the $YCuO_{2+x}$ system [32]. The $LaCuO_{2+x}$ system is also similar, except that $x$ values somewhat above 0.5 are also observed [19,20,33]. We also examined the range for $CuScO_{2+x}$ by reducing $CuScO_{2.5}$ with Zr metal in evacuated silica ampoules. This method was also unsuccessful in producing single phase materials with $x$ between 0.12 and 0.44.

### *2.4.2 On Physical Properties*

For oxides, the valence band is commonly the oxygen 2*p* band. Doping to produce holes in this band is not difficult, but the mobility of such holes has always been found to be very low. For p-type TCOs such as $CuAlO_2$, $CuGaO_2$ and $SrCu_2O_2$, the Hall mobilities were reported to be only 0.13 $cm^2V^{-1}s^{-1}$ [48], 0.23 $cm^2V^{-1}s^{-1}$ [49], and 0.46 $cm^2V^{-1}s^{-1}$ [50]. In delafossite structure there are only Cu–O–M–O–Cu linkages, and no contribution from M orbitals is found to the band structure near the Fermi level unless M is a transition metal such as Fe, Cr or V. Cuprous oxide, $Cu_2O$, is a well-known good p-type conductor with a mobility as high as 100 $cm^2V^{-1}s^{-1}$ [51]. The Cu–O–Cu linkages in $Cu_2O$ may give a valence band with more favorable mobility due to mixing of Cu 3*d* and O 2*p* states. However, p-type $Cu_2O$ is not considered to be a TCO because of its small band gap (2.1 eV).

The electronic conductivity due to holes in an oxygen 2*p* band is associated with low mobility and is highly activated; it can generally be measured only well above room temperature. Presumably, the holes in such oxides are like $O^{1-}$ species being trapped in a sea of $O^{2-}$ species, and they may even form $(O_2)^{2-}$ peroxide dimers to further lower the hole mobility. A cation *s* or *d* band seems to be a better solution than the O 2*p* band for offering a higher hole mobility, giving an order of choice $s > 4d$, $5d > 3d$. The best reported p-type TCOs so far are all based on a valence band that is largely 3*d* in character.

Transport properties of doped bulk delafossites have been studied since 1984 [10,52-55]. The room temperature p-type conductivity of $CuAlO_2$ and $CuFeO_2$ with no intentional doping is $1.7 \times 10^{-3}$ $S{\cdot}cm^{-1}$ and 1.5 $S{\cdot}cm^{-1}$ for sintered pellets. Doping with 2% Mg increased the p-type conductivity of $CuFeO_2$ to 9 $S{\cdot}cm^{-1}$. Doping of $CuGaO_2$, $CuCrO_2$ and $CuYO_2$ with Ca all produced improved p-type conductivity. The Hall mobilities, however, were too low to be measured directly. The estimated value of hole mobility from thermoelectric power was up to 0.1 $cm^2V^{-1}s^{-1}$.

Transport and optical properties of p-type TCO thin films of delafossite compounds have been widely investigated since 1997. Films of $CuAlO_2$ 500 nm thick showed 80% transmission of visible light and a room temperature conductivity of 0.95 $S{\cdot}cm^{-1}$ [11]. Films of $CuInO_2$ and $CuGaO_2$ displayed p-type conductivities of

$2.8 \times 10^{-3}$ S·cm$^{-1}$ and 0.06 S·cm$^{-1}$ at room temperature and a transmission of 60% ~ 80% in the visible region [56,57].

Our study of $CuSc_{1-x}Mg_xO_{2+y}$ compositions showed a maximum p-type conductivity of 0.015 S·cm$^{-1}$ around $x = 0.06$ with Mg doping alone in sintered pellet samples, and 0.5 S·cm$^{-1}$ at $x = 0.05$ and $y = 0.23$ with both Mg doping and oxygen intercalation in cold-pressed bar samples at room temperature. The conductivity of unoxidized film is similar to that of the sintered pellets, but after oxygen intercalation the maximum conductivity reached 25 S·cm$^{-1}$ with a transmission of 70% for wavelengths longer than 700 nm and 50% at 550 nm [38]. Increasing Mg content has little effect on the transparency, but the film gradually darkens as oxygen is incorporated (Fig. 2.14).

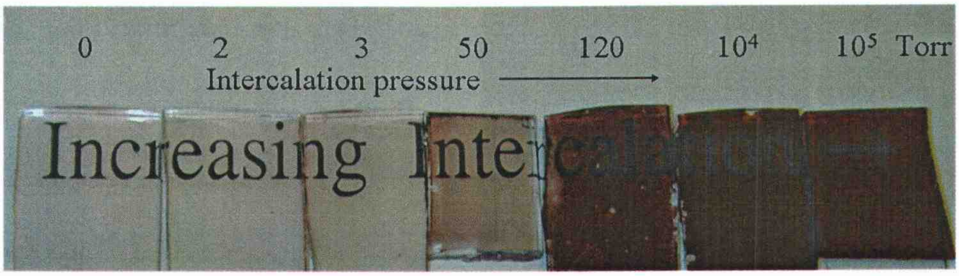

Figure. 2.14 Oxygen intercalation of $CuScO_2$ thin films varies with applied $O_2$ pressure (courtesy of Dr. J. Tate and A.D. Draeseke).

It is obvious that intercalation of oxygen into the delafossite structure increases the p-type conductivity much more than Mg doping. On the other hand, oxygen uptake peaks near the Mg solubility limit, implying some correlation between them. However, substitution of smaller $Mg^{2+}$ for larger $Sc^{3+}$ will shrink the cell edges along *a* axis and decrease the Cu–Cu distances which should inhibit oxygen from getting into the Cu planes instead of facilitating the intercalation. The impact of crystallite size could not be assessed by XRD data because all the crystallites are too large. The mechanism behind the codoping effect remains unclear. In addition, intercalated oxygen sitting in or near the Cu planes will push two adjacent Cu away from each other and break the weak Cu–Cu bonding which is supposed to enhance the conductivity; however, weak bonds formed between Cu and intercalated oxygen and provided a direct path for holes along the Cu–O–Cu linkages. At the same Mg doping level, increasing oxygen partial pressure helped with speeding up the intercalation and improving the conductivity at given oxidation time.

Each Mg creates one hole by substitution for Sc, and each oxygen contributes two holes by oxidation. The estimated mobility is only up to $10^{-4}$ $cm^2V^{-1}s^{-1}$ for oxidized powders, not too much higher than that of purely doped samples. Therefore, the larger conductivity induced by oxidation is mostly due to a higher carrier concentration caused more by oxidation than by Mg doping. The maximum intercalation is 0.5 oxygen in each $CuScO_2$, giving one hole per formula unit, while the up limit of Mg doping only gives 0.05 holes per $CuScO_2$.

The temperature dependent conductivity measurements always show a semi-conducting behavior, but $\ln\sigma$ vs. $1/T$ is not a straight line. Plots of $\ln\sigma$ vs. $1/T^{1/4}$ give essentially straight lines, suggesting a variable range hopping model applies to the hole conductivity in $CuSc_{1-x}Mg_xO_{2+y}$. An NMR study on $CuYO_2$ and $CuY_{1-x}Ca_xO_{2+y}$

indicated that it is the carrier concentration that changes with temperature, not the mobility [58].

## 2.5 References

1. K. Isawa, Y. Yaegashi, S. Ogota, M. Nagano, S. Sudo, K. Yamada, H. Yamauchi. *Phys. Rev. B.*, 57, 7950 (1998)
2. M. Hasegawa, I. Inagawa, M. Tanaka, I. Shirotani, H. Takei. *Solid State Commun.*, 121, 203 (2002)
3. T. He, J.J. Krajewski, M.A. Subramanian. *Abstracts*, 36th Middle Atlantic Regional Meeting of the American Chemical Society, Princeton, NJ, June 8-11, 2003; p 282
4. J.R. Monnier, M.J. Hanrahan, G. Apai. *J. Catal.*, 92, 119 (1985)
5. J. Christopher, C.S. Swamy. *J. Mater. Sci.*, 27, 1353 (1992)
6. P.F. Carcia, R.D. Shannon, P.E. Bierstedt, R.B. Flippen. *J. Electrochem. Soc.*, 127, 1974 (1980)
7. H. Hayashi, H. Hosono. Jpn. Patent JP 2002255548 A2 20020911, 2002
8. J.P. Doumerc, C. Parent, Z.J. Chao, G. Le Flem, A. Ammar. *J. Less-Common Met.*, 148, 333 (1989)
9. A. Jacob, C. Parent, P. Boutinaud, G. Le Flem, J.P. Doumerc, A. Ammar, M. Elazhari, M. Elaatmani. *Solid State Commun.*, 103, 529 (1997)
10. F.A. Benko, F.P. Koffyberg. *J. Phys. Chem. Solids*, 45, 57 (1984)
11. H. Kawazoe, M. Yasukawa, H. Kyodo, M. Kurita, H. Yanagi, H. Hosono. *Nature*, 389, 939 (1997)
12. N. Duan, A.W. Sleight, M.K. Jayaraj, J. Tate. *Appl. Phys. Lett.*, 77, 1325 (2000)

13. R. Nagarajan, N. Duan, M.K. Jayaraj, J. Li, K.A. Vanaja, A. Yokochi, A.D. Draeseke, J. Tate, A. W. Sleight. *Int. J. Inorg. Mater.*, 3, 265 (2001)

14. M.K. Jayaraj, A.D. Draeseke, J. Tate, A.W. Sleight. *Thin Film Solids*, 397, 244 (2001)

15. R. Nagarajan, A.D. Draeseke, A.W. Sleight, J. Tate. *J. Appl. Phys.*, 89, 8022 (2001)

16. J. Tate, M.K. Jayaraj, A.D. Draeseke, T. Ulbrich, A.W. Sleight, K.A. Vanaja, R. Nagarajan, J.F. Wager, R.L. Hoffman. *Thin Solid Films*, 411, 119 (2002)

17. R. Nagarajan, S. Uma, M.K. Jayaraj, J. Tate, A.W. Sleight. *Solid State Sci.*, 4, 787 (2002)

18. J. Li, A. Yokochi, T.G. Amos, A.W. Sleight. *Chem. Mater.*, 14, 2602 (2002)

19. R.J. Cava, H.W. Zandbergen, A.P Ramirez, H. Takagi, C.T. Chen, J.J. Krajewski, W.F. Peck, J.V. Waszczak Jr., G. Meigs, R.S. Roth, L.F. Schneemeyer. *J. Solid State Chem.*, 104, 437 (1993)

20. R.J. Cava, W.F. Peck, J.J. Krajewski Jr., S.W. Cheong, H.Y. Hwang. *J. Mater. Res.*, 9, 314 (1994)

21. D.B. Rogers, R.D Shannon, C.T. Prewitt, J.L. Gillson. *Inorg. Chem.*, 10, 723 (1971)

22. P.K. Mehrotra, R. Hoffmann. *Inorg. Chem.,* 17, 2187 (1978)

23. A., Buljan, M., Llunell, E. Ruiz, P. Alemany. *Chem. Mater.*, 13, 338 (2001)

24. R. Seshadri, C. Felser, K. Thieme, W. Tremel. *Chem. Mater.*, 10, 2189 (1998)

25. A. Buljan, P. Alemany, E. Ruiz. *J. Phys. Chem.*, B 103, 8060 (1999)

26. H.C. Kandpal, R. Seshadri. *Solid State Sci.*, 4, 1045 (2002)

27. M. Elazhari, A. Ammar, M. Elaatmani, M. Trari, J.P. Doumerc. *Eur. J. Solid State Inorg. Chem.*, 34, 503 (1997)

28. S. Park, D.A. Keszler. *J. Solid State Chem.*, 173, 355 (2003)

29. M. Trari, J. Topfer, J.P. Doumerc, M. Pouchard, A. Ammar, P. Hagenmuller. *J. Solid State Chem.*, 111, 104 (1994)

30. H. Yanagi, S. Park, A. D. Draeseke, D. A. Keszler, and J. Tate. *J. Solid State Chem.*, 175, 34 (2003)

31. K. Isawa, Y. Yaegashi, S. Ogota, M. Nagano, S. Sudo, M. Ohashi, K. Yamada. In *Advances in Superconductivity X*, Proceedings of the International Symposium on Superconductivity, 10th, Gifu, Japan, 1998; 1, p 395

32. G. Van Tendeloo, O. Garlea, C. Darie, C. Bougerol-Chaillout, P. Bordet. *J. Solid State Chem.*, 156, 428 (2001)

33. O. Garlea, C. Darie, C. Bougerol, O. Isnard, P. Bordet. *Solid State Sci.*, 5, 1095 (2003)

34. B.U. Kohler, M.Z. Jansen. *Anorg. Allg. Chem.*, 543, 73 (1986)

35. J.P. Doumerc, A. Ammar, A. Wichainchai, M. Pouchard, P. Hagenmuller. *J. Phys. Chem. Solids*, 48, 37 (1987)

36. M.W. Treacy, M.W. Deem. DIFFaX Version 1.807, 2000, original at ftp://ftp.nj.nec.com/pub/treacy/

37. S. Sakida, N. Kato, Y. Kawamoto. *Mater. Res. Bull.*, 37, 2263 (2002)

38. R. Kykyneshi, J. Li, B. Nielsen, J. Tate, A.W. Sleight. *J. Appl. Phys.*, 96(10), 6188-6194 (2004)

39. J. Rodriguez-Carvajal. Fullprof Version 2k, 2002, original at http://ccp14.semo.edu/ccp/ccp14/ftp-mirror/fullprof/pub/divers/fullprof.2k/

40. M. O'Keeffe, N.E. Brese. EUTAX Version 1.5 for Macintosh, 1991, EMLab Software

41. C. Hormillosa, S. Healy, T. Stephen, I.D. Brown. Bond Valence Calculator Version 2.0, 1993, original at http://ccp14.sims.nrc.ca/ccp/web-mirrors/i_d_brown/

42. R.D. Shannon. *Acta Crystallogr. Sect. A*, 32, 751 (1976)

43. K. Hayashi, N. Mizutani, M. Kato. *Nippon Kagaku Kaishi (J. Chem. Soc. Japan)*, NKAKB 1, 6 (1974)

44. K.J. Range, F. Ketterl. *Z. Naturforsch. Teil B. Anorg. Chem, Org. Chem.*, ZENBA 32, 1356 (1977)

45. A.M.M. Gadalla, J. White. *Trans. Br. Ceram. Soc.*, 63, 39 (1964)

46. J. Li, A.W Sleight. *J. Solid State Chem.*, 177, 889 (2004)

47. A.M.M. Gadalla, J. White. *Trans. Br. Ceram. Soc.*, 63, 535 (1964)

48. H. Yanagi, S-I. Inoue, H. Ueda, H. Kawazoe. *J. Appl. Phys.*, 88, 4159 (2000)

49. H. Kawazoe, H. Yanagi, K. Ueda, H. Hosono. *MRS Bull.*, 25, 28 (2000)

50. A. Kudo, H. Yanagi, H. Hosono, H. Kawazoe. *Appl. Phys. Lett.*, 73, 220 (1998)

51. *Solar Cell Device Physics*; S.J. Fonash, Ed.; Academic Press: New York, 1981; p 80

52. F.A. Benko, F.P. Koffyberg. *Can. J. Phys.*, 63, 1306 (1985)

53. F.A. Benko, F.P. Koffyberg. *J. Phys. Chem. Solids*, 48, 431 (1987)

54. F.A. Benko, F.P. Koffyberg. *Phys. Status Solidi A*, 94, 231 (1986)

55. F.A. Benko, F.P. Koffyberg. *Mater. Res. Bull.*, 21, 753 (1986)

56. H. Yanagi, T.Hase, S. Ibuki, K. Ueda, H. Hosono. *Appl. Phys. Lett.*, 78, 1583 (2001)

57. K. Ueda, T.Hase, H. Yanagi, H. Kawazoe, H. Hosono, H. Ohta, M. Orita, M. Hirano. *J. Appl. Phys.*, 89, 1790 (2001)

58. W.W. Warren Jr., A. Rajabzadeh, T. Olheiser, J. Liu, J. Tate, M.K. Jayaraj, K.A. Vanaja. *Solid State Nucl. Magn. Reson.*, 26, 209-214 (2004)

# Chapter 3

# Ionic and p-type Conductivities in ZnO Powders

## 3.1 Introduction

Highly conducting zinc oxide is readily obtain by substitution of F for O or substitutions of Al, Ga, In, or Ge for Zn. All such materials are n-type conductors. Most studies are on thin films, but highly conducting powders have also been reported [1-5]. Attempts to dope ZnO p-type have generally failed. Some Li can apparently be substituted for Zn, but the materials obtained are not p-type conductors. Instead, they become highly insulating because any n-type carriers due to impurities or defects are trapped by the Li centers [6]. This failure to dope zinc oxide p-type has been attributed to its work function [7]. This argument in chemical terms is that for oxides with a high work function holes in an oxygen 2*p* band will localize and combine on lattice oxygen converting $2O^{2-}$ to $O_2$, which then escapes the solid. This does not preclude the possibility of preparing a metastable p-type zinc oxide. However, such a material would evolve $O_2$ on heating and the holes would be lost.

There are very recent reports of p-type thin films of zinc oxide based on small substitutions of N for O [8-13]. Some of this work is based on codoping, such as doping with both N and Ga. More thorough work [14] has failed to confirm the codoping approach as a way to obtain p-type zinc oxide. Furthermore, the most convincing report [8] on N doped p-type zinc oxide does not utilize the codoping approach. This report also points out that many of the reports on p-type zinc oxides give unrealistically high carrier concentrations. Evidence for N doping of zinc oxide powders has been obtained through EPR studies [15]. However, the amount of N in the samples was not determined and no evidence for p-type behavior was sought.

Recently, zinc oxide prepared by decomposition of zinc peroxide was reported to be an electronic conductor [16]. The authors assumed that this conductivity was due to n-type carriers, but no direct evidence for n-type characteristics was presented. The purpose of this study was to search for p-type characteristics in zinc oxide powders produced through decomposition of zinc peroxide and in powders doped with nitrogen.

## 3.2 Experimental

The nanoparticles of zinc peroxide were prepared according to the method given by Uekawa and others [16,17]. Equal volumes of 0.1 mol/L $Zn(NO_3)_2{\cdot}6H_2O$ (Aldrich, 98%) and 0.1 mol/L NaOH (Mallinckrodt, AR) solutions were mixed at room temperature with continuous stirring. The white gel-like precipitate of $Zn(OH)_2$ was separated from the solution by a centrifuge at 3000 rpm for 5 min. The obtained $Zn(OH)_2$ was dispersed into distilled water, washed and separated by centrifugation for three times to remove the impurities. The purified $Zn(OH)_2$ was then mixed with 1 M $H_2O_2$ (Mallinckrodt, AR, 30% $H_2O_2$ soln.) aqueous solution, capped in an Erlenmeyer flask and heated at 75 °C for 2 hr. The resulting translucent sol was dried at 75 °C overnight in air. The pale yellow zinc peroxide powder was heated in an open glass beaker in air to certain temperatures at and above 220 °C for 20 min to prepare ZnO powder samples. The colors of peroxide-decomposed ZnO samples are from yellowish white to creamy-white depending on the decomposition temperature.

A variation of above method was used to make another ZnO sample. The $Zn(OH)_2$ precipitate was obtained in the same way, and without adding any $H_2O_2$ it was dried at 75 ~ 120 °C overnight in air. The full decomposition of $Zn(OH)_2$ gave a white ZnO powder.

Thermal decomposition of zinc oxalate also produces pure ZnO [18,19]. The $ZnC_2O_4 \cdot 2H_2O$ (Aldrich, 99.99%) precursor was heated under Ar with a slow increase of temperature up to 350 °C at which it was allowed to decompose for 5 hr. The resulting ZnO powder is white in color.

Some research showed that ZnO powder could be prepared by thermal decomposition of zinc nitrate, and the major decomposition of the nitrate ion occurs above 300 °C [15,20]. The ~ 8 g $Zn(NO_3)_2 \cdot 6H_2O$ (Aldrich, 98% or Alfa Aesar, 99.998%) was transfered into a glass beaker and heated to certain temperatures at and above 315 °C inside a hood, and allowed to decompose in air for 2 hr at each temperature. The resulting N-doped ZnO sample is a flaky yellow powder.

Highly crystalline zinc-rich ZnO sample was synthesized by reacting commercial ZnO powder with zinc metal vapor at 1200 °C in a sealed silica tube. The experimental detail was described in Ref. [3].

X-ray diffraction data were collected on a Siemens D5000 diffractometer at room temperature, and NIST Si 640b was added as an internal standard. Lattice parameters and crystallite size were refined by LeBail fit [21] using Fullprof software [22]. BET surface area was measured with a Micromeritics ASAP 2000 analyzer. Scanning electron microscope (SEM) was used to determine the morphology and particle size of ZnO samples. Thermogravimetric analysis and differential scanning calorimetry were carried out to measure the weight loss and the phase transition temperature of the samples under heating.

Iodometric titration [23,24] was employed to determine the concentration of $O_2^{2-}$ in zinc peroxide sample, the amount of excess oxygen in $ZnO_{1+x}$ samples prepared by decomposition of zinc peroxide and the amount of holes in $ZnO_{1-y}N_y$ samples prepared by decomposition of zinc nitrate. The reactions involved are:

(i) iodide is oxidized by active holes, $3\,I^- + 2\,h^+ \rightarrow I_3^-$;

(ii) released triiodide is titrated with sodium thiosulfate.

From the amount of thiosulfate used, the number of holes consumed can be calculated. The experimental procedures are as follows. Solutions of 0.001 M and 0.2 M $Na_2S_2O_3$ were prepared and standardized with $KIO_3$. Accurately weighed ZnO powder (~ 0.2 g) was dissolved in 10 mL 1.0 M HCl and 0.7 M KI and stirred with a Teflon coated magnetic stirring bar for 1 min before titration began. The solution was kept in a capped titration flask filled with Ar to prevent the oxidation of iodide by air. All the distilled water used was boiled and cooled under Ar flow right before the titration. The $Na_2S_2O_3$ solution was added from a 10 mL microburet for ZnO samples and from a 50 mL buret for zinc peroxide sample through a hole in the cap of the flask. An extra 10 mL DI water was added to the solution in the beginning of the titration, and the starch indicator was added close to the end point to achieve maximum sensitivity.

Chemical analysis was carried out for N-doped samples by Midwest Microlab. The method is a high temperature fusion with carbon powder and a Pt catalyst. Oxygen is converted to $CO_2$ and N to $N_2$. Gases evolved are measured by gas chromatography. Zn becomes zinc metal.

The conductivities of the powder samples were measured by complex impedance spectroscopy over a frequency range of 0.1 Hz to 5 MHz at room temperature using a Solartron SI 1287 electrochemical interface and a Schlumberger SI 1260 impedance/grain-phase analyzer. Powders were pressed into pellets or bars before the measurements. Some were further heated to different temperatures before the next measurements. The N-doped samples were measured in powder form; hence the conductivities were affected by the powder density and the contacts between grains. Therefore, the conductivities were measured at various applied pressures following the procedure used for Ga-doped ZnO samples [2]. Typical samples were ~ 0.5 g with a thickness of ~ 1 mm and a diameter of 12 mm.

Diffuse reflectance spectra of powdered samples between 250 nm and 900 nm were obtained using a Xe lamp and a grating double monochromator as the source. Light diffusely reflected by the powders was collected with an integrating sphere and detected with a Si diode detector. These data were normalized by adjusting the saturation regions to the same absorption values.

## 3.3 Results

### *3.3.1 Cell Dimension and Size Analysis*

A typical XRD pattern of peroxide-decomposed ZnO is shown in Figure 3.1 together with zinc peroxide and commercial ZnO for comparison. Commercial ZnO (Aldrich, 99.99%) is referred to as normal ZnO later in this Chapter. Zinc peroxide crystallizes in a pyrite type structure with space group $Pa\bar{3}$ (205), zinc in special position 0,0,0, and oxygen in $x,x,x$. Zinc oxide has a hexagonal wurtzite structure with all the oxygen in a hexagonal close packed array and Zn occupying half of the tetrahedral interstitial positions. The space group is $P6_3mc$ (186) with Zn in a special position 1/3,2/3,0 and oxygen in 1/3,2/3,$z$.

The decomposition of zinc peroxide is complete after heating in air or oxygen at 220 °C for 20 min. The diffraction peaks of peroxide-decomposed ZnO are much broader compared with those of normal ZnO due to the much smaller particle size.

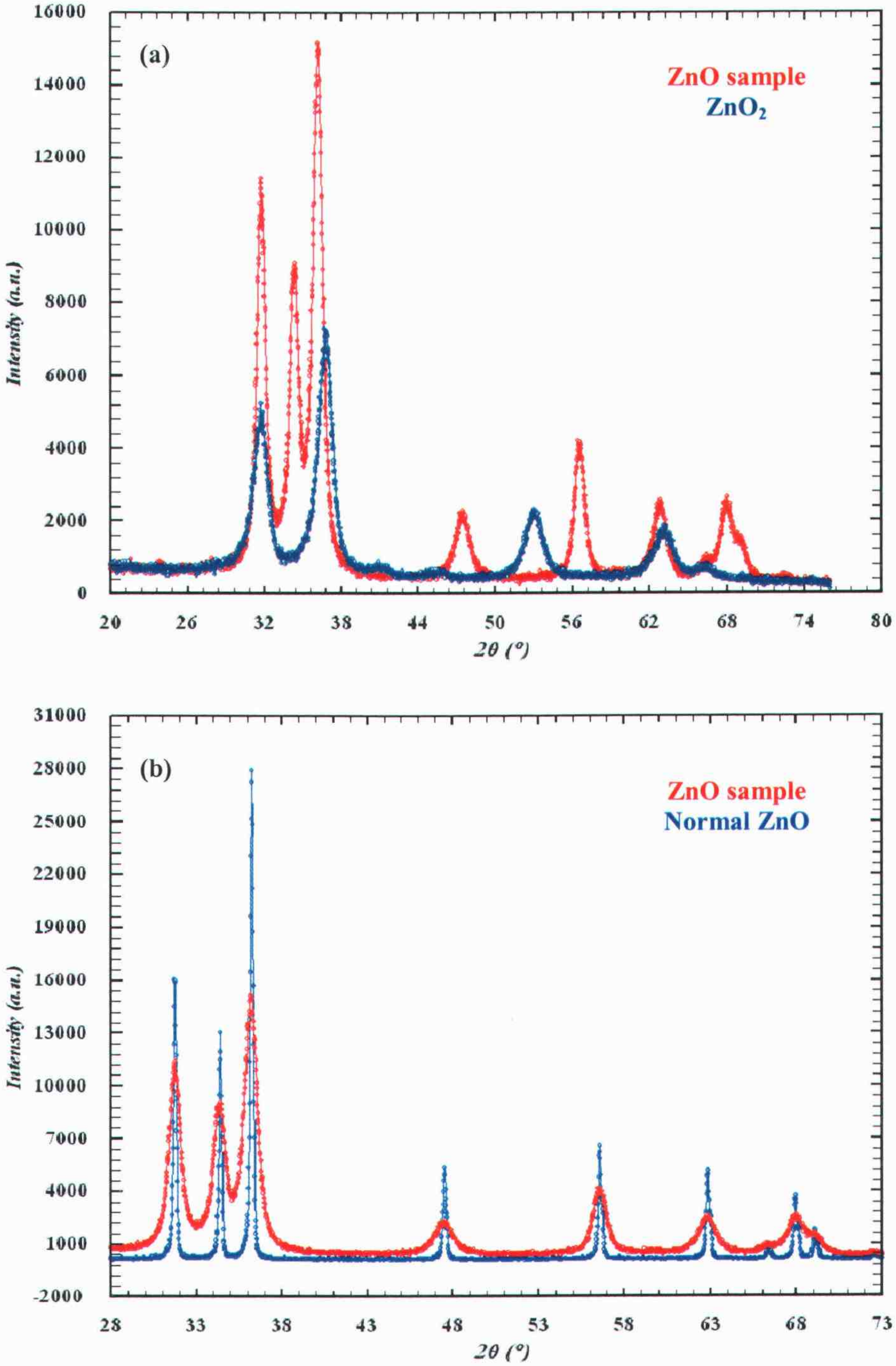

Figure 3.1 X-ray diffraction data of ZnO sample decomposed from zinc peroxide compared with (a) $ZnO_2$ and (b) normal ZnO.

The zinc-rich and N-doped ZnO samples, orange and yellow, are very crystalline with sharp diffraction peaks, the intensities of which are much higher than normal ZnO given the same experimental conditions of measurement. The white ZnO samples prepared from decomposition of $ZnC_2O_4$ and $Zn(OH)_2$ have similar diffraction patterns with peak width between those of normal ZnO and ZnO decomposed from zinc peroxide. The lattice parameters and crystallite sizes of different ZnO samples are shown in Figure 3.2. The trend of increasing cell edges with decreasing crystallite size is evident. The crystallite size of peroxide-decomposed ZnO is around 7 nm.

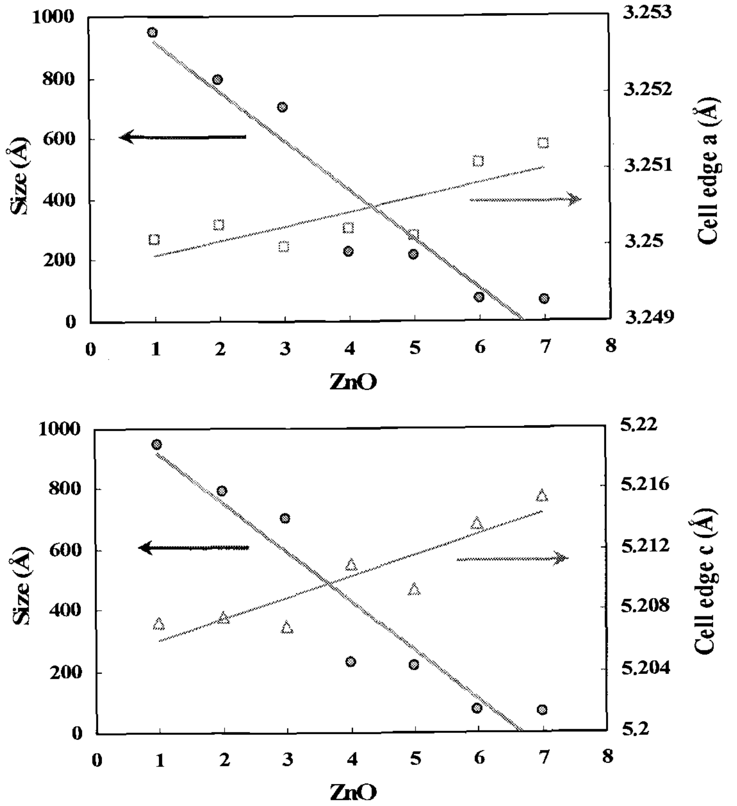

Figure 3.2 Unit cell dimensions and crystallite sizes of ZnO determined by XRD. The numbers on *x* axis refer to the ZnO samples: (1) zinc-rich, (2) N-doped, (3) normal, (4) hydroxide-decomposed, (5) oxalate-decomposed, (6) peroxide-decomposed in $O_2$ and (7) peroxide-decomposed in air.

The dependence of BET surface area of peroxide-decomposed ZnO on decomposition temperature of zinc peroxide is plotted in Figure 3.3. Larger surface area relates to smaller particles and vice versa. The surface area decreases with increasing decomposition temperature of zinc peroxide indicating a growing particle size of resulting ZnO with elevated synthesis temperature.

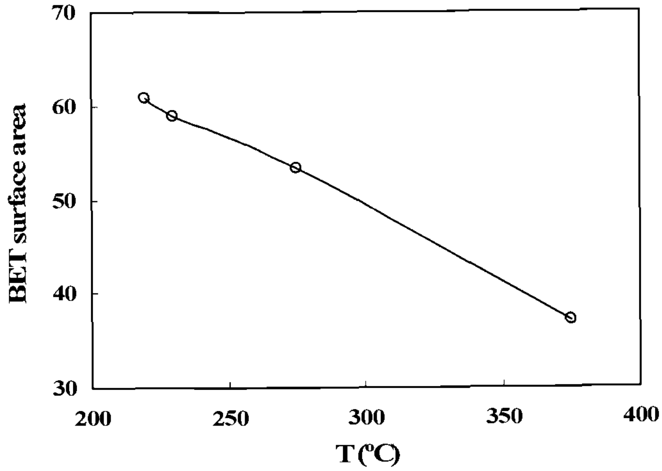

Figure 3.3 BET surface area ($m^2/g$) of ZnO samples prepared by decomposition of zinc peroxide at different temperatures.

SEM images of different ZnO samples are displayed in Figure 3.4, which gives not only the morphology of each sample but also the size of the particles in a qualitative manner. The zinc-rich ZnO was synthesized at the highest temperature; the sample is so crystalline that we can even see some hexagonal shaped crystals. The nitrate decomposed ZnO also has very big particles with shelled-bug shape. The hydroxide-decomposed sample shows nice needle-shaped particles and the oxalate-decomposed sample has cylinder-shaped particles. The decreasing particle size from (a) to (f) is consistent with the size analysis by XRD in Figure 3.2.

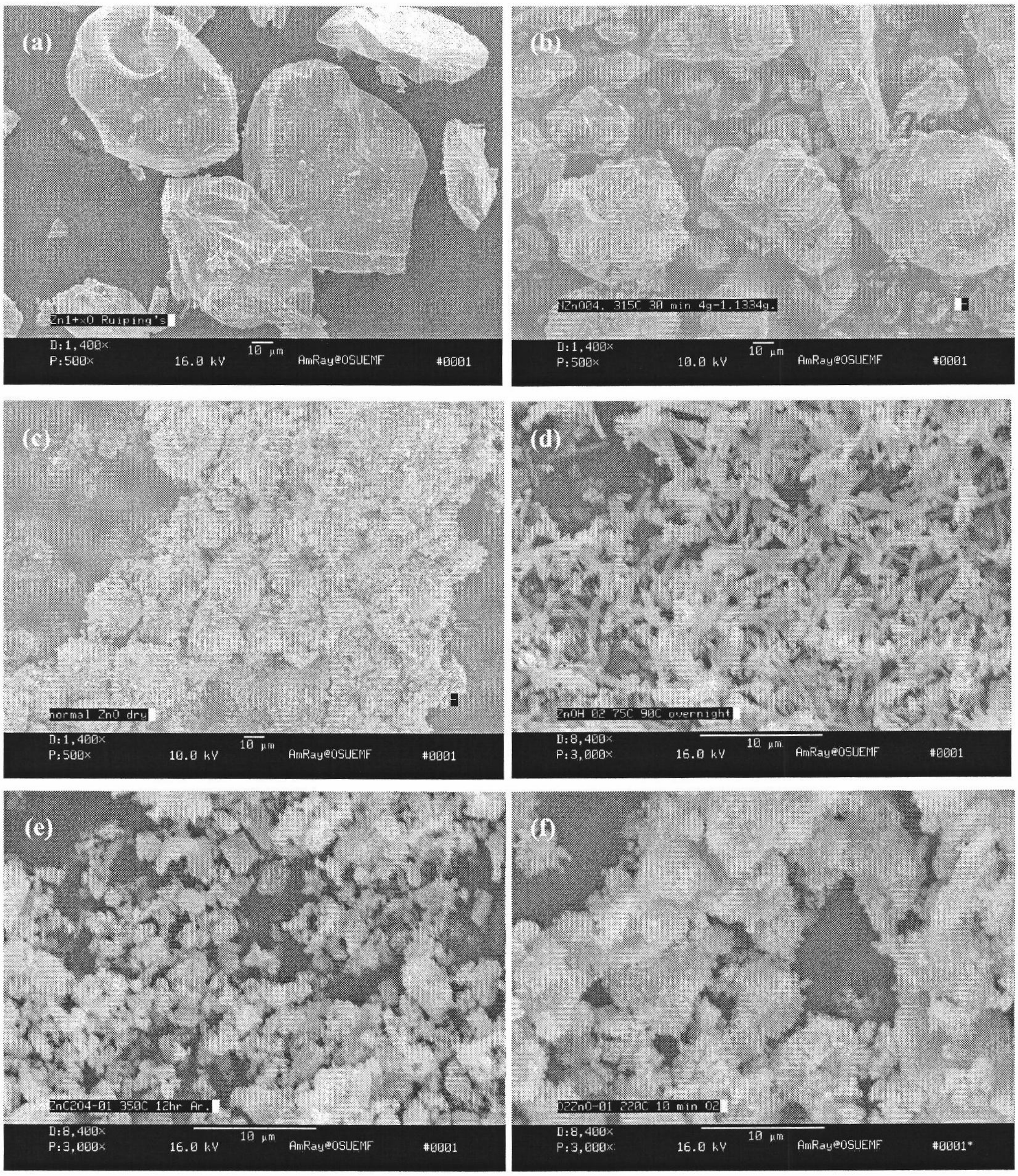

Figure 3.4 SEM images of ZnO samples prepared by different methods: (a) zinc-rich; (b) N-doped; (c) normal ZnO; (d) hydroxide-decomposed; (e) oxalate-decomposed; and (f) peroxide-decomposed. The marker in each image is 10 µm.

### *3.3.2 Thermal Analysis (TGA and DSC)*

The results of TGA and DSC measurements for a zinc peroxide sample are shown in Figure 3.5. The total weight loss is due to both oxygen release and water loss. The position of the exothermic peak in DSC curve agrees well with that of the steep weight loss in TGA curve, indicating a decomposition temperature around 210 °C.

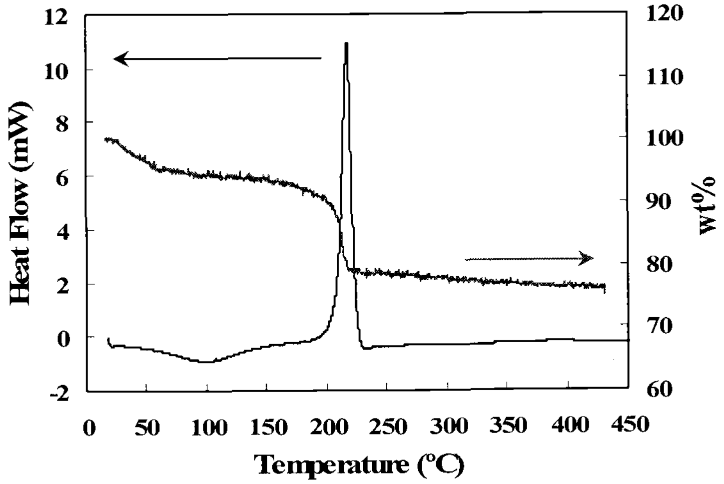

Figure 3.5 TGA and DSC curves of a zinc peroxide sample.

Thermal decomposition of zinc peroxide powder above 220 °C produces a pure phase of ZnO (Fig. 3.1(a)). The lower the decomposition temperature, the smaller the particle size (Fig. 3.3) and the higher the weight loss shown in the TGA measurement (Fig. 3.6). The weight loss below 100 °C is due to the absorbed moisture. The weight loss above 200 °C, however, is caused by the hydroxyl groups chemisorbed on the surface of these ZnO nanoparticles and maybe some trace amount of oxygen.

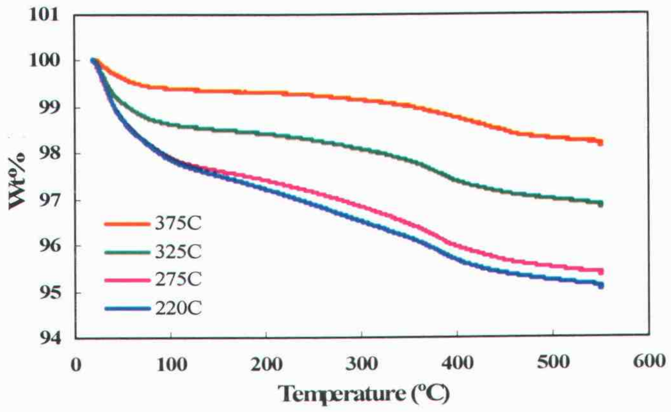

Figure 3.6 TGA weight loss of ZnO samples prepared by decomposition of zinc peroxide at different temperatures.

The ZnO samples synthesized using different methods were also analyzed by TGA. The results are compared in Figure 3.7. The weight loss seems to increase with decreasing particle size of the sample, suggesting the same reason for the weight loss as mentioned above.

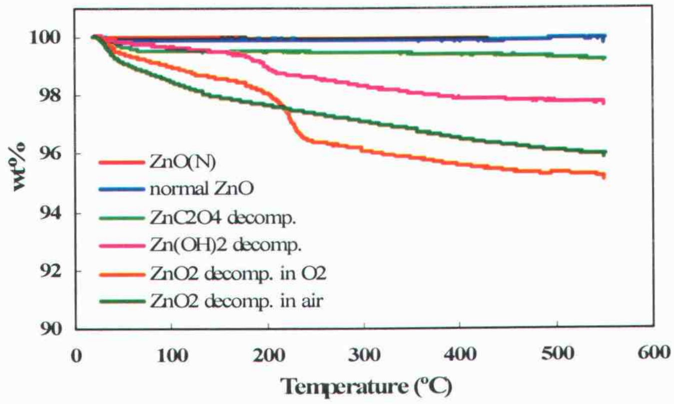

Figure 3.7 TGA curves of different ZnO samples.

### *3.3.3 Titration and Chemical Analysis*

Zinc peroxide is always hydrated [17]. Attempts to dehydrate below the $ZnO_2 \cdot 1/2H_2O$ composition invariably results in its decomposition [25]. Furthermore, chemical analysis always shows that the $(O_2)^{2-}$ concentration is less than the $Zn^{2+}$ concentration [26,27] with the average $ZnO_2$ content 63% ~ 65%. In our case, we typically find the peroxide content between 68.6% and 75.2%.

The amount of excess oxygen in $ZnO_{1+x}$ samples decreases with decomposition temperature of the peroxide precursor (Fig. 3.8). Decomposition in $O_2$ gives about 2.5 times more excess oxygen per ZnO formula unit than in air and 14 times more than in a Parr bomb. The impurities in zinc nitrate precursor for peroxide preparation seem to facilitate the hole doping by a factor of at least two given the same synthesis condition. Half of the excess oxygen was lost after heating the $ZnO_{1+x}$ sample in vacuum at 120 °C for 50 hr.

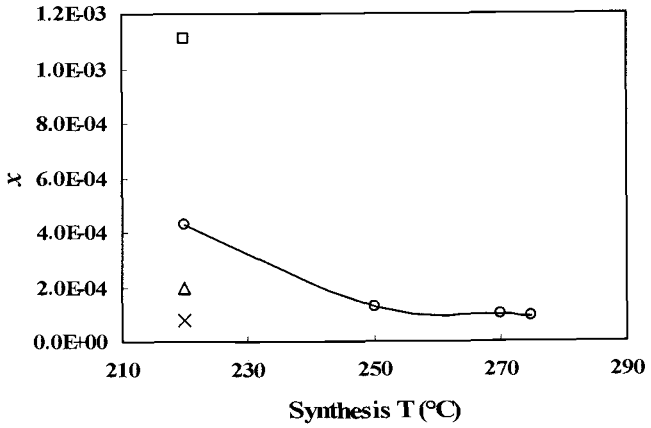

Figure 3.8 Dependence of hole concentration per Zn atom on peroxide decomposition temperature in $O_2$ (square), in air (circle, triangle) and in a Parr Bomb (cross point). The purity of zinc nitrate precursor is 98% for all the samples except the triangle which is 99.998%.

For $ZnO_{1-x}N_x$ samples, titrations normally show about $5.18 \times 10^{-5}$ holes per Zn atom in samples prepared at 315 °C and undetectable in samples prepared at 700 °C. Chemical analysis gives 0.049% (315 °C) and undetectable (700 °C) N content per formula unit for these samples. The highest hole concentration was found to be $9.37 \times 10^{-5}$ for a sample prepared by nitrate decomposition at 315 °C for 2 hr, and this is the sample that gives the most red shift in the DR spectra among all the N-doped samples. The impurities in the nitrate precursor seem to play an important role in the N doping because when using high purity zinc nitrate as a reactant, we were unable to detect either N or holes in our products by chemical analysis or titration regardless of the synthesis conditions.

Normal ZnO, annealed normal ZnO (at 1100 °C for 2.5 hr, yellow powder), and ZnO samples prepared from $Zn(OH)_2$ decomposition were also titrated for comparison. No holes were detected as expected.

Titrations indicate hole concentrations as high as 0.001 per Zn atom ($4.2 \times 10^{19}$/cc) for samples prepared by zinc peroxide decomposition at 220 °C. This then is lower than the $10^{20}$/cc to nearly $10^{21}$/cc carrier concentration found in highly conducting n-type ZnO. When using reagent grade zinc nitrate, chemical analyses for N in our samples prepared by nitrate decomposition at 315 °C indicate a composition of $ZnO_{0.997}N_{0.003}$, which would give a carrier concentration of $1.3 \times 10^{20}$/cc if all N atoms were effective dopants. However, titrations on such samples reveal only 0.00005 holes per Zn atom ($2.1 \times 10^{18}$/cc).

### *3.3.4 Transport and Optical Properties*

Attempts at measuring dc conductivity always gave unstable values, which drifted to higher values with increasing time. The ac conductivity was found to be frequency dependent in all cases. Thus, we determined conductivity by the complex impedance method. This method is sensitive to both ionic and electronic conductivity. It also has the potential to separate bulk and grain boundary conductivity. One must assume an equivalent circuit in order to interpret complex impedance data. Typically, one obtains two conductance values; these values could be due to either electronic or ionic conductivity. There is generally no way to be certain which of the two values is due to the bulk and which is due to grain boundary conductivity. The conductance value for the bulk can be converted to conductivity value based on the sample geometry. When a conductivity value for the grain boundaries is calculated based on the dimensions of the sample measured, only an upper limit is obtained. The true conductivity of this minority phase is lower by a factor of at least ten.

Our ZnO samples produced from zinc peroxide contain large amounts of hydroxyl groups at the surface, and it is likely that grain boundary conductivity is dominated by proton conductivity. It is impossible to completely remove these hydroxyl groups without also removing the holes, as detected by titration. One of these samples was pressed into a pellet of 2 mm thick and 12.6 mm in diameter, and heated to certain temperauters at and above 220 °C before each measurement taken at room temperature. The results are shown in Figure 3.9. The conductance values for both bulk and grain boundary have been converted to conductivity values based on the sample geometry. When treated at high temperatures, one conductivity value drops by several orders of magnitude, while the other value of conductivity remains nearly constant at about 2.5 × $10^{-5}$ S/cm, suggesting that this value represents the bulk conductivity and our titration results suggest that this is p-type conductivity. The grain boundaries, on the other hand, are responsible for the lower proton conductivity which decreases dramatically with heating temperature. The diamond and cross point are the two conductivity values for the cold-pressed pellet of above sample before any heat treatment. The square is the bulk conductivity (1.7 × $10^{-4}$ S/cm) for another cold-pressed pellet of a sample synthesized under the same condition in $O_2$, and it corresponds to the highest hole concentration determined by titration. As we can see, hole carriers are lost upon heating to 220 °C.

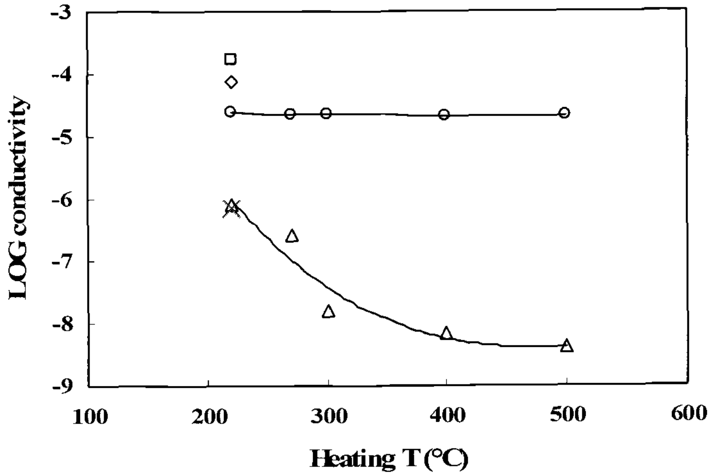

Figure 3.9 Dependence of conductivity on heating temperature of a ZnO sample prepared by decomposition of peroxide at 220 °C for 20 min in air. The bulk conductivity of another ZnO sample prepared under the same condition in $O_2$ is plotted as a square. The square, the diamond and the cross points are conductivities of cold-pressed pellets without any heating treatment.

For our N doped samples of zinc oxide, we typically find two conductance values. Converting these to conductivity based on sample dimensions gives values of about $2 \times 10^{-3}$ and $1 \times 10^{-7}$ S/cm. Both of these values are likely due to electronic conductivity because these samples show no detectable weight loss on heating, indicating a very low concentration of surface hydroxyl groups. Our titration results suggest that this conductance is due to p-type conductivity. It is impossible to know which conductivity value is due to bulk conductivity, but our higher value is close to that reported for N doped ZnO films, $2.5 \times 10^{-2}$ S/cm [8]. Our estimates of carrier concentration by chemical analyses suggest that we should expect somewhat lower conductivity. If our higher value of conductance is due to bulk conductivity, then the grain boundary conductivity is in fact much lower than $10^{-7}$ S/cm.

Diffuse reflectance spectra of our samples prepared from zinc peroxide show a red shift relative to normal zinc oxide (Fig. 3.10). This seems, however, not related to the hole carriers because the same red shift is found for samples prepared by decomposition of zinc hydroxide and oxalate. An even larger red shift is observed for zinc oxide prepared by nitrate decomposition, but this shift is related to both purity of the starting nitrate and calcination temperature. For comparison the red shift is shown for a sample of zinc oxide that has been heated at 1200 °C under zinc metal vapors. The composition of this orange zinc oxide is close to $Zn_{1.0003}O$. This color is likely from a deep trap associated with a nonionized Zn interstitial, or possibly from an oxygen vacancy.

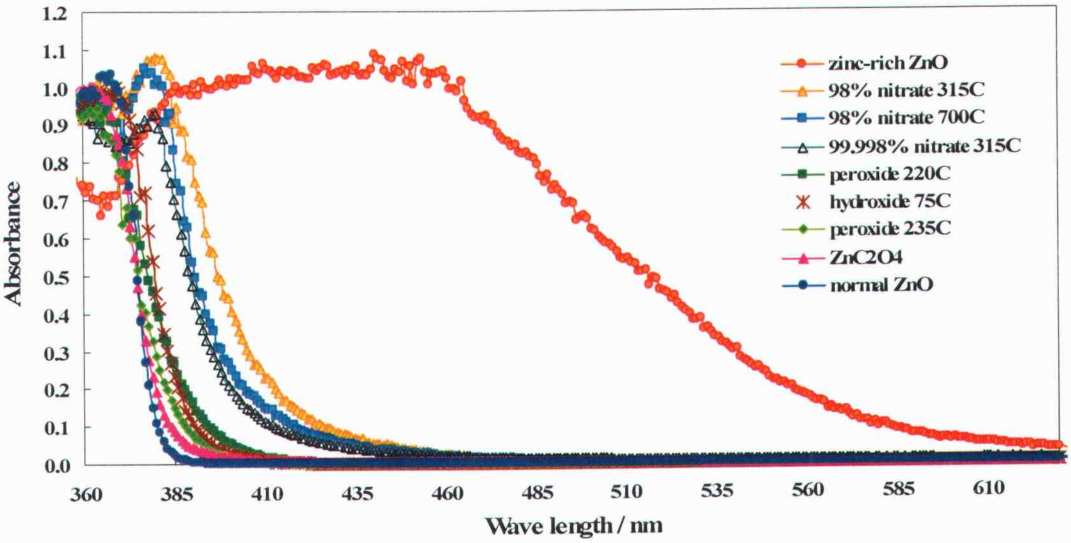

Figure 3.10 Diffuse reflectance spectra of ZnO powders prepared by different synthesis methods (courtesy of Dr. J. Tate and R. Kykyneshi).

### 3.4 Discussion

It was previously noted that the cell edges of zinc oxide produced from zinc peroxide increase as the synthesis temperature decreases [16]. This was attributed to an increased defect concentration associated with increased nonstoichiometry. We have confirmed this increase in cell dimensions, but we attribute this to a particle size effect. The cell edges increase with decreasing particle size regardless of the synthesis method. This correlation between particle size and cell edge for zinc oxide has been noted by others [28]. Determining changes in unit cell dimensions as particle size decreases is complicated because there are various ways to define peak position. This is not of great concern for very sharp and symmetrical peaks, but this becomes a big issue for broad peaks. There is generally a significant difference between the position of the maximum of a peak and the center of gravity of the peak. We have closely examined this issue for our samples. We conclude that regardless of how peak position is defined, the cell edges increase with decreasing particle size below about 1000 Å.

It has been previously demonstrated that iodine can be used to titrate carriers in n-type zinc oxide [2,3]. The carrier concentration so determined correlates very well with dopant level and carrier concentration obtained from Hall measurements [1-4]. The technique is sensitive enough to even determine the nonstoichiometry in reduced zinc oxide to be $Zn_{1.0003}O$ [3]. For the titration of n-type zinc oxide, it is the electrons in the conduction band that reduce $I^0$ to $I^{1-}$. None of the samples we prepared in this study reduce any $I^0$ to $I^{1-}$, consistent with a lack of electrons in the conduction band. One can expect that holes in the valence band will oxidize $I^{1-}$ to $I^0$. Titrations based on this reaction have been routinely used to determine the hole concentration in cuprate superconductors [24]. Indeed, many of our samples will oxidize $I^{1-}$ to $I^0$, indicating the presence of hole carriers. There are several reports of species such as $O^{1-}$, $(O_2)^{1-}$, and $(O_2)^{2-}$ on the surface of zinc oxides [29,30]. These can be produced when $O_2$ is chemisorbed on n-type zinc oxide. They are created by electron transfer from the conduction band to the chemisorbed oxygen. Such species can also occur during the photodecomposition of water on zinc oxide [31]. Our iodometric titrations would be sensitive to any of these species. However, our titrations on slurries show a negligible concentration of such surface species for our products.

Our N doped zinc oxide shows a carrier concentration much less than that expected for the level of N substitution. This has also been observed for thin films of N doped zinc oxide [10]. Evidence has been presented for the films that the N dopant is largely compensated by interstitial H. This explanation may also apply to our powders.

One previous study of the conductivity of zinc oxide powders by the complex impedance method concluded that the only conductance that could be measured was due to grain boundaries [32]. The conductivity of the grains themselves was too low to be measured even at temperature as high as 600 °C. This result is not surprising because the zinc oxide studied was not doped. The temperature range of measurement (450 ~ 600 °C) precluded the possibility that this conductivity was due to protons. The conductance dependence on oxygen partial pressure indicated that this conductivity was n-type. A study of In doped ZnO by complex impedance spectroscopy indicated that both bulk and grain boundary conductance could be determined [33]. In this case, the bulk conductance was higher than the grain boundary conductance.

In the case of n-type zinc oxide powders, high conductivity is obtained only when the synthesis temperature is about 1000 to 1200 °C. Here the entropy at high temperatures favors a high doping level. The opposite situation applies for p-type doping. Low temperature favors a high hole concentration, and hole concentrations become too low to measure at temperatures as high as 500 °C.

It is common for small particles to show decrease unit cell size and a blue shift of the absorption band. This correlation between size and absorption edge is expected because shorter and stronger bonds will cause an increase in band gap. The opposite effect in small particles seems only to be observed in oxides. Perhaps the effect in oxides is related to the high concentration of hydroxide groups at the surface. This may weaken metal-oxygen bonds, giving then larger metal oxygen distances and the red shift of the absorption edge. The much larger red shift for N-doped samples is easier to explain because the band gap of an oxide of a given element is always larger than the nitride of that element. Nitrate precursor samples calcined at 500 °C or higher show no detectable N by chemical analysis and no holes by titration. The red shift is reduced in a sample heated to 700 °C, but there is still a red shift relative to normal zinc oxide sample, suggesting that some N is still present. A red shift also occurs for zinc oxide that has been annealed under zinc metal vapor [3,4]. This is presumably related to zinc interstitials that are not ionized. Conductivity does not increase with this red shift. It is thus possible, but unlikely, that the red shift in our samples is also caused by such zinc interstitials.

## 3.5 References

1. R.P. Wang, L.L.H. King, A.W. Sleight. *J. Mater. Res.*, 11(7) 1659 (1996)
2. R.P. Wang, A.W. Sleight. D. Cleary. *Chem. Mater.*, 8, 433-439 (1996)
3. R.P. Wang, A.W. Sleight, R. Platzer, J.A. Gardner. *J. Solid State Chem.*, 122, 166-175 (1996)
4. A.W. Sleight, R.P. Wang. *Mater. Res. Soc. Symp. Proc.*, 453, 323 (1997)

5. J. Hu, R.G. Gordon. *Mater. Res. Soc. Symp. Proc.*, 242, 743 (1992)

6. R. Helbig. *J. Cryst. Growth*, 15, 25-31 (1972)

7. S.B. Zhang, S.H. Wei, A. Zunger. AIP Conference Proceedings, Golden, 1999

8. D.C. Look, D.C. Reynolds, C.W. Litton, R.L. Jones, D.B. Eason, G. Cantwell. *Appl. Phys. Lett.*, 81(10), 1830-1832 (2002)

9. C. Wang, Z.G. Ji, K. Liu, Y. Xiang, Z.Z. Ye. *J. Cryst. Growth*, 259(3), 279-281 (2003)

10. A. Kaschner, U. Haboeck, M. Strassburg, M. Strassburg, G. Kaczmarczyk, A. Hoffmann, C. Thomsen, A. Zeuner, H.R. Alves, D.M. Hofman, B.K. Meyer. *Appl. Phys. Lett.*, 80 (11), 1909 (2002)

11. A.V. Singh, R.M. Mehra, A. Wakahara, A. Yoshida. *J. Appl. Phys.*, 93(1), 396 (2003)

12. M. Joseph, H. Tabata, T. Kawai. *Jpn. J. Appl. Phys.*, 38(11A), Pt.2, L1205, (1999)

13. G. Xiong, J. Wilkinson, B. Mischuck, S. Tuzemen, K.B. Ucer, R.T. Williams. *Appl. Phys. Lett.*, 80(7), 1195 (2002)

14. A Tsukazaki, H. Saito, K. Tamura, M. Ohtani, H. Koinuma, M. Sumiya, S. Fuke, T. Fukumura, M. Kawasaki. *Appl. Phys. Lett.*, 81(2), 235 (2002)

15. I.D. Campbell. *J. Chem. Soc. Faraday Trans. 1: Phys. Chem. Condens. Phases*, 73(3), 487-493 (1977)

16. N. Uekawa, N. Mochizuki, J. Kajiwara, F. Mori, Y.J. Wu, K. Kakegawa. *Phys. Chem. Chem. Phys.*, 5(5), 929-934 (2003)

17. G. Cogne. Compt. Rend., 206, 1119-1120 (1938); S.Z. Makarov, L.V. Ladeinova. *Zh. Neorg. Khim.*, 1, 2708-2711 (1956)

18. C. Chauvin, J. Saussey, J.C. Lavalley, G. Djega-Mariadassou. *Appl. Catal.*, 25, 59-68 (1986)

19. J.I. Langford, A. Boultif, J.P. Auffredic, D. Louer. *J. Appl. Crystallogr.*, 26, 22-23 (1993); J.P. Auffredic, A. Boultif, J.I. Langford, D. Louer. *J. Am. Ceram. Soc.*, 78(2), 323-328 (1995)

20. M. Maneva, N. Petrov. *J. Therm. Anal.*, 35, 2297-2303 (1989)

21. A. Le Bail, H. Duroy, J.L. Fourquet. *Mater. Res. Bull.*, 23, 447-452 (1988)

22. J. Rodriguez-Carvajal. Fullprof Version 2k, 2002, original at http://ccp14.semo.edu/ccp/ccp14/ftp-mirror/fullprof/pub/divers/fullprof.2k/

23. A.I. Vogel *et al. A Text-Book of Quantitative Inorganic Analysis Including Elementary Instrumental Analysis,* 3rd ed.; John Wiley & Sons: New York, 1961

24. In *Chemistry of Superconductor Materials, Preparation, Chemistry, Characterization and Theory*; T.A. Vanderah, Ed.; Noyes Publications: New Jersey, 1992

25. S.Z. Makarov, L.V. Ladeinova. *Izv. Akad. Nauk, S. S. S. R., Otdel. Khim. Nauk*, 139-142 (1957)

26. E.D. Volova, T. Bychatina. *Zh. Prikl. Khim.*, 18, 172-174 (1945)

27. N.G. Vannerberg. *Ark. Kemi*, 14(13), 119-124 (1959)

28. O.Garcia-Martinez, R.M. Rojas, E. Vila, J.L. Martin de Vidales. *Solid State Ionics*, 63-65, 442-449 (1993)

29. D.J.M. Bevan, J.S. Anderson. *Discuss. Faraday Soc.*, 8, discussion 241-6, 238-41 (1950)

30. R.J. Kokes. *J. Phys. Chem.*, 66, 99-103 (1962)

31. M. Anpo, K. Chiba, M. Tomonari, S. Coluccia, M. Che, M.A. Fox. *Bull. Chem. Soc. Jpn.*, 64, 543-551 (1991)

32. J. Lee, J.H. Hwang, J.J. Mashek, T.O. Mason, A.E. Miller, R.W. Siegel. *J. Mater. Res.*, 10(9), 2295 (1995)

33. M. Seitz, F. Hampton. W. Richmond. *Advances in Ceramics*, 7(Addit. Interfaces Electron. Ceram.), 60-70 (1983)

# Chapter 4

# Clues to the Giant Dielectric Constant of $CaCu_3Ti_4O_{12}$ in the Defect Structure of "$SrCu_3Ti_4O_{12}$"

## 4.1 Introduction

The relentless miniaturization in integrated circuit technology has led to enhanced chip performance in terms of processing speeds and to expanded memory capacities. In memory devices based on capacitive components, such as static and dynamic random access memories, the degree of size shrinking will eventually be decided by the static dielectric constant $\kappa$ of the material used in the storage capacitors.

Perovskites are well known as high $\kappa$ materials and have been widely studied for various microelectronic applications [1-3]. Dielectric constant higher than 1000, however, has always been associated with either a ferroelectric or a relaxor. In both cases the dielectric constant shows a peak as a function of temperature and hence limits the practical application of the material.

A few years ago, very interesting and unexpected dielectric properties were discovered in $CaCu_3Ti_4O_{12}$ (CCTO) with perovskite structure [4]. The dielectric constant $\kappa$ of CCTO has been found to be 10,000 in sintered pellets [4,5] and thin films [6], and 100,000 in single crystals [7]. This very high $\kappa$ remains essentially unchanged from 100 to 500 K. Furthermore, structural studies show that CCTO maintains a centric structure at all temperatures with no phase transitions [4,5]. There is not yet a completely satisfactory explanation for this unique and remarkable behavior. However, it is established that this behavior is not related to a ferroelectric transition [4], and the consensus is that the behavior is not intrinsic [7-16]. The high κ of CCTO has been interpreted as due to conducting grains with insulating grain boundaries, according to a well established barrier layer mechanism for high dielectric constant [9-11]. However, the exceptionally high κ in CCTO crystals [7] dictates that the insulating barriers must be inside the crystals rather than between them. Very high concentrations of twin boundaries seem always to be present in CCTO crystals, and it has been suggested that these somehow become the insulating barriers [4,8]. Other planar defects, such as antiphase boundaries or dislocations, are also candidates for these insulating barriers. An understanding of the dielectric properties of CCTO requires (1) an explanation of how this titanate develops conducting regions and (2) a description of the insulating boundaries between the conducting regions.

The unusual variation of the perovskite structure found for CCTO is shown in Figure 4.1. The closest analogue to CCTO might be considered to be $SrCu_3Ti_4O_{12}$. Attempts to prepare this compound have failed [17]. These attempts readily give a dominant phase with the CCTO structure, but impurities including $SrTiO_3$ are always present. The purpose of this investigation has been to determine the composition and structure of the CCTO type phase in the Sr/Cu/Ti/O system by combining neutron and synchrotron X-ray diffraction data. The dielectric properties of this phase could then be determined on a phase-pure sample. Furthermore, the defects related to the nonstoichiometry of "$SrCu_3Ti_4O_{12}$" could provide important clues as to the defects that must also be present in CCTO. In fact, a defect we discovered in "$SrCu_3Ti_4O_{12}$" suggests a mechanism to produce conducting titanates under conditions that normally produce insulating titanates.

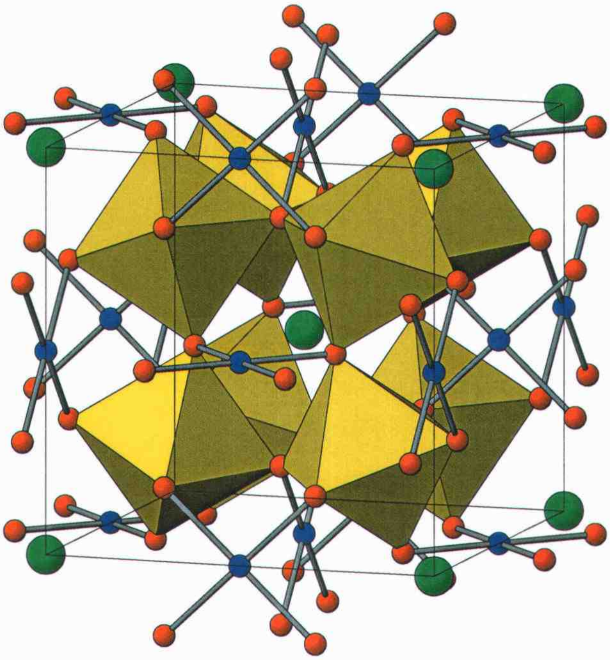

Figure 4.1 Structure of $ACu_3Ti_4O_{12}$ shown as $TiO_6$ octahedra, Cu atoms bonded to four oxygen atoms, and large A (A = Ca, Sr) atoms without bonds.

Efforts were also made to look for evidence of such internal barriers in CCTO crystals through complex impedance spectroscopy. The crystal used in this study was the same one used for the measurement of dielectric constant [7].

## 4.2 Experimental

Reactants were $SrCO_3$, CuO, and $TiO_2$, all from Aldrich with a listed purity of

99.99%. Appropriate amounts of reactants were thoroughly mixed by grinding together in an agate mortar. The mixed powder was calcined at 900 °C for 12 hr. The calcined powder was reground, pressed into pellets of 1 ~ 2 mm thick and 12.7 mm in diameter, and sintered in air at 1000 ~ 1100 °C for 24 hr. X-ray powder diffraction patterns were recorded with Rigaku MiniFlex diffractometer in DuPont. All attempts to synthesize a single-phase composition of a formula $SrCu_3Ti_4O_{12}$ resulted in the formation of multiphase samples with a dominant CCTO-type phase but having significant impurities with $SrTiO_3$ being the major impurity.

Neutron powder diffraction data were collected using the BT-1 32-counter high resolution diffractometer at the NIST Center for Neutron Research at the National Institute of Standards and Technology. A Cu(311) monochromator with a 90° take-off angle giving a wave length of 1.5402(2) Å and in-pile collimation of 15 min of arc were used. The beam was masked to 1.1 cm × 5.1 cm at the sample. Data were collected over a $2\theta$ range of 3 ~ 168° with a step size of 0.05°. The sample was sealed in a vanadium container 15.6 mm in diameter and 50 mm high. The data were refined by Rietveld method using GSAS software [18,19].

X-ray powder diffraction data were collected at beamline 5BMC of the DuPont-Northwestern-Dow Collaborative Access Team at the Advanced Photon Source, Argonne National Laboratory. The sample was ground in an agate mortar, placed in a 0.5 mm glass capillary, and spun at 1 revolution/second. The diffracted beam was monitored with a scintillation detector equipped with a Ge <220> analyzer tuned to the incident wavelength of 0.40985 Å. The data were refined using GSAS with 22963 data points over the range $6° \leq 2\theta \leq 28°$.

A disc sample of SCTO was polished to produce a flat uniform surface and electroded with silver paint. The painted sample was dried at 100 °C overnight. Capacitance and loss tangent measurements were taken from 40 to 573 K on an HP 4275A LCR meter in DuPont.

Seebeck coefficients were measured in DuPont using a home-made apparatus with high purity Ag blocks as hot and cold ends. The principle used is based on the static method where different temperature gradients ($\Delta T$) are created at both ends of the sample and the corresponding Seebeck potentials generated were measured using a dc nanovoltmeter. Seebeck coefficient values were obtained by extrapolating the ($\Delta V/\Delta T$) vs. $\Delta T$ plots to zero $\Delta T$ at a given temperature. The sign of the cold junction was taken as the sign of Seebeck coefficient indicating the type of charge carriers present in the sample.

Impedance measurements of the ceramic SCTO sample were carried out using a SI 1260 Schlumberger Impedance/Grain-Phase Analyzer at 373 ~ 853 K over a frequency range 0.1 Hz to 5 MHz with an applied voltage of 1 V. Data were analyzed using ZView V2.80 written by Derek Johnson. The conversion of conductance to conductivity assumes that both phases are bulk phases. If the less conducting phase is present as thin barriers, the conductivity of this phase is actually significantly lower.

Crystals of CCTO were grown by the traveling-solvent floating-zone method in an image furnace, details of which was described in Ref. [7]. A disc of ~ 1 mm thick was cut from the middle of the boule and the front of the disc was polished to flat mirrorlike surface onto which Au electrodes were sputtered (Fig. 4.2).

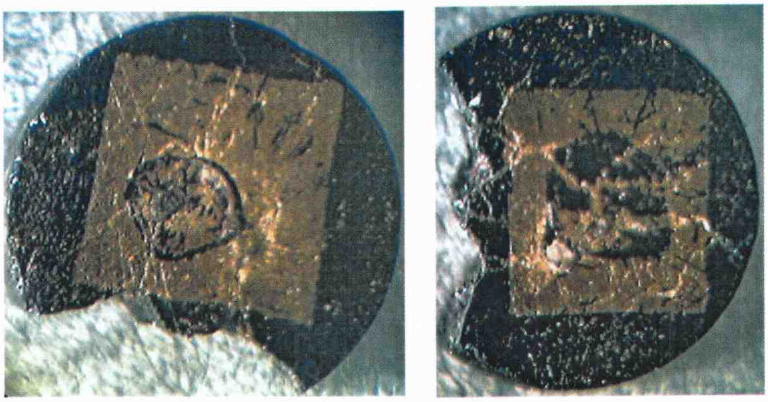

Figure 4.2 Images of two sides of the CCTO crystal grown by S. Wakimoto and obtained from A.P. Ramirez. The disc is 3.90 mm in diameter and 0.77 mm thick.

Neutron diffraction patterns of this material showed the symmetry of the higher Laue group [20], when in fact we know that the structure of CCTO must be described in the lower Laue group. The same observation was made from X-ray diffraction on several smaller CCTO crystals [4]. The observation of the symmetry of the higher Laue group means not only that the crystals are twinned, but also that the amounts of the twins in the different orientations are essentially the same. This strongly indicates that the twining is on a fine scale.

Complex impedance spectra of CCTO crystal were measured with a Schlumberger SI 1260 impedance/grain-phase analyzer and a Solartron SI 1287 electrochemical interface at 289 ~ 456 K over a frequency range of 0.1 Hz to 5 MHz with an applied voltage of 800 mV. Data were analyzed in the same manner as for the SCTO sample.

## 4.3 Results

### *4.3.1 Ceramic Sample of SCTO*

The neutron powder diffraction data of SCTO were refined in space group Im$\bar{3}$. Positions for the atoms are 0,0,0 for Sr; 0,1/2,1/2 for Cu(Ti); 1/4,1/4,1/4 for Ti; and $x$,$y$,0 for O. Agreement between observed and calculated intensities is shown in Figure 4.3, and the final refined parameters are given in Table 4.1.

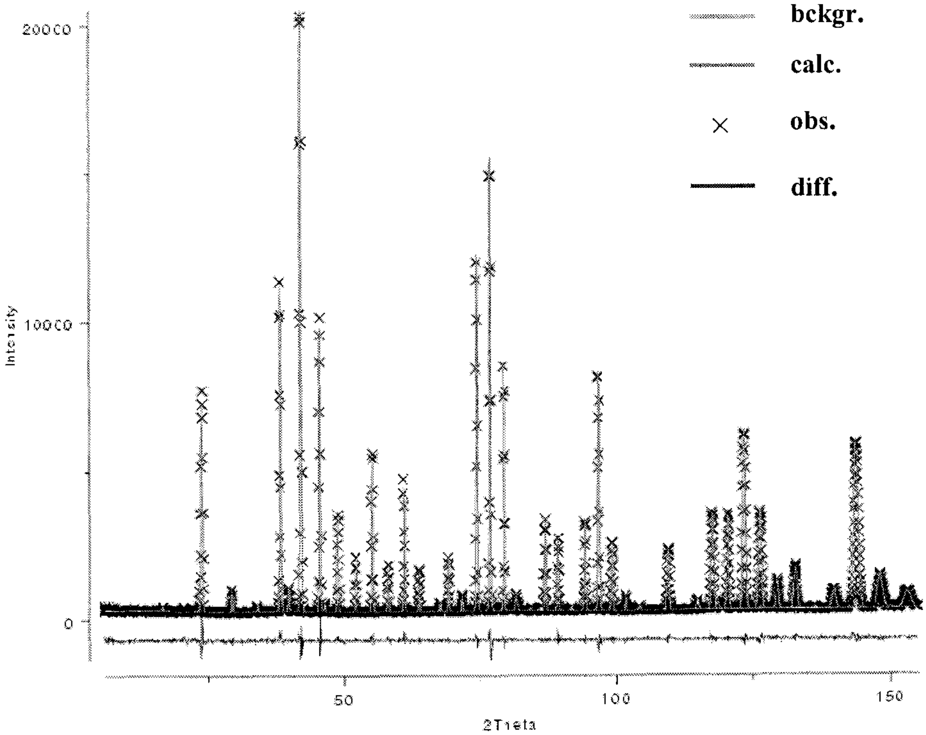

Figure 4.3 Agreement between observed (cross points) and calculated (solid line) neutron diffraction intensities for SCTO. Bottom curve is the difference ($I_{obs} - I_{calc}$) pattern on the same scale.

Table. 4.1 Refinement results of neutron diffraction data at 298 K.

| | **SCTO (this work)** | **CCTO (Ref. [8])** |
|---|---|---|
| $\chi^2$ | 1.749 | – |
| $R_{\mathrm{wp}}$ (%) | 4.93 | 6.22 |
| $R_{\mathrm{p}}$ (%) | 3.96 | 2.36 |
| $a$ (Å) | 7.4276(1) | 7.4037(5) |
| $x$ (O) | 0.30509(8) | 0.3026(2) |
| $y$ (O) | 0.18135(9) | 0.1798(2) |
| Occ. (A) | 0.946(9) | 1 |
| Occ.(Cu) | 0.982(3) | 1 |
| Occ. (Ti) | 0.018(3) (in Cu site) | 0 |
| $U_{11}$ (A) | 0.0060(4) | 0.009 |
| $U_{11}$(Cu) | 0.0045(8) | 0.005 |
| $U_{22}$ (Cu) | 0.0053(6) | 0.005 |
| $U_{33}$ (Cu) | 0.0078(6) | 0.009 |
| $U_{11}$ (Ti) | 0.0062 (2) | 0.005 |
| $U_{12}$ (Ti) | -0.0004(4) | 0.000 |
| $U_{11}$ (O) | 0.0068(3) | 0.008 |
| $U_{22}$ (O) | 0.0067(4) | 0.007 |
| $U_{33}$ (O) | 0.0048(4) | – |
| $U_{12}$ (O) | 0.0004(2) | 0.002 |

A = Sr in SCTO or Ca in CCTO.
Sr: $U_{11} = U_{22} = U_{33}$, $U_{12} = U_{13} = U_{23} = 0$; Cu: $U_{12} = U_{13} = U_{23} = 0$.
Ti: $U_{11} = U_{22} = U_{33}$, $U_{12} = U_{13} = U_{23}$; O: $U_{13} = U_{23} = 0$.

The extra peaks in the diffraction pattern could be attributed to about 2.5% $SrTiO_3$, and very small amounts of CuO and $SrCuO_2$. It was evident from initial refinement of the neutron diffraction data on our sample of overall composition $SrCu_3Ti_4O_{12}$ that the Ti site was completely occupied with Ti and that the oxygen site was completely occupied by oxygen. It was also evident that the Sr site was not completely occupied. This situation leaves only the Cu site as a possibility to attain charge balance. A small substitution of Ti on this site refined to a value that achieved charge balance. The formula was then known to be $A_{0.946}(Cu_{2.946}Ti_{0.054})Ti_4O_{12}$. The amount of Ti on the Cu site is known very precisely due to the large difference in neutron scattering lengths of Ti and Cu (-0.34 for Ti and +0.77 for Cu). However, the neutron data cannot preclude some Cu on the Sr site due to the similarity of the neutron scattering lengths of Sr and Cu (+0.70 for Sr and +0.77 for Cu). Thus, X-ray diffraction data from a synchrotron were used to address this issue. Analysis of these data showed no detectable amount of Cu on the Sr site. Thus, using both neutron and X-ray data, the formula refines unambiguously to $Sr_{0.946}(Cu_{2.946}Ti_{0.054})Ti_4O_{12}$ (SCTO). Synthesis using this formula leads to a single-phase product. Attempts to vary $x$ in the formula $Sr_{1-x}(Cu_{3-x}Ti_x)Ti_4O_{12}$ failed. The structure and bonding of CCTO and SCTO are compared in Table 4.2.

Table 4.2 Bond lengths (Å), angles(°) and valences [21].

| | **SCTO (this work)** | **CCTO (Ref. [8])** |
|---|---|---|
| A–O | 2.6362(6) | 2.608(1) |
| Cu–O | 1.9774(5) | 1.978(1) |
| T–iO | 1.9686(2) | 1.9625(4) |
| O–Ti–O | 88.41(1) | 89.44(4) |
| O–Ti–O | 91.59(1) | 90.56(4) |
| Ti–O–Ti | 141.21(3) | 141.33(6) |
| O–Cu–O | 94.13(4) | 95.32(6) |
| O–Cu–O | 85.87(4) | 84.68(6) |
| BV(A) | 2.95 | 2.12 |
| BV (Cu) | 1.78 | 1.78 |
| BV (Ti) | 3.96 | 4.02 |
| BV (O) | 2.01 | 1.96 |

A = Sr in SCTO or Ca in CCTO; BV is bond valence.

The κ and loss for SCTO from 50 to 575 K are given in Figure 4.4. The change in κ and the peak in loss at about 100 K are at essentially the same temperature as such features in CCTO [5]. These features are characteristic of a barrier layer capacitor when the conducting region is semiconducting with a small activation energy [12]. This same behavior is generally observed for $ACu_3Ti_4O_{12}$ compounds, but only CCTO shows exceptionally high κ.

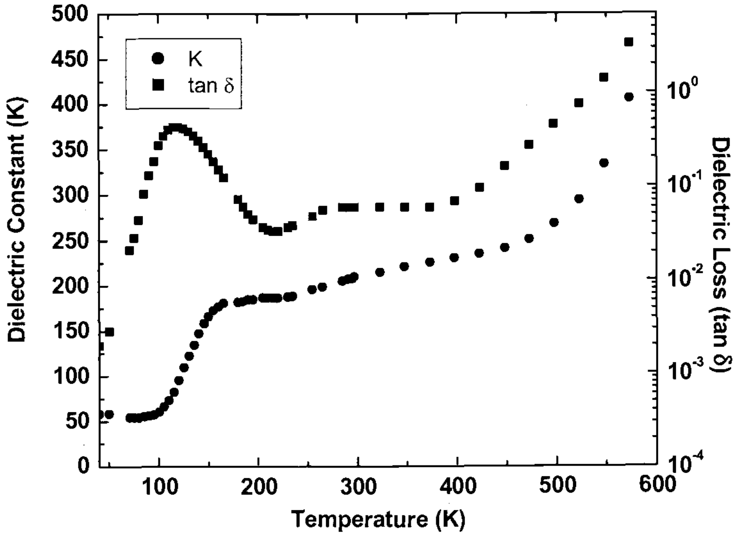

Figure. 4.4 Dielectric constant and loss for SCTO from 50 to 575 K (courtesy of Dr. M.A. Subramanian).

Examples of the impedance spectroscopy data of SCTO are plotted in Figure 4.5 (a) ~ (c), and the data were modeled on an equivalent circuit shown in Figure 4.5 (d). Each semicircle we see here corresponds to the response of the insulating grain boundary regions, while the nonzero intercept indicates the resistance of semiconducting grains in our ceramic sample.

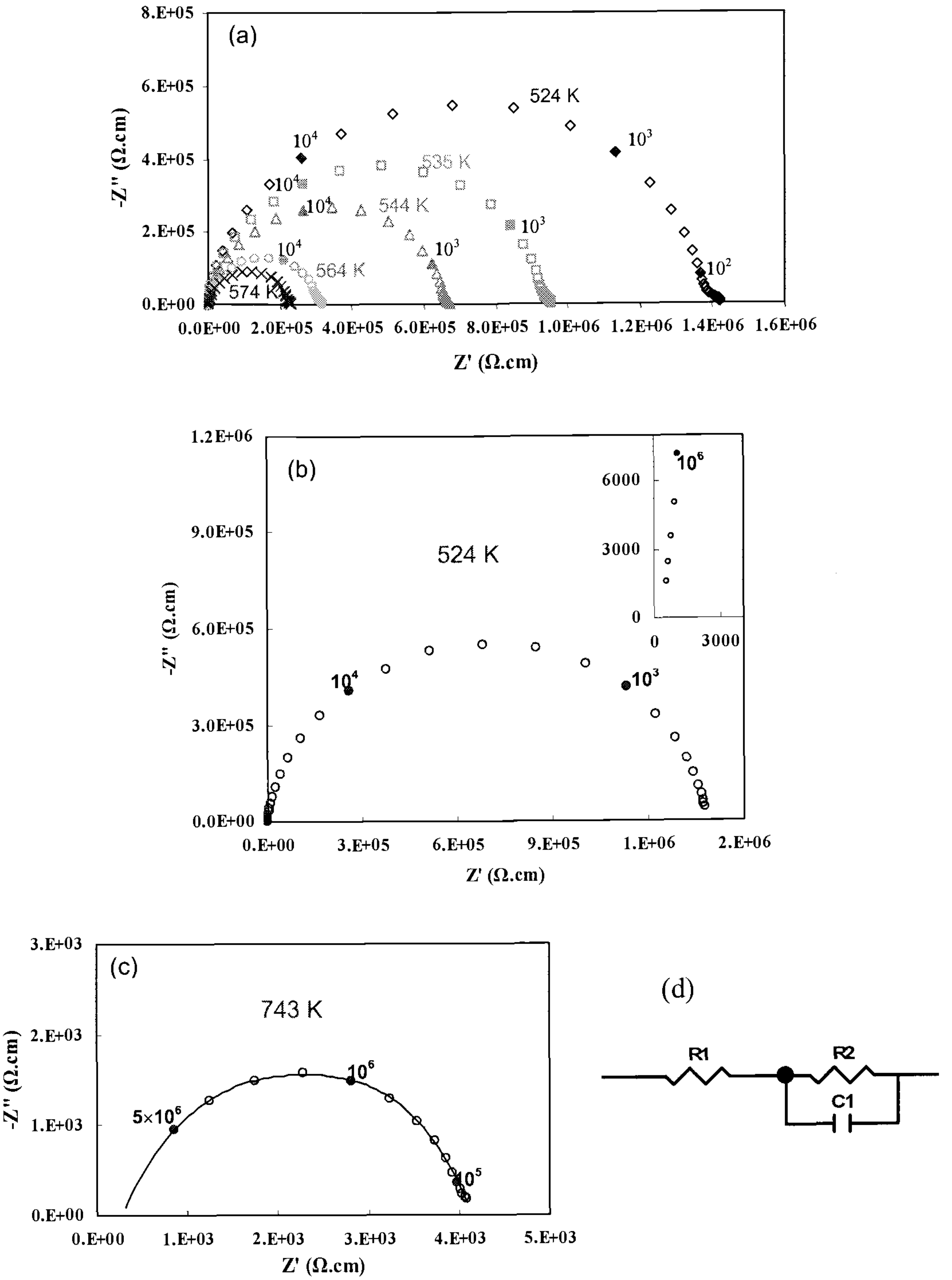

Figure 4.5 Impedance complex plane plots at (a) 524, 535, 544, 564, 574 K, (b) 524 K, the inset an expanded view of the high frequency data close to the origin, and (c) 743 K for SCTO. The equivalent circuit used for data modeling is shown in (d). Filled symbols in (a) ~ (c) indicate selected frequencies in Hz.

The arc of bulk grains is outside the available frequency range due to their much smaller relaxation time and therefore response at much higher frequencies.

Conductivities for SCTO derived from the complex impedance data are plotted in Figure 4.6. This plot is similar to a plot reported for CCTO [9]. There is a conducting phase (~ $10^{-2}$ S/cm) with a small temperature dependence of conductivity and a phase having much lower conductivity, which is significantly activated (~ 0.7 eV).

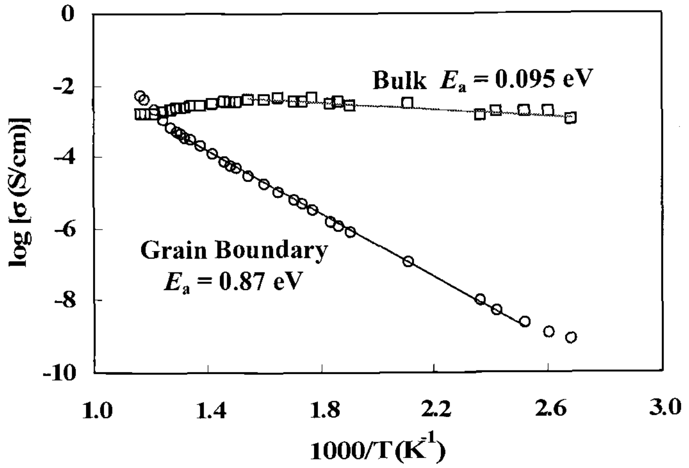

Figure. 4.6 Arrhenius plot of conductivity data for the two phases in SCTO.

Our thermoelectric power measurements show that SCTO is an n-type conductor with Seebeck coefficient values of –300 μV/K at 400 K and –210 μV/K at 500 K. Our samples of SCTO are too insulating to measure the Seebeck coefficients below 400 K. The higher conductivity of CCTO allows a reliable Seebeck coefficient to be determined at a temperature as low as 350 K, where we find a value of –110 μV/K.

### *4.3.2 Crystal Sample of CCTO*

A representative Cole-Cole plot of the CCTO crystal sample is shown in Figure 4.7. Two values of the resistance are determined from the two intercepts made by the semicircle. The conductivity values derived from such plots are shown in Figure 4.8. Our results for the crystal of CCTO are very similar to the results for ceramic samples of CCTO [9] and SCTO (this work). Two different phases are detected by impedance spectroscopy. One has a conductivity that is significantly activated. The second phase has higher conductivity, and the conductivity is much less temperature dependent. The assumption is that the more conducting phase is the bulk phase and that the less conducting phase is the barrier phase.

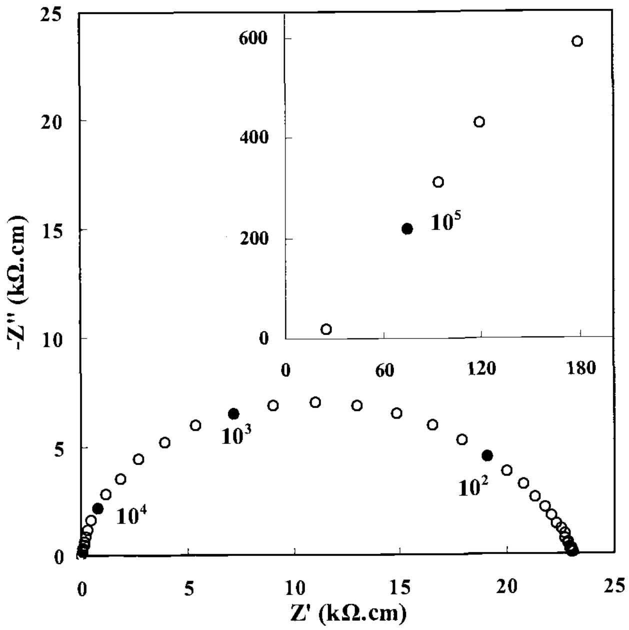

Figure 4.7 Cole-Cole plot at 289 K for $CaCu_3Ti_4O_{12}$ (CCTO) crystal. The inset shows an expanded view of the high frequency data close to the origin (units in Ω.cm). Selected frequencies (in Hz) are marked with filled circles.

There is no way of accurately converting conductance to conductivity for these two phases because their dimensions are unknown. The conversion was made in all three cases (CCTO ceramic, CCTO crystal, and SCTO ceramic) on the assumption that the dimensions of each phase are the dimensions of the sample measured. This is essentially correct for the bulk phase. However, the barrier phase must be much thinner. Therefore, its conductivity must be much lower than shown in Figure 4.8 and much lower than shown in similar plots for ceramic samples of CCTO and SCTO.

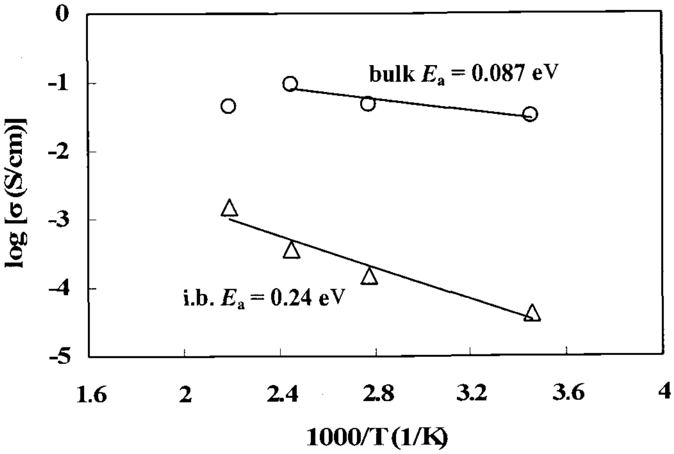

Figure 4.8 Temperature dependence of bulk and internal barrier (i.b.) conductivities for $CaCu_3Ti_4O_{12}$ (CCTO) crystal.

The complex impedance report on ceramic CCTO indicated that the conductivity of the bulk phase increased with temperature over the measured range of 104 to 400 K. We also see an initial increase in conductivity with increasing temperature for both ceramic SCTO and the CCTO crystal. However, we have measured to temperatures higher than 400 K where we find that the conductivity decreases for both ceramic

SCTO and the CCTO crystal. The conductivity found for the bulk phase is about $10^{-2}$ S/cm for the crystal of CCTO and for ceramic CCTO and SCTO. This value is relatively free from error associated with sample dimensions. The true conductivity of the less conducting phase, which is assumed to be the barrier phase, must be much lower than the values given. The activation energy for this phase should, however, be reasonably accurate. This activation energy is 0.60 eV for ceramic CCTO, 0.87 eV for ceramic SCTO, and 0.24 eV for the CCTO crystal.

## 4.4 Discussion

Ideal perovskite compounds have the formula $AMO_3$, and the structure is a network of corner-shared $MO_6$ octahedra where all the M–O–M angles are 180° with coordination numbers of six and twelve for the M and A cations, respectively. The unusual variation of this structure was found in 1967 [17] for compounds of the type $ACu_3Ti_4O_{12}$ (A = Ca, Cd), and the accurate structure of $CaCu_3Ti_4O_{12}$ (CCTO) at room temperature was determined in 1979 by neutron powder diffraction [22].

In the CCTO structure the $TiO_6$ octahedra of the perovskite framework tilt to form square planar coordination for Cu, and the framework becomes very rigid (Fig. 4.1). The space for the A cation is thus highly restricted. This space is somewhat too small for Ca, but it is much too small for Sr. It is thus understandable that stoichiometric $SrCu_3Ti_4O_{12}$ will not form. The Ca–O distance expected in CCTO based on ionic radii is 2.72 Å, much larger than the 2.61 Å distance observed [4,8]. Thus, Ca is under compression and is overbonded with a calculated bond valence of 2.12 instead of the expected 2.0.

The situation is far more extreme in SCTO. The expected Sr–O distance is 2.82 Å compared to the 2.64 Å distance observed. This leads to an extremely overbonded situation with a calculated bond valence of 2.95 for Sr. In the case of CCTO the somewhat too large Ca stretches the weak Cu–O bonds leading to a low bond valence for Cu. In going from CCTO to SCTO, the much too large Sr stretches the Ti–O bonds but does not stretch the Cu–O bonds beyond the values found for CCTO (Table 4.2). Stretching the Ti–O bonds in SCTO would be expected to increase the polarizability of the $TiO_6$ octahedra as occurs on going from $SrTiO_3$ to $BaTiO_3$. The fact that SCTO does not show an exceptionally high dielectric constant is further evidence that the very high $\kappa$ in CCTO is not intrinsic.

Vacancies on the A site are well established for the CCTO family. Some examples are phases of the type $A_{2/3}Cu_3Ti_4O_{12}$ where A may be a rare earth or Bi [4,8]. More extreme examples are $Cu_3Ti_2Ta_2O_{12}$, $Cu_3Ti_2Sb_2O_{12}$ and $Cu_2Ta_4O_{12}$ where there are no A site cations [8]. Thus, the A site vacancies in SCTO are not surprising. The manner in which these vacancies are compensated in SCTO is surprising. Titanium substitution on the Cu site implies square planar coordination, which is apparently unknown for Ti(IV) in oxides. The Ti(IV) coordination in oxides is usually octahedral, but can be tetrahedral or square pyramidal. A factor favoring substitution of Ti on the Cu site is that the Ti–O and Cu–O distances in this structure are essentially the same (Table 4.2).

The conductivity (~ $10^{-2}$ S/cm) and activation energy (~ 0.09 eV) for the conducting phases in CCTO and SCTO are typical [23] of reduced $SrTiO_3$ with a room temperature carrier concentration of $10^{17}/cm^3$, suggesting a similar concentration of electrons in the Ti 3*d* conduction band of CCTO and SCTO even though the materials have not been intentionally reduced. The impact of a Cu–O conduction band can be discounted because there are no extended Cu–O–Cu connections. The question then becomes how do $ACu_3Ti_4O_{12}$ phases become reduced, given that they are synthesized under conditions that normally give fully oxidized, insulating titanates? The clue may be the small amount of Ti we find on Cu sites in SCTO which could also be on the Cu sites in CCTO. On heating Cu(II) becomes unstable and reduces to Cu(I). The reduction of CuO to $Cu_2O$ occurs at 1025 °C in air. For $YBa_2Cu_3O_{6+x}$ the oxidation state situation is $YBa_2Cu^{2+}_2Cu^{1+}_1O_6$ during synthesis at about 927 °C in air but becomes $YBa_2Cu^{2+}_2Cu^{3+}_1O_7$ on cooling in air. We have found that for $CuScO_{2+x}$ the $Cu^{2+}$ reduction to $Cu^{1+}$ can occur as low as 440 °C on heating in air [24]. We suggest that during synthesis of CCTO a slight reduction of Cu(II) to Cu(I) occurs and this is compensated by a slight substitution of Ti(IV) on the Cu site to maintain the average oxidation state on this site at two and achieve overall charge balance for the compound. On cooling, the Cu(I) would convert to Cu(II) with the liberated electrons going into the Ti 3*d* conduction band as indicated below, where $Ti^{3+}$ represents charge carriers in the Ti 3*d* conduction band.

$$\underset{\text{High temperature}}{Ca^{2+}(Cu^{2+}_{1-3x}Cu^{1+}_{2x}Ti^{4+}_{x})_3Ti^{4+}_{4}O_{12}} \Leftrightarrow \underset{\text{Low temperature}}{Ca^{2+}(Cu^{2+}_{1-x}Ti^{4+}_{x})_3(Ti^{4+}_{4-6x}Ti^{3+}_{6x})O_{12}} \tag{1}$$

An $x$ value of less than 0.0001 could account for the conductivity of the conducting regions. This deviation from ideal stoichiometry is far too small to detect by refining site occupancies from diffraction data. In the case of SCTO, there is much more Ti on the Cu site, but most of this is compensated by Sr vacancies; only a very small amount is compensated by Cu(I). Higher synthesis temperatures for CCTO give higher values of $x$ and materials that are more conducting with higher $\kappa$ and higher loss. The highest $\kappa$ is observed in CCTO crystals prepared from the melt because this is the highest possible synthesis temperature.

The activation energies that we find for the conducting phase in ceramic SCTO (Fig. 4.6) and CCTO crystal (Fig. 4.8) in the low temperature range are very similar to that found for ceramic CCTO from data measured over the temperature range of 104 ~ 400 K. In the high temperature range of our measurements on SCTO and CCTO, we find that the conductivity of the conducting phase decreases with increasing temperature. Such behavior is unexpected given the level of the conductivity and the activation energy found at lower temperatures. However, this is the behavior anticipated based on equation (1).

Behavior similar to that of CCTO has been reported for some $AFe_{1/2}B_{1/2}O_3$ perovskites where A = Ba, Sr, Ca and B = Nb, Ta, Sb [12]. Dielectric constants as large as 25,000 were obtained but these always decreased at some temperature on cooling, just as in the case of CCTO. The authors argue that this behavior is based on a barrier layer mechanism. They further show that the temperature of the drop in dielectric constant can be related to activation energy of the semiconducting grain boundary. These Fe containing phases are all treated at high temperatures (1470 ~ 1820 K), where some reduction of $Fe^{3+}$ to $Fe^{2+}$ occurs. This reduction would increase the conductivity of the grains. We would expect, however, that on cooling in air the $Fe^{2+}$ in the grain boundaries would oxidize to $Fe^{3+}$ but the $Fe^{2+}$ in the grains would remain largely unoxidized, leading to conducting grains and much less conducting grain boundaries.

Recently, it has been suggested that the high dielectric constant for CCTO is due to electrode polarization effects [14]. However, no explanation is offered as to why among many the titanates known with the CCTO structure, only CCTO itself shows a giant dielectric constant [8] regardless of how it is prepared and regardless of the electrode material used [25].

In summary, this study has identified a defect not previously established for the CCTO type structure, Ti on the Cu site. The Ti on Cu sites may indirectly provide the charge carriers for the Ti 3*d* band, which are necessary to form conducting regions. The difference between CCTO and other compounds with the CCTO structure is that the insulating barriers are within grains in CCTO whereas these barriers are only between grains for other compounds. Thus, the enhancement of $\kappa$ is modest, except in the case of CCTO. It is also possible that Ti on Cu sites has a role at the twin boundaries in CCTO, giving a modified coordination for Ti and an insulating barrier. Complex impedance spectroscopy on a CCTO crystal shows the same general behavior as found for ceramics of CCTO. This result further shows that the grain boundary model for the giant dielectric constant in CCTO does not apply. Our results are consistent with a model based on insulating barriers within a crystal and with the model based on electrode polarization.

## 4.5 References

1. D.E. Kotecki, J.D. Baniecki, H. Shen, R.B. Labibowitz, K.L. Saenger, J.J. Lian, T.M. Shaw, S.D. Athavale, C. Cabral, Jr.,P.R. Duncombe, M. Gutsche, G. Kunkel, Y.J. Park, Y.Y. Wang, R. Wise. *IBM J. Res. Dev.*, 43, 367 (1999)

2. H.C. Li, W. Si, A.D. West, X.X. Xi. *Appl. Phys. Lett.*, 73, 464 (1998)

3. G.A. Sumara, L.A. Boatner. *Phys. Rev. B*, 61, 3889 (2000)

4. M.A. Subramanian, D. Li, N. Duan, B.A. Reisner, A.W. Sleight. *J. Solid State Chem.*, 151, 323 (2000)

5. A.P. Ramirez, M.A. Subramanian, M. Gardel, G. Blumberg, D. Li, T. Vogt, S.M. Shapiro. *Solid State Commun.*, 115, 217 (2000)

6. Y. Lin, Y.B. Chen, T. Garret, S.W. Liu, C.L. Chen, L. Chen, R.P. Bontchev, A. Jacobson, J.C. Jiang, E.I. Meletis, J. Horwitz, H.D. Wu. *Appl. Phys. Lett.*, 81, 631 (2002)

7. C.C. Homes, T. Vogt, S.M. Shapiro, S. Wakimoto, A.P. Ramirez. *Science*, 293, 673 (2001)

8. M.A. Subramanian, A.W. Sleight. *Solid State Sci.*, 4, 347 (2002)

9. D.C. Sinclair, T.B. Adams, F.D. Morrison, A.R. West. *Appl. Phys. Lett.*, 80(12), 2153 (2002)

10. T.B. Adams, D.C. Sinclair, A.R. West. *Adv. Mater.*, 14, 1321 (2002)

11. A.R. West, T.B. Adams, F.D. Morrison, D.C. Sinclair. *J. Eur. Ceram. Soc.*, 24, 1439 (2004)

12. I.P. Raevski, S.A. Prosandeev, A.S. Bogatin, M.A. Malitskaya, L. Jastrabik. *J. Appl. Phys.*, 93, 4130 (2003)

13. C.C. Homes, T. Vogt, S.M. Shapiro, S. Wakimoto, M.A. Subramanian, A.P. Ramirez. *Phys. Rev. B*, 67, 092106 (2003)

14. P. Lunkenheimer, R. Fichtl, S.G. Ebbinghaus, A. Loidl. *Phys. Rev. B*, 70, 172102 (2004)

15. A. Tselev, C.M. Brooks, S.M. Anlage, H. Zheng, L. Salamanca-Riba, R. Ramesh, M.A. Subramanian. *Phys. Rev. B*, 70, 144101 (2004)

16. G. Chiodelli, V. Massarottie, D. Capsoni, M. Bini, C.B. Azzoni, M.C. Mozzati, P. Lupotto. *Solid State Commun.*, 132, 241 (2004)

17. A. Deschanvres, B. Raveau, F. Tollemer. *Bull. Soc. Chim. Fr.*, (11), 4077 (1967)

18. B.H. Toby. EXPGUI, a graphical user interface for GSAS, *J. Appl. Crystallogr.*, 34, 210 (2001)

19. A.C. Larson, R.B. Von Dreele. Generalized Structure Analysis System (GSAS). LANSCE, Los Alamos National Laboratory (2001)

20. Y. J. Kim, S. Wakimoto, S. M. Shapiro, P. M. Gehring, A. P. Ramirez. *Solid State Commun.*, 121, 11 (2002)

21. C. Hormillosa, S. Healy, T. Stephen, I.D. Brown. Bond Valence Calculator Version 2.0, 1993, original at http://ccp14.sims.nrc.ca/ccp/web-mirrors/i_d_brown/

22. B. Bochu, M.N. Deschizeaux, J.C. Joubert, A. Collomb, J Chenavas, M. Marezio. *J. Solid State Chem.*, 29, 291 (1979)

23. C. Lee, J. Yahia, J.L. Brebner. *Phys. Rev.B*, 3(8), 2525 (1971)

24. J. Li, A.F.T. Yokochi, A.W. Sleight. *Solid State Sci.*, 6, 831 (2004)

25. A.P. Ramirez, G, Lawes, A. Butko, M.A. Subramanian. con-mat/0209498 (unpublished)

# Chapter 5

# Magnetic Structure and Properties of the Ferromagnetic Semiconductor $La_2NiMnO_6$

## 5.1 Introduction

There is a long history concerning materials where a magnetic or electric field alters optical properties. These magnetooptic and electrooptic materials have been essential for the development of optical communication [1]. Spintronics, on the other hand, offers the potential for non-volatile memories, faster data processing speeds with less power usage, larger storage densities and additional functionalities, such as quantum computation, which are not possible with conventional semiconductor devices [2-4]. Present spintronic devices, e.g. GMR read heads and sensors, consist of ferromagnetic metallic alloys wherein spin-dependent scattering and tunneling effects have been successfully applied for commercial use. However, in order to fully achieve the potential of practical spintronic devices, the next generation of spintronic materials should be based on ferromagnetic semiconductors that exhibit magnetoresistance or magnetodielectric behavior at or close to room temperature.

The search for room-temperature ferromagnets that are semiconducting has been extremely difficult due to conflicting requirements in the crystal structure, chemical bonding and electronic properties of semiconductors and ferromagnetic materials [2,4]. Generally, ferromagnetic semiconductors and insulators only exhibit magnetic ordering at very low temperatures, such as EuS ($T_C$ = 16 K) [5], EuO ($T_C$ = 77 K) [6],

$CdCr_2Se_4$ (Tc= 130 K) [7], $EuGd_2S_4$ (Tc = 6 K) [8], $BiMnO_3$ (Tc= 100 K) [9], and $SeCuO_3$ (Tc= 25 K) [10], which precludes their use in devices.

Compounds are known that show large changes in electrical resistance during the application of a magnetic field, but this magnetoresistance behavior has been observed only below a temperature of 250 K. A small magnetoresistance effect has been reported for $Sr_2FeReO_6$ at room temperature [11]. A few compounds are also known that show changes in dielectric constant on application of a magnetic field, but such magnetodielectric behavior has only been observed below about 150 K [9,10].

We find an ordered double-perovskite $La_2Ni^{2+}Mn^{4+}O_6$, an apparent ferromagnetic semiconductor that has a Curie temperature very close to room temperature (Tc ~ 280 K), exhibits both magnetoresistance and magnetodielectric behaviors in the range where devices can be built with commercially available solid-state thermoelectric (Peltier) coolers.

Earlier studies [12-15] on $La_2NiMnO_6$ were focused on verification of Goodenough-Kanamori's (GK) rules [16], which predict that ferromagnetism results when an empty *d* orbital of one metal site overlaps a half-filled *d* orbital of another metal site in a 180° superexchange interaction (Fig. 1.5). These rules assume that the interaction of $e_g$ orbitals will dominate over interactions between $t_{2g}$ orbitals due to the greater cation-anion overlap in the case of the $e_g$ orbitals. Actually, the prediction of these rules was generally violated for double perovskites. For $A_2MReO_6$ (M = Fe, Mn, or Ni) [17], $A_2FeMoO_6$ [18], and $ALaMnRuO_6$ [19], the coupling between the two transition metal cations is, in fact, antiferromagetic despite the fact that the $e_g$

interaction should give ferromagnetism in all of these cases. Instead, it is the $t_{2g}$ interaction that dominates giving rise to ferrimagnetism in these compounds. Sleight rationalized this behavior on the basis of energies of the $t_{2g}$ levels for the two cations being much more similar than the energies of the $e_g$ levels [17]. This violation of the GK rules is a direct result of coupling a 3*d* cation with a 4*d* or 5*d* cation. The GK rules as originally set forth might still apply if the two different cations were 3*d* cations and this seems to be confirmed in the artificially structured $La_2FeCrO_6$ double perovskite [20]. It was also suggested that $La_2NiMnO_6$ is a ferromagnetic semiconductor with ordered $Ni^{2+}$ ($d^8$: $t_{2g}^6e_g^2$) and $Mn^{4+}$ ($d^3$: $t_{2g}^3e_g^0$) ions occupying the metal centers of corner-sharing $MO_6$ octahedra in a distorted perovskite structure [12,13]. While studies using $^{55}Mn$ NMR [21,22] and X-ray absorption spectroscopy [23] support the presence of $Ni^{2+}/Mn^{4+}$ ordering in this material, two neutron diffraction studies [24,25] disagreed with whether the oxidation states are $Ni^{2+}/Mn^{4+}$ or $Ni^{3+}/Mn^{3+}$. The structure of $La_2NiMnO_6$ is rhombohedral $R\overline{3}$ at high temperatures and transforms to monoclinic $P2_1/n$ at low temperatures. These two structures typically coexist over a significant temperature range including room temperature [15]. The coexistence of structures is presumably related to local inhomogeneities due to the fact that this phase exists over a range of Ni/Mn ratios and that there is a small amount of antisite disorder on the Ni/Mn sites.

In present work, large magnetic field-induced changes in the resistivity and dielectric properties of $La_2NiMnO_6$ are found at temperatures as high as 280 K. This is a much higher temperature than previously observed for such a coupling between the magnetic, electric and dielectric properties in a ferromagnetic semiconductor. The ferromagnetism of $La_2NiMnO_6$ was confirmed through neutron diffraction studies. $La_2NiMnO_6$ is a rare example of a multifunctional single-material platform with multiple functions where the spins, electric charge and dielectric properties can be tuned by magnetic and/or electric fields.

## 5.2 Experimental

Stoichiometric amounts of the metal nitrates were mixed and dissolved in water. The solution was evaporated and the residue was dried at 130 °C for one to two days. The resulting brown powder was ground, placed in a dense alumina crucible and heated in air at 600 °C for 30 min, further treated at 1100 °C for 16 hr, and cooled slowly to room temperature. The powder sample was then ground, pressed into a pellet, heated at 1100 °C for 16 hr, and cooled slowly to room temperature. The sample was reground, repelletized and reheated several times until no further changes in the diffraction pattern were observed.

Powder X-ray diffraction with Cu Kα radiation was employed to characterize the samples during synthesis. Neutron powder diffraction data were collected using the BT-1 32-counter high resolution diffractometer at the NIST Center for Neutron Research at the National Institute of Standards and Technology. A Cu(311) monochromator with a 90° take-off angle giving a wave length of 1.5402(2) Å and in-pile collimation of 15 min of arc were used. The beam was masked to 1.1 cm × 5.1 cm at the sample. Data were collected over a $2\theta$ range of 3 ~ 168° with a step size of 0.05° at 3.5, 200 and 295 K, respectively. The nuclear and magnetic structures were refined by Rietveld method using GSAS software suit [26-28].

The magnetic, transport, and dielectric properties of the samples were characterized using a Quantum Design Physical Property Measurement System (PPMS) in DuPont. The magnetization measurements were taken both as a function of temperature at fixed fields and as a function of applied magnetic field at fixed temperatures. Transport properties were measured from 320 to 200 K and 0.0 to 1.0 Tesla using the four-wire resistivity option of the PPMS. The samples for capacitance measurements were prepared by applying silver paint to opposite faces of the sintered pellet and attaching Cu wires to each face using silver epoxy. The capacitance was measured using an HP 4284 LCR meter. The dielectric measurements were performed over a frequency range of 10 kHz to 1 MHz with an excitation of 1 V from 100 to 320 K. The temperatures and applied magnetic fields were controlled by the PPMS during the capacitance measurements.

## 5.3 Results and Discussion

### *5.3.1 Nuclear and Magnetic Structures*

The neutron diffraction patterns of $La_2NiMnO_6$ at various temperatures are shown in Figure 5.1. On cooling the sample from room temperature to 3.5 K no new diffraction peaks were observed on magnetic ordering, as would be expected if the ordering were ferromagnetic. However, significant increases in intensity due to magnetic scattering were observed for some peaks, most notably the (200) peak based on the pseudocubic cell.

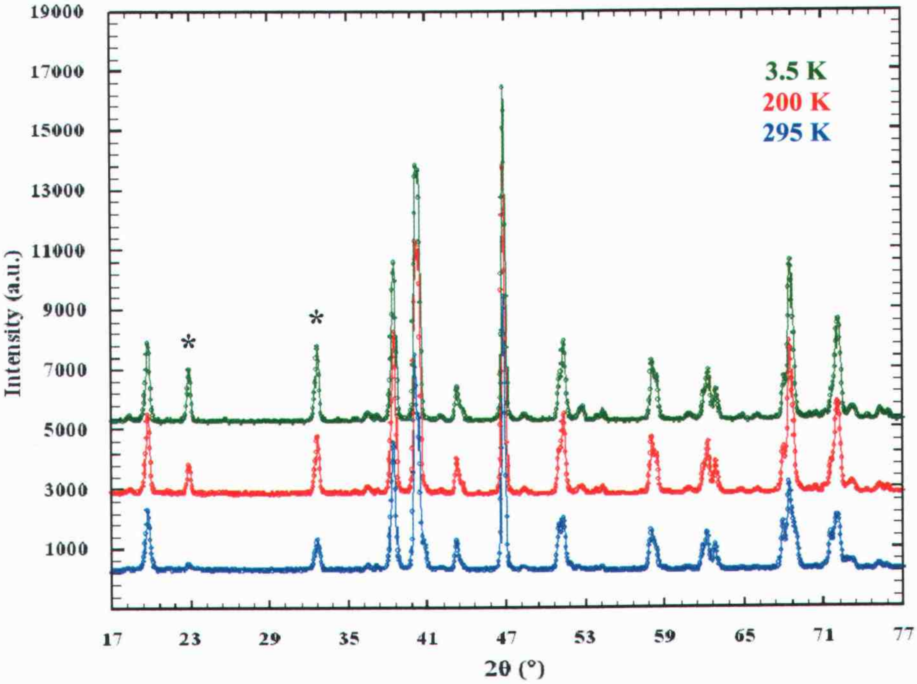

Figure 5.1 Temperature dependence of neutron diffraction data of $La_2NiMnO_6$. Asterisks denote the peaks with strong magnetic contribution.

The sample was a mixture of the $P2_1/n$ and $R\overline{3}$ structures at room temperature but was 100% $P2_1/n$ at 3.5 K. A very small amount of the structure $R\overline{3}$ could be detected at 200 K. The intensity due to the magnetic ordering could only be fitted assuming ferromagnetic order. Figure 5.2 shows the fit between observed and calculated intensities at 3.5 K.

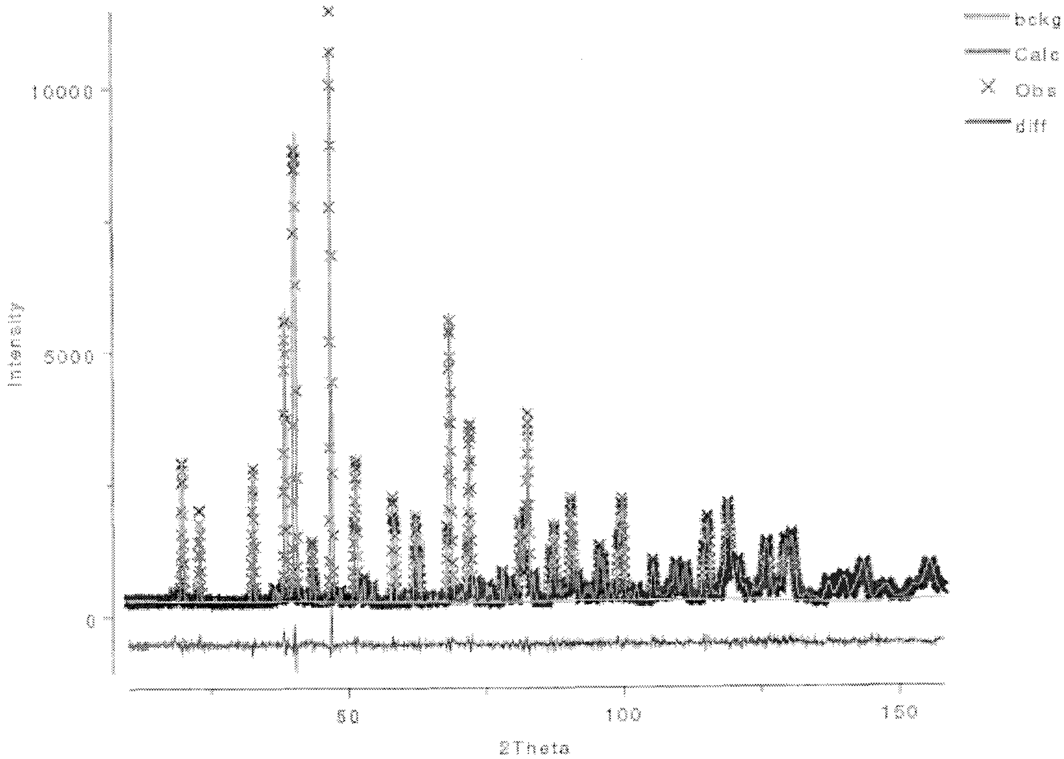

Figure 5.2 Observed (cross points) and calculated (solid line) neutron diffraction patterns of $La_2NiMnO_6$ at 3.5 K. The difference ($I_{obs}$ – $I_{calc}$) curve is shown at the bottom of the figure.

In space group $P2_1/n$ Ni is at 0,½,0 and Mn is at ½,0,0. In space group $R\bar{3}$ Ni is at 0,0,0 and Mn is at 0,0,½. The rhombohedral phase at room temperature was refined in $R\bar{3}$ H space group with unit cell dimensions $a$ = 5.5144 (2) Å, $c$ = 13.2472(5) Å, atomic positions of La at 0,0,0.2497(3), and O at 0.5523(7),–0.008(1),0.2483(3). The ratio of the $R\bar{3}$ to $P2_1/n$ structures in our sample at room temperature is about 1/3.

Rietveld refinement results of the structural analyses at various temperatures are summarized in Table 5.1. Bond distances and angles are given in Table 5.2. The nuclear and magnetic structures are shown in Figure 5.3.

Table 5.1 Rietveld refinement results of $La_2NiMnO_6$ neutron data at different temperatures. *Results reported in Ref. [25] are listed for comparison.

| **Parameters** | **3.5 K** | **200 K** | **295 K** | **295 K Bull *et al.**** |
|---|---|---|---|---|
| $R_p$(%) | 4.16 | 3.72 | 4.15 | 6.93 |
| $R_{wp}$(%) | 5.08 | 4.57 | 4.96 | 9.02 |
| $\chi^2$ | 1.772 | 1.492 | 1.455 | 15.02 |
| Space Group | P $2_1$/n | P $2_1$/n | P $2_1$/n | P $2_1$/n |
| $a$ (Å) | 5.50635(9) | 5.5105(1) | 5.5148(1) | 5.46704(3) |
| $b$ (Å) | 5.45574(9) | 5.45815(9) | 5.4616(1) | 5.51048(3) |
| $c$ (Å) | 7.7315(1) | 7.7350(1) | 7.7415(2) | 7.75124(4) |
| $\beta$ (°) | 89.909(1) | 89.890(1) | 89.899(3) | 90.1199 |
| $V$ (Å$^3$) | 232.263(7) | 232.646(7) | 233.173(9) | 233.513(5) |
| Phase% | 98.59(8) | 94.4 | 72.4 | 100% |
| La, $x$ | 0.0034(3) | 0.0026(3) | 0.0022(5) | 0.00214(1) |
| La, $y$ | 0.0214(2) | 0.0192(2) | 0.0174(3) | 0.052(1) |
| La, $z$ | 0.2497(3) | 0.2495(2) | 0.2493(4) | 0.26290(7) |
| La, $U_{iso}$ (Å$^2$) | 0.0040(2) | 0.0078(3) | 0.0103(4) | 0.0045(1) |
| Ni, $U_{iso}$ (Å$^2$) | 0.0019(5) | 0.0033(5) | 0.0067(8) | 0.0287(2) |
| μNi ($\mu_B$) | 1.9(3) | 1.4(4) | 0 | – |
| Mn, $U_{iso}$ (Å$^2$) | 0.0019(5) | 0.0033(5) | 0.005(2) | 0.0287(2) |
| μMn ($\mu_B$) | 3.0(2) | 2.1(3) | 0 | – |
| O1, $x$ | 0.2811(5) | 0.2790(5) | 0.2774(8) | 0.2506(1) |
| O1, $y$ | 0.2677(5) | 0.2652(5) | 0.2642(8) | 0.2347(1) |
| O1, $z$ | 0.0358(4) | 0.0353(5) | 0.0346(8) | 0.2315(1) |
| O1, $U_{iso}$ (Å$^2$) | 0.0070(8) | 0.0109(8) | 0.012(1) | 0.058(1) |
| O2, $x$ | 0.2632(4) | 0.2632(5) | 0.2617(8) | 0.2943(1) |
| O2, $y$ | 0.2779(5) | 0.2777(5) | 0.2781(9) | 0.2928(1) |
| O2, $z$ | 0.4668(4) | 0.4670(4) | 0.4664(8) | 0.4747(2) |
| O2, $U_{iso}$ (Å$^2$) | 0.0044(7) | 0.0072(7) | 0.012(1) | 0.0055(1) |
| O3, $x$ | 0.5659(3) | 0.5647(3) | 0.5664(5) | 0.5434(3) |
| O3, $y$ | -0.0066(3) | -0.0061(3) | -0.0055(5) | 0.0361(3) |
| O3, $z$ | 0.2439(4) | 0.2428(4) | 0.2438(6) | 0.2430(3) |
| O3, $U_{iso}$ (Å$^2$) | 0.0076(4) | 0.0108(5) | 0.0133(7) | 0.0077(1) |

Note: The fractional occupancies of Ni and Mn sites in the monoclinic phase were refined to be 0.824(8) and 0.968(7) at room temperature. The unequal ordering of the two sites may result from the presence of 1.4% NiO as the only impurity phase.

Table 5.2 Bond lengths (Å), bond angles (°) and bond valences (BV) for $La_2NiMnO_6$. *Values calculated from atomic coordinates given in Ref. [25] are also listed for comparison. Bond valences were calculated using the software in Ref. [29].

| | 3.5 K | 200 K | 295 K | 295 K Bull *et al.** |
|---|---|---|---|---|
| La–O1 | 2.621(4) | 2.619(4) | 2.622(5) | 2.210 |
| La–O1’ | 2.466(3) | 2.480(4) | 2.489(4) | 1.709 |
| La–O1” | 2.776(4) | 2.789(4) | 2.798(4) | 4.060 |
| La–O1’’’ | 3.134(3) | 3.112(4) | 3.096(5) | 4.367 |
| La–O2 | 2.613(4) | 2.625(4) | 2.628(5) | 2.646 |
| La–O2’ | 2.492(3) | 2.490(3) | 2.487(6) | 2.584 |
| La–O2” | 2.782(4) | 2.785(4) | 2.796(6) | 2.645 |
| La–O2’’’ | 3.101(3) | 3.094(3) | 3.091(4) | 3.223 |
| La–O3 | 2.414(2) | 2.418(2) | 2.407(6) | 2.514 |
| La–O3’ | 2.604(2) | 2.618(2) | 2.634(6) | 2.965 |
| La–O3” | 2.906(2) | 2.892(2) | 2.881(3) | 2.680 |
| La–O3’’’ | 3.101(2) | 3.101(2) | 3.114(4) | 2.854 |
| Mn–O1, ×2 | 1.913(2) | 1.911(3) | 1.913(3) | 2.600 |
| Mn–O2, ×2 | 1.906(2) | 1.908(2) | 1.902(4) | 1.983 |
| Mn–O3, ×2 | 1.921(3) | 1.913(3) | 1.923(5) | 1.908 |
| Ni–O1, ×2 | 2.020(2) | 2.021(2) | 2.018(4) | 2.688 |
| Ni–O2, ×2 | 2.017(2) | 2.017(2) | 2.025(4) | 1.976 |
| Ni–O3, ×2 | 2.013(3) | 2.021(3) | 2.016(5) | 2.016 |
| Mn–O1–Ni | 160.4(2) | 161.1(2) | 161.7(3) | 94.4 |
| Mn–O2–Ni | 162.3(2) | 162.4(2) | 162.3(3) | 157.2 |
| Mn–O3–Ni | 158.61(9) | 159.0(1) | 158.5(2) | 161.8 |
| O1–Mn–O2 | 90.7(2) | 91.2(2) | 91.4(3) | 78.0 |
| O1–Mn–O3 | 90.4(1) | 90.4(1) | 90.2(2) | 48.0 |
| O2–Mn–O3 | 90.0(1) | 90.0(1) | 90.1(2) | 86.5 |
| O1–Ni–O2 | 92.4(2) | 91.9(2) | 91.8(3) | 84.9 |
| O1–Ni–O3 | 90.5(1) | 90.6(1) | 90.2(3) | 57.0 |
| O2–Ni–O3 | 90.2(1) | 90.0(1) | 90.1(2) | 83.7 |
| BV(La) | 3.066 | 3.031 | 3.015 | 6.277 |
| BV(Mn) | 3.89 | 3.918 | 3.896 | 2.592 |
| BV(Ni) | 2.25 | 2.234 | 2.234 | 1.712 |

Note: Some O–Ni–O and O–Mn–O angles are fixed by symmetry to be 180°. Both $NiO_6$ and $MnO_6$ octahedra show only very small distortions from ideal values. The bond valences of Mn and Ni were calculated to be 2.64, 4.49 respectively if assuming the oxidation states of both Ni and Mn ions to be +3 as suggested by Ref. [25].

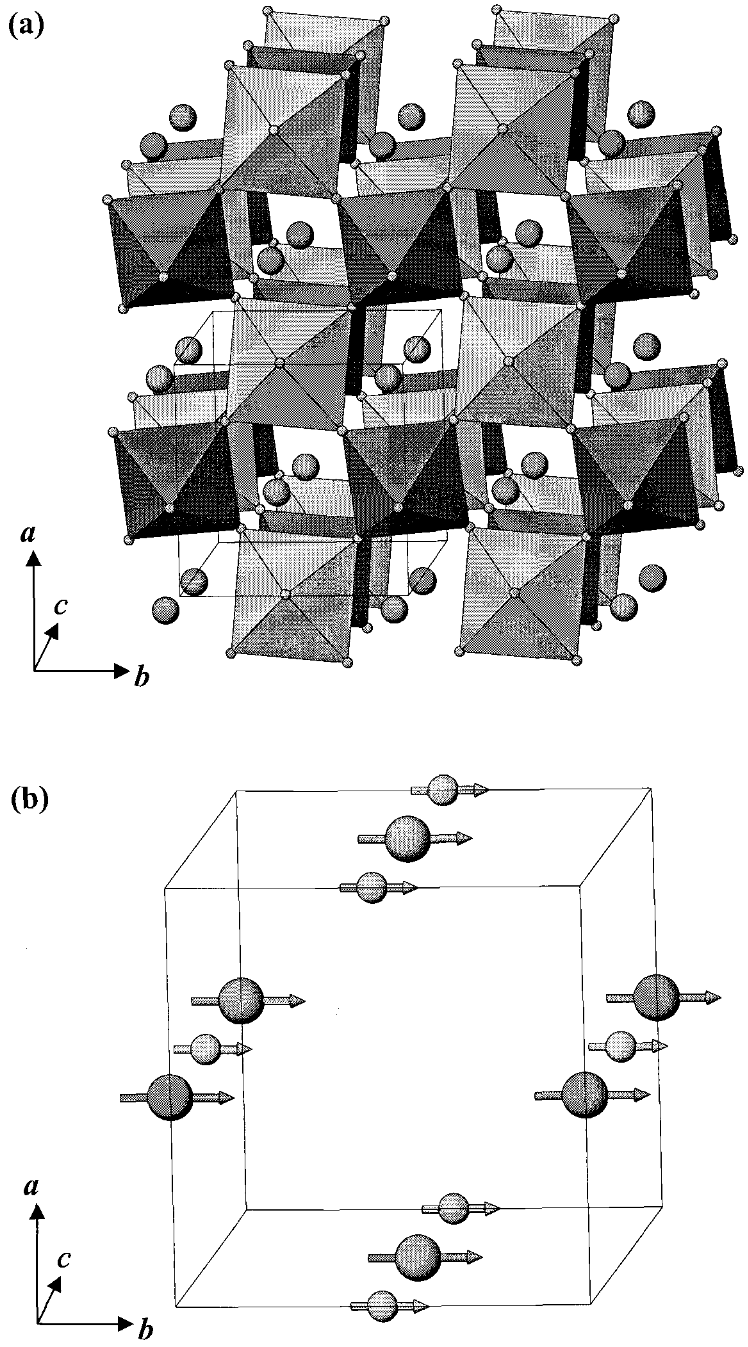

Figure 5.3 Nuclear (a) and magnetic (b) structures of $La_2NiMnO_6$. (a) Dark polyhedra are $MnO_6$, light polyhedra are $NiO_6$, large spheres are $La^{3+}$, and small spheres are $O^{2-}$; (b) Large spheres are $Mn^{4+}$, small spheres are $Ni^{2+}$, magnetic moments aligned along the *b* axis.

A least-squares refinement of the magnetic moments gave a moment of 3.0(2) $\mu_B$ on the Mn site and 1.9(3) $\mu_B$ on the Ni site, which are in good agreement with the values of 3.0 and 2.0 as expected for $Mn^{4+}$ ($d^3$, $t_{2g}{}^3e_g{}^0$) and $Ni^{2+}$ ($d^8$, $t_{2g}{}^6e_g{}^2$), respectively. The spins are parallel to the *b* axis (Fig. 5.3 (b)). Refinement of atomic positions gave the three Ni–O–Mn angles in a range of 159 ~ 162°. Despite this deviation from 180° the expectations of the GK rules for a 180° interaction are obeyed.

There have been two previous refinements of the $La_2NiMnO_6$ structure based on neutron diffraction data obtained at room temperature [24,25]. The first reports using the $P2_1/n$ space group but gives neither cell dimensions nor positional parameters. The results of the second paper are compared with our results in Tables 1 and 2. Our agreement factors are significantly better, and there are significant differences between the values of the refined parameters in the two studies. One notable discrepancy is that we find *a* to be larger than *b*, but Bull *et al.* [25] report *b* larger than *a*. This is not a minor discrepancy because the symmetry in space group $P2_1/n$ is such that these two axes cannot be interchanged, and we find it impossible to fit our data properly with *b* larger than *a*. In the same paper, Bull *et al.* report *a* larger than *b* for $La_2CoMnO_6$. There are also significant discrepancies in the refined positional parameters, the most notably being the *z* parameter for O1. Another problem with the paper of Bull *et al.* is that the positional parameters reported are inconsistent with the interatomic distances given. The main problem again is with the *z* parameter of O1. We conclude that this parameter should have been given as 0.03 instead of 0.23. However, this does not completely solve the problem. The Bull *et al.* paper gives one of the Mn–O distances as 1.88 Å, and one of the Ni–O distances as 2.011 Å, instead of 2.600 and 2.688 Å as given in Table 2, which are calculated from the reported atomic coordinates. Either set of data gives highly distorted octahedra and unreasonable bond valences for both Mn and Ni. Based on the distorted $MnO_6$ octahedron, they suggest that Mn is in fact $Mn^{3+}$ due to the Jahn-Teller distortion of $Mn^{3+}$ ion with an electronic configuration of $t_g^3e_g^1$. We find very regular octahedra with distances that support the $Ni^{2+}/Mn^{4+}$ states.

### 5.3.2 *Magnetotransport Properties*

The magnetic susceptibility $\chi(T)$ of $La_2NiMnO_6$ in an applied field of 1 Tesla is shown in Figure 5.4. The $\chi(T)$ shows a magnetic transition at ~ 280 K indicating the onset of long-range ferromagnetic (FM) ordering and agrees well with the literature. The inverse susceptibility $1/\chi$ plot is also shown in the figure as an inset. The high temperature data, from 300 to 320 K, were fitted to the Curie-Weiss law, from which the Curie (C) and Weiss ($\theta$) constants were determined as C = 3.84 emu·K/mol f.u. and $\theta = +\ 274$ K. The large positive $\theta$ value indicates strong FM interactions between the $Ni^{2+}$ and $Mn^{4+}$ spins. The effective paramagnetic moment ($\mu_{eff}$) was calculated to be 5.5 $\mu_B$, which is less than the simple prediction of a spin system with non-interacting electron spins ($\mu_{calc} = 5.92\ \mu_B$). The field dependence of the magnetization of $La_2NiMnO_6$ is also shown in Fig. 5.4 as an inset. The *M* vs *H* plot shows a small magnetic hysteresis ($H_c \approx 300$ Oe) at 5 K.

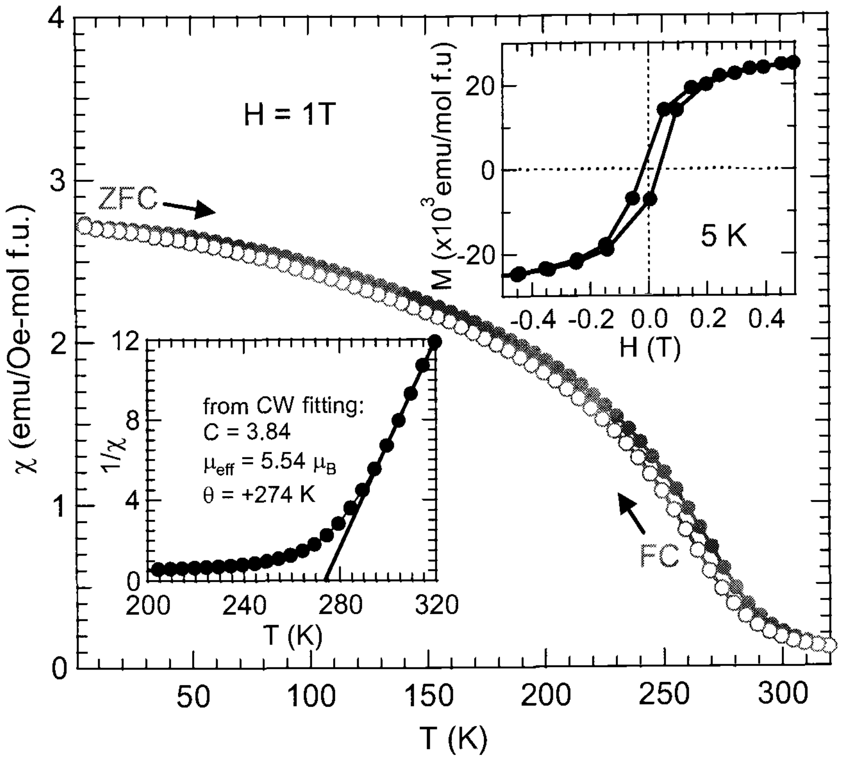

Figure 5.4 Magnetic susceptibility $\chi(T)$ at 1 Tesla on zero-field (ZFC) and field cooling (FC). Insets show a plot of $1/\chi$ vs $T$ fitted to the Curie Weiss law (lower left) and field-dependent magnetization data at 5 K (upper right) (courtesy of Dr. M.A. Subramanian and Dr. N.S. Rogado).

The field dependence of the magnetization at different temperatures is shown in Figure 5.5. The highest saturated magnetization at 5 K under an applied field of 5 Tesla is ~ 27,700 emu/mol (equivalent to 4.96 $\mu_B$/f.u.), which is very close to the full magnetization of 5.0 expected for a ferromagnetic system with spin –5/2. The magnetization decreases gradually as the temperature increases. At 200 K, the material still exhibits 70% of its full moment. Ferromagnetic interactions are observed to persist even at 300 K.

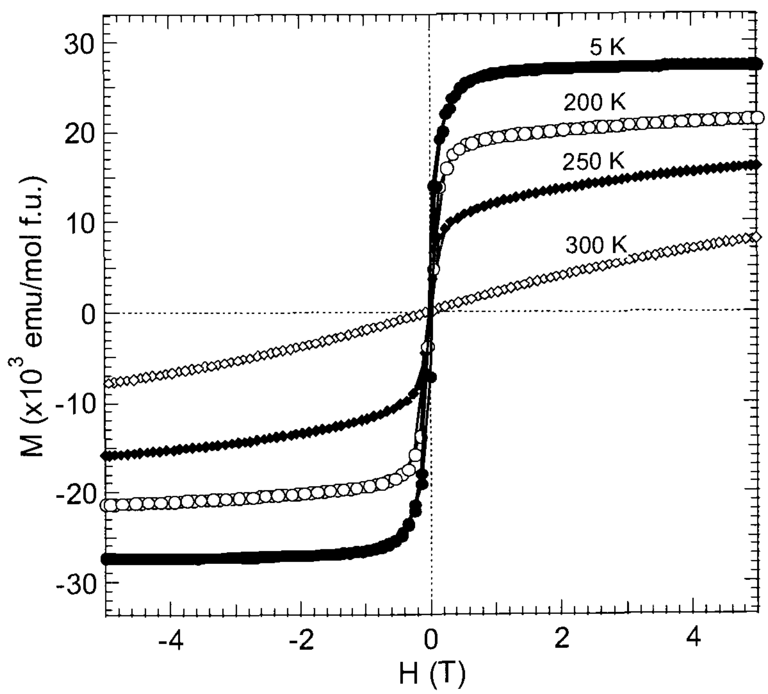

Figure 5.5 Magnetization data of $La_2NiMnO_6$ as a function of applied field at different temperatures (courtesy of Dr. M.A. Subramanian and Dr. N.S. Rogado).

The resistivity of a sintered $La_2NiMnO_6$ pellet as a function of temperature is shown in Figure 5.6 (a). The field-dependent resistivity of the same sample is shown in Figure 5.6 (b). $La_2NiMnO_6$ is found to be semiconducting with a high resistivity, ~ $10^2$ Ω·cm, at room temperature. At 200 K, this material shows a 2.5% decrease in resistance in a 1 Tesla field. This behavior is likely a tunneling type magnetoresistance as has been proposed for another ordered-double perovskite, $Sr_2FeMoO_6$ [11].

Figure 5.7 shows the temperature dependence of the dielectric constant ε of $La_2NiMnO_6$ at 10 kHz and at selected magnetic fields. At or above room temperature, the dielectric constant of $La_2NiMnO_6$ is approximately 600. At zero field, a gradual decrease in the dielectric constant is observed with decreasing temperature until it reaches 220 K, below which ε decreases steeply. When a magnetic field is applied, this transition moves to higher temperatures, 280 K for a 0.1 Tesla field and 295 K for a 1 Tesla field. This shift results in a large change in the dielectric response of $La_2NiMnO_6$ in the vicinity of the transition temperature (270 ~ 280 K) in the presence of a magnetic field (inset).

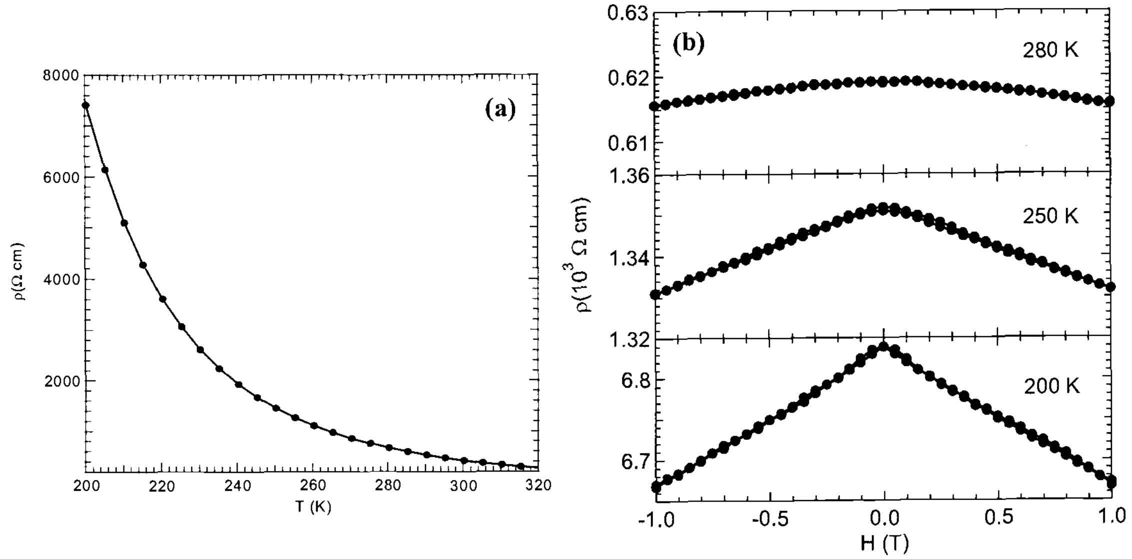

Figure 5.6 Temperature-dependent resistivity in zero magnetic field (a) and field dependence of the electrical resistivity at different temperatures (b) for a sintered pelletized $La_2NiMnO_6$ sample (courtesy of Dr. M.A. Subramanian and Dr. N.S. Rogado).

The appearance of both magnetoresistance and magnetocapacitance effects in the ferromagnetic semiconducting compound, $La_2NiMnO_6$, indicates coupling between the magnetic, electronic and dielectric properties, which may be controlled by the application of magnetic and/or electric fields. The fact this behavior is observed very close to room temperature provides optimism for practical spintronic applications.

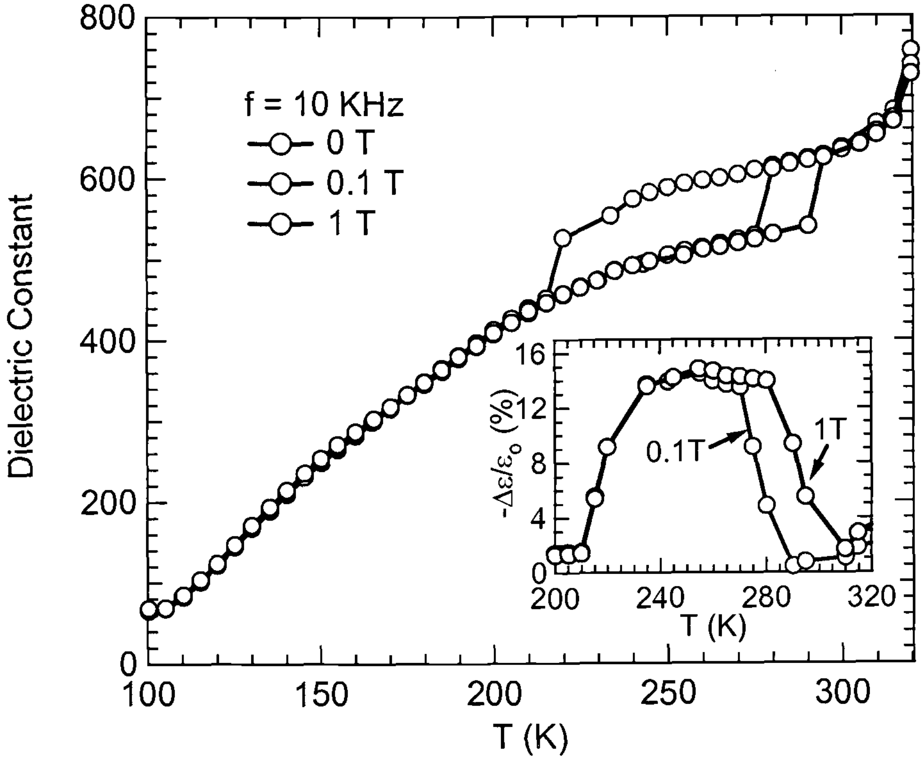

Figure 5.7 Temperature dependence of the dielectric constant at 10 kHz for 0, 0.1, and 1 Tesla. Inset shows the magnetocapacitance effect with 0.1 and 1 T applied fields (courtesy of Dr. M.A. Subramanian and Dr. N.S. Rogado).

## 5.4 References

1. S. Miyazawa. *Opto-Electronics Rev.*, 11, 77-84 (2003)
2. S.A. Wolf, D.D. Awschalom, R.A. Buhrman, J.M. Daughton, S. von Molnar, M.L. Roukes, A.Y. Chtchelkanova, D.M. Treger. *Science*, 294, 1489 (2001)
3. G.A. Prinz. *Science*, 282, 1660 (1998)
4. D.D. Awschalom, M.E. Flatte, N. Samarth. *Sci. Am.*, 286, 67 (2002)
5. S. Van Houten. *Phys. Lett.*, 2, 215 (1962)
6. B.T. Matthias, R.M. Bozorth, J.H. Van Vleck. *Phys. Rev. Lett.*, 7, 160 (1961)
7. P.K. Baltzer, H.W. Lehmann, M. Robbins. *Phys. Rev. Lett.*, 15, 493 (1965)
8. F. Hulliger, O. Vogt. *Phys. Lett.*, 17(3), 238-9 (1965)
9. T. Kimura, S. Kawamoto, I. Yamada, M. Azuma, M. Takano, Y. Tokura. *Phys. Rev. B*, 67, 180401 (2003)
10. M.A. Subramanian, A.P. Ramirez, W.J. Marshall. *Phys. Rev. Lett.*, 82, 1558-1561 (1999); G. Lawes, A.P. Ramirez, C.M. Varma, M.A. Subramanian. *Phys. Rev. Lett.*, 91, 257208/1-4 (2003)
11. K.I. Kobayashi *et al. Nature*, 395, 677-680 (1998)
12. A. Wold, R.J. Arnott, J.B. Goodenough. *J. Appl. Phys.*, 29, 387 (1958)
13. J.B. Goodenough, A. Wold, R.J. Arnott, N. Menyuk. *Phys. Rev.*, 124, 373 (1961)
14. N.Y. Vasanthacharya, P. Ganguly, J.B. Goodenough, C.N.R. Rao. *J. Phys. C: Solid State Phys.*, 17, 2745 (1984)
15. R.I. Dass, J.Q. Yan, J.B. Goodenough. *Phys. Rev. B*, 68, 064415/1-064415/12 (2003)
16. J.B. Goodenough. *Phys. Rev.*, 100, 564-573 (1955); J. Kanamori. *J. Phys. Chem. Solids*, 10, 87-98 (1959)

17. A.W. Sleight, J.F. Weiher. *J. Phys. Chem. Solids*, 33, 679-687 (1972)

18. F. Patterson, C. Moeller, R. Ward. *Inorg. Chem.*, 2, 196 (1963)

19. K. Ramesha., V. Thangadurai, D. Sutar, S.V. Subramanyam, G.N. Subbanna, J. Gopalakrishnan. *Mater. Res. Bull.* 35, 559-565 (2000)

20. K. Ueda, H. Tabata, T. Kawai. *Science*, 280, 1064 (1998)

21. K. Asai, H. Sekizawa, S. Iida. *J. Phys. Soc. Jpn.*, 47, 1054 (1979)

22. M. Sonobe, K. Asai. *J. Phys. Soc. Jpn.*, 61, 4193 (1992)

23. M.C. Sanchez, J. Garcia, J. Blasco, G. Subias, J. Perez-Cacho. *Phys. Rev. B*, 65, 144409 (2002)

24. J. Blasco, M.C. Sanchez, J. Perez-Cacho, J. Garcia, G. Subias, J. Campo. *J. Phys. Chem. Solids*, 63, 781 (2002)

25. C.L. Bull, D. Gleeson, K.S. Knight. *J. Phys.: Condens. Matter*, 15, 4927 (2003)

26. B.H. Toby. EXPGUI, a graphical user interface for GSAS, *J. Appl. Crystallogr.*, 34, 210 (2001)

27. A.C. Larson, R.B. Von Dreele. Generalized Structure Analysis System (GSAS). LANSCE, Los Alamos National Laboratory (2001)

28. J. Cui, B.H. Toby, and Q. Huang. Magnetic Structure Refinement Using GSAS and EXPGUI. Gaithersburg, NIST Center for Neutron Research at the National Institue of Standards and Technology, 2004

29. C. Hormillosa, S. Healy, T. Stephen, I.D. Brown. Bond Valence Calculator, Version 2.00, 1993

# Chapter 6

# Trends in Negative Thermal Expansion Behavior for $AMO_2$ Compounds with the Delafossite Structure

## 6.1 Introduction

Strong negative thermal expansion (NTE) has now been established for many oxides with network structures having oxygen in two-fold coordination [1]. The NTE behavior in these cases is caused by the thermal motion of oxygen transverse to the M–O–M linkages. The exceptionally large NTE behavior found for $Zn(CN)_2$ is presumably also related to transverse thermal motion of C and N in the Zn–C–N–Zn linkage [2]. There is apparently just one known example of NTE behavior in an oxide where the oxygen coordination is three. This is $Zn_2SiO_4$ where all oxygen atoms are three coordinated in an arrangement very close to planar [3]. This NTE behavior is presumably caused by oxygen thermal motion perpendicular to the plane of the three cations to which oxygen is bonded. This mechanism for NTE would then be analogous to the situation in graphite. Carbon is three coordinated, and thermal motion perpendicular to the strong bonds in the sheets results in NTE behavior for the *a* and *b* cell edges. The distance between the sheets increases with increasing temperature, leading to strong positive thermal expansion along the *c* axis.

The thermal expansion behavior of several compounds isostructural with $Zn_2SiO_4$ has been studied; some show low thermal expansion, but none show any NTE behavior [4]. NTE behavior is also known in $PbTiO_3$, where the behavior is driven by the polyhedra becoming more regular with increasing temperature [1]. In nonoxides, NTE behavior can be caused by a change in electronic configuration with temperature, as in $Sm_{0.75}Y_{0.25}S$ [5], or by an internal redox mechanism as in YbGaGe [6].

NTE behavior can also occur in oxides where the cation is in two-fold coordination. This coordination is rare, and the only two cations that are known to support two-fold coordination and NTE behavior are Cu(I) and Ag(I). The same cubic structure is found for $Cu_2O$ and $Ag_2O$, and both compounds exhibit negative thermal expansion behavior [7]. Compounds with the $AMO_2$ formula having the delafossite structure (Fig. 6.1) have two-fold coordination for the A cation, which can be Cu(I) or Ag(I), and M is a trivalent cation in octahedral coordination, which can range in size from Al to La. Depending on the stacking along the *c* direction, 2H or 3R forms are observed for this type of structure. Several years ago, $CuMO_2$ phases were investigated as a possible route to superconductors. More recently, $CuMO_2$ type phases have been of interest as p-type transparent conductors. We found 2H $CuScO_2$ shows NTE behavior for the *c* cell edge below room temperature [8].

The purpose of this work is to compare the thermal expansion in the delafossite structure as the M and A cations are varied. Compounds investigated are $CuAlO_2$, $CuInO_2$, $CuLaO_2$, 2H $CuScO_2$, 3R $CuScO_2$, and $AgInO_2$. Besides our study of 2H $CuScO_2$, there is only one publication on structure variation with temperature of a compound with delafossite structure. This is for $CuAlO_2$, where the temperature range was 295 K to 1200 K [9]. No NTE behavior was observed over that temperature range.

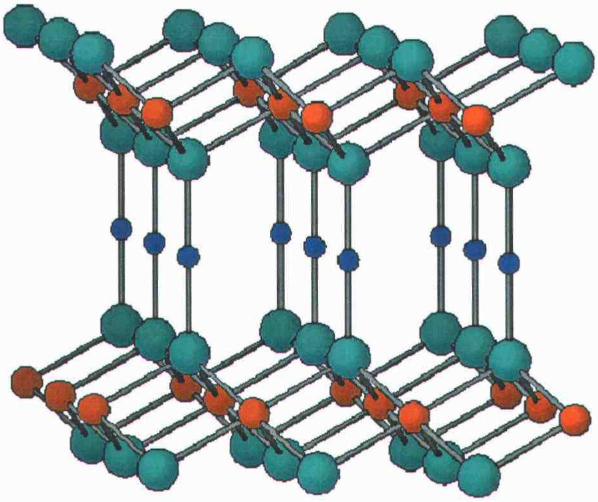

Figure 6.1 A fragment of the 3R $AMO_2$ delafossite structure with the *c* axis vertical. Small atoms are A (A = Ag, Cu), medium atoms are M (M = La, In, Sc, Al), and large atoms are O. The 3R and 2H forms differ by stacking along the *c* axis: ABC stacking for 3R and ABAB for 2H.

## 6.2 Experimental

### *6.2.1 Synthesis*

Reagents used were $Cu_2O$ (Cerac, 99%), $La_2O_3$ (Aldrich, 99.99%), $Al_2O_3$ (Aldrich, 99.8%), $Sc_2O_3$ (Stanford Materials, 99.99%), CuCl (Alfa Aesar, 99%), $Li_2CO_3$ (Sigma, 99.6%), MgO (Aldrich, 99%), $In_2O_3$ (Cerac, 99.99%), $Na_2CO_3$ (Aldrich, 99.99%), $AgNO_3$ (Spectrum, 99.0%), KOH (Mallinckrodt, AR) and PbO (Cerac, 99.99%). Samples of CuCl obtained from several manufacturers were all badly contaminated with Cu(II) oxyhydroxide. This impurity was removed by washing with dilute hydrochloric acid.

The $CuLaO_2$ sample was synthesized by the solid state reaction of $Cu_2O$ and $La_2O_3$ following the method of Cava *et al.* [10]. Freshly calcined $La_2O_3$ (1000 °C, air, overnight) was mixed with $Cu_2O$ in a stoichiometric ratio, ground and pressed into pellets. These pellets were buried in powders of the same composition in an alumina crucible, covered, and heated in an argon flow at 1000 °C for 24 hr.

The $CuAlO_2$ sample was prepared by a solid state reaction in air. Equimolar amounts of $Cu_2O$ and $Al_2O_3$ were mixed by grinding in an agate mortar and pressed into pellets. These pellets were heated at 1100 °C for 24 hr and quench cooled in air.

The $CuInO_2$ sample was prepared by an ion exchange reaction similar to that of 3R $CuScO_2$ [11]. Equimolar amounts of $Na_2CO_3$ and $In_2O_3$ were mixed and heated at 1000 °C in air for 12 hr. The $NaInO_2$ powder obtained was mixed with purified CuCl in a molar ratio of 1:1.3, and the mixture was placed in a Cu crucible inside a stainless steel vessel with Ar flowing through. The vessel was then heated to 550 °C for 6 hr. The reaction product was washed with 2 M aqueous $NH_3$ to remove NaCl and excess CuCl. The final product was dried in air.

The polycrystalline sample of $AgInO_2$ was synthesized by a hydrothermal reaction. Stoichiometric amounts of $AgNO_3$ and $In_2O_3$ in 5 M KOH aqueous solution were sealed in a PTFE autoclave within a Parr bomb. The reaction was carried out at 250 °C for 7 days. The resulting orange highly crystalline $AgInO_2$ was washed with distilled water to remove the adsorbed $KOH/KNO_3$ solution.

Our synthesis methods for 2H and 3R $CuScO_2$ samples have previously been reported [8,11]. To prepare the pure 2H sample free of the 3R form 5% Mg is substituted for Sc. Single crystals of 2H $CuScO_2$ were grown in a PbO flux in a Cu crucible under Ar using a PbO : $CuScO_2$ molar ratio of 2 : 1. The sample was heated at 50 °C/hr to 950 °C. The cooling rate from this temperature was 2 °C/hr until 820 °C and then 30 °C/hr to room temperature.

### *6.2.2 X-ray and Neutron Diffraction*

Single-crystal X-ray diffraction data of 2H $CuScO_2$ were obtained at room temperature on a Rigaku AFC6R diffractometer with monochromatic Mo Kα radiation ($\lambda = 0.71069$ Å). No decay in intensity was noted during data collection. The observed intensities were corrected for Lorentz polarization and absorption. Data reduction was carried out using a local program, capable of creating a data file containing the crystal dependent direction cosines of the diffracted and reverse incident beam, for purposes of correction of absorption anisotropy problems. Correction for the effects of absorption anisotropy was carried out using the program SORTAV [12] in the software collection WinGX v1.64.02 [13]. Structure solution was carried out using Patterson map interpretation as programmed in SHELXS-90, and refined using full-matrix least-squares refinement on $F^2$ using the program SHELXL-97 [14].

Neutron powder diffraction data were collected using the BT-1 32-counter high resolution diffractometer at the NIST Center for Neutron Research at the National Institute of Standards and Technology. A Cu(311) monochromator with a 90° take-off angle giving a wave length of 1.5402(2) Å and in-pile collimation of 15 min of arc were used. The beam was masked to 1.1 cm × 5.1 cm at the sample. Data were collected over a $2\theta$ range of 3 ~ 168° with a step size of 0.05° and a temperature range of 30 ~ 600 K. The data of 2H $CuScO_2$ were collected from 11 to 1206 K under the same condition and further collected at 3.6 K using a Ge(733) monochromator with a 120° take-off angle giving a wavelength of 1.1976(2) Å. Additional data were also collected for $CuLaO_2$ at very low temperatures down to 4 K.

Samples of 2H and 3R $CuScO_2$ and $AgInO_2$ were sealed in vanadium containers 15.6 mm in diameter and 50 mm high, and samples of $CuLaO_2$, $CuAlO_2$ and $CuInO_2$ were sealed in vanadium containers 10.8 mm in diameter and 50 mm high. The measurement time for each temperature was 2 to 3 hr. A vacuum furnace was used for measurements above room temperature, and a closed-cycle He refrigerator was used for measurements below room temperature. The data of $CuScO_2$, $CuInO_2$ and $AgInO_2$ were corrected for absorption [15]. All the data were fit by the Rietveld method using GSAS software [16,17].

## 6.3 Results

### *6.3.1 Single Crystal and Polycrystalline 2H $CuScO_2$*

The structure for 2H $CuScO_2$ is described in space group $P6_3/mmc$ with Sc at 0,0,0, Cu at 1/3,2/3,1/4, and oxygen at 1/3,2/3,$z$, where $z$ is approximately 0.09. Results of the single crystal refinement are listed in Table 6.1.

Table 6.1 Crystal data and structure refinement for $CuScO_2$ single crystal.

| | |
|---|---|
| Space group | $P6_3/mmc$ |
| Formula | $CuScO_2$ |
| Formula weight | 140.50 |
| Temperature | 290(2) K |
| Wavelength | 0.710693 Å |
| Unit cell dimensions | $a = 3.215(1)$ Å<br>$c = 11.386(1)$ Å |
| Volume | 101.89(5) $Å^3$ |
| $Z$ | 2 |
| Density (calculated) | 4.579 $Mg/m^3$ |
| Absorption coefficient | 13.357 $mm^{-1}$ |
| F(000) | 132 |
| Crystal size | 0.10 mm × 0.10 mm × 0.10 mm |
| $\theta$ range for data collection | 3.58 to 49.99° |
| Index ranges | $-6 \leq h \leq 6$, $-6 \leq k \leq 6$, $-1 \leq l \leq 24$ |
| Reflections collected | 2112 |
| Independent reflections | 246 [$R$(int) = 0.0237] |
| Completeness to $\theta = 49.99°$ | 91.9 % |
| Max. and min. transmission | 0.3622 and 0.7758 |
| Refinement method | Full-matrix least-squares on $F^2$ |
| Data / restraints / parameters | 246 / 0 / 9 |
| Goodness-of-fit on $F^2$ | 1.255 |
| Final $R$ indices [$I > 2\sigma(I)$] | $R = 0.0187$, $R_w = 0.0351$ |
| $R$ indices (all data) | $R = 0.0235$, $R_w = 0.0358$ |
| Extinction coefficient | 0.8(3) |
| Largest diff. peak and hole | 0.955 and −1.999 e/$Å^3$ |
| $z$(O) | 0.08928(7) |

The temperature dependence of neutron diffraction patterns of 2H $CuScO_2$ powder sample within certain $2\theta$ ranges is shown in Figure 6.2. From back to the front, temperature increases from 11 to 1206 K. Miller indices *hkl* are marked for the four different diffraction peaks. The shift of these peaks to the low angle region with increasing temperature is very obvious at high temperature range, indicating a normal positive thermal expansion; the most shifted peak is 110 and the least shifted is 004, indicating a much larger thermal expansion along cell edge *a* than along *c*. Moreover, the 004 peak seems to slightly shift to the high angle region with increasing temperature at low temperature range, implying a somewhat small negative thermal expansion along the *c* axis.

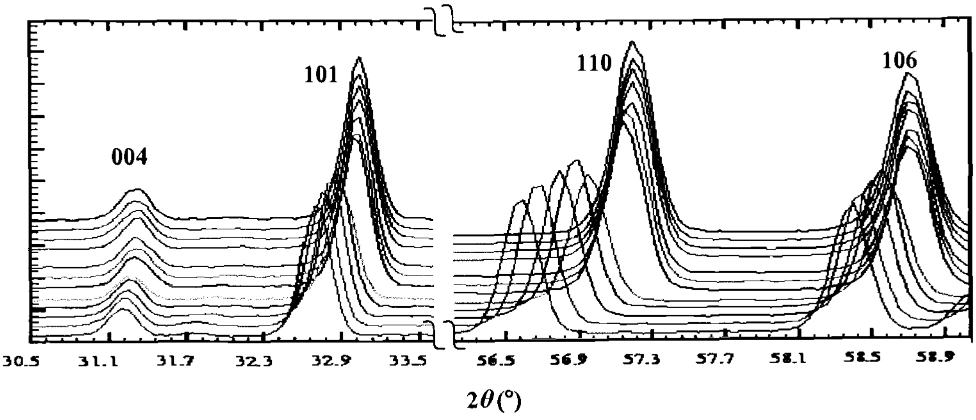

Figure 6.2 Temperature dependence of neutron powder diffraction data of 2H $CuScO_2$.

Rietveld refinements of the neutron powder diffraction data at various temperatures gave $R$ in the range 4.4 to 5.4, $R_w$ 5.5 to 6.0, and $\chi^2$ 1.4 to 1.8. LeBail fits to the same data gave fit parameters about 10% better. A typical plot of the observed and calculated intensities is given in Figure 6.3.

In Figure 6.4(a) the unit cell edges and volume are plotted vs. temperature. The behavior exhibited by the *a* cell edge can be considered typical thermal expansion behavior. For the *c* cell edge, negative thermal expansion occurs from 11 to 300 K. Above 300 K normal positive thermal expansion is observed. The combined effect of negative thermal expansion for *c* and positive thermal expansion for *a* yields a negative volume expansion only below 50 K. The cause of the negative thermal expansion of the *c* cell edge is apparent in Figure 6.4(b). There is a strong negative thermal expansion of the apparent Cu–O bond length from 11 to 300 K. This is for an O–Cu–O linkage parallel to the *c* axis. Thermal expansion of the Sc–O bond vs. temperature can be considered normal, and this is directly related to the thermal expansion of the *a* cell edge.

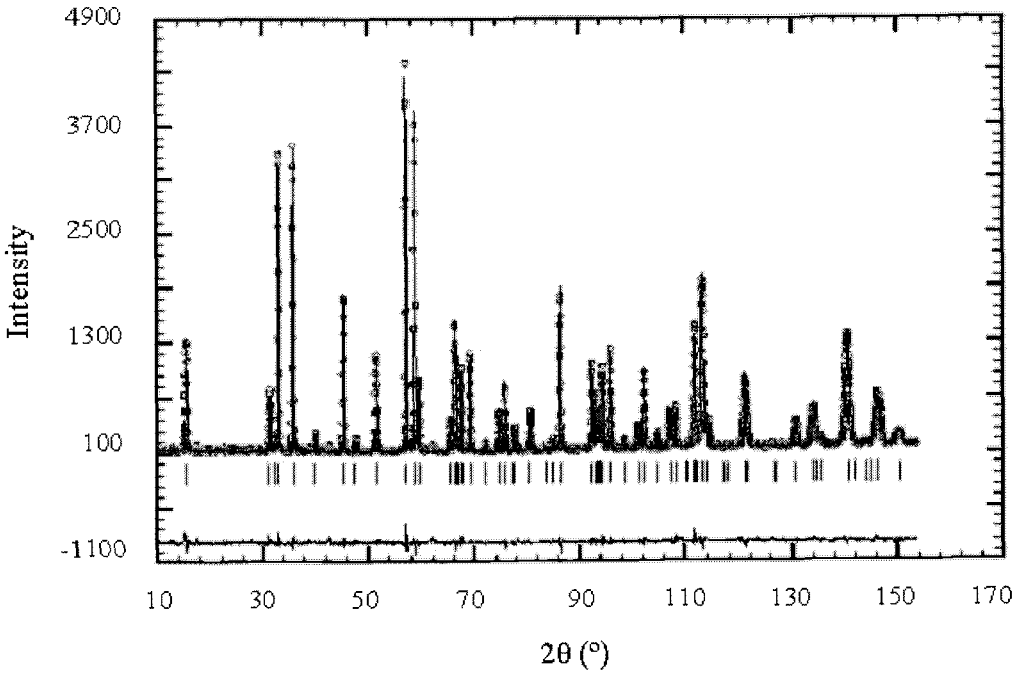

Figure 6.3 Observed (open circles), calculated (solid line), and difference profiles (bottom curve) for 2H $CuScO_2$ at room temperature. The vertical bars indicate allowed peak positions.

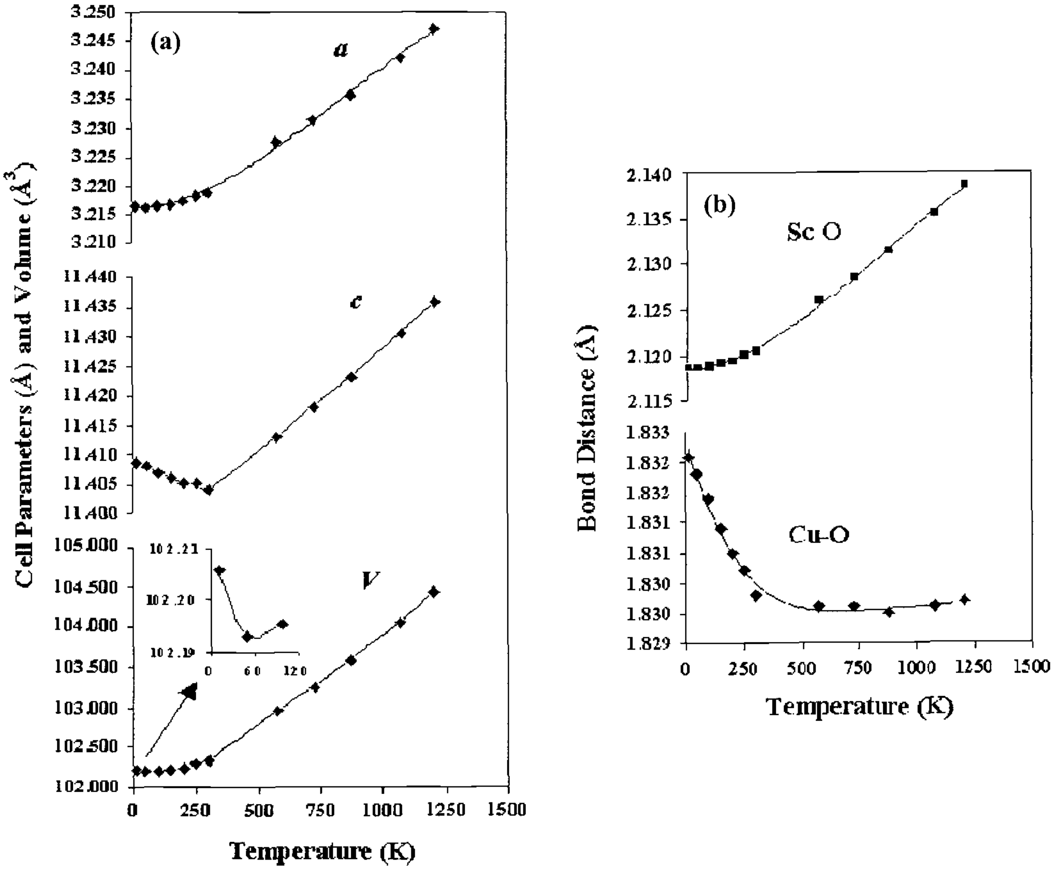

Figure 6.4 Variation of (a) unit cell edges and volume and (b) Cu–O and Sc–O bond lengths with temperature.

Figure 6.5(a) shows the Cu–Cu distance vs. temperature. This is also the value of the Sc–Sc distance vs. temperature. One of the O–O distances is the same as the Cu–Cu and Sc–Sc distances. This is an O–O pair that does not define a shared edge for the $ScO_6$ octahedra. The O–O distance across the shared edge is considerably shorter as expected. Bond angles vs. temperature are given in Figure 6.5(b). The O–Sc–O angles are equivalent to the Sc–O–Sc angle due to lattice symmetry.

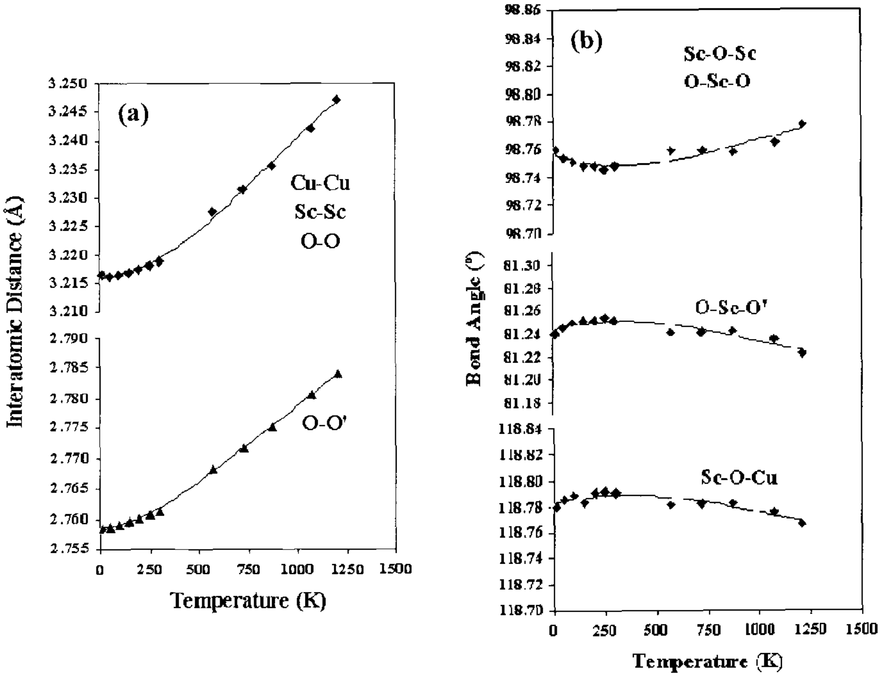

Figure 6.5 Variation of (a) metal-metal, O–O interatomic distances and (b) bond angles with temperature.

Refined thermal displacement factors all increase monotonically with increasing temperature. The $U_{33}$ values for both Cu and O become negative at the lowest temperatures. For oxygen this can be ignored because the $U_{11}$ values are within a couple of standard deviations of zero. The negative $U_{33}$ values for Cu cannot be ignored because $U_{33}$ for Cu has become six times the standard deviation at the lowest temperature. This apparent failure of the thermal ellipsoid model will be discussed later in this Chapter. Within the thermal ellipsoid model we can conclude that thermal motion along $z$ becomes immeasurably small at low temperatures for both Cu and O.

### 6.3.2 $AMO_2$ Delafossite Compounds

All the polycrystalline $AMO_2$ (A = Cu or Ag; M = Al, Sc, In or La) compounds investigated have the 3R form of the delafossite structure, except that in the case of $CuScO_2$ both the 2H and the 3R forms exist. The 3R structure was refined in space group $R\bar{3}m$ with hexagonal atom positions of Cu or Ag (0,0,0), Sc (0,0,1/2), and O (0,0,$z$). This study encompasses results from 49 different refinements, results are hence only presented here graphically. The absence of interstitial oxygen was confirmed by placing oxygen in the Cu triangles within the Cu planes. The occupancy of such sites always refined to values indistinguishable from zero.

Figure 6.6 shows the variations of $a$, $c$ cell edges and $c/a$ ratio with temperature. NTE behavior was observed at low temperature for all the compounds investigated. Usually the NTE behavior was just for the $c$ cell edge. The low temperature value of $\alpha$ was $-1.0$ to $-1.8 \times 10^{-6}$/K in most cases but was only $-0.4$ and $-0.5 \times 10^{-6}$/K for $CuAlO_2$ and $CuInO_2$, which makes the NTE effect of these two compounds difficult to see in Fig. 6.6(b). In the case of $CuLaO_2$ NTE behavior was found for both $a$ and $c$. In no case was there NTE behavior for any cell edge above room temperature. The temperature dependence of $c/a$ ratio indicates that the thermal expansion is generally highly anisotropic, which is expected for such an anisotropic structure. However, nearly isotropic thermal expansion is found in the case of $CuLaO_2$.

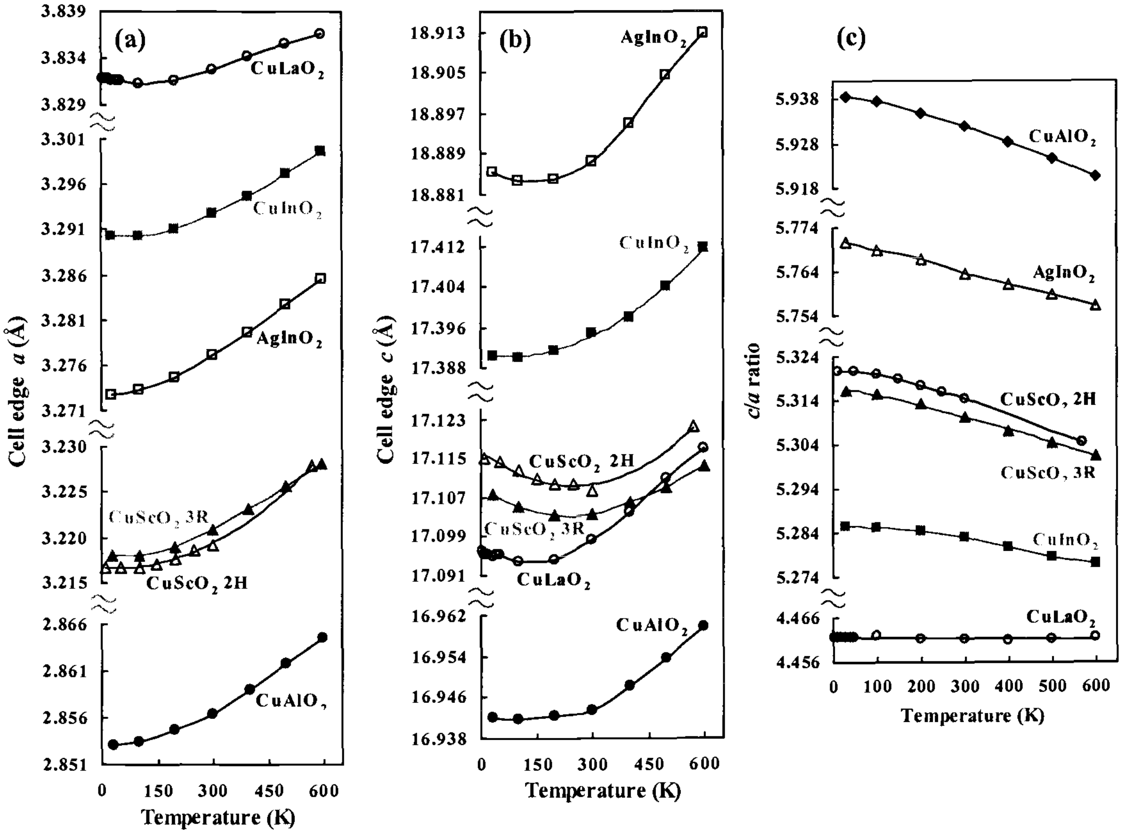

Figure 6.6 Temperature dependence of (a) cell edge *a*; (b) cell edge *c*; and (c) *c/a* ratio. Values of cell edge *c* for 2H $CuScO_2$ have been multiplied by 3/2 to allow direct comparison.

The term atomic displacement factor has generally replaced the term thermal parameter because atomic displacements are not always thermally induced. We use the term thermal parameter here because the temperature dependences of these terms indicate they are basically true thermal parameters. Figure 6.7 shows the variation of thermal parameters with temperature.

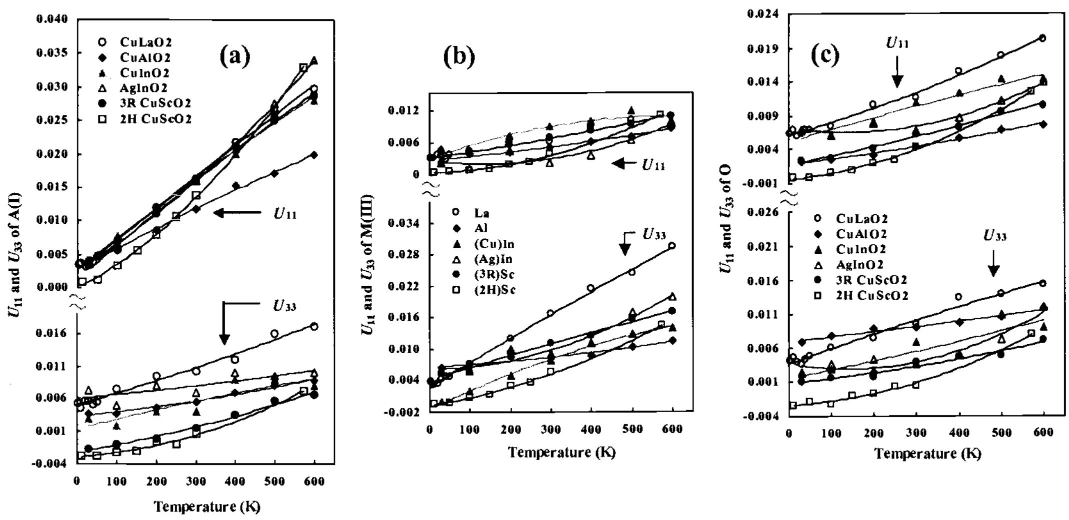

Figure 6.7 Thermal displacement factors of (a) A(I) cation (A = Cu or Ag); (b) M(III) cation (M = Al, Sc, In or La); and (c) oxygen vs temperature.

All atoms are on a three-fold axis. Thus, the thermal ellipsoids are either extended or flattened along this axis. $U_{11}$ is perpendicular to the *c* axis, and $U_{33}$ is parallel to the *c* axis. The most extreme anisotropic *U*s are for the A cation. As expected for two-fold linear coordination, the ellipsoids are flattened, and the $U_{11}/U_{33}$ ratio can be four or higher. The opposite situation is generally found for the M cations. The ellipsoids are usually elongated along the *c* axis. Anisotropic thermal motion would not be expected in a regular octahedron, but this octahedron is highly distorted. The more pronounced motion is in the direction of the two faces that are much larger than the other four faces. The main exception is found for $CuInO_2$, where the distortion from a regular octahedron is not so great. The thermal motion of oxygen is nearly isotropic, but there is a tendency of $U_{11}$ to be somewhat higher than that of $U_{33}$. The standard uncertainties for *U* values vary from about the same size of the points ($CuLaO_2$) to about twice of the size of the points ($CuInO_2$) in Figure 6.7. It is physically unreasonable for $U_{11}$ or $U_{33}$ to be negative, and these values were found to be positive for all atoms in all compounds at room temperature. However, some of these parameters did sometimes minimize to negative values at low temperatures, usually within a few standard uncertainties of zero. Applying corrections for absorption did not always rectify this. The lower range of these values is attributed to correlation between the $U$ values and other fitted values, likely the background parameters. This conclusion was supported by collecting data for 2H $CuScO_2$ at 3.6 K using a shorter neutron wavelength. This approximately doubles the number of accessible reflections, which increases the sensitivity of the fit to the thermal parameters. With this greater range of data, all $U$ parameters refined to positive values or zero.

Figure 6.8 plots our data for Cu $U_{11}$ in $CuAlO_2$, together with the data from the previous single crystal X-ray study [9].

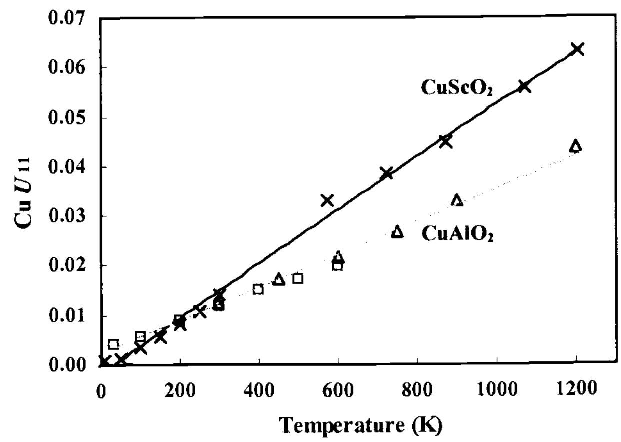

Figure 6.8 Comparison of thermal displacement factors of Cu $U_{11}$. Squares (this work, powder neutron diffraction) and triangles ([9], single crystal XRD) are for 3R $CuAlO_2$. Cross points are for 2H $CuScO_2$ ([8], powder neutron diffraction).

The agreement in the overlap area is very good. Our Cu $U_{11}$ data for 2H $CuScO_2$ are also plotted for comparison, showing that Cu(I) maintains a larger thermal motion perpendicular to the *c* axis in 2H $CuScO_2$ than in $CuAlO_2$ up to high temperatures.

The variation of the A–O distances with temperature before and after correction is shown in Figure 6.9(a), indicating that strong NTE behavior persists in some cases up to our maximum measuring temperature of 600 K. The M–O distances and the thicknesses of the $(MO_2)^{1-}$ layers as a function of temperature are shown in Figure 6.9(b) and (c). Due to the high symmetry of this structure, the A–A distance, the M–M distance, and one O–O distance are the same as *a* cell edge.

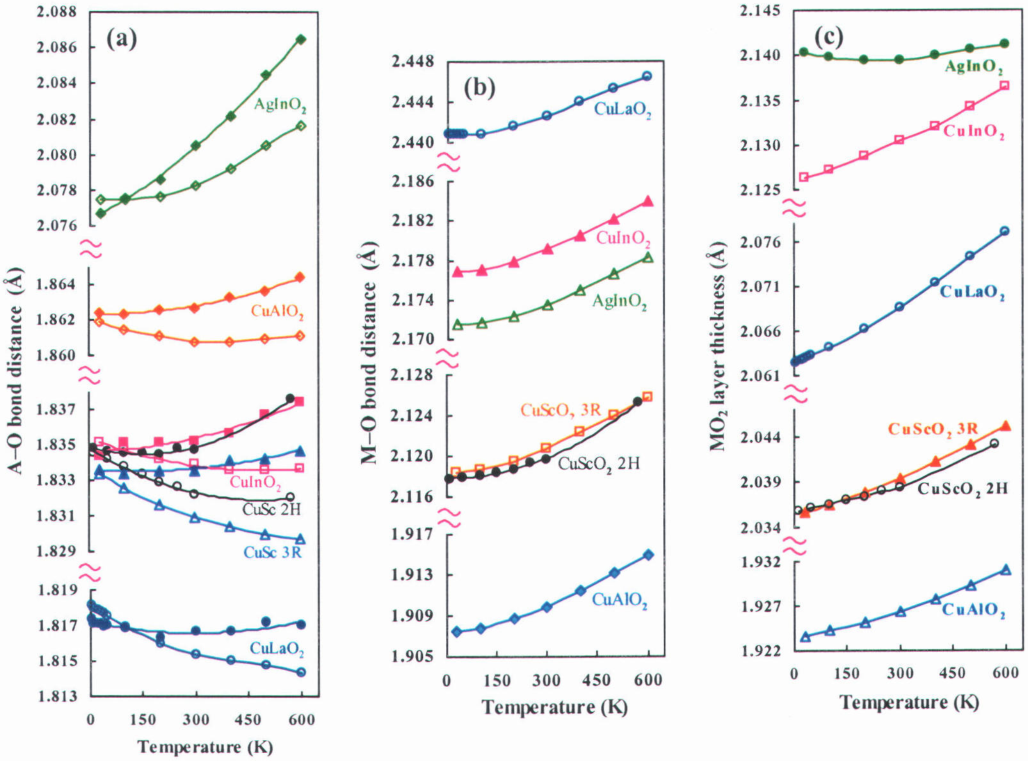

Figure 6.9 The temperature dependence of (a) A–O bond distances; (b) M–O bond distances; and (c) thickness of $(MO_2)^{1-}$ layers. Open symbols in (a) are uncorrected bond distances; solid symbols in (a) are corresponding bond distances corrected by riding model (see 6.4.1 in this Chapter).

The values of the cell edges can be determined with greater accuracy than the bond distances. Thus, the estimated errors for *a*, *c*, and *T* are less than the size of the points in Figure 6.6. The estimated errors for the values in Figure 6.9, however, depend on the accuracy of the determination of the O(*z*) parameter. Estimated uncertainties vary with the intensities of the various diffraction patterns giving the following estimates for the strongest pattern ($CuLaO_2$) and the weakest pattern ($CuInO_2$) respectively: 0.0001 to 0.0003 Å for M–O, 0.0003 to 0.0007 Å for A–O, and 0.0006 to 0.0015 Å for the sheet thickness.

## 6.4 Discussion

### *6.4.1 NTE in 2H $CuScO_2$*

A cation in two-fold coordination is rare except for $d^{10}$ cations such as Cu(I), Ag(I), and Hg(II). The structure of $Cu_2O$ contains linear O–Cu–O linkages, and the thermal expansion of $Cu_2O$ below 323 K is negative but very low, $-0.6 \times 10^{-6}$/K [18]. Above 323 K the thermal expansion coefficient of $Cu_2O$ is very low but positive, $+0.25 \times 10^{-6}$/K. The structure of $Ag_2O$ is the same as $Cu_2O$, thus again having the cation in two-fold linear coordination to oxygen. The thermal expansion for $Ag_2O$ was originally reported positive from 150 to 520 K [18], but it has been found to be strongly negative over the entire investigated temperature range of 40 ~ 470 K [7].

In cubic $Cu_2O$ the thermal expansion coefficient for the Cu–O bond is the same as for the unit cell edges. Thus, the negative expansion for $Cu_2O$, $-0.6 \times 10^{-6}$/K, is much less pronounced than the negative thermal expansion for the Cu–O bond in 2H $CuScO_2$ below room temperature, $-4.0 \times 10^{-6}$/K. Assuming interference of the transverse thermal motion of Cu with its Cu neighbors, the reason for this might be the much larger Cu–Cu distance in 2H $CuScO_2$, 3.22 Å, compared to 3.02 Å in $Cu_2O$. Apparently, there are no other measurements of the Cu(I)–O bond thermal expansion below room temperature. There is, however, a measurement of the thermal expansion of the Cu(I)–O bond above room temperature in $CuAlO_2$ [9]. This expansion in $CuAlO_2$ is $5.4 \times 10^{-6}$/K whereas it is only $1.1 \times 10^{-6}$/K in 2H $CuScO_2$. Brown *et al.* [19] have pointed out that the thermal expansion of the Cu–O bond in $CuAlO_2$ is much less than expected based on bond valence considerations. Thus, the thermal expansion of the Cu–O bond in 2H $CuScO_2$ above room temperature can be considered exceptionally low. Assuming that the low thermal expansion of the apparent Cu–O distance is related to the transverse thermal motion of Cu in the O–Cu–O linkage, we can again invoke interference with this motion by neighboring Cu atoms. The Cu–Cu distance in $CuAlO_2$ is only 2.86 Å compared to the 3.22 Å value in 2H $CuScO_2$. This is also consistent with the Cu $U_{11}$ values from single-crystal X-ray diffraction at room temperature (Table 2). Our value for 2H $CuScO_2$ is two times greater than three published values for $CuAlO_2$ [19-21]. Although the thermal expansion coefficient for the Cu–O bond below room temperature is $-4.0 \times 10^{-6}$/K, the thermal expansion of the *c* cell edge over this temperature range is only $-1.3 \times 10^{-6}$/K due to compensation by the positive thermal expansion of the Sc–O bond (Fig. 6.4(b)).

Table 6.2 Anisotropic thermal displacement parameters (Å × $10^3$) for 2H $CuScO_2$.

| | Cu | Sc | O | | Cu | Sc | O |
|---|---|---|---|---|---|---|---|
| $U_{11}$ | **14.8(3)** | **4.5(1)** | **5.4(3)** | $U_{33}$ | **0.4(4)** | **6.5(2)** | **2.5(4)** |
| | 28(1) | 18(1) | 20(1) | | 18(1) | 21(1) | 19(1) |

Note: The anisotropic displacement factor exponent takes the form: $-2\pi^2 [\, h^2 a^{*2} U_{11} + \cdots + 2\, h\, k\, a^* \, b^* \, U_{12} \,]$. For all atoms $U_{22} = U_{11}$, $U_{12} = 1/2U_{11}$, and $U_{23} = U_{13} = 0$. Bold values are from neutron diffraction; others from single-crystal X-ray diffraction.

The negative $U_{33}$ values for Cu below room temperature suggest that the thermal motion of Cu should be described as a torus instead of a thermal ellipsoid (Fig. 1.9(b) in Chapter 1). This is a conclusion reached by other workers [22] in the case of oxygen in Sc–O–W linkages in $Sc_2W_3O_{12}$, a compound that exhibits negative thermal expansion [23]. We therefore explored a torus model for the thermal motion of Cu. This was done by placing 3, 6, or 12 Cu atoms around the six-fold axis and refining the torus radius using an isotropic displacement parameter for Cu. All three torus models and the ellipsoid model gave essentially the same agreement factors at all temperatures. The results are given in Figure 6.10(a) along with root mean square (rms) displacements calculated from the thermal ellipsoid $U_{11}$ values. As might be expected the torus values are somewhat larger than the rms values. Although we cannot distinguish between the torus model and the thermal ellipsoid model based on agreement factors, the torus model is a physically reasonable model at all temperatures whereas the $U_{33}$ parameter for Cu in the ellipsoid model is physically impossible below room temperature. Even at room temperature, the shape of the thermal ellipsoid for Cu is extreme (Fig. 6.10(b)). The thermal motion of Cu perpendicular to the O–Cu–O linkage is not unusually high, but the Cu motion along the Cu–O bond is very low.

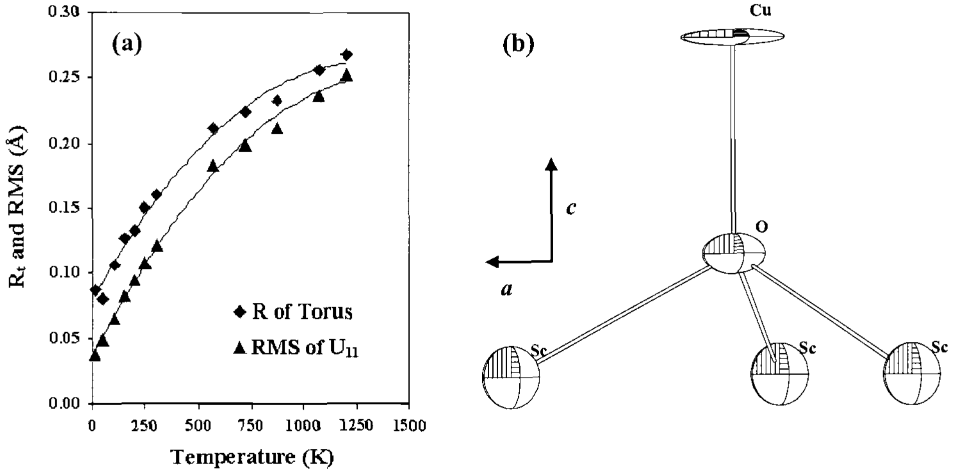

Figure 6.10 (a) Root-mean-square displacement values and torus radii as a function of temperature; (b) Partial view of $CuScO_2$ structure at room temperature showing thermal ellipsoids.

Structural refinements of $CuMO_2$ delafossites based on single-crystal X-ray diffraction data are available for M = Al, Ga, Fe, Rh, Sc and Y [19-21,24-27]. Such studies are also available for $YBa_2Cu_3O_6$ [28-31], $PrBa_2Cu_3O_6$ [32], $PbCu_2O_2$ [33], $Cu_4O_3$ [34], and $Cu_2O$ [35-37]. All of these compounds have linear O–Cu(I)–O linkages, and the Cu thermal motion perpendicular to these linkages is always considerably higher than along the Cu–O bond. This is the expected behavior, but our attempts to find a correlation of $U_{11}$ or $U_{11}/U_{33}$ with Cu–Cu distance or Cu–O distance failed. This may in large part simply reflect the unreliability of the $U$ values from routine X-ray diffraction studies. This problem is indicated in Table 2 where our room temperature $U$ values obtained from powder neutron diffraction data are significantly different than those found from our single-crystal X-ray diffraction data.

It has long been recognized that apparent bond lengths should be corrected for thermal motion, especially when the thermal motion is high. The most conservative correction would be the correction assuming a riding motion [38]. In this model the two oxygen atoms of the O–Cu–O linkage move in the same direction as Cu when Cu is moving transverse to the O–Cu–O linkage (Fig. 6.11).

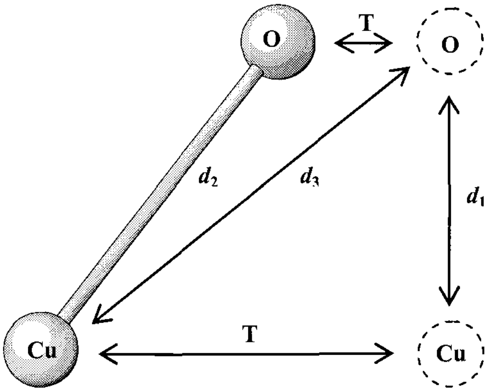

Figure 6.11 Correction of apparent bond length $d_1$ for thermal motion using a riding model gives a corrected bond length $d_2$. If the riding motion not assumed, the corrected bond length would be $d_3$ or even longer.

The results of this correction are shown in Figure 6.12. This correction alone is enough to completely eliminate the negative thermal expansion behavior of the Cu–O bond. The correction based on the torus model is much larger (Fig. 6.12), mainly because the oxygen atoms are considered to be stationary in this model. In this model the thermal expansion of the Cu–O bond is +5.46 × $10^{-6}$/K over a broad temperature range. This is a very common thermal expansion for a metal-oxygen bond distance.

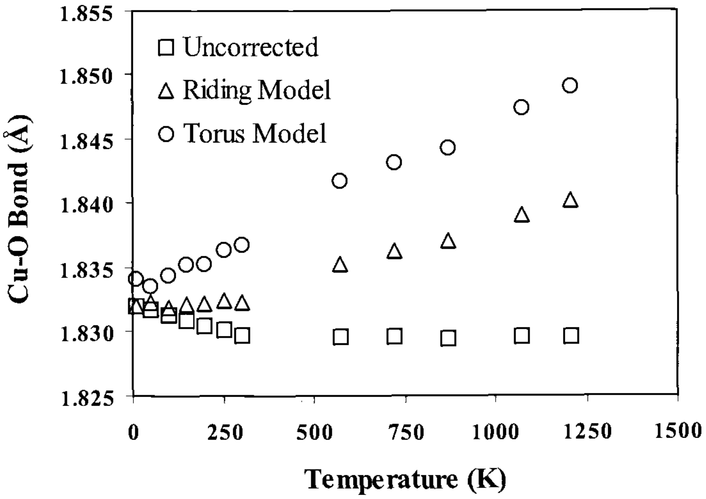

Figure 6.12 Cu–O bond distances vs. temperature showing riding model and torus model corrections.

### 6.4.2 *Trends with Composition in $AMO_2$ Series*

Before discussion of trends with temperature in $AMO_2$ series, it is important to discuss some trends in the delafossite structure with variations of the A and M cations. It has been previously noted by Jansen that the Cu–O distance in $CuMO_2$ delafossites decreases as the size of M and consequently the Cu–Cu distance increases [39]. We also note the same trend for the Ag–O distances in $AgMO_2$ delafossites (Fig. 6.13). Jansen had rationalized this behavior for $CuMO_2$ delafossites on the basis of competition between Cu–O bonding and Cu–Cu bonding. Thus, as one bond becomes shorter and stronger, the other bond becomes longer and weaker. One would not normally expect any bonding interaction between $nd^{10}(n+1)s^{0}$ cations such as Cu(I) and Ag(I). However, strong *d-s* hybridization occurs on Cu and Ag due to the linear O–A–O linkages. This effectively transfers some electron density from the filled *d* shell to the empty *s* shell. The A–A interaction then becomes weakly bonding, creating an attractive force that is balanced by repulsion between the cores. It is this direct A–A bonding interaction that presumably provides the conduction mechanism for p-doped $CuMO_2$ compounds with the delafossite structure. However, the A–A bond appears too weak to explain the trend in Figure 6.13.

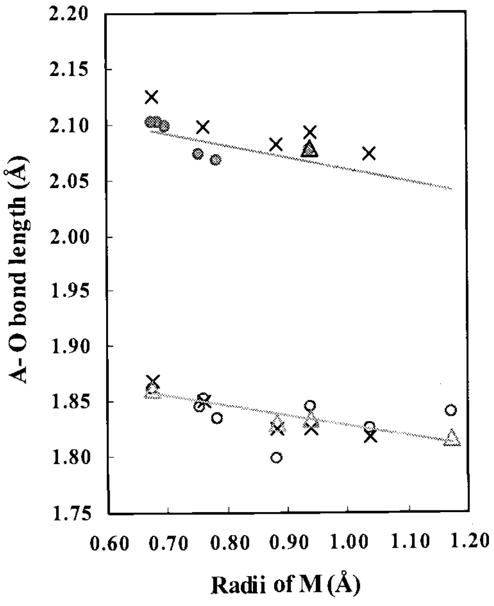

Figure 6.13 Variation of A–O bond distances with the size of M cations. Solid circles, from left to right, are for $AgAlO_2$ [40], $AgCoO_2$ [41], $AgNiO_2$ [41], $AgCrO_2$ [42], $AgFeO_2$ [43,44], and $AgInO_2$ [45]. Open circles, from left to right, are for $CuAlO_2$ [9], $CuCrO_2$ [46], $CuGaO_2$ [24], $CuFeO_2$ [43,44], $CuScO_2$ [47], $CuInO_2$ [48], $CuYO_2$ [24], and $CuLaO_2$ [49]. Triangles are data points from this work. Cross points are calculated data (GGA) by Kandpal *et al* [50].

We have suggested an alternate explanation [51]. The $s$-$d_{z^2}$ hybridization of the A cations necessary to form the two-fold linear bonds to oxygen effectively polarizes the filled shell (Fig. 6.14) leading to an increase of the A–A repulsion. As the A cations are forced closer by the smaller M cations, this polarization is forced to decrease, forcing increased antibonding electron density for the A–O bond. Thus, the A–O bond becomes weaker and longer. This explanation was subsequently supported by calculations [50].

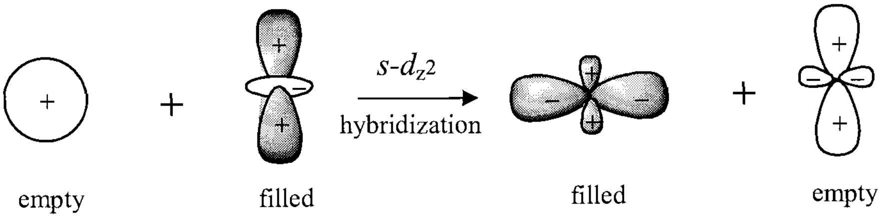

Figure 6.14 The $s$-$d_{z^2}$ hybridization of the A cation transfers some electron density from filled $d_{z^2}$ orbital to the empty $s$ orbital giving a filled hybridized orbital, which effectively polarizes the core. The empty hybridized orbital facilitates bonding with oxygen atoms by overlapping with filled oxygen $2p_z$ orbitals.

Because all the O–A–O linkages are strictly parallel to the $c$ axis, one expects that the value of the $a$ cell edge will scale only with the size of the M cation. Thus, the magnitudes of the $a$ cell edges for $AgMO_2$ and $CuMO_2$ compounds with the same M cation are nearly the same (Fig. 6.15(a)). The small differences that do exist in the $a$ cell edges for compounds with the same M cation can give important clues as to the nature of the A–A interaction. For small values of the $a$ cell edge, the $AgMO_2$ compound has a larger $a$ cell edge than does the $CuMO_2$ compound. This can be rationalized on the basis that Ag is larger than Cu, and Ag–Ag repulsive forces will dominate at the smaller A–A distances. The opposite trend occurs at larger A–A distances: the $CuMO_2$ compounds have a larger *a* cell edge than do the corresponding $AgMO_2$ compounds. This crossover has been predicted from calculations [50]. Such a crossover indicates potential energy curves as shown in Figure 6.15(b). It is assumed that the A–A interaction becomes attractive at large A–A distances, but a crossover could also be consistent with the A–A interaction being repulsive at all distances.

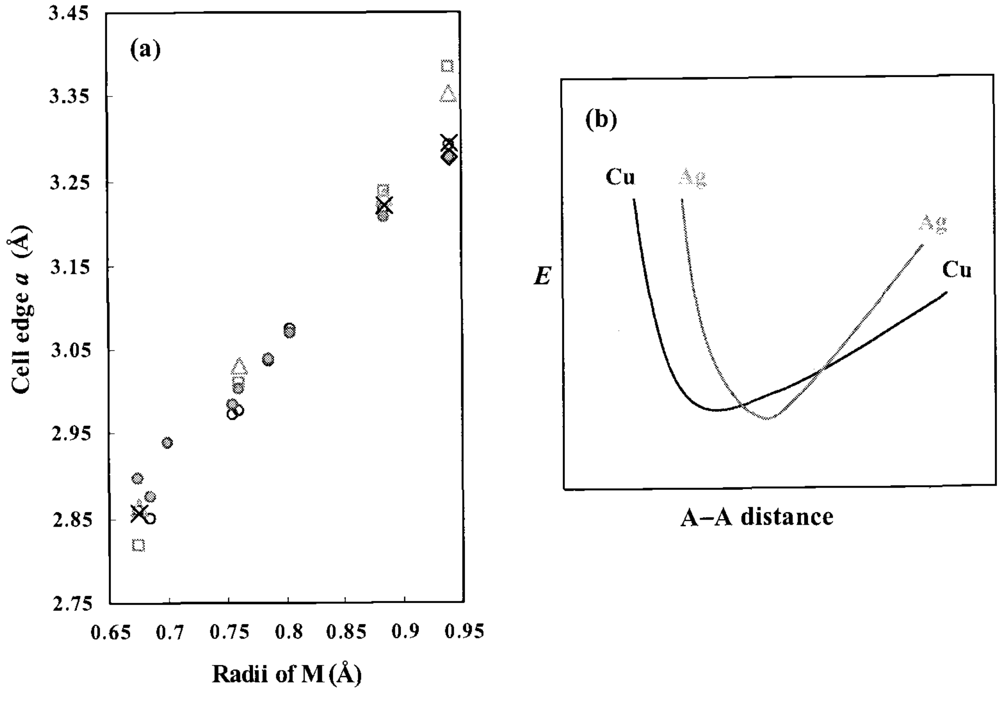

Figure 6.15 (a) Variation of cell edge *a* with the size of M cations. Solid circles, from left to right, are for $AgAlO_2$ [40], $AgCoO_2$ [41], $AgNiO_2$ [41], $AgCrO_2$ [42], $AgGaO_2$ [47], $AgFeO_2$ [43,44], $AgRhO_2$ [43], $AgScO_2$ [51] and $AgInO_2$ [45]. Open circles, from left to right, are for $CuAlO_2$ [9], $CuCoO_2$ [43], $CuCrO_2$ [46], $CuGaO_2$ [24], $CuFeO_2$ [43,44], $CuRhO_2$ [43], $CuScO_2$ [47], and $CuInO_2$ [48]. The diamond is for $AgInO_2$ (this work), and cross points are for $CuMO_2$ (this work). Triangles are calculated (GGA) data for $AgMO_2$ and squares are calculated (GGA) data for $CuMO_2$ [50]; (b) Schematic of potential energy vs. A–A distance (A = Ag, Cu).

The length of the *c* cell edge is influenced by both the A–O distance and the M–O distance. If the Cu–O and Ag–O distances remained constant, one would expect a significant increase in the *c* cell edge as the size of M increases. However as noted above, the A–O distances actually decrease as the size of M increases (Fig. 6.13). Thus, changes of the A–O and M–O distances as M is varied tend to compensate. The slightly larger increase in the size of the *c* cell edge with increasing M size for $AgMO_2$ compounds (Fig. 6.16) relative to $CuMO_2$ compounds is related to the crossover of the *a* cell edge of $CuMO_2$ and $AgMO_2$ compounds (Fig. 6.15(a)). The *a* cell edge does not increase as rapidly with M size for $AgMO_2$ compounds as it does for $CuMO_2$ compounds. Thus, this increase in the size of M has a more pronounced impact on the *c* cell edge for the $AgMO_2$ compounds.

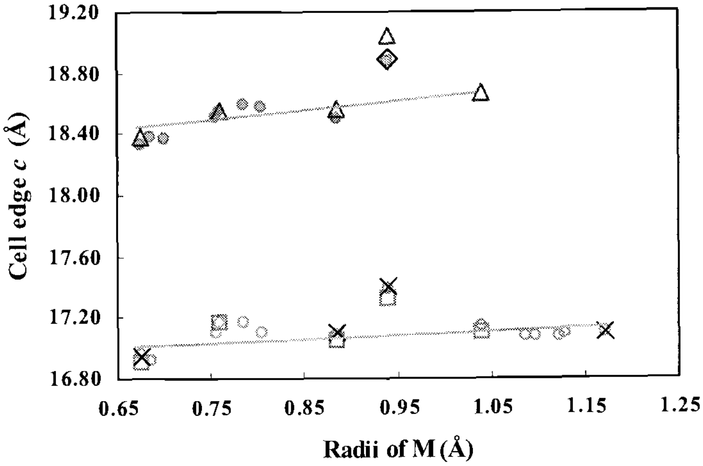

Figure 6.16 Variation of cell edge *c* with the size of M cations. Solid circles, from left to right, are for $AgAlO_2$ [40], $AgCoO_2$ [41], $AgNiO_2$ [41], $AgCrO_2$ [42], $AgGaO_2$ [47], $AgFeO_2$ [43,44], $AgRhO_2$ [43], $AgScO_2$ [51] and $AgInO_2$ [45]. Open circles, from left to right, are for $CuAlO_2$ [9], $CuCoO_2$ [43], $CuCrO_2$ [46], $CuGaO_2$ [24], $CuFeO_2$ [43,44], $CuRhO_2$ [43], $CuScO_2$ [47], $CuInO_2$ [48], $CuYO_2$ [24], $CuEuO_2$ [49], $CuSmO_2$ [49], $CuNdO_2$ [52], $CuPrO_2$ [49], $CuLaO_2$ [49]. The diamond is for $AgInO_2$ (this work), and cross points are for $CuMO_2$ (this work). Triangles are calculated (GGA) data for $AgMO_2$ and squares are calculated (GGA) data for $CuMO_2$ [50].

One must also consider the impact of cation-cation repulsion across the edge-shared octahedra of the $(MO_2)^{1-}$ sheets. This repulsion will increase with the real charge on the M(III) cations and will thus increase as the M(III) cations become more electropositive. The lowest repulsion among M(III) cations we have studied is expected for In, because In has the highest electronegativity. Thus, for $CuInO_2$ and $AgInO_2$ the $(MO_2)^{1-}$ sheets are less stretched and are therefore thicker (Fig. 6.9(c)), causing a larger *c* cell edge than would be otherwise expected (Figs. 6.6(b) & 6.16).

The differences between $CuInO_2$ and $AgInO_2$ are also interesting. The Ag–O bond being weaker than the Cu–O bond causes the In–O bond to be stronger and shorter in $AgInO_2$ than in $CuInO_2$ (Fig. 6.9(b)). This in turn results in the *a* cell edge for $AgInO_2$ being smaller than for $CuInO_2$ (Fig. 6.6(a)).

A curious feature of the delafossite structure is that the M–O–M angle is constrained by space group symmetry to be exactly the same as one of the two O–M–O angles. The sum of the two O–M–O angles is 180°. This angle is plotted vs. the size of M(III) in Figure 6.17. Oxygen is tetrahedrally coordinated (A + 3M), and M is octahedrally coordinated. It is impossible for the M–O–M and O–M–O angles to have the ideal values of 109° and 90°. Thus, this angle is always intermediate between these two ideal values and tends to increase with increasing size of M (Fig. 6.17).

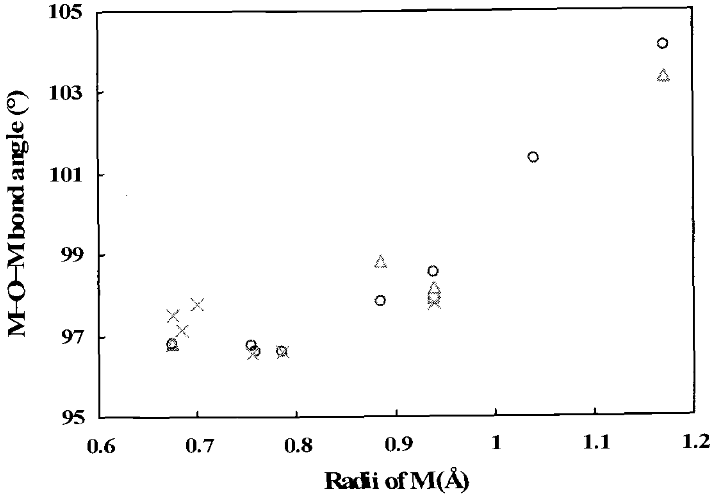

Figure 6.17 Bond angles M–O–M (or O–M–O) vs the size of M cations. Cross points, from left to right, are for $AgAlO_2$ [40], $AgCoO_2$ [41], $AgNiO_2$ [41], $AgCrO_2$ [42], $AgFeO_2$ [43,44] and $AgInO_2$ [45]. Open circles, from left to right, are for $CuAlO_2$ [9], $CuCrO_2$ [46], $CuGaO_2$ [24], $CuFeO_2$ [43,44], $CuScO_2$ [47], $CuInO_2$ [48], $CuYO_2$ [24], $CuLaO_2$ [49]. The square is for $AgInO_2$ (this work), and the triangles are for $CuMO_2$ (this work).

### *6.4.3 Trends with Temperature in $AMO_2$ Series*

NTE behavior of the *c* cell edge is observed in all six compounds we examined (Fig. 6.6(b)). The NTE behavior for *c* axis exists only below room temperature because with increasing temperature it is overwhelmed by the positive thermal expansion of the M–O bonds (Fig. 6.9(b)). For $CuMO_2$ compounds, the NTE behavior of *c* can always be attributed to the apparent NTE behavior of the Cu–O bond distance (Fig. 6.9(a)). This behavior can in turn be related to the large thermal displacements of Cu perpendicular to the O–Cu–O linkage. Correction for this thermal motion always gives Cu–O distances that increase with increasing temperature (Fig. 6.9(a)). The riding motion correction [38], as used for 2H $CuScO_2$, assumes that the thermal motion of the A cation is in the same direction as the thermal motion of oxygen. If this correlation were not assumed, the corrected A–O distances would increase even more with increasing temperature (Fig. 6.11). We had previously suggested that the degree of negative thermal expansion behavior was linked to the Cu–Cu distance [8]. As this distance becomes smaller, the transverse thermal motion of the A cation would be impeded. In fact, the smallest $U_{11}$ values for Cu are found in $CuAlO_2$ where the Cu–Cu distance is the smallest (Fig. 6.7(a)). Furthermore, the strongest low temperature NTE behavior for the apparent Cu–O distance is found in $CuLaO_2$ ($\alpha = -6.4 \times 10^{-6}$/K) compared to $\alpha = -5.9 \times 10^{-6}$/K in 3R $CuScO_2$ and $\alpha = -3.2 \times 10^{-6}$/K in $CuAlO_2$. Also, the NTE behavior for the apparent Cu–O distance has disappeared by 500 K for $CuAlO_2$ whereas it continues strong to higher temperatures in $CuLaO_2$. The NTE behavior of the corrected Cu–O distance at low temperature in $CuLaO_2$ suggests that the riding motion correction is too conservative.

There is no indication of NTE behavior for the Ag–O distance in $AgInO_2$ (Fig. 6.9(a)). This might be considered surprising in view of the stronger NTE behavior of $Ag_2O$ compared to that of $Cu_2O$ [7]. However, the Ag–Ag distance in $Ag_2O$ is 3.42 Å whereas this distance is only 3.28 Å in $AgInO_2$. Thus, the Ag thermal displacements perpendicular to O–Ag–O linkages will be inhibited in $AgInO_2$ relative to $Ag_2O$. In fact, the magnitude of the thermal motion of Ag perpendicular to the O–Ag–O linkage in $Ag_2O$ is reported to be more than two times what we find in $AgInO_2$ [53,54]. Thus, although the $U_{11}$ values for Ag in $AgInO_2$ are comparable to those of $CuMO_2$

compounds showing NTE behavior, this is not enough to compensate for the very large intrinsic thermal expansion of the Ag–O bond. Weaker bonds show higher thermal expansion than stronger bonds, and a Ag–O bond is weaker than a Cu–O bond. Thus, the high temperature thermal expansion in $AgInO_2$ for both the Ag–O distance and the *c* cell edge is much higher than the corresponding values for the $CuMO_2$ delafossites (Figs. 6.6(b) and 6.9(a)).

For $AMO_2$ delafossites it is the decrease in the M–O distance with decreasing temperature that primarily causes the *a* cell edge to decrease with decreasing temperature. However, the forces between the A cations can also be expected to have some impact on the thermal expansion of the *a* cell edge, and Ag–Ag and Cu–Cu repulsive or attractive forces are not the same (Fig. 6.15(b)). The A–A distances for the $AInO_2$ compounds lie to the right of the minima in Figure 6.15(b). Thus, the Ag–Ag attractive forces in $AgInO_2$ are expected to be stronger than the Cu–Cu attractive forces in $CuInO_2$. On cooling, this could in turn cause a stronger contraction of the *a* cell edge in $AgInO_2$ than in $CuInO_2$, as observed in Figure 6.6(a). This greater thermal contraction with decreasing temperature of the *a* cell edge for $AgInO_2$ causes the slight expansion of the $(InO_2)^{1-}$ layer at lower temperatures (Fig. 6.9(c)) and consequently a small NTE effect for the *c* axis (Fig. 6.6(b)).

Comparisons of trends for 2H and 3R $CuScO_2$ are complicated by the fact that Mg substitution for Sc was used to stabilize the 2H form. We know that it is this substitution that causes the smaller *a* cell edge and the larger *c* cell edge for our 2H sample [11]. The effect of the smaller Mg(II) for Sc(III) is also clearly seen in the plot of M–O distances vs. temperature in Figure 6.9(b). The larger Cu–O distance and resultant longer *c* cell edge for 2H $CuScO_2$ are again more likely due to the Mg substitution than the different stacking along the *c* axis.

The most surprising NTE behavior found in this study is that of the *a* cell edge for $CuLaO_2$ at low temperatures (Fig. 6.6(a)). Data were collected at more temperatures in the low temperature range for $CuLaO_2$ to confirm with certainty the cause of this behavior. This NTE behavior is not caused by NTE behavior of the La–O distance (Fig. 6.9(b)). Rather it is caused by continued shrinkage of the thickness of the $(LaO_2)^{1-}$ sheet with decreasing temperature (Fig. 6.9(c)), even after the La–O distance has leveled off. The other $(MO_2)^{1-}$ sheets also show continued shrinkage down to low temperatures, but not as strongly so as for $CuLaO_2$. Furthermore, the La–O distance flattens out sooner with decreasing temperature than for the other compounds. Geometric considerations dictate that a decreasing $(LaO_2)^{1-}$ sheet thickness coupled with an invariant La–O distance will directly cause an increase in the *a* cell edge.

## 6.5 References

1. A.W. Sleight. *Inorg. Chem.*, 37, 2854-2860 (1998)
2. D.J. Williams, D.E. Partin, F.J. Lincoln, J. Kouvetakis, M. O'Keeffe. *J. Solid State Chem.*, 134, 164-169 (1997)
3. G.K. White, R.B. Roberts. *Aust. J. Phys.*, 41, 791-795 (1988)
4. G.A. Slack, I.C. Huseby. *J. Appl. Phys.*, 53, 6817-6822 (1982)

5. H.A. Mook, F. Holtzberg. In *Valence Fluctuations in Solids*; L.M. Falicov, W. Hanke, M.B. Maple, Eds.; North-Holland Publishing Company, 1981; pp 113-118.

6. J.R. Salvador, F. Guo, T. Hogan, M.G. Kanatzidis. *Nature*, 425, 702-705 (2003)

7. W. Tiano, M. Dapiaggi, G. Artioli. *J. Appl. Crystallogr.*, 36, 1461-1463 (2003)

8. J. Li, A. Yokochi, T.G. Amos, A.W. Sleight. *Chem. Mater.*, 14, 2602-2606 (2002)

9. T Ishiguro, N. Ishizawa, N. Mizutani, M. Kato. *J. Solid State Chem.*, 41, 132-137 (1982)

10. R.J Cava, H.W. Zandbergen, A.P. Ramirez, H. Takagi, C.T. Chen, J.J. Krajewski, W.F. Peck, Jr., J.V. Waszczak, G. Meigs, R.S. Roth, L.F. Schneemeyer. *J. Solid State Chem.*, 104, 437-452 (1993)

11. J. Li, A.F.T. Yokochi, A.W. Sleight. *Solid State Sci.*, 6, 831-839 (2004)

12. R.H. Blessing. *Acta Crystallogr., Sect A*, 51, 33 (1995)

13. L.J. Farrugia. *J. Appl. Crystallogr.*, 32, 837 (1999)

14. G.M. Sheldrick. SHELX97 [Including the programs SHELXS97, SHELXL97, and CIFTAB] — Programs for Crystal Structure Analysis (Release 97-2). Institüt für Anorganische Chemie der Universität: Göttingen, Germany, 1998

15. *International Tables for X-ray Crystallography*; J.S. Kasper, K. Lonsdale, Eds.; The Kynoch Press, 1959; Vol. II, pp 295-297

16. B.H. Toby. EXPGUI, a graphical user interface for GSAS, *J. Appl. Crystallogr.*, 34, 210-221 (2001)

17. A.C. Larson, R.B. Von Dreele. Generalized Structure Analysis System (GSAS), LANSCE, Los Alamos National Laboratory, 2001

18. D. Taylor. *Br. Ceram. Trans. J.*, 84(1), 9 (1985)

19. I.D. Brown, A. Dabkowski, A. McCleary. *Acta Crystallogr., Sect B*, 53, 750 (1997)

20. T. Ishiguro, N. Ishizawa, N. Mizutani, M. Kato. *Acta Crystallogr., Sect. B*, 39, 564 (1983)

21. T. Ishiguro, A. Kitazawa, N. Mizutani, M. Kato. *J. Solid State. Chem.*, 40, 170 (1981)

22. M.T. Weller, P.F. Henry, C.C. Wilson. *J. Phys. Chem. B*, 104, 12224 (2000)

23. J.S. Evans, T.A. Mary, A.W. Sleight. *J. Solid State Chem.*, 137, 148 (1998)

24. B.U. Kohler, M. Jansen. *Z. Anorg. Allg. Chem.*, 543, 73-80 (1986)

25. H. Effenberger. *Acta Crystallogr., Sect C*, 47, 2644 (1991)

26. M.A Subramanian, W. Marshall. E. I. Du Pont De Nemours & Co., Inc., unpublished data.

27. T. Ishiguro, N. Ishizawa, N. Mizutani, M. Kato. *J. Solid State Chem.*, 49, 232 (1983)

28. W.J. Jang, H. Mori, M. Watahiki, S. Tajima, N. Koshizuka, S. Tanaka. *J. Solid State Chem.*, 130, 42 (1997)

29. M.F. Garbauskas, R.W. Green, R.H. Arendt, J.S. Kasper. *Inorg. Chem.*, 27, 871 (1988)

30. G. Roth, B. Renker, G. Heger, M. Hervieu, B. Domenges, B. Raveau. *Z. Phys. B, Condens. Matter,* 69, 53 (1987)

31. J.S. Swinnea, H. Steinfink. *J. Mater. Res.*, 2(4), 424 (1987)

32. C.K. Lowe-Ma, T.A. Vanderah. *Physica C (Amsterdam), PHYCE*, 201, 233 (1992)

33. H. Szillat, C.L. Teske. *Z. Anorg. Allg. Chem.*, 620, 1307 (1994)

34. M.O. Keeffe, J.O. Bovin. *Am. Mineral.*, 63, 180 (1978)

35. T. Lippmann, J.R. Schneider. *Acta Crystallogr., Sect A*, 56, 575 (2000)

36. A. Kirfel, K. Eichhorn. *Acta Crystallogr., Sect A*, 46, 271 (1990)

37. R. Restori, D. Schwarzenbach. *Acta Crystallogr., Sect B*, 42, 201 (1986)

38. R.W. Busing, H.A. Levy. *Acta Crystallogr.*, 17, 142 (1964)

39. M. Jansen. *Angew. Chem. Int. Ed. Engl.*, 26, 1098-1110 (1987)

40. G. Brachtel, M. Jansen. *Cryst. Struct. Commun.*, 10, 173-174 (1981)

41. Y.J. Shin, J.P. Doumerc, P. Dordor, M. Pouchard, P. Hagenmuller. *J. Solid State Chem.* 107, 194-200 (1993)

42. S. Angelov, J. P. Doumerc. *Solid State Commun.*, 77, 213-214 (1991)

43. R.D. Shannon, D.B. Rogers, C.T. Prewitt. *Inorg. Chem.*, 10, 713-718 (1971)

44. C.T. Prewitt, R.D. Shannon, D.B. Rogers. *Inorg. Chem.*, 10, 719-723 (1971)

45. B.U. Kohler, M. Jansen. *J. Solid State Chem.*, 71, 566-569 (1987)

46. O. Crottaz, F. Kubel, H. Schmid. *J. Solid State Chem.*, 122, 247-250 (1996)

47. J.P. Doumerc, A. Ammar, A. Wichainchai, M. Pouchard, P. Hagenmuller. *J. Phys. Chem. Solids*, 48, 37-43 (1987)

48. M. Shimode, M. Sasaki, K. Mukaida. *J. Solid State Chem.*, 151, 16-20 (2000)

49. V.H. Haas, E. Kordes. *Z. Kristallogr. Bd.*, 129, S. 259-270 (1969)

50. H.C. Kandpal, R. Seshadri. *Solid State Sci.*, 4, 1045-1052 (2002)

51. R. Nagarajan, N. Duan, M.K. Jayaraj, J. Li, K.A. Vanaja, A. Yokochi, A. Draeseke, J. Tate, A.W. Sleight. *Int. J. Inorg. Mater.*, 3, 265-270 (2001)

52. M. Elazhari, A. Ammar, M. Elaatmani, M. Trari, J.P. Doumerc. *Eur. J. Solid State Inorg. Chem.*, 34, 503-509 (1997)

53. G. Artioli. In *Energy Modeling in Minerals*; C.M. Gramaccioli Ed.; EMU Notes in Mineralogy; Budapest, 2002; Vol. 4

54. S.A. Beccara, G. Dalba, P. Fornasini, R. Grisenti, A. Sanson, F. Rocca. *Phys. Rev. Lett.*, 89, 025503(1-4) (2002)

# Chapter 7

# Structure of β-$AgAlO_2$ and Structural Systematics of Tetrahedral MM'$X_2$ Compounds

## 7.1 Introduction

Two forms of $AgAlO_2$ have been reported [1-3]. Reaction of $LiAlO_2$ with molten $AgNO_3$ gives α-$AgAlO_2$, which has the delafossite structure where Al is octahedrally coordinated and Ag is in two-fold linear coordination to oxygen [1]. This form has also been prepared at high pressure by a direct reaction between $Ag_2O$ and $Al_2O_3$ [2]. Crystals obtained in this reaction were used for a refinement of the structure [2]. Reaction of β-$NaAlO_2$ with molten $AgNO_3$ or an aqueous solution of $AgNO_3$ gives β-$AgAlO_2$ [3]. Based on a comparison of X-ray powder diffraction patterns, it was concluded that β-$AgAlO_2$ is isomorphous with β-$NaAlO_2$, a structure in which all atoms are tetrahedrally coordinated.

We present here for the first time a refinement of the orthorhombic β-$AgAlO_2$ structure, which is based on the hexagonal ZnO structure. It has been reported that both $AgFeO_2$ and $AgGaO_2$ can also be prepared in this structure; however, neither positional parameters nor cell edges were given [4,5].

The structures of hexagonal ZnO and cubic ZnS may be viewed as tetrahedra sharing corners. Replacing divalent Zn with equal amounts of univalent and trivalent cations leads to an extensive series of MM'$X_2$ compounds, known as $136_2$ tetrahedral compounds. Nitride and phosphide MM'$X_2$ compounds form an isostructural series of

$245_2$ compounds with divalent and tetravalent cations. Starting with the cubic structure, ordering of the M and M' cations leads to a tetragonal structure whereas starting with the polar hexagonal structure leads to a polar orthorhombic structure. We discuss the distortions to this orthorhombic $MM'X_2$ structure that necessarily occur when M and M' differ in size.

## 7.2 Experimental

$NaAlO_2$ was first prepared by reaction of $Al_2O_3$ (Aldrich, 99.8%) with a stoichiometric amount of $Na_2CO_3$ (Aldrich, 99.95% ~ 100.05%) at 1050 °C for 12 hr. This white β-$NaAlO_2$ powder was mixed with $AgNO_3$ (Spectrum, 99.0%) and $KNO_3$ (Mallinckrodt, 99.97%) using a molar ratio of 1:1.03:1 in an agate mortar. This mixture was pressed into a pellet and heated in air at 210 °C for 24 hr. The resulting pellet was pulverized, washed with water, and dried at room temperature in air. An X-ray diffraction pattern of this product indicates a pure phase of β-$AgAlO_2$ according to ICSD [6] database.

Neutron powder diffraction data were collected using the BT-1 32-counter high resolution diffractometer at the NIST Center for Neutron Research at the National Institute of Standards and Technology. A Cu (311) monochromator, yielding a wavelength of 1.5402 Å, was employed. Collimation of 15', 20', and 7' of arc were used before the monochromator, before the sample, and before the detectors respectively. The sample was loaded in a vanadium can sample container of length 50 mm and diameter 12.4 mm. Data were collected at room temperature over a $2\theta$ range of 3 ~ 168°. Rietveld refinement of the neutron data shows an impurity phase of 1.7% $\alpha$-$Al_2O_3$.

The $\beta$-$AgAlO_2$ structure was also refined using DLS (Distance Least Squares) [7]. In this least squares refinement, prescribed distances for the bonds and the edges of the tetrahedra are used as the observations.

## 7.3 Structure of $\beta$-$AgAlO_2$

A Rietveld refinement of the neutron data in space group $Pna2_1$ using GSAS software [8] starting with the positional parameters reported for $\beta$-$NaAlO_2$ led to $R_{wp} = 5.71\%$, $R_p = 4.69\%$, and $\chi^2 = 1.065$ with $a = 5.4306(1)$ Å, $b = 6.9802(1)$ Å, $c = 5.3751(1)$ Å. The cell parameters are very close to those given in PDF file #21-1070I [6]. The final positional and displacement parameters are given in Table 7.1. One $z$ parameter must be fixed in this structure; thus, $z$(Al) was fixed at 0.0.

Interatomic distances and angles are given in Table 7.2. Figure 7.1 shows the agreement between the observed and calculated neutron diffraction patterns. Figure 7.2 shows a fragment of the structure where atoms are given as thermal ellipsoids, and Figure 7.3 shows the $\beta$-$AgAlO_2$ structure as corner sharing tetrahedra.

Table 7.1 Structure refinement results of β-$AgAlO_2$.

| | **Ag** | **Al** | **O1** | **O2** |
|---|---|---|---|---|
| $x$ | 0.0532(4) | 0.0610(5) | 0.0311(3) | 0.1283(3) |
| $y$ | 0.6268(4) | 0.1250(6) | 0.0723(3) | 0.6765(3) |
| $z$ | 0.9968(7) | 0.000000 | 0.3208(8) | 0.4344(7) |
| $U_{iso}$ | 1.40(5) | 0.59(6) | 0.87(4) | 0.80(4) |
| $U_{11}$ | 1.73(9) | 0.8(2) | 1.12(9) | 0.78(8) |
| $U_{22}$ | 1.18(8) | 0.6(1) | 1.04(8) | 0.61(8) |
| $U_{33}$ | 1.40(9) | 0.7(1) | 0.64(7) | 1.05(8) |
| $U_{12}$ | -0.23(8) | -0.3(1) | -0.06(9) | -0.21(7) |
| $U_{13}$ | -0.23(9) | -0.1(1) | -0.08(9) | -0.05(8) |
| $U_{23}$ | -0.14(7) | 0.1(1) | 0.02(8) | 0.05(7) |
| BV | 0.895 | 2.729 | 1.797 | 1.827 |

Note: Thermal displacement parameters $U_{ij}$ (Å$^2$) are multiplied by 100 and defined as $T = \exp[-2\pi^2(U_{11}h^2a^{*2} + U_{22}k^2b^{*2} + U_{33}l^2c^{*2} + 2U_{12}hka^*b^* + 2U_{13}hla^*c^* + 2U_{23}klb^*c^*)]$. Bond valences (BV) are calculated by VaList [9].

Table 7.2 Bond length (Å) and angles (°).

| | | | |
|---|---|---|---|
| Ag—O1 | 2.477(2) | Al—O1 | 1.771(4) |
| Ag—O1′ | 2.349(3) | Al—O1′ | 1.753(4) |
| Ag—O2 | 2.412(3) | Al—O2 | 1.761(3) |
| Ag—O2′ | 2.359(3) | Al—O2′ | 1.761(4) |
| | | | |
| O1—Ag—O1′ | 99.3(1) | O1—Al—O1′ | 110.2(2) |
| O1—Ag—O2 | 103.91(9) | O1—Al—O2 | 109.0(2) |
| O1—Ag—O2′ | 100.9(1) | O1—Al—O2′ | 107.8(2) |
| O1′—Ag—O2 | 107.3(1) | O1′—Al—O2 | 108.9(2) |
| O1′—Ag—O2′ | 131.59(9) | O1′—Al—O2′ | 110.0(2) |
| O2—Ag—O2′ | 109.8(1) | O2—Al—O2′ | 111.0(2) |

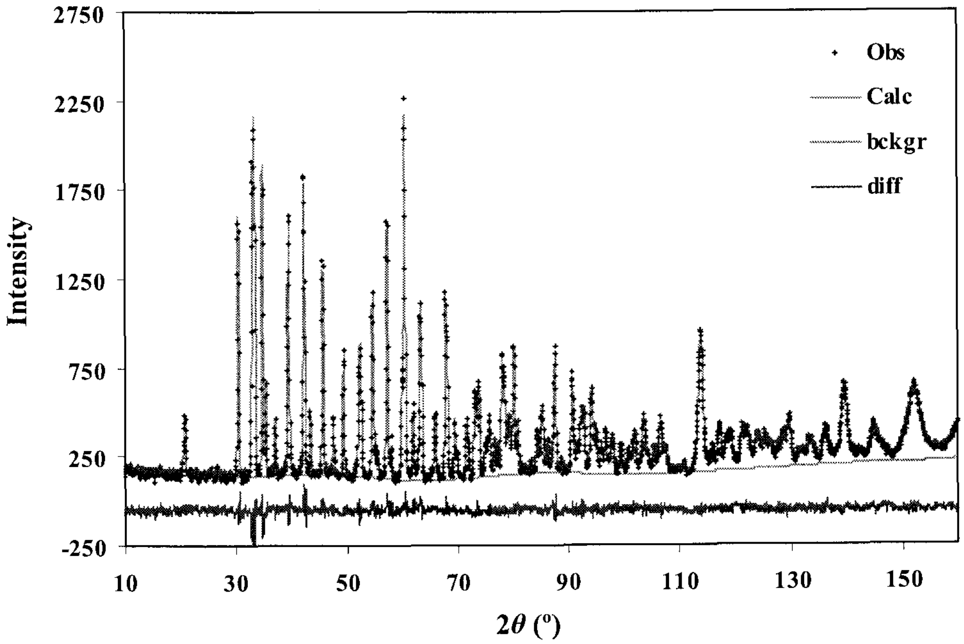

Figure 7.1 Observed (cross points) and calculated (solid line) neutron diffraction patterns of β-$AgAlO_2$ with the difference pattern below.

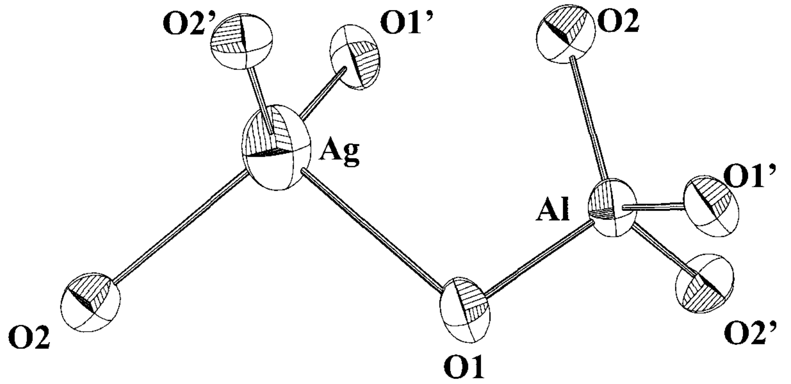

Figure 7.2 Structure of β-$AgAlO_2$ using ellipsoids to show relative thermal displacements where anion labels relate to Table 2.

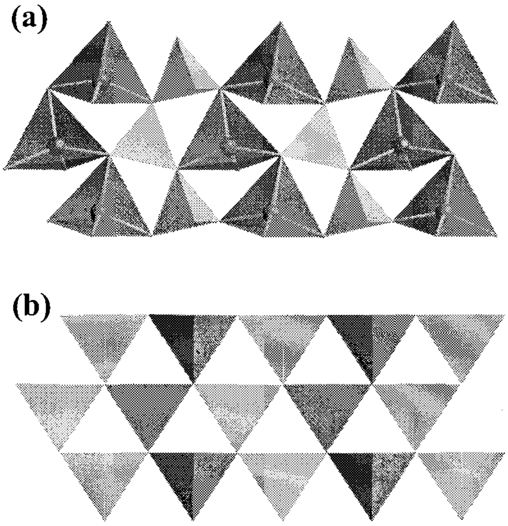

Figure 7.3 Structure of β-$AgAlO_2$ as corner sharing tetrahedral: (a) dark $AgO_4$ and light $AlO_4$ tetrahedra, (b) dark and light $OAg_2Al_2$ tetrahedra with a central O1 and O2 atom, respectively. Same projection for (a) and (b) with the *c* axis vertical.

## 7.4 Structural Systematics of MM'X Compounds

In a simple cubic lattice each atom has 6 nearest neighbors. A one-to-one ordering of unlike atoms in this lattice can lead to a structure where each atom has only the other atoms as near neighbors, i.e., the NaCl structure. The analogy for one-to-one ordering of cations is found in the $AMX_3$ perovskite structure where the M cations form a simple cubic lattice. Ordering of M and M' cations leads to the $A_2MM'X_6$ ordered perovskite structure where the M and M' cations have adopted a NaCl type arrangement, and the cubic symmetry can be retained. One-to-one ordering of cations becomes much more complicated starting with either a hexagonal or cubic closed-packed lattice. It is now geometrically impossible to order such that each cation will have only unlike cations as its 12 near neighbors. The most that can be accomplished is to have 8 unlike and 4 like near neighbors. Such ordering leads to a lower symmetry crystal class. Ordering in the cubic ZnS structure leads to tetragonal $MM'X_2$ compounds with a doubling of the unit cell volume. Ordering in the hexagonal ZnO structure leads to orthorhombic $MM'X_2$ compounds with a unit cell volume four times that of ZnO. Figure 7.4 shows the cation environment around Ag in β-$AgAlO_2$, which is analogous to the cation environment around Al. This figure shows how the ordering of cations has destroyed the hexagonal symmetry.

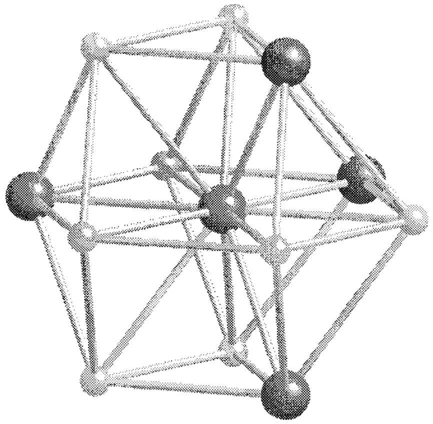

Figure 7.4 Near cation environment around Ag where the 8 Ag–Al distances from central Ag range from 3.20 to 3.50 Å and average 3.34 Å, and the 4 Ag–Ag distances range from 3.21 to 3.27 Å and average 3.24 Å. The *c* axis is vertical.

The number of variable parameters in the tetragonal tetrahedral $MM'X_2$ structure is three: *a*, *c*, and an *x* parameter for the anion. With just these three parameters, this structure can accommodate M and M' cations of different sizes while maintaining rather regular tetrahedra. The M–X distances are all equal to one another; the M'–X distances are all equal to one another; the angles are all close to the ideal tetrahedral value. The situation is very different for the orthorhombic $MM'X_2$ structure based on the hexagonal ZnO structure. The number of variable parameters is now fourteen: *a*, *b*, *c*, and 11 positional parameters associated with the two cations and the two crystallographically distinct anions. Despite the much greater number of variable parameters in this structure, this structure cannot as easily accommodate M and M' cations of different sizes. Our DLS calculations confirm that undistorted tetrahedra of different sizes cannot link together in this structure. A considerable range of M–X and M–X' bond lengths necessarily develops as the M/M' radius ratio deviates from unity, and the angles deviate strongly from the ideal tetrahedral value. This trend is most pronounced for the angles of the M(I) cation, and angle distortion indexes for the M(I) cation are shown in Figure 7.5 for the $MM'O_2$ series.

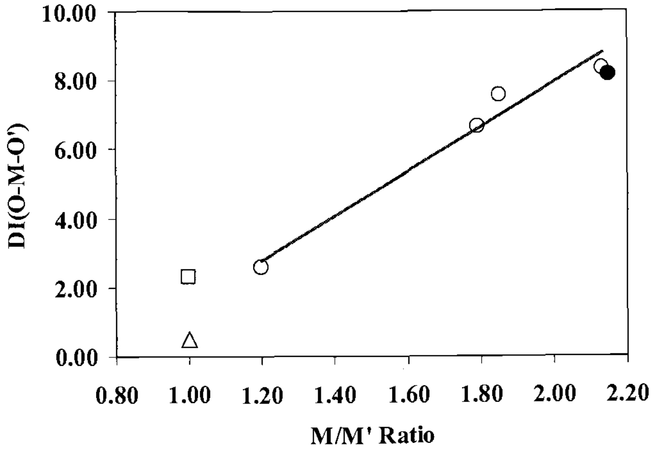

Figure 7.5 Angle distortion indexes for the M cation vs. the M/M' radius ratio [10] in orthorhombic $MM'O_2$ compounds. The square and triangle are for hexagonal ZnO [11] and BeO [12] respectively; open circles, from left to right, are for orthorhombic $LiGaO_2$ [13], $NaFeO_2$ [14], $NaGaO_2$ [15] and $NaAlO_2$ [16] respectively; and the solid circle is for $AgAlO_2$ (this work).

This distortion index is defined as the mean of the absolute value of the difference between the observed angles and the ideal tetrahedral angle of 109.5°. These values can be significant even when the size of M and M' are the same. For example, the angle distortion indexes for BeO and ZnO are 0.49 and 2.31, respectively. However, these indexes become much larger as the M/M' ratio deviates from unity (Fig. 7.5).

In the MM'$X_2$ series the cation tetrahedra tilt increasingly as the M/M' ratio deviates from unity. This tilting is shown for β-$AgAlO_2$ in Figure 7.3(a). This tilting is indicated by the difference in the *z* values for the two crystallographically distinct anions in this structure (Fig. 7.6). These two *z* values are exactly the same in hexagonal ZnO. The *z* values for the two cations would also be equal in the hexagonal ZnO structure, and these values remain very nearly the same in the orthorhombic structure. Thus, the anion tetrahedra do not show significant tilting (Fig. 7.3(b)).

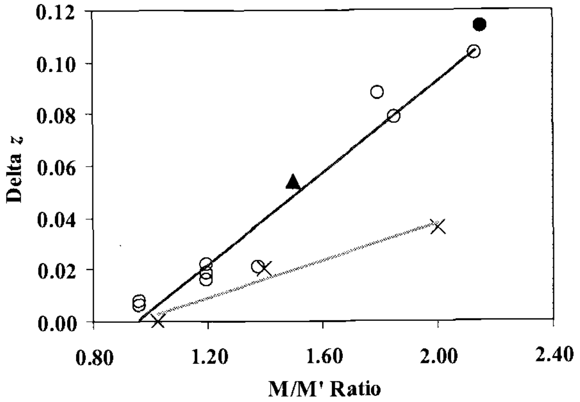

Figure 7.6 Anion delta *z* vs. the M/M' radius ratio in orthorhombic MM'$X_2$ compounds. Open circles, from top to bottom and left to right, are for $136_2$ type MM'$X_2$ compounds $LiInSe_2$ [17], $LiInS_2$ [18], $LiGaO_2$ [13], $LiGaS_2$ [19], $LiGaSe_2$ [19], $LiAlSe_2$ [20], $NaFeO_2$ [14], $NaGaO_2$ [15] and $NaAlO_2$ [16] respectively; solid triangle is for $AgInS_2$ [21] and solid circle is for $AgAlO_2$ (this work); cross points, from left to right, are for $245_2$ type MM'$X_2$ compounds $BeSiN_2$ [22], $ZnGeN_2$ [23] and $MnSiN_2$ [24].

Another change that occurs as the M/M' radius ratio deviates from unity is an increase of the *b*/*a* ratio (Fig. 7.7) from its ideal value of 1.155. Our DLS calculations show that both the increase in the *b*/*a* ratio and the increase in anion delta *z* are a direct result of having M and M' cations of different sizes.

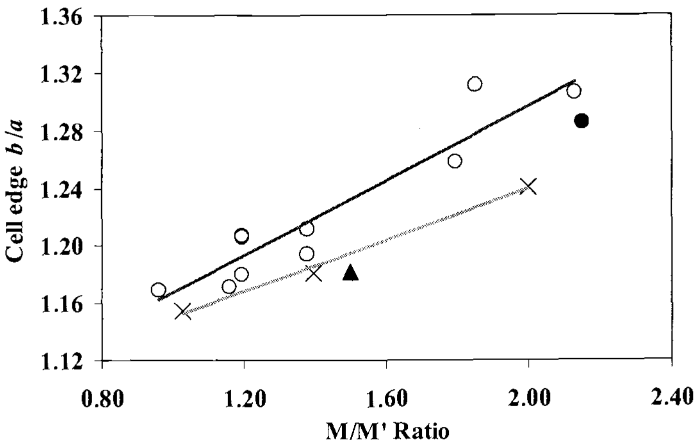

Figure 7.7 Cell edge *b*/*a* ratio vs. the M/M' radius ratio in orthorhombic MM'$X_2$ compounds. Open circles, from top to bottom and left to right, are for $136_2$ type MM'$X_2$ compounds $LiInSe_2$ [17], $LiInS_2$ [18] (overlapping with $LiInSe_2$), $LiFeO_2$ [25], $LiGaS_2$ [19], $LiGaSe_2$ [19] (overlapping with $LiGaS_2$), $LiGaO_2$ [13], $LiAlSe_2$ [20], $LiAlO_2$ [26], $NaFeO_2$ [14], $NaGaO_2$ [15] and $NaAlO_2$ [16] respectively; solid triangle is for $AgInS_2$ and solid circle is for $AgAlO_2$ [this work]; cross points, from left to right, are for $245_2$ type MM'$X_2$ compounds $BeSiN_2$ [22], $ZnGeN_2$ [23], and $MnSiN_2$ [24].

Bond valence calculations indicate significant underbonding of Ag in β-$AgAlO_2$ (Table 7.1). In fact, this is one more trend that correlates with the M/M' radius ratio (Fig. 7.8). Both M and M' cations appear to become underbonded as the M/M' radius ratio deviates from unity. This is most likely due to a failure of the usual bond valence approach to consider the effect of X–M–X angles or anion-anion repulsion. An M–X distance will be impacted both by the forces between M and X **and** the forces between X and X, which are not considered.

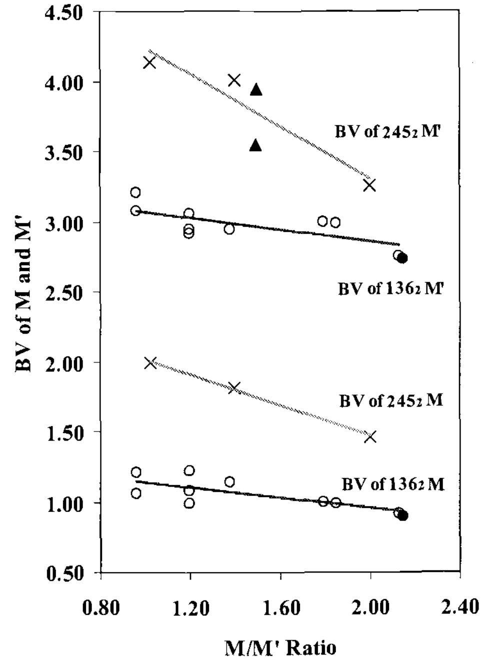

Figure 7.8 Bond valences of M and M’ vs. the M/M’ radius ratio in orthorhombic MM’$X_2$ compounds. Open circles, from top to bottom and left to right, are for $136_2$ type MM’$X_2$ compounds $LiInSe_2$ [17], $LiInS_2$ [18], $LiGaSe_2$ [19], $LiGaS_2$ [19], $LiGaO_2$ [13], $LiAlSe_2$ [20], $NaFeO_2$ [14], $NaGaO_2$ [15], $NaAlO_2$ [16]; solid triangles are for $AgInS_2$ [21] (top: BV of Ag, bottom: BV of In) and solid circles are for $AgAlO_2$ (this work); cross points, from left to right, are for $245_2$ type MM’$X_2$ compounds $BeSiN_2$ [22], $ZnGeN_2$ [23], and $MnSiN_2$ [24].

As a regular octahedron distorts, for example to a trigonal prism, anion-anion repulsion increases and the M–X distances are expected to increase. As the anion environment around a cation “distorts” from tetrahedral to square planar, the increased repulsion between anions is expected to give increased M–X distances. Thus, Shannon [10] gives the radius for tetrahedral Ag(I) to be 1.14 Å and the radius for square planar

Ag(I) to be 1.16 Å. Our observed Ag–O distances (Table 7.2) indicate underbonding only on the assumption of tetrahedral coordination. Although the bond distance approach accounts for the variation of Ag–O bond length, it does not account for the variation in O–Ag–O angles. Our observed distances agree well with Shannon radii if square planar Ag(I) is assumed instead of tetrahedral Ag(I). This may be considered as the appropriate correction when O–Ag–O angles deviate strongly from 109.5°.

It has previously been noted for tetrahedral MX compounds that higher ionicity favors the hexagonal structure over the cubic structure [27]. This is presumably due to the more favorable Madelung constant for the hexagonal structure. Figure 7.9 shows the stability field for tetrahedral tetragonal and orthorhombic compounds. Again, it is clear that the orthorhombic structure, which is based on the hexagonal structure, is favored by higher ionicity. Thus, all oxides and nitrides (top two rows) have the orthorhombic structure, and all tellurides and phosphides (bottom two rows) have the tetragonal structure. Both the tetragonal and orthorhombic structures are found for sulfides and selenides (middle two rows), but there is a clear dependency on ionicity. One compound, $AgInS_2$, is known in both structures [21,30]. With only this one exception, the orthorhombic structure is always found when the difference between the electronegativity on the anion and the average value for the cations is greater than 1.1, and the tetragonal structure is always found when this difference is less than 0.9.

Better characterization of orthorhombic $AgInS_2$ might resolve the issue of why it does not lie closer to the tetragonal-orthorhombic border in Fig. 7.9. The most recent structure study was based on X-ray powder diffraction data on a three-phase sample

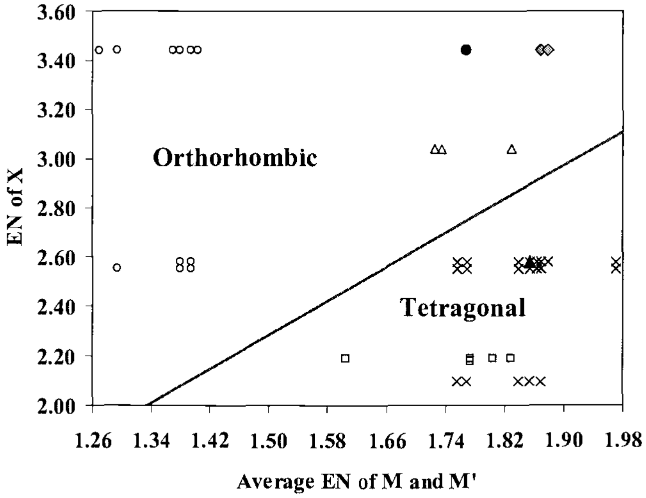

Figure 7.9 Stability field for tetragonal vs. orthorhombic MM'$X_2$ compounds. Pauling's electronegativity data were used [28]. Open circles and triangles are for $136_2$ and $245_2$ type orthorhombic MM'$X_2$ compounds mentioned above in this paper; solid circle is for $AgAlO_2$ [this work] and solid triangle is for $AgInS_2$ [21]; gray diamonds are for $AgFeO_2$ and $AgGaO_2$ [4,5]; cross points and squares are for $136_2$ [27] and $245_2$ [29] type tetragonal MM'$X_2$ compounds, respectively.

containing only 23% orthorhombic $AgInS_2$ [21]. All occupation factors were fixed at 100%, and individual thermal displacement factors were not refined. The cations Ag and In cannot be distinguished by X-ray diffraction due to their very similar scattering powers. Apparently no *z* parameter was fixed, which would likely lead to an unstable refinement. Note that even the *b*/*a* parameter for $AgInS_2$ does not fit the trend in Fig. 7.7. Furthermore, bond valences calculated for Ag and In based on the reported structure [21] are both too big (Fig. 7.8). Clearly, the structure and composition of "$AgInS_2$" need to be examined more closely.

## 7.5 References

1. W. Gessner. *Z. Anorg. Allg. Chem.*, 352, 145 (1967)
2. G. Brachtel, M. Jansen. *Cryst. Struct. Commun.*, 10, 173 (1981)
3. E. Thilo, W. Gessner. *Z. Anorg. Allg. Chem.*, 345, 151 (1966)
4. G. Hakvoort. *Therm. Anal., Proc. Int. Conf. 4th* ,1, 469 (1975)
5. G.A. Korteweg. *J. Magn. Reson.*, 42, 181 (1981)
6. G. Hakvoort. ICSD 21-1070I $AgAlO_2$, Delft, Netherlands, 1968
7. W.M. Meier, H. Villiger. *Z. Kristallogr.*, 129, 161 (1966)
8. B.H. Toby. *J. Appl. Crystallogr.*, 34, 210 (2001)
9. A.S. Wills, I.D. Brown. VaList, CEA, France (1999) Program available from ftp://ftp.ill.fr/pub/dif/valist/
10. R.D. Shannon. *Acta Crystallogr.*, A 32, 751 (1976)
11. O. Garcia-Martinez, R.M. Rojas, E. Vila, J.L. Vidales. *Solid State Ionics*, 63, 442 (1993)
12. G. Vidal-Valat, J.P. Vidal, K. Kurki-Suonio, R. Kurki-Suonio. *Acta Crystallogr.*, A 43, 540 (1987)
13. M. Marezio. *Acta Crystallogr.*, 18, 481 (1965)
14. E.F. Bertaut, A. Delapalme, G. Bassi. *J. Phys. (Paris) JOPQA*, 25, 545 (1964)
15. H.-P. Muller, R. Hoppe. *Z. Anorg. Allg. Chem.*, 611, 73 (1992)
16. J.A. Kaduk, S.Y. Pei. *J. Solid State Chem.*, 115, 126 (1995)
17. W. Hönle, G. Kühn, H. Neumann. *Z. Anorg. Allg. Chem.*, 543, 161 (1986)
18. Z.Z. Kish, A.S. Kanishcheva, Yu. N. Mikhailov, V.B. Lazarev, E.E. Semrad, E. Yu. Peresh. *Dokl. Akad. Nauk SSSR*, 280(2), 398 (1985)

19. L. Isaenko, A. Yelisseyev, S. Lobanov, A. Titov, V. Petrov, J.-J. Zondy, P. Krinitsin, A. Merkulov, V. Vedenyapin, J. Smirnova. *Cryst. Res. Technol.*, 38(3-5), 379 (2003)

20. J.Y. Kim, T. Hughbanks. *Inorg. Chem.*, 39(14), 3092 (2000)

21. G. Delgado, A. J. Mora, C. Pineda, T. Tinoco. *Mater. Res. Bull.*, 36, 2507 (2001)

22. P. Eckerlin. *Z. Anorg. Allg. Chem.*, 353, 225 (1967)

23. M. Wintenberger, M. Maunaye, Y. Laurent. *Mater. Res. Bull.*, 8(9), 1049 (1973)

24. M. Maunaye, R. Marchand, J. Guyader, Y. Laurent, J. Lang. *Bull. Soc. Fr. Miner. Cristallogr.*, 94(5-6), 561 (1972)

25. Honma Takahiko, Noritake Tatsuo, Ukyou Yoshio. Jpn. Patent JP 10241688 A2 19980911 Heisei, 1998

26. K. Dörhöfer. *J. Appl. Crystallogr.*, 12(2), 240 (1979)

27. E. Parthe. Crystal *Chemistry of Tetrahedral Structures*; Gordon and Breach Science Publishers: New York, 1964; pp 129

28. A.L. Allred. *J. Inorg. Nucl. Chem.*, 17, 215 (1961)

29. J.E. Jaffe, A. Zunger. *Phys. Rev. B: Condens. Matter, Mater. Phys.*, 30(2), 741 (1984)

30. R.S. Roth, H.S. Parker, W.S. Brower. *Mater. Res. Bull.*, 8, 333 (1973)

# Chapter 8

# Conclusions and Future Work

## 8.1 General Conclusions

In this thesis work we investigated five structure systems including ten transition metal oxides and their derived compounds. These materials exhibit a very rich chemistry of structural, electrical, optical, dielectric, magnetic and thermal properties.

In Chapter 2, both the 2H and 3R forms of $CuScO_2$ have been intercalated with oxygen to yield $CuScO_{2+x}$ phases where $x$ has been observed to range from 0.0 to 0.12 and 0.44 to 0.5. The position of the interstitial oxygen in the $CuScO_{2.5}$ phases was determined from powder neutron diffraction data. In both cases the interstitial oxygen resides in triangular sites in the Cu layer. However, in the 3R form the oxygen is displaced 0.3 Å toward a Sc atom above or below the Cu plane. When heating the 2H form of $CuScO_2$ under oxygen, the oxygen initially absorbed is released at about 440 °C. The 3R form does not lose oxygen under these conditions but it does lose oxygen around 580 °C when heated in air. These are exceptionally low temperatures for the thermal reduction of $Cu^{2+}$ to $Cu^{1+}$ in an oxide system, but it is consistent with the low calculated bond valence sum of 1.7 for interstitial oxygen compared to 2.0 calculated for the network oxygen. The weak bond formed between the interstitial oxygen and Sc in 3R $CuScO_2$ is presumably the reason why this oxygen is more strongly held in the 3R form relative to the 2H form. On oxygen intercalation there is a 1.46% increase of the hexagonal *a* cell edge for the 2H form and a 1.61% increase for the 3R form. The *c* cell edge expands by 0.23% on oxidation of the 2H form, but contracts by 0.30% on oxidation of the 3R form. This contraction of *c* and greater expansion of *a* for the 3R form can be attributed to the weak bond formed between Sc and the interstitial oxygen. Most synthesis routes to $CuScO_2$ give a mixture of the 2H and 3R forms, and this mixing can extend to the atomic level in the form of stacking faults.

Substitution of Mg for Sc systematically increases the p-type conductivity in $CuSc_{1-x}Mg_xO_2$ sintered powders, producing a maximum conductivity of 0.015 S/cm at $x \approx 0.06$. A similar level of conductivity is observed in transparent polycrystalline $CuSc_{1-x}Mg_xO_2$ films at the same doping level. Mg doping causes no significant increase in optical absorption at this level. Intercalation of oxygen into the delafossite structure leads to a much larger increase in p-type conductivity. In the $CuSc_{1-x}Mg_xO_{2+y}$ powders, the maximum conductivity is 0.5 S/cm at $y = 0.23$ and $x = 0.05$. In oxygen-intercalated films, the maximum conductivity was 25 S/cm.

In Chapter 3, zinc oxide powders prepared by peroxide and nitrate decompositions show evidence of holes in the O 2*p* band by iodometric titration. Chemical analysis also shows the presence of nitrogen in samples prepared by nitrate decomposition. The evidence for holes disappears on heating samples at 500 °C, eliminating the possibility of transport measurements on sintered samples. Complex impedance spectra suggest room temperature conductivities as high as $1.7 \times 10^{-4}$ and $2 \times 10^{-3}$ S/cm for these peroxide and nitrate derived zinc oxide powders. As zinc oxide particles become small there is an increase in cell dimensions and a red shift of the absorption band. An even stronger red shift is observed in the case of N doping.

In Chapter 4, the combination of neutron and synchrotron data has established the formula of "$SrCu_3Ti_4O_{12}$" as $Sr_{0.946}(Cu_{2.946}Ti_{0.054})Ti_4O_{12}$ (SCTO), indicating a highly unusual situation of Ti(IV) on the square planar sites of Cu(II). The temperature dependence of the dielectric constant for this phase is similar to that of $CaCu_3Ti_4O_{12}$ (CCTO), but the magnitude is very much lower. Complex impedance data for SCTO are consistent with a material composed of conducting regions separated by barriers of much higher resistivity. This same situation in CCTO apparently causes its high dielectric constant according to a barrier layer mechanism. The highly unusual properties of CCTO are rationalized on the basis of very small amounts of Ti on Cu sites. Complex impedance spectra were also obtained on a crystal of $CaCu_3Ti_4O_{12}$ (CCTO) from 289 to 456 K. As in the case of ceramic CCTO, these spectra can be interpreted as arising from a conducting material containing insulating barriers. This is the further evidence for the existence of planar defects within crystals of CCTO that act as insulating barriers and produce the large dielectric constant through a space charge mechanism.

Materials that show various responses to multiple external stimuli enable novel device applications. The behavior of systems with strong coupling between magnetic and electronic degrees of freedom provides both challenges for solid state theory as well as novel phenomena for applications such as colossal magnetoresistance in perovskite manganites. Similarly, a strong coupling between magnetism and dielectric properties in magnetic insulators or semiconductors should lead to devices based on magnetodielectric effect, where the dielectric properties can be controlled by a magnetic field. In Chapter 5, A ferromagnetic compound $La_2NiMnO_6$ was prepared by solid state reaction, the nuclear and magnetic structures were analyzed using neutron powder diffraction, and the magnetic structure was reported for the first time. Semiconducting behavior was proved with a resistivity of about $10^2$ Ω·cm at room temperature, and large magnetocapcitance and magnetoresistance were found near room temperature, which makes $La_2NiMnO_6$ a very promising candidate material for spintronics applications.

In Chapter 6, the structure of 2H $CuScO_2$ has been refined from single-crystal X-ray diffraction data obtained at room temperature and from neutron powder diffraction data obtained from 11 to 1206 K. Strong negative thermal expansion ($-4.0 \times 10^{-6}$/K) has been found for the apparent Cu–O bond length below 300 K. This is an unusual example of strong negative thermal expansion in a metal oxide based on an O–M–O linkage instead of a M–O–M linkage. It is now the transverse thermal motion of Cu, instead of the transverse thermal motion of oxygen that causes the negative thermal expansion. As expected for this mechanism for negative thermal expansion, the thermal displacement parameter for Cu is very pronounced perpendicular to the linear O–Cu–O linkage.

In addition, powder neutron diffraction data were obtained from 30 to 600 K for $CuAlO_2$, $CuInO_2$, $CuLaO_2$, 3R $CuScO_2$, and $AgInO_2$. Rietveld refinements of these data showed negative thermal expansion of the O–Cu–O linkage in all cases. This behavior was especially strong for $CuLaO_2$ and $CuScO_2$, where it persisted up to our maximum measuring temperature of 600 K. The negative thermal expansion behavior increases in the $CuMO_2$ series as the size of M increases. This negative thermal expansion in turn caused negative thermal expansion of the *c* cell edge, which was moderated by the positive thermal expansion of the M–O bonds. No negative thermal expansion behavior was found for the O–Ag–O linkage in $AgInO_2$; nonetheless, this compound did exhibit negative thermal expansion for the *c* cell edge at low temperatures. For $CuLaO_2$ there is negative thermal expansion for both the *a* and *c* cell edges at low temperatures. Structural trends for compounds with the delafossite structure are discussed with respect to both composition and temperature.

In Chapter 7, the structure of β-$AgAlO_2$ was refined from neutron diffraction data by the Rietveld method. The space group is $Pna2_1$ with $a = 5.4306(1)$ Å, $b = 6.9802(1)$ Å, $c = 5.3751(1)$ Å, and $Z = 4$. Both cations are tetrahedrally coordinated to oxygen. The tetrahedron around Al is quite regular with distances ranging from 1.75 to 1.77 Å and angles ranging from 107.8 to 111.0°. The tetrahedron around Ag is, however, highly distorted with distances ranging from 2.35 to 2.48 Å and angles ranging from 99.3 to 131.6°. The low bond valence calculated for Ag(I) of 0.895 is attributed to the strong deviation of the O–Ag–O angles from 109.5°. This structure is based on the hexagonal ZnO structure, and we show that the ordered arrangement of M(I) and M(III) cations in this structure directly causes the tetrahedra to distort and tilt (Fig. 8.1).

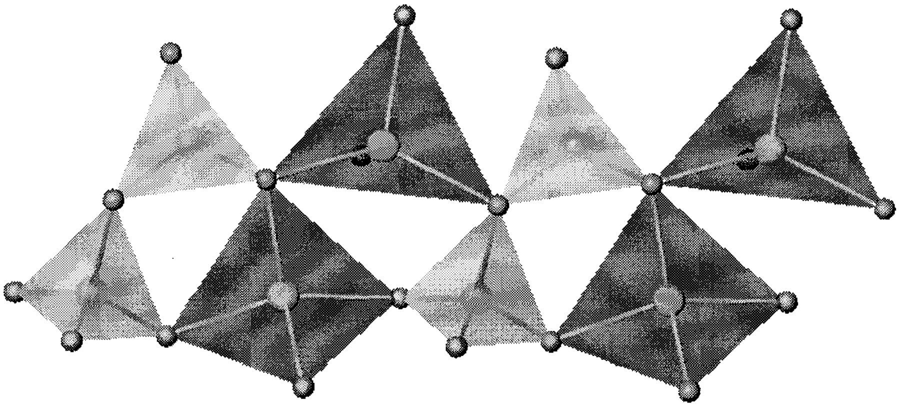

Figure 8.1 Structure of β-$AgAlO_2$ shown as corner-sharing $AlO_4$ (small) and $AgO_4$ (large) tetrahedra along the *c* axis.

## 8.2 Future Work

Knowledge has no limit. In the field of science, one finding always leads to another. The mission is not completed in this piece of work and it will never be. We can always find more work to do in the future. We could grow $CuSc_{1-x}Mg_xO_2$ single crystals big enough for transport property measurements and look for the anisotropic behavior along *a* and *c* axes separately. We could make thin films of ferromagnetic $La_2NiMnO_6$ and further incorporate it into spintronic devices to realize its applications. The research of p-type ZnO in this thesis is just a piece of preliminary work; lots of data collected need to be interpreted in a satisfactory way; lots of more work needs to be done to clear some doubts; and new synthesis routes need to be found to improve the p-type conductivity in the material.

# Bibliography

T.G. Amos. Negative Thermal Expansion in $AOMO_4$ Compounds. Ph.D. Thesis, Oregon State University, Corvallis, OR, 2001

T.G. Amos, A.W. Sleight. *J. Solid State Chem.*, 160, 230 (2001)

T.G. Amos, A. Yokochi, A.W. Sleight. *J. Solid State Chem.*, 14, 303 (1998)

P.W. Anderson. *Phys. Rev.*, 79, 350 (1950)

M.P. Attfield, A. W. Sleight. *Chem. Commun.*, 601-602 (1998)

M.P. Attfield, A. W. Sleight. *Chem. Mater.*, 10, 2013-2019 (1998)

G.E. Bacon. *Neutron Scattering in Chemistry*; Butterworths Inc.: Boston, 1977

K. Badeker. *Ann. Phys.* (Leipzig), 22, 749 (1907)

M.N. Baibich, J.M. Broto, A. Fert, F. Nguyen Van Dau, F. Petroff, P. Eitenne, G. Creuzet, A. Friederich, J. Chazelas. *Phys. Rev. Lett.*, 61, 2472 (1988)

F.A. Benko, F.P. Koffyberg. *J. Phys. Chem. Solids*, 45, 57 (1984)

F.A. Benko, F.P. Koffyberg. *Can. J. Phys.*, 63, 1306 (1985)

F.A. Benko, F.P. Koffyberg. *Phys. Status Solidi A*, 94, 596 (1986)

F.A. Benko, F.P. Koffyberg. *Mater. Res. Bull.*, 21, 753 (1986)

J.M. Bian, X.M. Li, X.D. Gao, W.D. Yu, L.D. Chen. *Appl. Phys. Lett.*, 84(4), 541 (2004)

J.M. Bian, X.M. Li, C.Y. Zhang, W.D. Yu, X.D. Gao. *Appl. Phys. Lett.*, 85(18), 4070 (2004)

G. Binasch, P. Grunberg, F. Saurenbach, W. Zinn. *Phys. Rev. B*, 39, 4828 (1989)

M. Blackman. *Philos. Mag.*, 9, 831 (1958)

J. Blasco, M.C. Sanchez, J. Perez-Cacho, J. Garcia, G. Subias, J. Campo. *J. Phys. Chem. Solids*, 63, 781 (2002)

J.P. Boilot, J.P. Salanie, G. Desplanches, D Le Potier. *Mater. Res. Bull.*, 14, 1469 (1979)

In *Ceramic Materials for Electronics, Processing, Properties, and Applications*; R.C. Buchanan Ed.; Marcel Dekker, Inc.: New York, 1986

C.L. Bull, D. Gleeson, K.S. Knight. *J. Phys.: Condens. Matter*, 15, 4927 (2003)

R.J. Cava, H.W. Zandbergen, A.P. Ramirez, H. Takagi, C.T. Chen, J.J. Krajewski, W.F. Peck Jr., J.V. Waszczak, G. Meigs, R.S. Roth, L.F. Schneemeyer. *J. Solid State Chem.*, 104, 437 (1993)

G. Chiodelli, V. Massarottie, D. Capsoni, M. Bini, C.B. Azzoni, M.C. Mozzati, P. Lupotto. *Solid State Commun.*, 132, 241 (2004)

K.L. Chopra, S. Major, T.K. Pandya. *Thin Solid Film*, 102, 1 (1983)

R.I. Dass, J.Q. Yan, J.B. Goodenough. *Phys. Rev. B*, 68, 064415/1-064415/12 (2003)

M.T. Dove, V. Heine, K.D. Hammonds. *Mineral. Magn.*, 59, 629 (1995)

N. Duan, U. Kameswari, A.W. Sleight. *J. Am. Chem. Soc.*, 121, 10432 (1999)

N. Duan, A.W. Sleight, M.K. Jayaraj, J. Tate. *Appl. Phys. Lett.*, 77, 1325 (2000)

M. Elazhari, A. Ammar, M. Elaatmani. *Eur. J. Solid State Inorg. Chem.*, 34, 503 (1997)

G. Ernst, C. Broholm, G.R. Kowach, A.P. Ramirez. *Nature*, 396(12) 147 (1998)

J.S.O. Evans, T.A. Mary, A.W. Sleight. *J. Solid State Chem.*, 137, 148 (1998)

J.S.O. Evans, T.A. Mary, T. Vogt, M.A. Subramanian, A.W. Sleight. *Chem. Mater.*, 8, 2809 (1996)

P.M Forster, A.W. Sleight. *Int. J. Inorg. Mater.*, 1, 123-127 (1999)

P.M. Forster, A. Yokochi, A.W. Sleight. *J. Solid State Chem.*, 140, 157 (1998)

In *Diluted Magnetic Semiconductors*; J.K. Furydna, J. Kossut. Eds.; Semiconductors and Semimetals; Academic Press: New York, 1988; Vol. 25

F.H. Gillery, E.A. Bush. *J. Am. Ceram. Soc.*, 42, 175-177 (1959)

E. Giulotto, M.C. Mozzati, C.B. Azzoni, V. Massarotti, D. Capsoni, M. Bini. *Ferroelectrics*, 298, 61 (2004)

J.B. Goodenough. *Magnetism and the Chemical Bond*; John Wiley & Sons: New York, 1963

J.B. Goodenough. *Prog. Solid State Chem.*, 5, 145 (1971)

J.B. Goodenough, A.L. Loeb. *Phys. Rev.*, 98, 391 (1955); J.B. Goodenough. ibid. 100, 564 (1955)

J.B. Goodenough, A. Wold, R.J. Arnott, N. Menyuk. *Phys. Rev.*, 124, 373 (1961)

R.G. Gordon. *MRS Bull.*, 25, 52 (2000)

I. Hamberg, C.G. Granqvist. *J. Appl. Phys.*, 60, R123 (1986)

L. He, J.B. Neaton, D. Vanderbilt, M.H. Cohen. *Phys. Rev. B*, 67, 012103 (2003)

M.F. Hochella, G.E. Brown, F.K. Ross, G.V. Gibbs. *Am. Mineral.*, 64, 337 (1979)

C.C. Homes, T. Vogt, S.M. Shapiro, S. Wakimoto, A.P. Ramirez. *Science*, 293, 673 (2001)

C.C. Homes, T. Vogt, S.M. Shapiro, S. Wakimoto, M.A. Subramanian, A.P. Ramirez. *Phys. Rev. B*, 67, 092106 (2003)

H. Iwahara, T. Esaka, H. Uchida, N. Maeda. *Solid State Ionics*, 3/4, 359 (1981)

M. Joseph, H. Tabata, T. Kawai. *J. Appl. Phys.*, Part 2 (11A), L1205 (1999)

Y. Kakehi, S. Nakao, K. Satoh, T. Yotsuya. *Thin Solid Films.*, 445, 294 (2003)

J. Kanamori. *J. Phys. Chem. Solids*, 10, 87 (1959)

H. Kawazoe, H. Yanagi, K. Ueda, H. Hosono. *MRS Bull.*, 25, 28 (2000)

H. Kawazoe, M. Yasukawa, H. Hyodo, M. Kurita, H. Yanagi, H. Hosono. *Nature*, 389, 939 (1997)

N. Khosrovani, V. Korthuis, A.W. Sleight, T. Vogt. *Inorg. Chem.*, 35, 485 (1996)

N. Khosrovani, A.W. Sleight. *J. Inorg. Mater.*, 1, 3-10 (1999)

N. Khosrovani, A.W. Sleight, T. Vogt. *J. Solid State Chem.*, 132, 355 (1997)

V. Korthius, N. Khosrovani, A.W. Sleight, N. Roberts, R. Dupree, W.W. Wareen Jr.. *Chem. Mater.*, 7, 412 (1995)

D.E. Kotecki, J.D. Baniecki, H. Shen, R.B. Labibowitz, K.L. Saenger, J.J. Lian, T.M. Shaw, S.D. Athavale, C. Cabral, Jr.,P.R. Duncombe, M. Gutsche, G. Kunkel, Y.J. Park, Y.Y. Wang, R. Wise. *IBM J. Res. Dev.*, 43, 367 (1999)

H.A. Kramers. *Physica*, 1, 182 (1934)

A. Kudo, H. Yanagi, H. Hosono, H. Kawazoe. *Appl. Phys. Lett.*, 73, 220 (1998)

A. Kudo, H. Yanagi, K. Ueda, H. Hosono, H. Kawazoe, Y. Yano. *Appl. Phys. Lett.*, 75, 2851 (1999)

R. Kykyneshi. M.S. Thesis, Oregon State University, Corvallis, OR, 2004

H.C. Li, W. Si, A.D. West, X.X. Xi. *Appl. Phys. Lett.*, 73, 464 (1998)

Y. Lin, Y.B. Chen, T. Garret, S.W. Liu, C.L. Chen, L. Chen, R.P. Bontchev, A. Jacobson, J.C. Jiang, E.I. Meletis, J. Horwitz, H.D. Wu. *Appl. Phys. Lett.*, 81, 631 (2002)

D.C. Look. *Mater. Sci. Eng. B*, 80, 383 (2001)

D.C. Look *et al. Phys. Status Solidi A*, 195(1), 171 (2003)

D.C. Look, D.C. Reynolds, C.W. Litton, R.L. Jones, D.B. Eason, G. Cantwell. *Appl. Phys. Lett.*, 81(10), 1830 (2002)

J.G. Lu, Z.Z. Ye, L. Wang, J.Y. Huang, B.H. Zhao. *Mater. Sci. Semicond. Proc.*, 5, 491-496 (2003)

P. Lunkenheimer, R. Fichtl, S.G. Ebbinghaus, A. Loidl. *Phys. Rev. B*, 70, 172102 (2004)

In *Impedance Spectroscopy : Emphasizing Solid Materials and Systems*. J.R. Macdonald Ed.; John Wiley & Sons: New York, 1987

T.A. Mary, J.S.O. Evans, A.W. Sleight, T. Vogt. *Science*, 272, 90 (1996)

R. Nagarajan, A.D. Draeseke, A.W. Sleight, J. Tate. *J. Appl. Phys.*, 89, 8022 (2001)

R. Nagarajan, N. Duan, M.K. Jayaraj, J. Li, K.A. Vanaja, A. Yokochi, A. Draeseke, J. Tate, A.W. Sleight. *Int. J. Inorg. Mater.*, 3, 265 (2001)

H. Ohno. *Science*, 281, 951 (1998); *J. Magn. Magn. Mater.*, 200, 110 (1999)

Y. Ohno, D.K. Young, B. Beschoten, F. Matsukura, H. Ohno, D.D. Awschalom. *Nature*, 402, 790 (1999)

H. Ohta *et al. Appl. Phys. Lett.*, 77(4), 475 (2000)

H. Ohta, M. Orita, M. Hirano, H. Tanji, H. Kawazoe, H. Hosono. *Appl. Phys. Lett.*, 77, 475 (2000)

T. Otabe, K. Ueda, A. Kudoh, H. Hosono, H. Kawazoe. *Appl. Phys. Lett.*, 72, 1036 (1998)

A. Pabst. *Am. Mineral.*, 31, 539 (1946)

E. Parthe. *Crystal Chemistry of Tetrahedral Structures*. Gordon and Breach Science Publishers: New York, 1964

G.A. Prinz. *Science*, 282, 1660 (1998)

I.P. Raevski, S.A. Prosandeev, A.S. Bogatin, M.A. Malitskaya, L. Jastrabik. *J. Appl. Phys.*, 93, 4130 (2003)

A.P. Ramirez, M.A. Subramanian, M. Gardel, G. Blumberg, D. Li, T. Vogt, S.M. Shapiro. *Solid State Commun.*, 115, 217 (2000)

R.M. Rose, L.A. Shepard, J. Wulff. *Electronic Properties*; John Wiley and Sons: New York, 1966

H. Sato, T. Minami, S. Takata, T. Yamada. *Thim Solid Films*, 236, 27 (1993)

R. Schad, C.D. Potter, P. Belien, G. Verbanck, V.V. Moschchalkov, Y. Bruynseraede. *Appl. Phys. Lett.*, 64, 3500 (1994)

D.R. Scifres, B.A. Huberman, R.M. White, R.S. Bauer. *Solid State Commun.*, 13, 1615 (1973)

G Shirane, S. Hoshino. *J. Phys. Soc. Jpn.*, 6, 265 (1951)

W. Si, E.M. Cruz, P.D. Johnson, P.W. Barnes, P. Woodward, A.P. Ramirez. *Appl. Phys. Lett.*, 81, 2056 (2002)

D.C. Sinclair, T.B. Adams, F.D. Morrison, A.R. West. *Appl. Phys. Lett.*, 80, 2153 (2002)

A.V. Singh, R.M. Mehra, A. Wakahara, A. Yoshida. *J. Appl. Phys.*, 93(1), 396 (2003)

A.W. Sleight. *Supercurrents*, 5, 2 (1988)

A.W. Sleight. *Endeavor*, 19(2), 64 (1995)

A.W. Sleight. *Inorg. Chem.*, 37(12), 2854-2860 (1998)

M.A. Subramanian, D. Li, N. Duan, B.A. Reisner, A.W. Sleight. *J. Solid State Chem.*, 151, 323 (2000)

M.A. Subramanian, A.W. Sleight. *Solid State Sci.*, 4, 347 (2002)

G.A. Sumara, L.A. Boatner. *Phys. Rev. B*, 61, 3889 (2000)

J.Z. Tao, A.W. Sleight. *J. Solid State Chem.*, 173, 45-48 (2003)

J.Z. Tao, A.W. Sleight. *J. Solid State Chem.*, 173, 442-448 (2003)

D. Taylor. *Br. Ceram. Trans. J.*, 83, 129 (1984)

D. Taylor. *Br. Ceram. Trans. J.*, 87, 39 (1988)

G. Thomas. *Nature*, 389, 907 (1997)

W. Tiano, M. Dapiaggi, G. Artioli. *J. Appl. Crystallogr.*, 36, 1461 (2003)

A. Tselev, C.M. Brooks, S.M. Anlage, H. Zheng, L. Salamanca-Riba, R. Ramesh, M.A. Subramanian. *Phys. Rev. B*, 70, 144101 (2004)

K, Ueda, T. Hase, H. Yanagi, H. Kawazoe, H. Hosono, H. Ohta, M. Orita, M. Hirano. *J. Appl. Phys.*, 89, 1790 (2001)

J.H. van Santen, G.H. Jonker. *Physica* (*The Hague*), 16, 599 (1950); G.H. Jonker, J.H. van Santen. ibid. 16, 337-349 (1950); J. Volger. ibid. 20, 49-66 (1954)

N.Y. Vasanthacharya, P. Ganguly, J.B. Goodenough, C.N.R. Rao. *J. Phys. C: Solid State Phys.*, 17, 2745 (1984)

R.P. Wang, A.W. Sleight, D. Cleary. *Chem. Mater.*, 8, 433-439 (1996)

R.P. Wang, A.W. Sleight, R.Platzer, J.A. Gardner. *J. Solid State Chem.*, 122, 166-175 (1996)

M.T. Weller, P.F. Henry, C.C. Wilson. *J. Phys. Chem. B*, 104, 12224 (2000)

A.R. West. *Basic Solid State Chemistry*, 2nd ed.; John Wiley & Sons: New York, 1999

A. Wold, R.J. Arnott, J. B. Goodenough. *J. Appl. Phys.*, 29, 387 (1958)

Q. Xu, D.P. Huang, W. Chen, J.H. Lee, B.H. Kim, H. Wang, R.Z. Yuan. *Ceram. Int.*, 30(3), 429-433 (2004)

T. Yamamoto, H. Katayama-Yoshida. *Jpn. J. Appl. Phys.*, 38, L166 (1999)

H. Yanagi, T. Hase, S. Ibuki, K. Ueda, H. Hosono. *Appl. Phys. Lett.*, 78, 1583 (2001)

H. Yanagi, S. Inoue, K. Ueda, H. Kawazoe, H. Hosono. *J. Appl. Phys.*, 88, 4159 (2000)

H. Yanagi, H. Kawazoe, A. Kudo, M. Yasukawa, H. Hosono. *J. Electroceram.*, 4, 427 (2000)

H. Yanagi, K. Ueda, H. Ohta, M. Orita, M. Hirano, H. Hosono. *Solid State Commun.*, 121, 15 (2002)

D.S. Yoon, J.S. Roh. *Crit. Rev. Solid State Mater. Sci.*, 27, 143 (2002)